

Improving the Limit on the Electron EDM: Data Acquisition and Systematics Studies in the ACME Experiment

A thesis presented

by

Paul William Hess

to

The Department of Physics

in partial fulfillment of the requirements

for the degree of

Doctor of Philosophy

in the subject of

Physics

Harvard University

Cambridge, Massachusetts

May 2014

©2014 - Paul William Hess

All rights reserved.

Thesis advisor

Gerald Gabrielse

Author

Paul William Hess

Improving the Limit on the Electron EDM: Data Acquisition and Systematics Studies in the ACME Experiment

Abstract

The ACME collaboration has completed a measurement setting a new upper limit on the size of the electron's permanent electric dipole moment (EDM). The existence of the EDM is well motivated by theories extending the standard model of particle physics, with predicted sizes very close to the current experimental limit. The new limit was set by measuring spin precession within the metastable H state of the polar molecule thorium monoxide (ThO). A particular focus here is on the automated data acquisition system developed to search for a precession phase odd under internal and external reversal of the electric field. Automated switching of many different experimental controls allowed a rapid diagnosis of major systematics, including the dominant systematic caused by an imperfect reversal of electric fields coupled with laser polarization gradients. Polarimetry measurements made it possible to quantify and minimize the polarization gradients in our state preparation and probe lasers. Three separate measurements were used to determine the non-reversing electric field component which changes the field's magnitude correlated with its direction. The new bound of $|d_e| < 8.7 \times 10^{-29} e \cdot \text{cm}$ is over an order of magnitude smaller than previous limits, and strongly limits T-violating physics at TeV energy scales.

Contents

Title Page	i
Abstract	iii
Table of Contents	iv
List of Figures	vii
List of Tables	x
Acknowledgments	xi
1 Introduction	1
1.1 EDMs and T-Violating Extensions to the Standard Model	3
1.2 An EDM Experiment in ThO	7
1.2.1 Statistical Sensitivity	9
1.2.2 ThO Molecular Structure	11
1.3 Advantages of ThO	15
1.3.1 Large Effective Electric Field	16
1.3.2 Systematic Rejection through Omega Doublets	18
1.3.3 Small Magnetic Moment	19
1.3.4 Experimental Simplifications	20
2 The ACME Experiment: Measurement Procedure and Apparatus	22
2.1 Spin Precession Measurement	23
2.2 Data Analysis: Notation and Procedure	28
2.3 Apparatus	30
2.3.1 Beam Source	31
2.3.2 Ground State Rotational Enhancement	32
2.3.3 Interaction Region	33
3 <i>C</i> State Lifetime and Linestrength Calculations	36
3.1 Measurement of the <i>C</i> State Lifetime	37
3.2 Molecular Transition Matrix Elements	43
3.3 Molecular Constants From <i>C</i> State Lifetime	47
3.3.1 Partial Decay Rates	48

3.3.2	Branching Ratios	50
3.3.3	$X \rightarrow C$ Transition Dipole Moment	54
3.3.4	Optical Absorption Cross Section	56
3.3.5	Fluorescence Saturation Intensity	58
3.3.6	Optical Excitation Rate	61
4	Properties of State Preparation and Probe Lasers	63
4.1	Optical Configuration	63
4.1.1	Laser Amplification and Shaping	64
4.1.2	Fast Polarization Switching	67
4.2	Temporal Profile: Sub-Bin Signal Dependence	71
4.2.1	Saturation and Fluorescence Model	73
4.2.2	Fluorescence Profiles in a Molecular Beam	76
4.3	Spatial Profile: Polarization Gradients	80
4.3.1	Thermally Induced Stress Birefringence	81
4.3.2	Polarization Effects of Thermal Birefringence	82
4.3.3	Measuring Circular Polarization Gradients	87
4.4	Contrast Lineshapes	90
5	ACME Data Acquisition System	94
5.1	Data Acquisition Structure	95
5.1.1	Block and Superblock Switches	96
5.1.2	Longer Switches and Interleaved Systematic Checks	99
5.2	Switching Timescales	102
5.2.1	Duty Cycle	103
5.2.2	Switch Rates and Noise Filtering	106
5.3	\mathcal{E}^{nr} Suppression Through Lead Switching	111
5.4	Experimental Switches	115
5.4.1	Electric Field Control	115
5.4.2	Frequency Switching for \mathcal{N} and \mathcal{P} State Selection	118
5.4.3	Polarization Control	123
5.4.4	Magnetic Field Control	124
5.5	Acquisition of Phase Precession Data	125
6	Measuring Electric Fields with ThO	128
6.1	Relevant Field Components	130
6.2	Raman Measurement	132
6.2.1	Stimulated Raman Transitions and Measurement Procedure	133
6.2.2	Experimental Configuration	136
6.2.3	Raman Lineshape	139
6.2.4	Data Acquisition and Results	142
6.3	Microwave Measurement	146

6.4	A Comparison of \mathcal{E} -Field Maps	151
6.5	Measuring H and C State Molecule Fixed Dipole Moments	156
7	Systematic and Statistical Limits	159
7.1	The \mathcal{E}^{nr} and $\Omega_r^{\mathcal{N}\mathcal{E}}$ Systematics	160
7.1.1	Modeling the AC Stark Shift Phases	161
7.1.2	Measurement of \mathcal{E}^{nr} Correlations	168
7.1.3	Measurement of $\Omega_r^{\mathcal{N}\mathcal{E}}$ Correlations	172
7.2	Systematic Error Budget	175
7.2.1	Observed EDM Correlated Systematics	177
7.2.2	Systematic Errors without Observed Correlations	181
7.3	Statistical Analysis	183
7.4	Results and Interpretation	185
8	Conclusion and Future Steps	188
A	ACME PMTs	192
A.1	PMT Enclosure Assembly and Operation	193
A.2	Setting Discriminator Level for Photon Counting	196
B	Stokes Polarimeter System	200
B.1	Useful Definitions in Polarimetry	201
B.2	Polarimeter Fundamentals of Operation	204
B.3	Assembly and Alignment	206
B.4	Calibration	208
B.4.1	Fixed Calibration and Analysis Polarizer	209
B.4.2	Removing the Quarter-Wave Plate	210
B.4.3	Full 2D Fit	211
C	Running the ACME Experiment: VI Operation Specifics	213
C.1	Programming a Run	214
C.2	Doppler Scans of Pump and Probe Lasers	218
D	Linearized Decay Fitting	221
E	Complete List of Systematic Checks	223
	Bibliography	226

List of Figures

1.1	P and T violation due to an electron EDM	6
1.2	Complete history of published electron EDM limits	8
1.3	Angular momentum coupling in Hund's case (c)	12
1.4	Electronic states of ThO relevant for the ACME experiment	13
1.5	Level diagram of the H state in the limit of large electric field	14
1.6	Unpolarized fraction of the H state wavefunction as a function of electric field	18
1.7	Angular momentum cancellations leading to a reduced magnetic moment in the H state	20
2.1	Relevant energy levels for the spin precession measurement	24
2.2	Schematic of the EDM apparatus	30
3.1	Schematic of the C state lifetime measurement apparatus	39
3.2	Example decay curves plotted on linear and log scales	40
3.3	The dependence of τ_C on the PMT supply voltage	42
3.4	Notation diagram for state labels and rotational transition branches	44
3.5	Diagram of the model used to consider saturation of the $X \rightarrow C$ transition	59
3.6	Saturation of observed fluorescence intensity from the $X \rightarrow C$ transition	60
4.1	Intensity profile of the state preparation beam with intentional spherical aberration	65
4.2	Layout of beam shaping and polarization control optics outside the interaction region	67
4.3	Trigger waveforms for polarization switching plotted alongside measured fluorescence signals.	69
4.4	Time resolved Stokes parameters while polarization switching with an EOM	70
4.5	Simplified level scheme relevant for optical pumping out of the H state	72
4.6	Fluorescence decay curves from $H \rightarrow C$ optical pumping	74

4.7	Diagram and fits of two components that contribute to temporal shape of observed H state probe fluorescence	77
4.8	Measured linear relationship between optical excitation rate and probe laser power	79
4.9	Circular polarization gradients in the probe laser beam with at various input polarization angles	88
4.10	Angular dependence of thermally induced polarization gradients	89
4.11	Power dependence of thermally induced polarization gradients	90
4.12	Contrast lineshape models	92
5.1	Example state switching waveform within a block	104
5.2	Dead-time required to actuate each block and superblock switch	105
5.3	Histogram of switching periods for block and superblock switches	107
5.4	Model of phase drifts with two switches	108
5.5	A wiring schematic of the voltage applied to the field plates with two switches, to accompany the model presented in Section 5.3	111
5.6	The wiring diagram for the electric field plates	117
5.7	Frequency switching layout for \mathcal{N} and \mathcal{P} state selection	119
6.1	Relevant energy levels for the Raman electric field probe scheme	134
6.2	Optical configuration for Raman \mathcal{E} -field probe measurement	137
6.3	Efficiency relationship of cascaded AOMs for balancing power	138
6.4	Simulated and measured Raman lineshapes	141
6.5	Drifts in electric field measured with Raman side-of-fringe measurements and voltage monitors	144
6.6	Apparatus and relevant energy levels for the microwave \mathcal{E} -field measurement	147
6.7	Asymmetry versus microwave frequency and time after ablation for \mathcal{E} -field measurements	149
6.8	Strobed fluorescence signal used for extracting molecule velocity distributions	150
6.9	Map of \mathcal{E} -field magnitude in the interaction region	152
6.10	Map of \mathcal{E}^{nr} in the interaction region	154
6.11	Fit to determine the dipole moment of the $ C, J = 1, M = \pm 1\rangle$ states	157
7.1	Relevant energy levels for prep and probe laser ac Stark shifts model	163
7.2	Diagram of intensity and polarization gradients in the state preparation laser beam	164
7.3	AC Stark shift induced phase as a function of detuning	167
7.4	Diagram depicting how a non-reversing electric field \mathcal{E}^{nr} can generate an EDM correlated detuning $\Delta^{\mathcal{N}\mathcal{E}}$	169
7.5	Sensitivity of ac Stark shift phases to prep laser angle	171
7.6	Eliminating the \mathcal{E}^{nr} systematic	176

List of Figures

7.7	Comparison of EDM values under changing field magnitudes $ \mathcal{E}_z $, $ \mathcal{B}_z $, and laser pointing $\hat{k} \cdot \hat{z}$	178
7.8	Measurement of leakage currents by monitoring dc Stark Shifts	180
7.9	Histogram of $\omega^{\mathcal{N}\mathcal{E}}$ measurements from published data set	184
A.1	PMT enclosure assembly	194
A.2	Integrating a sweep of the MCS discriminator level to measure a pulse height spectrum	197
A.3	Discriminator level settings and associated lifetime measurements	198
B.1	The polarization ellipse and Poincaré sphere	202
B.2	Residual S_I for polarization optics with extinction ratio R_e	204
B.3	Stokes polarimeter photograph with annotated components	212
C.1	Examples of creating switch waveforms using “Generate Block Sequence” VI	215
C.2	The “Master Run VI” used for executing block waveform switches	217
C.3	The scan VIs used to center the pump and probe laser frequencies on resonance	220

List of Tables

3.1	Estimated electronic branching ratios	52
5.1	Frequency shifts necessary for the High and Low \mathcal{E} -field \mathcal{N} and \mathcal{P} state switching	122
6.1	\mathcal{E}^{nr} components from Raman data set on 7/2/2013	142
7.1	Systematic error budget	185
A.1	Components for sealed ACME PMT enclosure	195
B.1	Components for ACME Stokes Polarimeter	207
E.1	Category 1 IPVs: Parameters that were varied far from their values under normal conditions of the experiment.	224
E.2	Category 2 IPVs: Parameters for which all values are considered consistent with normal conditions of the experiment.	225

Acknowledgments

“Yes, I am here. And you are lucky to be here too after all the absurd things you’ve done since you left home.” ~ J.R.R. Tolkien

While completing this thesis, my life has been touched by people too numerous to acknowledge on just one page, but here are just a few. My advisor Jerry Gabrielse provided the motivation necessary to complete this long process. Dave DeMille and John Doyle always provided a unique perspective and lively collaboration meetings. This work could not have been completed without the help of the other ACME students and postdocs, who tolerated my meticulous pace of work over the years. Amar, Yulia, Emil, Nick, Ben, Elizabeth, Brendon, Adam, Jacob, and Cris; you have all left your own indelible marks on the ACME experiment. In addition, my friends throughout the Gabrielse, Doyle, and Lukin labs were always available for chats about physics, or something else entirely. Thanks to the NSF for providing ACME with the freedom to buy all necessary equipment, and to the DoE:SCGF for supporting and enriching me through my graduate fellowship.

Stan Cotreau and Jim MacArthur helped construct pieces of the apparatus, gave technical advice, and some laughs. I’m grateful for Stuart and Jay McNeil’s willingness to pursue our difficult requests, including drilling the holes for our LISE↔Jefferson fiber path. Thanks to Jan Ragusa for always helping me keep Jerry’s schedule straight, and Lisa Cacciabauda for helping me get across the finish line.

Finally, thanks to my family for being so supportive through the ups and downs of this process. But most of all, thanks to my wife Shelby, for keeping me grounded while still inspiring my academic sense of wonder.

Chapter 1

Introduction

Like a good friend with a dark past, the electron is a fundamental particle that is simultaneously ubiquitous and familiar, but we suspect holds mysteries that keep us digging for answers. Ever since the original suggestions of Ramsey and Purcell [1], the electron's permanent electric dipole moment (EDM) has been sought with increasing precision over the years, but never found. The ACME (Advanced Cold Molecule Electron EDM) Collaboration's recent result [2] represents a jump forward in the evolution of these experimental searches, but we rest on the shoulders of giants. Our experiment is heavily inspired by the extremely precise phase precession measurements using thallium beams [3], and the ground-breaking work bringing the peculiarities of molecular structure to bare in enhancing EDM experimental sensitivity [4, 5, 6]. Using the polar molecule thorium monoxide (ThO), we measured $d_e = (-2.1 \pm 3.7_{\text{stat}} \pm 2.5_{\text{syst}}) \times 10^{-29} e \cdot \text{cm}$. This corresponds to an upper limit of $|d_e| < 8.7 \times 10^{-29} e \cdot \text{cm}$ with 90% confidence, more than an order of magnitude

improvement in sensitivity relative to the previous best limit.¹

Our ACME team moved from conception to debugging and analysis of a precise EDM experiment in just over five years, a much shorter time scale than is usual for such measurements. By combining a high flux molecular beam source [8] with classic spin precession experiments adapted for ThO [9], we avoided the pitfalls of many previous experiments by constructing one with experimental simplicity in mind [10]. The search for the electron EDM is motivated by particle physics but implemented using atomic physics techniques. The results are significant, and in the context of many theories beyond the Standard Model, our results constrain T-violating physics at the TeV energy scale [11, 12], a comparable energy scale to those currently being probed at the Large Hadron Collider.

This thesis provides an overview of the ACME EDM experiment with emphasis on those aspects I worked on most closely. It is organized as follows:

- Chapter 1 provides the motivations for an electron EDM search and outlines the benefits of using ThO.
- Chapter 2 details the experimental procedure and describes the major components of the apparatus.
- Chapter 3 describes a measurement of the excited C state lifetime and calculates the appropriate transition strengths.
- Chapter 4 describes properties of the state preparation and probe lasers, including imperfections that contributed to the leading experimental systematic

¹The previous best limits on d_e came from experiments with thallium (Tl) atoms [3] ($|d_e| < 1.6 \times 10^{-27}$ e-cm) and ytterbium fluoride (YbF) molecules [4, 7] ($|d_e| < 1.06 \times 10^{-27}$ e-cm).

error.

- Chapter 5 details the implementation of our data acquisition system.
- Chapter 6 discusses measurements of our electric fields using the ThO beam.
- Chapter 7 summarizes important features of the data interpretation and analysis.
- Chapter 8 concludes with the present status of ACME generation II upgrades.

Portions of the text are adapted from [2], as I was one of the primary drafters and editors of that paper.

1.1 EDMs and T-Violating Extensions to the Standard Model

The Standard Model of particle physics is known to be incomplete. On one hand, this theory has had monumental success in encompassing all known fundamental particles and interactions into one self-consistent framework. It has demonstrated incredible breadth and precision, for example, in its ability to predict the electron's magnetic moment to one part in a trillion [13]. Recently, the theory has been further bolstered by the discovery of the Higgs Boson at the Large Hadron Collider (LHC) [14, 15] as predicted by the Brout-Englert-Higgs mechanisms put forth half a century ago [16, 17]. However, the Standard Model fails to account for a broad array of the observed cosmological phenomena in our universe. Observations confirm that both dark matter and dark energy account for 95% of the total content of the universe, but

neither is predicted by the Standard Model. Moreover, the model does not contain a mechanism which explains the inherent asymmetries implied by the prevalence of matter over antimatter in the observed universe. Indeed, the Standard Model predicts many orders of magnitude less baryonic matter, which prevents the existence of the matter dominated universe we live in today [18, 19].

Extensions to the Standard Model seek to solve some of these problems, while still staying consistent with the model's successful predictions. Both in theory and experiment, identifying and testing possible Standard Model extensions is one of the most active fields of fundamental physics research. For example, weak scale supersymmetry posits the existence of new particles and interactions which serve as candidates for weakly interacting dark matter particles [20]. One way of testing these theories is through direct detection of the predicted particles. If these particles have masses around the electroweak scale of ~ 200 GeV, they could be created in collisions at high energy TeV-scale particle accelerators like the LHC [21]. Or, assuming they constitute dark matter particles, extremely sensitive and low background experiments could observe their minuscule interactions with regular matter [22]. As of yet, such experiments have shown no sign of these exotic particles, and therefore provide no direct validation of theories like supersymmetry.

As an alternative approach, one can precisely measure how the structure of more commonplace particles is modified by these standard model extension theories. Of particular interest are those theories that include additional sources of time reversal (T) violation beyond the mechanism present in the Standard Model [23]. An enhanced amount of T-violation is required to generate the matter antimatter asym-

metry according to Sakharov's conditions [24, 25]. Standard Model extensions that are asymmetric under time reversal nearly always predict small yet potentially measurable electric dipole moments of fundamental particles [26, 27]. The EDM of a fundamental fermion is an asymmetric charge distribution along the particle's spin \vec{S} that is also asymmetric under T (Figure 1.1).

Since their importance was first proposed by Purcell and Ramsey [1], permanent EDMs have been sought in a wide array of systems, from bottles of ultracold neutrons [28] to muons in storage rings [29, 30]. So far, no permanent EDMs have been detected for any of these fundamental particles, but experiments continue to improve their precision and prescribe tighter upper limits. These searches are complimentary to one another, as they probe different regions of the parameter space of theories beyond the Standard Model. For instance, in the minimal supersymmetric standard model (MSSM), the two complex phases which give rise to T-violation have different behaviors in the leptonic and hadronic sectors. Limits on the neutron, electron, and mercury atom EDMs together place stringent bounds on this parameter space [26].

By utilizing techniques for precision measurements of atomic structure, experiments can be sensitive to these tiny T-violating effects in electrons and nucleons [33, 34]. Of particular interest are electron EDMs, d_e , which along with T-violating electron nucleon interactions, can generate detectable effects in paramagnetic atoms and molecules. Many well motivated theories predict an electron electric dipole moment in the range of 10^{-27} to 10^{-30} e-cm [12, 35]. The exceptionally high internal effective electric field \mathcal{E}_{eff} of heavy neutral atoms and molecules causes an interaction term $V_{\mathcal{E}} = -\vec{d}_e \cdot \vec{\mathcal{E}}_{\text{eff}}$ which can be used to precisely probe for d_e via the associated energy

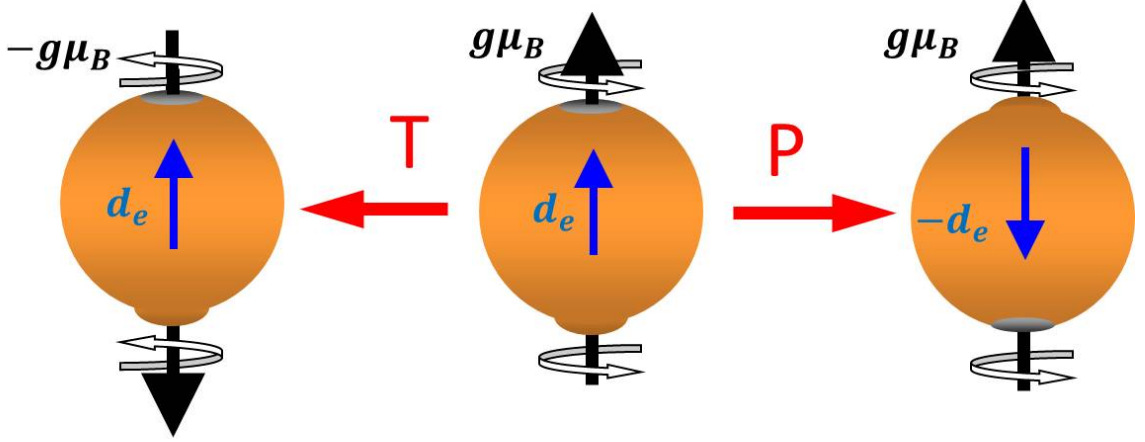


Figure 1.1: P and T violation due to an electron EDM. Assuming magnetic ($g\mu_B$) and electric (d_e) dipole moments are initially aligned, under either symmetry transformation they become anti-aligned. The system is not invariant under either P or T transformations unless one of the moments is zero [31]. The magnetic moment is clearly nonzero, being the most precisely measured property of an elementary particle [32].

shifts. Valence electrons travel relativistically near the heavy nucleus, making \mathcal{E}_{eff} up to a million times the size of any static laboratory field [36, 37, 38].

The small T-violation in the Standard Model's CKM mixing matrix predicts an electron EDM which is less than $10^{-38} e \cdot \text{cm}$ [39]. A measurably large EDM requires new mechanisms of T-violation, which is equivalent to combined charge-conjugation and parity (CP) violation, given the CPT invariance theorem. Nearly every extension to the Standard Model [35, 11] introduces new CP-violating phases ϕ_{CP} . It is difficult to construct mechanisms that systematically suppress ϕ_{CP} , so model builders typically assume $\sin(\phi_{\text{CP}}) \sim 1$ [27]. An EDM arising from new particles at energy Λ in an

n -loop Feynman diagram will have size

$$\frac{d_e}{e} \sim \kappa \left(\frac{\alpha_{\text{eff}}}{4\pi} \right)^n \left(\frac{m_e c^2}{\Lambda^2} \right) \sin(\phi_{\text{CP}}) (\hbar c) \quad (1.1)$$

where α_{eff} (about $4/137$ for electroweak interactions) encodes the strength with which the electron couples to the new particles, m_e is the electron mass, and $\kappa \sim 0.1$ to 1 is a dimensionless prefactor [37, 26, 12]. In models where 1- or 2- loop diagrams produce d_e , our result typically sets a bound on CP violation at energy scales $\Lambda \sim 3$ TeV or 1 TeV, respectively [35, 11, 27, 12]. Hence, within the context of many models, our EDM limit constrains CP violation up to energy scales similar to, or higher than, those explored directly at the Large Hadron Collider.

1.2 An EDM Experiment in ThO

A wide array of atomic [40, 3, 41], molecular [42, 4, 6, 43, 2], and solid state [44] systems have been used to search for EDMs in of the bound valence electrons (Figure 1.2). The basic protocol of all these experiments involves measuring the spin dependent shifts associated with the interaction of the electron EDM with an external field [37]. An electron with both magnetic moment μ and electric dipole moment d_e experiences dipole interaction terms

$$V_{\mathcal{B}} = -\vec{\mu} \cdot \vec{\mathcal{B}}, \quad (1.2)$$

$$V_{\mathcal{E}} = -\vec{d}_e \cdot \vec{\mathcal{E}} \quad (1.3)$$

under the influence of electric \mathcal{E} and magnetic \mathcal{B} fields. Energy levels with opposite spin orientations relative to \mathcal{B} and \mathcal{E} experience energy level shifts linearly proportional to the applied fields.

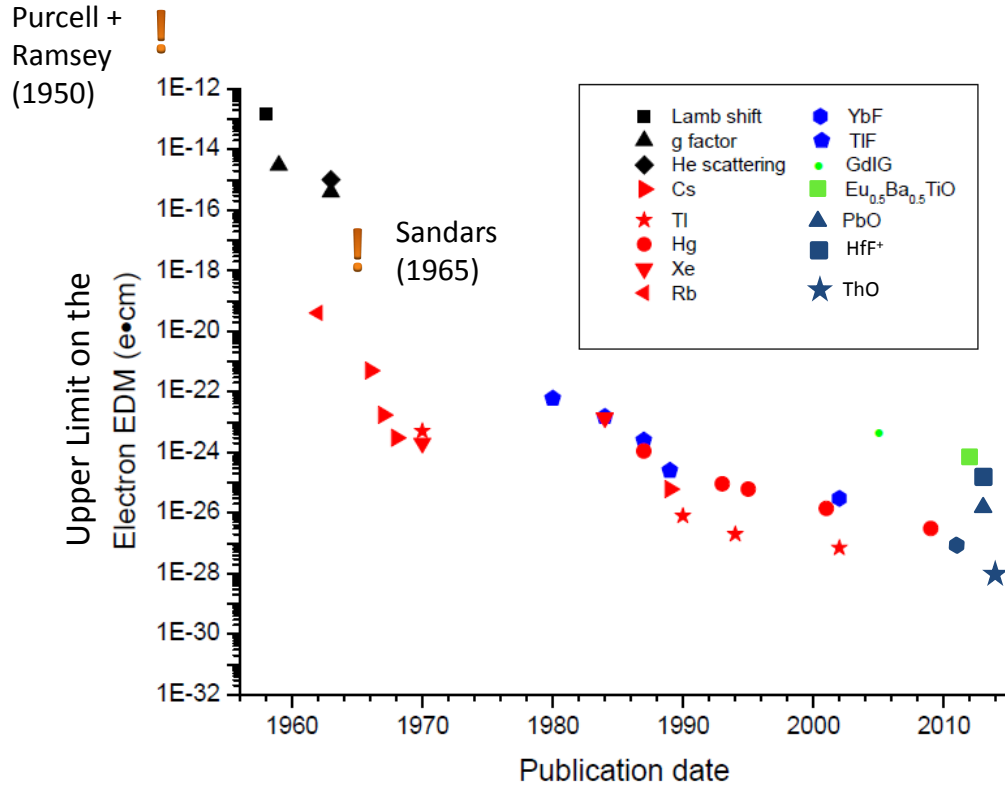


Figure 1.2: Complete history of published electron EDM limits. Following Purcell and Ramsey’s proposal [1], EDMs limits were first set using the Lamb shift [45], electron g -factor measurements [46, 47], and scattering experiments [48]. Sandar’s calculation of the enhancement factors in atoms [36], led to their measurement in the paramagnetic atoms Rb [49, 50], Cs [51, 52, 53, 54, 55, 56, 40], and Tl [57, 58, 59, 3]. Extremely precise measurements in diamagnetic atoms are also sensitive to electron EDMs, including measurements in Xe [60, 61, 62] and ^{199}Hg [63, 64, 65, 66, 41]. Measurements in molecules include those in TlF [67, 68, 69, 42], YbF [70, 4], PbO [6], HfF⁺ [43], and ThO [2]. Some solid state systems have also been used, including nickel-zinc ferrite [71], gadolinium-iron garnet [72], gadolinium gallium garnet [73], and Eu_{0.5}Ba_{0.5}TiO₃ [44]. Figure updated from Paul Hamilton’s thesis to include recent results [74].

A bare electron cannot have \mathcal{E} -fields applied to it without accelerating it into the walls of the measurement apparatus. Electron EDM experiments measuring anomalous Larmor precession frequency of free electron beams due to $\vec{v} \times \vec{B}$ electric fields are over a trillion times less sensitive than our current limit [47]. In a molecule, the electron experiences an effective electric field (\mathcal{E}_{eff}) which is much greater than the applied laboratory fields (Section 1.3.1). The well known Zeeman shifts sum with the analogous EDM shifts, so measurement of the energy level splitting contains a term proportional to d_e . These Zeeman shifts are much larger than EDM shifts, and therefore accurate measurement of d_e requires reversing the sign of $\vec{\mathcal{E}}$ to extract the \mathcal{E} -field correlated energy splitting. A Ramsey type phase precession measurement is typically the most sensitive way of measuring these small correlated phases (Section 2.1).

1.2.1 Statistical Sensitivity

The statistical sensitivity of an ideal EDM experiment follows from the Heisenberg energy-time uncertainty principle $\Delta E_{d_e} \tau = \hbar$, where τ is the time allowed for phase precession [37]. A single phase precession measurement has an EDM resolution $\delta d_e \propto 1/(\mathcal{E}_{\text{eff}} \tau)$, which is limited by the energy shift enhancement factor \mathcal{E}_{eff} and the maximum achievable coherence time τ . Repetition of the experiment N times improves the signal-to-noise by a factor of $1/\sqrt{N}$, assuming a small detection efficiency

and an experiment limited by photon detection shot noise.² The EDM sensitivity can therefore be cast into the form

$$\delta d_e = \frac{\hbar}{2\mathcal{E}_{\text{eff}}\tau\sqrt{\dot{N}T}} \quad (1.4)$$

where \dot{N} is rate of EDM measurements and T is the total integration time. Therefore, the best EDM experiments have large effective electric field (\mathcal{E}_{eff}), long coherence times (τ), high measurement fluxes (\dot{N}) and the potential for long integration times (T). The ACME experiment has achieved a statistical sensitivity of about $\delta d_e \approx 4 \times 10^{-28} e \cdot \text{cm}/\sqrt{\text{Day}}$.

Of other electron EDM searches actively under pursuit, the HfF⁺ experiment at JILA [77, 43] and the next generation of the YbF experiment at Imperial college [4, 7] are the most competitive with our new limit. The YbF experiment uses the familiar technique of measuring the spin resonance in a molecular beam. Unlike ThO, this experiment is performed in the molecule’s ground state, and therefore the coherence time can be extended well beyond the $\sim 600 \mu\text{s}$ used to set the previous best limit. A laser cooled molecular fountain represents their ultimate goal, allowing precession times of $\sim 250 \text{ ms}$, and ultimate projected sensitivities at the $1 \times 10^{-30} e \cdot \text{cm}$ level. The HfF⁺ experiment can achieve similar precession times through an entirely different technique, using an RF Paul trap to confine the molecules for arbitrary lengths of time.

Despite small numbers in the trap, these long coherence times make their statistical

²Because our photon detection efficiency is $\ll 100\%$, we are limited by shot noise on the photon detection, not on the number of molecules. Almost 100% of molecules that undergo phase precession emit a photon, but only $\sim 10\%$ of those photons are collected and sent to our photomultiplier tubes. These tubes have a 10% quantum efficiency, so only $\sim 1\%$ of emitted photons are detected as photo electrons. Increasing the detection efficiency to 100% would make us limited by quantum projection noise. The signal to noise could potentially be improved at this point by employing spin squeezing to reach the Heisenberg limit for quantum measurements, and achieve sensitivity scaling $\delta d_e \propto 1/N$ [75, 76].

sensitivity per root day competitive with ACME's. This would represent the first time a trapped ion would be used to measure an electron EDM, which warrants a lengthy study of systematics for full confidence in a new result.

1.2.2 ThO Molecular Structure

As in atoms, electronic states in diatomic molecules can be characterized in terms of their orbital (\vec{L}), spin (\vec{S}), and total (\vec{J}_e) angular momentum. However, molecules are complicated by the broken symmetry of their internuclear axis (\hat{n}). This allows for rotation of the molecule with a rotational angular momentum \vec{R} , which contributes to the total angular momentum $\vec{J} = \vec{J}_e + \vec{R}$. Moreover, in diatomic molecules electronic angular momentum may be projected onto the internuclear axis, which defines an extra set of quantum numbers. The projections of ($\vec{L}, \vec{S}, \vec{J}_e$) are (Λ, Σ, Ω), and the sum relation $\Omega = \Lambda + \Sigma$ holds between these scalar quantities. Therefore, the total angular momentum must satisfy $J \geq |\Omega|$ (Figure 1.3). Outside of the molecule fixed frame, \vec{J} has the usual $(2J + 1)$ projections along the \hat{z} axis $M = (-J, -J + 1, \dots, J)$.

ThO molecule is best described in a Hund's case (c) basis where each state typically can be characterized with quantum numbers $|J, M, \Omega\rangle$. For Hund's case (c) molecules, L , S , Λ , Σ , and J_e are not good quantum numbers. General discussions of diatomic molecular structure can be found in several textbooks [78, 79] and other sources [80, 81], including summaries of molecular quantum number notation and Hund's cases for angular momentum coupling.

In an environment free of external \mathcal{E} and \mathcal{B} fields, the isotropy of electromagnetic interactions dictates that the molecular eigenstates be simultaneous eigenvectors of

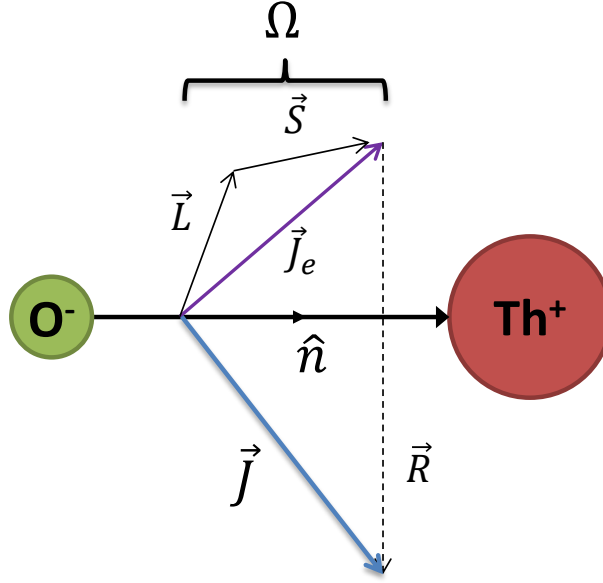


Figure 1.3: Angular momentum coupling in Hund's case (c), the best coupling scheme for ThO. Adapted from [78].

both energy and parity. For states with $|\Omega| > 0$, there are two possible projections $\pm\Omega$. Confusingly, pure rotational states $|J, M, \Omega\rangle$ are not simultaneous eigenstates of the parity operator $P|J, M, \Omega\rangle = (-1)^{J-\Omega}|J, M, -\Omega\rangle$ [78, 80]. Good parity eigenstates are linear combinations of $|J, M, \pm\Omega\rangle$

$$|J, M, \pm\rangle = \frac{1}{\sqrt{2}}(|J, M, +\Omega\rangle \pm |J, M, -\Omega\rangle). \quad (1.5)$$

Molecular rotation lifts the degeneracy between these $|J, M, \pm\rangle$ states with a splitting $\Delta_\Omega = aJ(J+1)$ [82].

The electronic energy levels relevant for the ACME experiment are shown in Figure 1.4, along with leading term symbols. ThO molecules are produced primarily in the ground $X^1\Sigma^+$ state, and the EDM experiment is performed in the lowest lying metastable ($\tau_H \sim 2$ ms) $H^3\Delta_1$ state. Higher electronic states are used for incoherently populating the H state (via the A state) or transferring population out of H

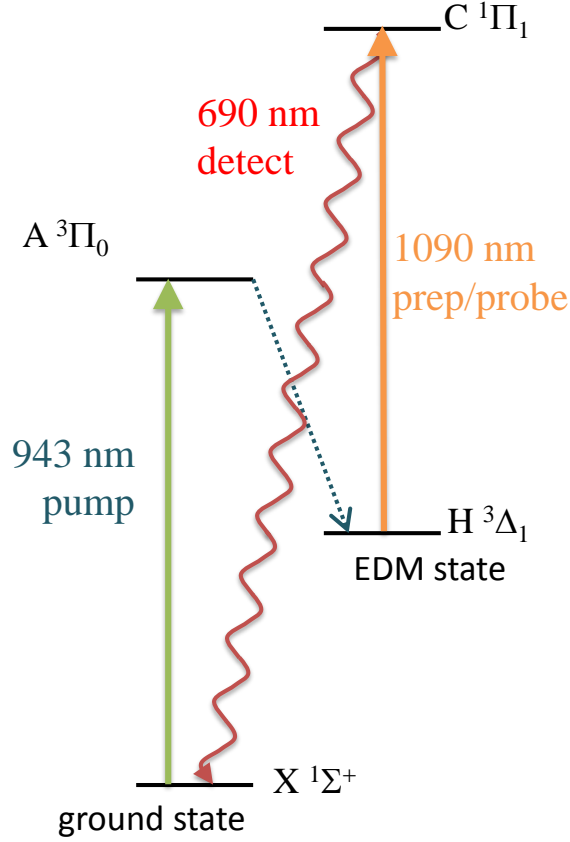


Figure 1.4: Electronic states of ThO relevant for the ACME experiment. States are labeled with lettered names and the leading order Hund’s case (a) term ($^{2S+1}\Lambda_\Omega$).

(via the C state). The H state is $|\Omega| = 1$ and we perform the EDM experiment in the lowest rotational $J = 1$ state where there are a total of $2(2J + 1) = 6$ sublevels.

When static electric fields (\mathcal{E}) are applied, the opposite parity $|J, M, \pm\rangle$ omega doublet sublevels of the H state are mixed by the dc Stark interaction $V_{dc} = -\vec{D} \cdot \vec{\mathcal{E}}$.

The interaction hamiltonian is

$$H = \begin{pmatrix} |J, M, +\rangle & |J, M, -\rangle \\ -\frac{\Delta_{\Omega(H)}}{2} & -D_H \mathcal{E} \\ -D_H \mathcal{E} & \frac{\Delta_{\Omega(H)}}{2} \end{pmatrix}, \quad (1.6)$$

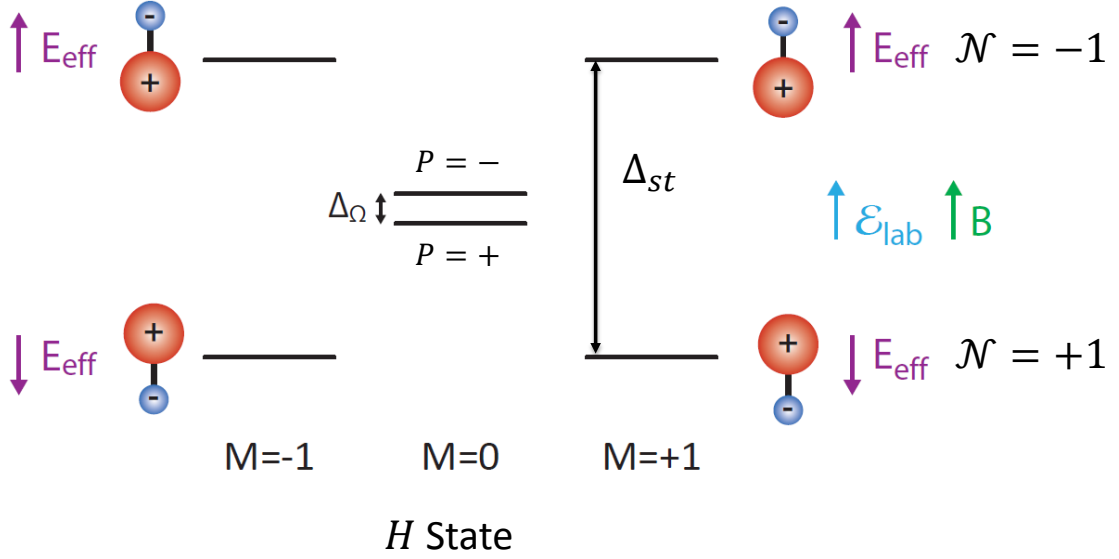


Figure 1.5: Level diagram of the H state in the limit of large electric field. Opposite orientations of the molecule are split by the dc Stark Shift Δ_{st} , while the $M = 0$ states maintain good parity with a zero field omega doublet splitting $\Delta_{\Omega} = 360$ kHz. The upper $M = 0$ has parity $P = -$, as verified using microwave spectroscopy [81].

where $D_H = \frac{D^0 M \Omega}{J(J+1)}$ is the expectation value of the dipole moment operator in high field (Section 3.2). This results in an \mathcal{E} -field dependent shift between the omega doublet states

$$\Delta_{st} = \sqrt{\Delta_{\Omega(H)}^2 + (2D_H \mathcal{E})^2}. \quad (1.7)$$

In the high field limit, the eigenstates have completely mixed parity and evolve towards states with a single value of Ω . The polarization is defined as $P_H = \langle \Omega \rangle / |\Omega|$ [74, 80, 7], which is explicitly

$$P_H = \frac{D_H \mathcal{E}}{\sqrt{(D_H \mathcal{E})^2 + (\Delta_{\Omega(H)}/2)^2}}. \quad (1.8)$$

For a fully saturated state, it is useful to define $\mathcal{N} = M \Omega \hat{\mathcal{E}} \cdot \hat{z}$, such that the internuclear axis points along the molecule's dipole $\hat{n} = \hat{D} = \mathcal{N} \hat{\mathcal{E}}$. Then $\mathcal{N} = +1(-1)$

has been defined such that the molecule’s dipole is either aligned(anti-aligned) with the laboratory \mathcal{E} -field and the doublet of spin states ($M = \pm 1$) is lower(higher) in energy than the unshifted $M = 0$ state [10, 81] (Figure 1.5). Note that the $M = 0$ states are unshifted to first order for the same reason that E1 transitions with $\Delta J = 0$, $M'' = M' = 0$ are forbidden, because the Clebsch-Gordan coefficient is zero.

In this high electric field limit, the frequency shifts of H state sublevels with quantum numbers M and \mathcal{N} include (from left to right) the Zeeman interaction, the EDM interaction, and the linear dc Stark shift

$$E_H(M, \mathcal{N}) = - \left[(g_H \mu_B + \eta |\mathcal{E}_z| \mathcal{N}) \mathcal{B}_z + d_e \mathcal{E}_{\text{eff}} \mathcal{N} \tilde{\mathcal{E}} \right] M - D_H |\mathcal{E}_z| \mathcal{N} \quad (1.9)$$

where $\eta |\mathcal{E}_z| \mathcal{N}$ describes the \mathcal{E} -field dependent difference in g value between upper and lower omega doublets [83]. The M dependent term will cause spin precession when a superposition of $M = \pm 1$ states is created (Section 2.1).

1.3 Advantages of ThO

This result is the first time that ThO has been used for an EDM experiment. The benefits of using a $^3\Delta_1$ state in a heavy polar molecule have been understood for some time [84, 5, 85, 86], inspiring a new class of EDM experiments in molecules with similar structure, including PbO [6], HfF⁺ [43], and WC [87]. Each molecule has slight differences requiring variations in experimental procedure. Currently, ThO holds the edge over other EDM experiments thanks to the molecule’s high internal electric field \mathcal{E}_{eff} and our bright and robust molecular beam [8], in addition to unique

features for the rejection of common systematics.

1.3.1 Large Effective Electric Field

A valence electron in an atom or molecule, when polarized in an electric field, experiences an interaction $V_{\mathcal{E}} = -\vec{d}_e \cdot \vec{\mathcal{E}}_{\text{eff}}$ that shifts the energy levels proportional to an effective electric field \mathcal{E}_{eff} produced by the nucleus. The H $^3\Delta_1$ electronic state in the thorium monoxide (ThO) molecule provides an $\mathcal{E}_{\text{eff}} \approx 84$ GV/cm, larger than those previously used in EDM measurements³ [88, 89]. As first pointed out by Sandars [36], heavy atoms or molecules can have effective electric fields that greatly exceed the polarizing laboratory field. The energy level shifts caused by an electron EDM in state ψ_0 are [90]

$$\Delta E_{d_e} = \langle \psi_0 | -d_e(\gamma^0 - 1)\Sigma \cdot \mathcal{E}_{\text{eff}} | \psi_0 \rangle. \quad (1.10)$$

These matrix elements are only nonzero between atomic states with parity mixed by a laboratory electric field \mathcal{E} .

Useful reviews of these calculations can be found in [80, 38, 90, 91], and we find that the energy level shifts can be parameterized using

$$\Delta E_{d_e} = -d_e \mathcal{E}_{\text{eff}} P, \quad (1.11)$$

where $0 \leq P \leq 1$ describes the amount of mixing between opposite parity sublevels. Schiff's theorem [92] claims that ΔE_{d_e} should be zero in the non-relativistic limit, because an electron bound in a neutral molecule must experience electric fields that

³We use the value $\mathcal{E}_{\text{eff}} = 84$ GV/cm value from [88] throughout this thesis. See Section 7.4 for discussion.

time average to zero $\langle \vec{\mathcal{E}}_{\text{eff}} \rangle_t = 0$. This energy level shift is only nonzero in the relativistic limit, where the electron's EDM experiences length contraction close to the nucleus, so $\langle \vec{d}_e \cdot \vec{\mathcal{E}}_{\text{eff}} \rangle_t \neq 0$ [90]. The relativistic component that contributes to \mathcal{E}_{eff} typically scales like Z^3 , and therefore heavy atoms or molecules (Tl, Yb, Th, ...) are most useful for EDM searches.

Insofar as polar molecules can be fully polarized in laboratory-scale electric fields, $P_m \approx 1$, and then ΔE_{d_e} is only determined by \mathcal{E}_{eff} and can be much greater than in atoms. The polarization mixing of an atom according to perturbation theory is

$$P_a \approx -\mathcal{E} \frac{D_{\perp}}{E_p - E_s}, \quad (1.12)$$

where D_{\perp} is the transition dipole moment between opposite parity states with energy E_s and E_p . Nearest opposite parity states in atoms are typically split by the fine structure splitting ($E_p - E_s$) $\approx 0.1(e^2/a_0) \sim 10-100$ THz, so for a large but achievable laboratory field of 200 kV/cm, $P_a \approx 10^{-4}$. Rotational spacing in molecules provides one source of closely spaced opposite parity sublevels not present in atoms. For heavy molecules typically used for EDM searches, rotational splittings on the order of 10 GHz allow the polarization to near saturation at electric fields of ~ 10 kV/cm [7]. Polar diatomic molecules therefore can have as much as a 10^4 enhancement in their sensitivity to d_e .

In particular, the $|H, J = 1\rangle$ state of ThO has closely spaced opposite parity levels provided by the very small zero field omega doublet splitting $\Delta_{\Omega} = 360$ kHz [93, 94] (confirmed with our own microwave spectroscopy [81]). In this limit, it is best to calculate the polarization non-perturbatively, and according to Equation 1.8, the H state is almost completely polarized if $\mathcal{E} \gg \Delta_{\Omega(H)}/(2D_H) = 0.17$ V/cm (Figure 1.6).

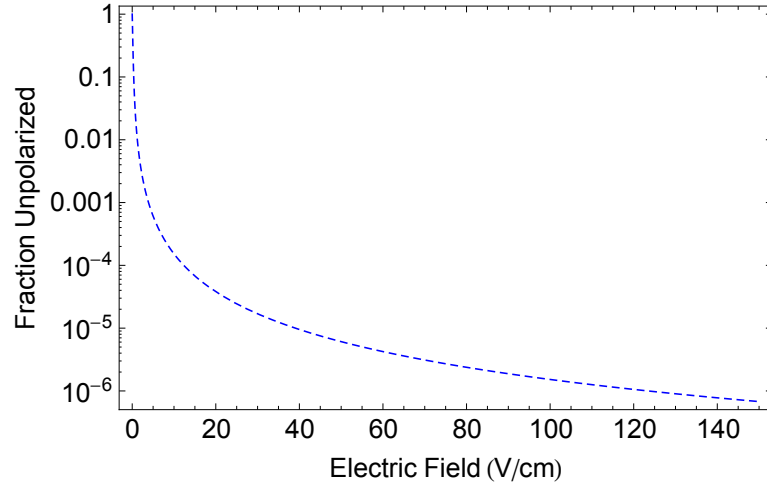


Figure 1.6: Unpolarized fraction ($1 - P_H$) of the H state wavefunction as a function of electric field. We operate our experiment at 141 and 36 V/cm, where the unpolarized fraction is less than a part in 10^5 , and there is no measurable difference in \mathcal{E}_{eff} .

This provides very modest requirements on our electric field magnitudes, requiring voltage supplies operate only up to a few hundred volts. The ACME experiment was the first to achieve saturation of the EDM sensitivity. Moreover, because we could easily apply ~ 100 V/cm field, we had the freedom to run the experiment at multiple electric field values without sacrificing EDM sensitivity. This is a powerful tool for eliminating potential systematics related to high electric fields, such as leakage and charging current correlated magnetic fields [3, 41].

1.3.2 Systematic Rejection through Omega Doublets

Improved systematic error rejection is possible because internal state selection allows the reversal of $\vec{\mathcal{E}}_{\text{eff}}$ with no change in the laboratory electric field [95, 5]. As indicated in Figure 1.5, the large polarizability of the H state means oppositely oriented omega doublet states can easily be spectroscopically resolved in \mathcal{E} -fields over a

few V/cm. The spin doublets $|M = \pm 1, \mathcal{N}\rangle$ used for a phase precession measurement can be selected simply by detuning the state preparation and probe lasers. Traditionally, EDM experiments reverse the \mathcal{E} -field to separate out background phases, but effects such as leakage currents create systematic phase shifts correlated with \mathcal{E} , mimicing an EDM. There is a far smaller class of systematic effects that reverse with both a laboratory electric field \mathcal{E} and omega doublet state \mathcal{N} , and therefore an EDM correlated with both is more robust against such systematics [74, 10, 86, 6].

The large polarizability due to omega doublets also suppresses both the motional magnetic fields and geometric phases that limited the T1 measurement [3]. Once the H state is fully polarized with with $\mathcal{E} > 1$ V/cm, the dc Stark shift splits the $M = \pm 1$ states from the $M = 0$ states at a rate of $D_H \approx 1$ MHz/(V/cm). This is much greater than the Zeeman interaction $g_H \mu_B \approx 5$ Hz/G, so the molecules are always electric field quantized. Motional magnetic fields $\vec{\mathcal{B}}_{\text{mot}} \propto \vec{v} \times \vec{\mathcal{E}}$ are necessarily transverse to the \hat{z} quantization axis, and the resulting systematics are suppressed to first order [60, 96], as first demonstrated with Xe atoms [60] and later applied to alkali atoms [96]. The YbF experiment first demonstrated this suppression using molecules [70].

1.3.3 Small Magnetic Moment

The H state's unusually small magnetic moment of $(4 \times 10^{-3})\mu_B$ reduces the experiment's sensitivity to spurious magnetic fields [10, 97]. As mentioned above, many systematics are caused by magnetic phases that are electric field correlated, as is the EDM. A smaller magnetic moment reduces the size of these phase shifts

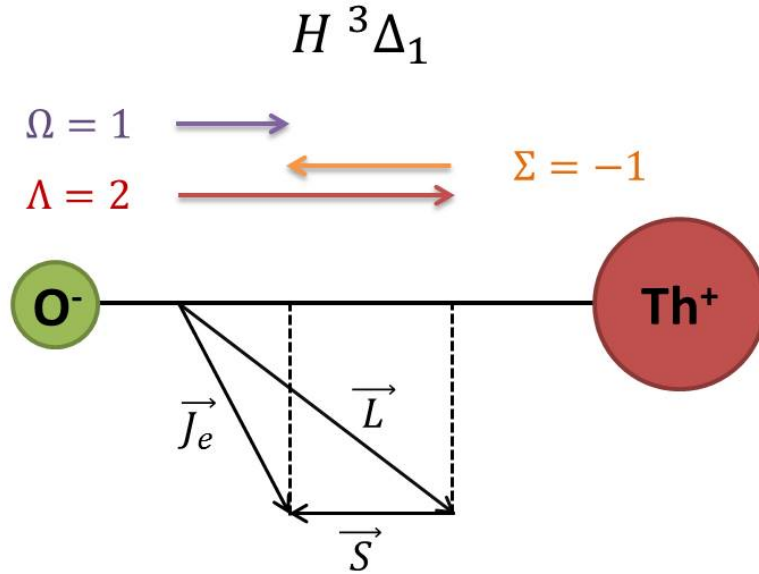


Figure 1.7: Angular momentum cancellations leading to a reduced magnetic moment in the H state. Orbital and Spin projections (Λ and Σ) must oppose each other such that $\Lambda + \Sigma = \Omega$. Since the spin angular momentum has twice the gyromagnetic ratio of orbital angular momentum, the total magnetic moment $\mu_H \propto 2(\Sigma) + \Lambda \approx 0$.

relative to those from the EDM itself. Moreover, magnetic Johnson noise [38, 98] is a difficult to avoid noise source, which will dominate over photon shot noise if signal sizes are large enough. The small magnetic moment in the H state makes the magnetic Johnson noise nearly irrelevant. The small magnetic moment is the result of the opposition of the spin and orbital angular momentum in the ${}^3\Delta_1$ state, which cancel a large fraction of the magnetic moment [83] (Figure 1.7).

1.3.4 Experimental Simplifications

Not to be understated are the experimental simplifications afforded by an EDM experiment with ThO. All transitions necessary for the generation and detection of spin precession in H are accessible via solid state diode lasers (Figure 1.4). Turnkey

fiber amplifiers provide ample power to saturate the $H \rightarrow C$ transition, and have well stabilized output powers. Moreover, we have demonstrated that ThO production via ablation in a buffer gas cell is a remarkably efficient way to produce high flux beams of molecules [8]. Using this technique, we have been able to produce a slow molecular beam with $v_{\text{beam}} \approx 200$ m/s. With the $\tau = 2$ ms lifetime of the H state setting our maximum coherence time, a precession length greater than $L \approx 22$ cm currently used would not significantly improve the sensitivity of the experiment [10]. This eliminates much of the complication of generating interaction \mathcal{E} and \mathcal{B} fields that are uniform over very long distances, as would be necessary with a faster molecular beam.

Chapter 2

The ACME Experiment: Measurement Procedure and Apparatus

Our experimental result of $|d_e| < 8.7 \times 10^{-29} e \cdot \text{cm}$ required us to search for EDM correlated energy level shifts $\omega^{\mathcal{N}\mathcal{E}} < 1.7 \times 2\pi$ mHz. Directly measuring such minuscule level shifts via Rabi flopping would require a narrow transition linewidth and well-stabilized frequency reference [99]. By instead performing a measurement analogous to the Ramsey technique of separated fields [100], we lift these requirements and can achieve linewidths of $\Delta\omega = \pi/\tau$, for separation time τ [33].

To measure d_e we perform a spin precession measurement [10, 101, 9] on pulses of $^{232}\text{Th}^{16}\text{O}$ molecules from a cryogenic buffer gas beam source [102, 8, 103]. The molecules pass between parallel plates that generate a laboratory electric field $\mathcal{E}_z \hat{z}$. A coherent superposition of two spin states, corresponding to a spin aligned in the

xy plane, is prepared using optical pumping and state preparation lasers. Parallel electric ($\vec{\mathcal{E}}$) and magnetic ($\vec{\mathcal{B}}$) fields exert torques on the electric and magnetic dipole moments, causing the spin vector to precess in the xy plane. The precession angle is measured with a probe laser and fluorescence detection. The change in this angle as $\vec{\mathcal{E}}_{\text{eff}}$ is reversed is proportional to d_e .

Our phase precession time is $\tau = 1.1$ ms, leading to a relatively wide fringe of width $\Delta\omega \approx 10^5 \times 2\pi$ mHz $\gg \omega^{\mathcal{N}\mathcal{E}}$. Therefore, significant averaging and careful study of statistical lineshapes and systematic errors was necessary to achieve the quoted experimental precision. This required us to push the spin precession measurement to the shot noise limit [9] and build a robust beam source [8] and data acquisition system (Chapter 5) suited for long integration times. This chapter discusses the details of the measurement procedure, the apparatus that allows us to perform that procedure, and the fundamental data analysis steps from which we extract a measurement of d_e .

2.1 Spin Precession Measurement

In more detail, molecules in the ground $X \ ^1\Sigma^+$ state enter the electric field plates with most population in the $|X, J = 1\rangle$ states due to the ground state rotational cooling performed outside the shielded region (Section 2.3.2). A linearly polarized 943 nm laser beam tuned to the $|X, J = 1\rangle \rightarrow |A, J = 0\rangle$ transition optically pumps molecules into the lowest rotational level, $J = 1$, of the metastable electronic $H \ ^3\Delta_1$ state. Our measurements of $A \rightarrow H$ branching ratio reveal that about 30% of the population in a single $|X, J = 1, M\rangle$ sublevel is pumped into $|H, J = 1\rangle$ manifold in an incoherent mixture of the $|\mathcal{N} = \pm 1, M = \pm 1\rangle$ and $|M = 0, P = -1\rangle$ states. The pump

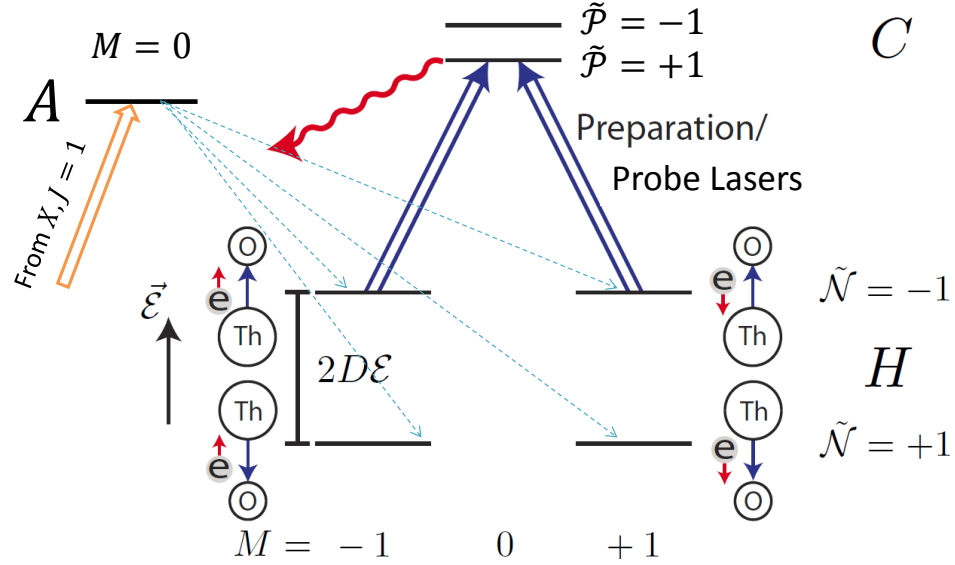


Figure 2.1: Relevant energy levels for the spin precession measurement. The H state is populated via optical pumping from $X \rightarrow A$ (orange arrow) and incoherent decay from A (dashed lines). The state preparation and readout lasers (double-lined blue arrows) drive one molecule orientation $\tilde{\mathcal{N}} = \pm 1$ (split by $2D_{H\mathcal{E}} \sim 100$ MHz) in the H state to C , with parity $\tilde{\mathcal{P}} = \pm 1$ (split by 50 MHz). Population in the C state decays via spontaneous emission, and we detect the resulting fluorescence (red wiggly arrow). H state levels are accompanied by cartoons displaying the orientation of $\vec{\mathcal{E}}_{\text{eff}}$ (blue arrows) and the spin of the electron (red arrows) that dominantly contributes to the d_e shift.

laser is retroreflected after rotation of the polarization by 90° , pumping all population out of the $M = \pm 1$ magnetic sublevels ($2/3$ of the total $|X, J = 1\rangle$ population).

The spin state is polarized by a method similar to coherent population trapping [104]. Just 5 mm downstream of optical pumping, the linearly polarized state preparation laser's frequency is resonant with the

$$|H, J = 1, M = \pm 1, \tilde{\mathcal{N}}\rangle \leftrightarrow |C, J = 1, M = 0, \tilde{\mathcal{P}}\rangle$$

transition at 1090 nm (Figure 2.1). For a given spin precession measurement, the laser frequency determines the $\tilde{\mathcal{N}}$ and $\tilde{\mathcal{P}}$ states that are addressed. Our 1 MHz laser

linewidth is much larger than the ~ 100 Hz Zeeman shift between $|M = +1\rangle$ and $|M = -1\rangle$ states, so a single laser couples them via the $|C\rangle$ state and projects the 3-level system into a “bright” and “dark” state basis. The C state is short lived with a lifetime of about 500 ns and has a negligible branching fraction for decay back to the H state (Chapter 3). Therefore, the state preparation laser optically pumps the bright superposition of the two resonant $M = \pm 1$ sublevels out of the H state, leaving behind the orthogonal dark superposition that cannot absorb the laser light; we use this dark state as our initial state. For a linearly polarized laser at angle θ , the bright and dark states are

$$|D\rangle = \frac{1}{\sqrt{2}} \left(e^{i\theta} |M = +1, \mathcal{N}\rangle + e^{-i\theta} |M = -1, \mathcal{N}\rangle \right), \quad (2.1)$$

$$|B\rangle = \frac{1}{\sqrt{2}} |\mathcal{P}\rangle + \frac{1}{2} \left(-e^{i\theta} |M = +1, \mathcal{N}\rangle + e^{-i\theta} |M = -1, \mathcal{N}\rangle \right). \quad (2.2)$$

Consider a state preparation laser polarized along \hat{x} such that $\theta = 0$, then the prepared state

$$|\psi(\tau = 0), \mathcal{N}\rangle = \frac{|M = +1, \mathcal{N}\rangle + |M = -1, \mathcal{N}\rangle}{\sqrt{2}}, \quad (2.3)$$

is the dark state with the electron spin aligned along the \hat{y} axis.

Molecules then travel over the $L \approx 22$ cm distance between state preparation and probe regions, under the influence of $\vec{\mathcal{E}} = \mathcal{E}_z \hat{z}$ and $\vec{\mathcal{B}} = B_z \hat{z}$ fields. The dipole interactions $V_{\mathcal{B}} = -\vec{\mu}_H \cdot \vec{\mathcal{B}}$ and $V_{\mathcal{E}} = -\vec{d}_e \cdot \vec{\mathcal{E}}_{\text{eff}}$ give rise to energy level shifts between our spin states (Equation 1.9). This leads to spin precession in the xy plane by an angle ϕ to

$$|\psi(\tau), \mathcal{N}\rangle = \frac{e^{i\phi} |M = +1, \mathcal{N}\rangle + e^{-i\phi} |M = -1, \mathcal{N}\rangle}{\sqrt{2}}. \quad (2.4)$$

Because $\vec{\mathcal{E}}$ and $\vec{\mathcal{B}}$ are aligned along \hat{z} , the phase ϕ is determined by $|B_z| = |\vec{\mathcal{B}} \cdot \hat{z}|$, its

sign, $\tilde{\mathcal{B}} = \text{sgn}(\vec{\mathcal{B}} \cdot \hat{z})$, and the electron's EDM, d_e :

$$\phi \approx \frac{(\mu_B g_H \tilde{\mathcal{B}} |B_z| + \tilde{\mathcal{N}} \tilde{\mathcal{E}} d_e \mathcal{E}_{\text{eff}}) \tau}{\hbar} \quad (2.5)$$

where $\tilde{\mathcal{E}} = \text{sgn}(\vec{\mathcal{E}} \cdot \hat{z})$, $\tau \approx 1.1$ ms is the spin precession time, and $\mu_B g_H$ is the magnetic moment of the of the $|H, J = 1\rangle$ state, where $g_H = -0.0044 \pm 0.0001$ is the gyromagnetic ratio and μ_B is the Bohr magneton [9, 80, 97]. The sign of the EDM term, $\tilde{\mathcal{N}} \tilde{\mathcal{E}}$, arises from the relative orientation between $\vec{\mathcal{E}}_{\text{eff}}$ and the electron spin.

We measure ϕ by optically pumping on the same $H \rightarrow C$ transition with the probe laser. The H state population is again projected into the bright and dark basis, and the bright state is depleted by the laser coupling to the C state. Light collection optics in the probe region allow us to measure the bright state population through 690 nm fluorescence photons from the decay of C to the ground state. The probe laser's linear polarization rapidly alternates between orthogonal states \hat{X} and \hat{Y} every 5 μs , which are defined such that \hat{X} is at an angle θ with respect to \hat{x} in the xy plane, and \hat{Y} is at an angle $\theta + \pi/2$. This procedure amounts to a projective measurement of the spin onto \hat{X} and \hat{Y} with probabilities

$$P_X = 1 - \cos(2(\phi - \theta)) \quad (2.6)$$

$$P_Y = 1 + \cos(2(\phi - \theta)). \quad (2.7)$$

We record the modulated fluorescence signals $S_X = S_0 P_X$ and $S_Y = S_0 P_Y$, where S_0 is proportional to the total number of molecules, which fluctuates by 20% between pulses of our molecular beam source [8]. We require the successive measurements of S_X and S_Y be made much faster than variations in S_0 within the molecule pulse (see Section 4.1).

Therefore, we can normalize the spin precession signal and eliminate the noise from these molecule number fluctuations by computing the asymmetry [10],

$$\mathcal{A} = \frac{S_X - S_Y}{S_X + S_Y} = -\mathcal{C} \cos(2(\phi - \theta)). \quad (2.8)$$

The contrast \mathcal{C} , which is $94 \pm 2\%$ on average, accounts for imperfect measurements due to detector background counts, finite $H \rightarrow C$ excitation time, and dephasing from the transverse velocity distribution of our molecules.

We set $|B_z|$ and θ such that

$$\phi - \theta \approx \frac{\pi}{4}(2n + 1) \quad (2.9)$$

for integer n , so that the asymmetry is linearly proportional to small changes in ϕ and is maximally sensitive to the EDM. Linearizing around these points, small changes in phase can be computed using

$$\delta(\phi - \theta) = (-1)^n \frac{\mathcal{A}}{2\mathcal{C}} \quad (2.10)$$

given measurements of the asymmetry and contrast. We operate with either n even or odd, depending on the magnitude of the \mathcal{B} -field. Notice that by dithering θ between two nearby values that differ by $\Delta\theta \leq 0.1$ rad, we can solve for the contrast $\mathcal{C} = \Delta A / (2\Delta\theta)$. The state of this switch is denoted by $\tilde{\theta} = \pm 1$. In this linear regime, the contrast is equivalent to our experiment's sensitivity to small changes in phase. Although many other EDM experiments measure \mathcal{C} in a similar way by making controlled changes in ϕ [4, 3], our technique of switching the measurement basis angle θ has the benefit of straightforward control via a motorized waveplate and calibration via polarimetry of the laser.

2.2 Data Analysis: Notation and Procedure

We perform spin precession measurements repeatedly under varying experimental conditions to (i) distinguish the EDM energy shift from background phases and (ii) search for and monitor possible systematic errors. By reversing experimental quantities that have a given parity relationship with d_e , we can isolate the EDM phase (second term in Equation 2.5) from other terms by applying parity even/odd sums between phase measurements.

First a bit of notation useful for describing the data analysis. We define the switch state for an experimental parameter u

$$\tilde{u} = \text{sgn}(u) = \pm 1. \quad (2.11)$$

We denote the switch parity of a quantity G with a superscript, u , listing the switch labels under which the quantity is odd; it is even under all unlabeled switches. Using these definitions, we can decompose any quantity into switch correlated components

$$G = G^0 + G^{u_1} \tilde{u}_1 + G^{u_2} \tilde{u}_2 + \dots + G^{u_1 u_2} \tilde{u}_1 \tilde{u}_2 + \dots + G^{u_1 u_2 \dots u_N} \tilde{u}_1 \tilde{u}_2 \dots \tilde{u}_N \quad (2.12)$$

where there are 2^N terms corresponding to all combinations of the N total binary switches. After performing a series of measurements $G_{\text{meas}}(\tilde{u}_1, \tilde{u}_2, \dots, \tilde{u}_N)$ for all 2^N switch combinations, we can extract the “switch parity components” G^u which are linear combinations of the $G_{\text{meas}}(\tilde{u}_1, \tilde{u}_2, \dots, \tilde{u}_N)$ that are odd or even under these switch operations [6, 74].

For example, the switch parity component odd under two switches (i, j) , out of N total experimental switch parameters is formally

$$G^{u_i u_j} = \frac{1}{N} \sum_{\tilde{u}_1, \tilde{u}_2, \dots, \tilde{u}_N = \pm 1} G_{\text{meas}}(\tilde{u}_1, \tilde{u}_2, \dots, \tilde{u}_N) \tilde{u}_i \tilde{u}_j. \quad (2.13)$$

This formal definition can describe any switch parity component, and is useful because of the large number of switches we implemented for the experiment (Section 5.1). It is used to describe the parity of measured quantities such as asymmetries and contrasts, and also the correlations of any experimental parameters. For the rest of the section we restrict the discussion to the four switches needed to measure the EDM.

Particularly important switches are $\tilde{\mathcal{N}}$, $\tilde{\mathcal{E}}$, $\tilde{\mathcal{B}}$, and $\tilde{\theta}$ because the four of these taken together allow us to calculate the EDM. We perform sequential spin precession measurements, grouped into a “block”, for all $2^8 = 256$ combinations of these binary switch parameters, and compute the asymmetry of each state from Equation 2.8. Within each block, we extract the switch parity components of the asymmetries \mathcal{A}^u using Equation 2.13, where asymmetries are always taken as even under the $\tilde{\theta}$ switch. As described previously, the $\tilde{\theta}$ switch is used to measure our contrast, and for a particular state $(\tilde{\mathcal{N}}, \tilde{\mathcal{E}}, \tilde{\mathcal{B}}, \tilde{\theta})$, the contrast is

$$\mathcal{C}(\tilde{\mathcal{N}}, \tilde{\mathcal{E}}, \tilde{\mathcal{B}}) = \frac{\mathcal{A}(\tilde{\mathcal{N}}, \tilde{\mathcal{E}}, \tilde{\mathcal{B}}, +1) - \mathcal{A}(\tilde{\mathcal{N}}, \tilde{\mathcal{E}}, \tilde{\mathcal{B}}, -1)}{2\Delta\theta}. \quad (2.14)$$

We can also define contrast correlations $\mathcal{C}^u = A^{u\theta}/(2\Delta\theta)$. Armed with a contrast and asymmetry for each state, we can calculate the phases

$$\phi(\tilde{\mathcal{N}}, \tilde{\mathcal{E}}, \tilde{\mathcal{B}}) = \frac{\mathcal{A}(\tilde{\mathcal{N}}, \tilde{\mathcal{E}}, \tilde{\mathcal{B}})}{2\mathcal{C}(\tilde{\mathcal{N}}, \tilde{\mathcal{E}}, \tilde{\mathcal{B}})} \quad (2.15)$$

and the phase parity components ϕ^u using Equation 2.13.

For example, the EDM contributes to a phase component

$$\phi^{\mathcal{N}\mathcal{E}} = \frac{-d_e \mathcal{E}_{\text{eff}} \tau}{\hbar}. \quad (2.16)$$

We extract the mean precession time τ from

$$\phi^{\mathcal{B}} = -\frac{\mu_B g_H |B_z| \tau}{\hbar} \quad (2.17)$$

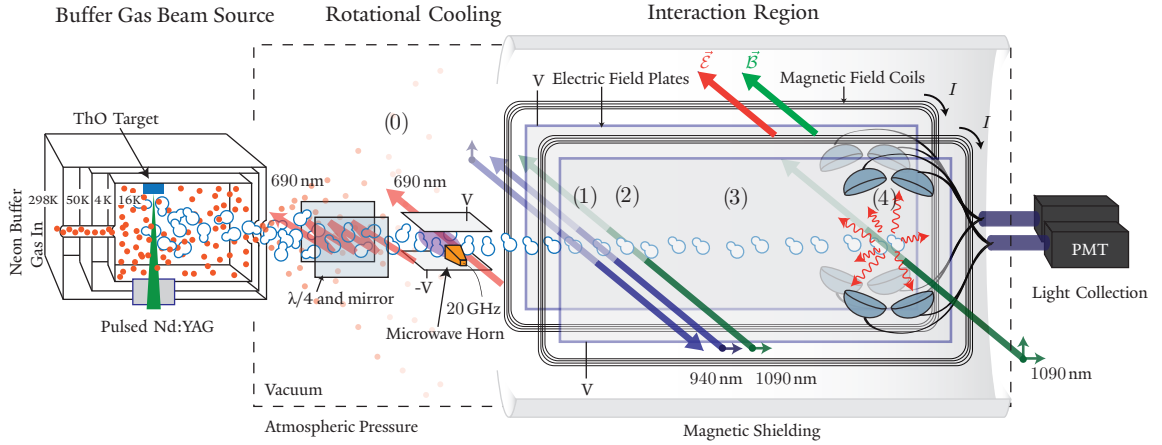


Figure 2.2: Schematic of the EDM apparatus. All major segments are shown, including beam production in the cryogenic cell, rotational cooling in a room temperature vacuum chamber, and the spin precession measurement in the magnetically shielded region. This figure was originally produced by B. O’Leary (unpublished).

and compute the frequencies

$$\omega^u = \frac{\dot{\phi}^u}{\tau}. \quad (2.18)$$

The EDM value is obtained from $\omega^{\mathcal{N}\mathcal{E}}$ using $d_e = -\hbar\omega^{\mathcal{N}\mathcal{E}}/\mathcal{E}_{\text{eff}}$. Mean values and errors are calculated as EDM correlated precession frequencies up until the final steps, so that the uncertainty in the theoretical determination of \mathcal{E}_{eff} does not affect our experimental results (only the interpretation).

2.3 Apparatus

The following is a more detailed description of the EDM apparatus, breaking up the trajectory of the beam into stages (Figure 2.2). Other sources or sections within this thesis contain specifics of the construction of the various components, and are cited accordingly.

2.3.1 Beam Source

We create a pulsed molecular beam of ThO using the buffer gas beam technique [102, 8, 103, 81]. Neon buffer gas was chosen (as opposed to helium) because it can efficiently be cryopumped by the large surface area of our 4 K shields. This allowed us to operate the molecular beam continuously for ~ 24 hours before brief (2 hour) warmup and pumpout cycles were required to regenerate the cryopumping. Careful studies showed there was not a significant change in beam centerline brightness for neon versus helium buffer gas. The rotational temperature has been measured to be around 4 K with neon [8], and the ground state rotational population distribution is peaked at $J = 1$ for that temperature. The rotational temperature and transverse and longitudinal velocity temperature seem to depend on the position of the ThO ablation target within the cell. Positioning it further from the cell exit aperture produced colder beams, presumably because the ThO experienced more Ne collisions before extraction.

Each packet of molecules leaving the source contains $\sim 10^{11}$ ThO molecules in the $J = 1$ rotational level of the ground electronic and vibrational state and are produced at a repetition rate of 50 Hz. The packet is 2-3 ms wide and has a center of mass speed of $v_{\text{beam}} \approx 200$ m/s. The chamber background pressure of $< 10^{-6}$ Torr suggests a ThO-background gas collision probability of $\lesssim 1\%$ during the spin precession measurement which could cause a small decrease in fluorescence signal or contrast. A set of field plates at 200 V/cm remove ions from the beam to prevent them from coating the field plates in the interaction region.

2.3.2 Ground State Rotational Enhancement

After leaving the cryogenic beam source chamber, the ground state molecules are in a thermal distribution of rotational states at about 4 K with a rotational constant of $B_R h/k_B \approx 0.5$ K. Most of the population is distributed amongst the lowest four rotational levels. We use a series of lasers and microwaves to enhance the population of a single rotational state, $|X, J = 1\rangle$ [105]. The molecules travel through a pair of optical pumping lasers resonant with the $|X, J = 2\rangle \rightarrow |C, J = 1\rangle$ and $|X, J = 3\rangle \rightarrow |C, J = 2\rangle$ transitions. Both lasers are multipassed to increase interaction time with the ~ 10 mW 690 nm laser beams, and the polarization is rotated along each pass to prevent the creation of dark states. When driving the P-branch transitions in the absence of electric fields, E1 selection rules conserve parity so only P- and R-branch $C \rightsquigarrow X$ decay is allowed. However, we found it increased the ultimate $|X, J = 1\rangle$ population to apply a weak electric field while optical pumping, thus mixing C state omega doublets, and allowing some Q-branch decay. This optical pumping effectively depletes the population of the $|X, J = 2, 3\rangle$ states and concentrates it into the $|X, J = 0, 1\rangle$. The $C \rightsquigarrow X$ branching ratio of $\sim 80\%$ reduces the efficiency of this process to below unity, depending on the magnitude of the applied electric field.

The molecules then encounter a \hat{z} polarized microwave field resonant with the $|X, J = 0\rangle \leftrightarrow |X, J = 1, M = 0\rangle$ transition in a weak electric field. The microwave transition is saturated, so it mixes the populations of $|X, J = 0, M = 0\rangle$ and $|X, J = 1, M = 0\rangle$ resulting in a 50:50 redistribution of the original population of those states. The quantization axis is not preserved between the microwave ground

state enhancement region and the field plates surrounding the spin precession region. Therefore, the population of the three M sublevels of $|X, J = 1\rangle$ are mixed.¹ The combined result of lasers and microwaves is an overall population increase in $|X, J = 1\rangle$ by a factor of ~ 2 .

2.3.3 Interaction Region

The molecules then pass through adjustable and fixed collimating apertures before entering the magnetically shielded interaction region, where we perform the spin precession measurement on H state molecules, as outlined in detail in Section 2.1. The normalization scheme requires the laser's $\hat{k} \parallel \vec{\mathcal{E}} \parallel \hat{z}$, which can be achieved if our field plates are transparent at 1090 nm and 943 nm. The electric field is provided by two 17" \times 9" plates of 12.7 mm thick glass coated with a layer of indium tin oxide (ITO) on one side, and an anti-reflection coating on the other. The ITO coated side of the plates face each other with a gap of 25 mm, and a voltage is applied to the ITO to create a uniform electric field. All lasers travel through the electric field plates, so all stages of the spin precession measurement are performed inside the uniform electric field.

Phase precession by $\pi/4$ requires applying $|B_z| \sim 20$ mG, therefore Earth's 500 mG field must be shielded. The EDM measurement is performed in a vacuum chamber surrounded by five layers of μ -metal shielding [106]. In principle they provide a shielding factor of 10^5 , but so far we have only had the ability to measure their

¹Other schemes for ground state enhancement use stronger electric fields and an additional optical pumping laser tuned to $|X, J = 1, M = \pm 1\rangle \rightarrow |C, J = 1, M = \pm 1\rangle$ to spin polarize the population into the $|X, J = 1, M = 0\rangle$ state. A quantization \mathcal{E} -field must be maintained to the interaction region to avoid remixing of the magnetic sublevels. Since the current experiment lacked this feature, this additional laser actually decreased the total signal due to the $C \rightsquigarrow X$ branching ratio.

shielding factor at DC to the 10^3 level. Degaussing is required to demagnetize the shields after changing the magnetic field. The somewhat jarring process of assembling the shields pins in magnetic domains which require an especially high current degauss cycle to eliminate [107]. The applied magnetic field is supplied by a cosine-theta coil [108], wound on high density plastic frame outside the vacuum chamber. Shim coils, also wound on this frame, should be run with currents $4.4\times$ those in the cosine-theta coil to create a more uniform magnetic field, minimizing dB_z/dx within the precession region [80]. We apply transverse magnetic fields and gradients for systematic checks using six independent coil windings. Two coils wound around the cosine-coil frame provide B_x fields, while plates with four windings parallel to the xz plane generate B_y fields. Changes in the magnetic field are monitored by four 3-axis fluxgate magnetometers inside the magnetic shields, and the magnetic fields were mapped out before and after the experimental dataset was taken by sliding a 3-axis fluxgate down the beamline.

All laser light in the experiment originates from external cavity diode lasers (ECDL), frequency stabilized via an Invar transfer cavity [109] to a CW Nd:YAG laser locked to a molecular iodine transition [110, 111]. The scanning transfer cavities and software based locking program [112] provide robust laser locking stable to ~ 1 MHz over several days [80]. To achieve stability against atmospheric pressure changes, the Invar cavities were sealed in KF nipples at atmospheric pressure. Additional software routines were used to relock the lasers to the ThO resonances and therefore improve the short term (20 minute) stability (Section C.2).

The transparent electric field plates allow us to collect $\sim 40\%$ of the solid angle

of fluorescence from the molecules. Fluorescence travels through the field plates into an eight-lens system (four behind each plate) which focuses the light into an optical fiber bundle [81]. The four bundles on each side are coupled into a fused quartz light pipe, which carries the fluorescence to a PMT (outside the magnetic shields). The net detection efficiency, including collection solid angle, transmission loss, and detector quantum efficiency, is about 1% [105]. We typically register about 1000 photon counts per molecule pulse. The PMT photocurrents are read as analog signals by a low-noise, high-bandwidth amplifier, and then sent to a 24-bit digitizer operating at 5 megasamples per second. The control and timing for all experimental parameters is managed by a single computer, and the timing jitter is less than one digitizer sampling period ($0.2 \mu\text{s}$). See Chapter 5 for further details regarding the data acquisition.

Chapter 3

C State Lifetime and Linestrength Calculations

The ACME Collaboration has now measured both the *H* and *C* state lifetimes in ThO using separate techniques in different apparatus. The metastable *H* state lifetime of τ_H limits the maximum spin precession time and therefore the sensitivity of an EDM measurement. The *H* state is the lowest lying excited state in ThO and transitions to the ground state are mostly dipole forbidden, both of which contribute to the states's metastability. This lifetime dictates the appropriate range of molecular beam velocities and interaction region lengths for maximum sensitivity. The $H \rightarrow C$ transition is used as a probe of *H* state population via fluorescence back to the ground state. Therefore, the *C* state lifetime τ_C determines the rate of decay and temporal profile of our fluorescence signals (Section 4.2).

This chapter outlines a measurement of the *C* state lifetime and reviews calculations of transition dipole moments and other useful quantities for ThO spectroscopy.

Other molecular constants were determined previously, including all required transition frequencies and state assignments [113, 114, 115, 80], electric and magnetic dipole moments([97, 9], Section 6.5), and saturation intensities and branching ratios for most relevant states and transitions [105].

Previous work measured the lifetime of the H state to be consistent with $\tau_H \approx 1.8$ ms [10, 116]. These measurements were performed by probing H state population in a cryogenic buffer gas cell of ThO, similar to those used to produce our molecular beams, but without the necessary exit aperture to form a beam [103]. Density dependent effects had to be carefully controlled to separate the desired radiative lifetime from collisional decay of the H state. Radiative lifetime measurements made in molecular beams have the potential for higher accuracy due to the low densities and spatial filtering provided by the moving molecules [117, 118]. Because molecules travel a distance of $\tau_H v_{\text{beam}} \approx 36$ cm while they decay, much larger than the diameter of the probe laser which monitors the H state population, we cannot employ the current method of monitoring fluorescence with a fixed detector. However, using a system of separated probes on translation stages, it would be possible to improve our measurement of τ_H using the molecular beam [119, 120].

3.1 Measurement of the C State Lifetime

In contrast to the metastable H state, ThO's C state is strongly coupled to the ground X state via an allowed E1 transition, and therefore has the much shorter lifetime of $\tau_C = 490 \pm 40$ ns. This section describes a measurement of this lifetime by time resolved photon counting of the $C \rightsquigarrow X$ decay photons. The experiment

was performed in a collisionless molecular beam, were the decay flight distance of $\tau_C v_{\text{beam}} \sim 0.1$ mm is much smaller than the acceptance window of our photon collection, allowing lifetime measurements with a single static detector. The measurements were made in the “mini-beam” dewars (MB1 and MB2), the precursors of our main beam source. Specifics on their constructions are described in more detail elsewhere [106, 105].

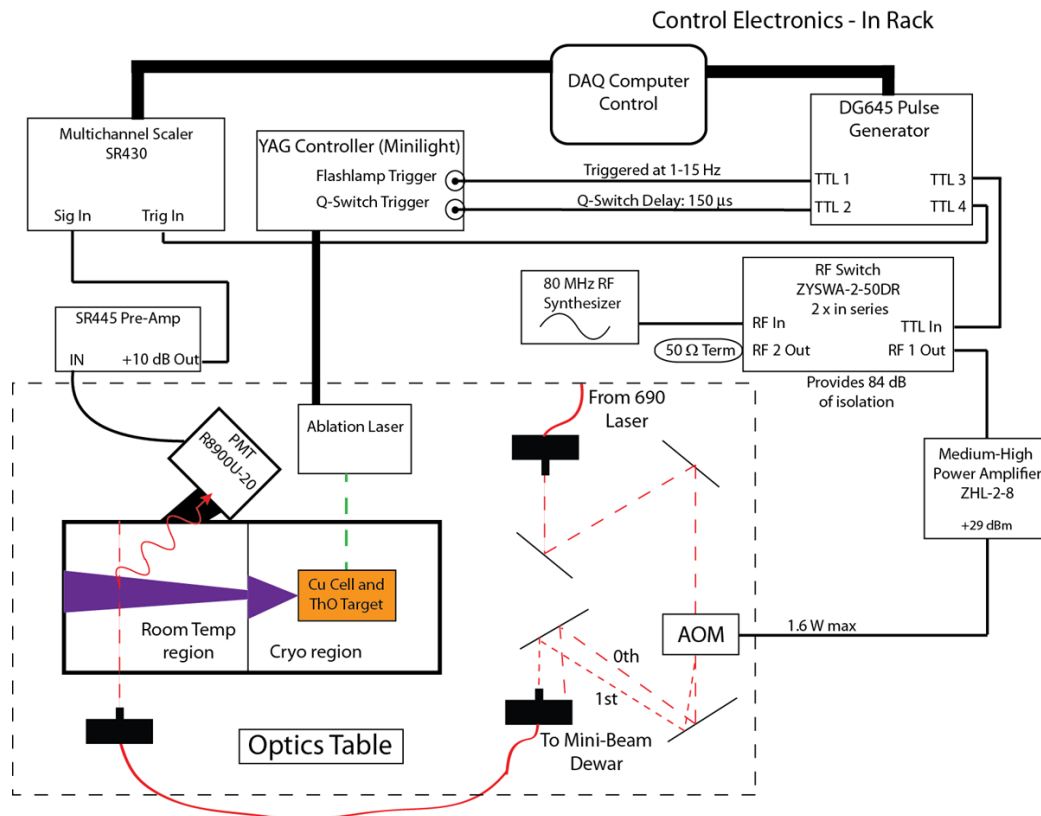
Fluorescence on the $C \rightsquigarrow X$ transition (690 nm) was monitored using a photomultiplier tube (Hamamatsu R8900U-20), and single photons were counted using a multichannel scaler (SR430) [121]. The observed photon counting signal is proportional to the C state population N_C . The decay rate $\gamma_C = 1/\tau_C$ describes a fractional change in population per unit time, and a simple one component exponential decay

$$\frac{dN_C}{N_C} = -\gamma_C dt \quad \rightarrow \quad N_C(t) = N_C(0)e^{-t/\tau_C}. \quad (3.1)$$

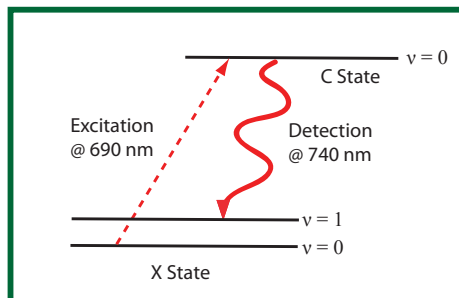
This total decay rate γ_C is equal to the sum of many decay paths over separate electronic and vibrational branches to lower energy states.¹

Molecules in the ThO beam are excited to the C state using a 690 nm diode laser tuned to the Q(1) transition (14489.98 cm^{-1}), driving $|X, \nu'' = 0, J'' = 1\rangle \rightarrow |C, \nu' = 0, J' = 1\rangle$. The laser passes through an AOM, and the first order diffracted beam is delivered to the experiment via an optical fiber. Using a TTL driven RF switch (ZYSWA-2-50DR) this excitation laser can be extinguished in as little as 50

¹It is perhaps counterintuitive that we aren’t measuring a partial decay rate, even though we are only measuring fluorescence photons emitted by decay between a particular pair of states. If we could measure radiation simultaneously from other decay channels (e.g. to $|X, \nu'' = 1\rangle$), the ratio of signal sizes would give us information about the relative partial widths (branching ratios), but the decay timescale of each signal would be identical. In practice such a measurement of branching ratios requires careful calibration of photon collection and detection efficiency between the simultaneously monitored channels.



(a) Experiment Schematic



(b) Off-Diagonal Decay

Figure 3.1: (a) Schematic of the *C* state lifetime measurement apparatus. Measurements were made in two different mini-beam dewars, but this diagram represents the data taken from MB2. Fluorescence was collected via a light pipe perpendicular to the excitation laser. (b) Relevant energy levels for off-diagonal fluorescence detection.

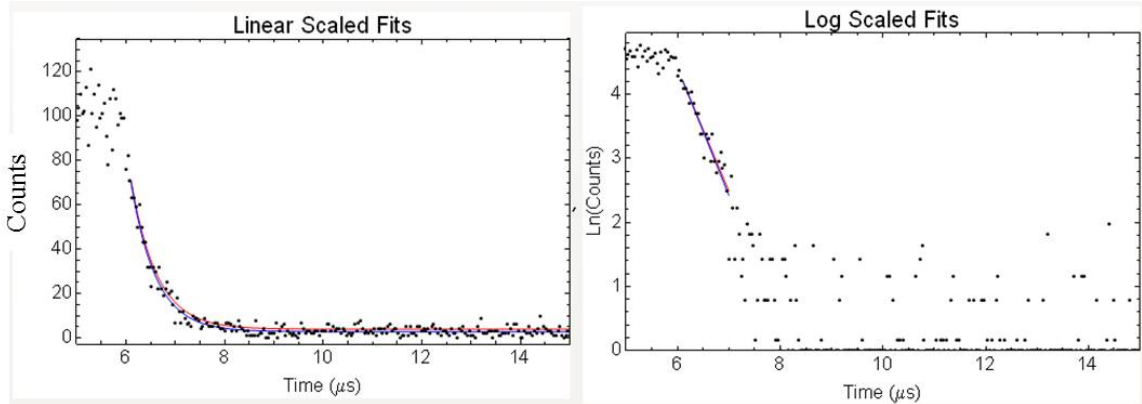


Figure 3.2: Example decay curves plotted on linear and log scales with linear/log fits.

ns. This is sufficiently fast that a convolution of the decay lineshape with the laser extinction lineshape was not necessary for data analysis. The acquisition is triggered with the RF switch, and we observe the fluorescence both before after the laser turns off.

The PMTs are filtered so they are only sensitive to photons emitted from $C \rightsquigarrow X$ decay. By using 10 nm passband filters around either 690 nm (Thorlabs FB690-10) or 740 nm (Thorlabs FB740-10), we can selectively detect either the $\Delta\nu = 0$ photons at 690.1 nm, or the “off-diagonal” decay to $|X, \nu'' = 1\rangle$ at 735.6 nm. The vibrational branching ratios require that the off diagonal transition produces a factor of 5.6 fewer photons, which combined with the reduced quantum efficiency of the PMT and rolloff in transmission of the 740 nm filters at 735 nm, makes the off-diagonal signal ~ 10 times smaller. However, scattered 690 nm excitation light adds backgrounds to signals that makes fitting routines less straightforward, so detection at 740 nm was frequently used. An apparatus schematic is shown in Figure 3.1, along with the relevant energy levels for the excitation and detection scheme.

The decaying fluorescence was fit to the function

$$S(t) = Ae^{-(t-t_0)/\tau} + B \quad (3.2)$$

with free parameters A , B , and τ . Non-linear fitting determined the three parameters, using approximate linearized fitting to supply the initial guesses (see Appendix D). Studies of fit sensitivity to t_0 were used to select a start time suitably delayed from the trigger such that all effects of the 50 ns laser shutoff were removed. These and other potential “lineshape systematics” were evaluated using Monte Carlo simulated data, testing fits under various regimes of A , B , and τ values. The fitting procedure accurately reproduced the input parameters and uncertainties associated with the Monte Carlo data.

The measurement was checked against the effects of numerous systematics. The lifetime was shown to be independent of laser power and $X \rightarrow C$ saturation effects. The background pressure was controlled by increasing the buffer gas flow rate or by reducing the speed of the backing turbo, and no density dependence of the lifetime was observed. Data collected in MB1 and MB2 also showed excellent agreement, further ruling out effects due to pressure differences, laser powers, and fluorescence collection geometries. The data was collected as a function of the photon counter’s discriminator level, which confirmed the optimal setting between the noise and signal peaks measured in a pulse height analysis (Figure A.3).

Careful studies of the effects of PMT supply voltage (G) revealed that above the recommended operating value of 800 V, the measured lifetime was greatly exaggerated (Figure 3.3). This effect was found to be dependent on the photon counting rates > 1 MHz, indicating it might be related to pulse pile up [122]. By operating below

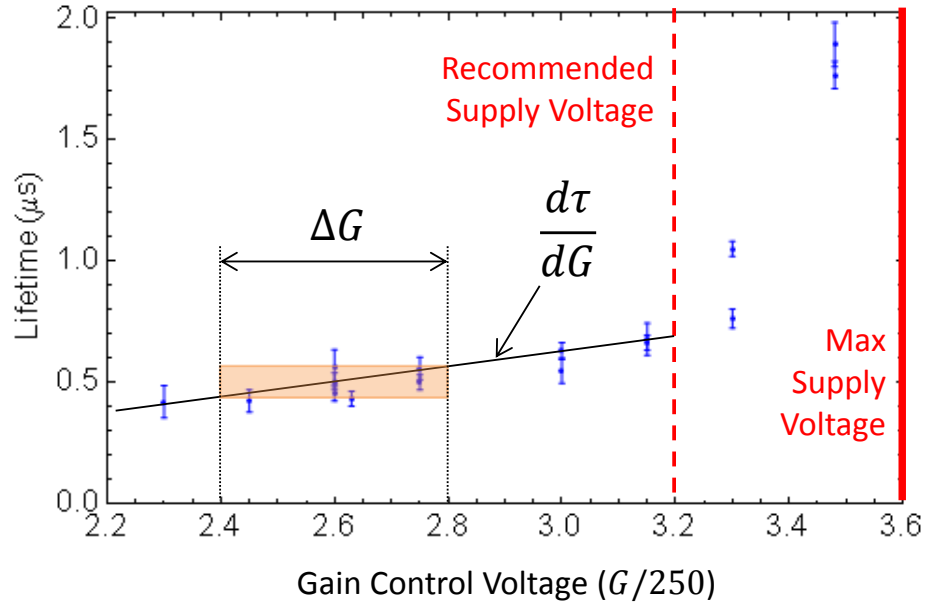


Figure 3.3: The dependence of τ_C on the PMT supply voltage (G). The lifetime is plotted as a function of the control voltage to the HV module ($G = 250 \times V_{\text{ctrl}}$). A linear fit to measurements less than the recommended supply voltage of 800 V yields the systematic sensitivity $d\tau/dG$. The range of acceptable settings is ΔG .

this 1 MHz threshold, the counting rate dependence of the lifetime was eliminated, although a dependence on G remained. The gain of the PMT tubes is a function of G , which modifies the shape of the pulse height spectrum. A voltage setting of $G = 650$ V seemed to produce well behaved pulse spectra, and struck a balance between signal loss due to low gain and high voltage after-pulsing effects. A range of acceptable gain settings corresponding to $G = 650 \pm 50$ V were deemed to be equally valid for lifetime measurements, according to a pulse height analysis (Appendix A).

Even in the region below 800 V we observed a small dependence of the lifetime on G . This was quantified by the residual slope $d\tau/dG$ of a linear fit to the data

$G < 800$ V. A systematic error bar

$$\Delta\tau_{\text{syst}} = \Delta G \left(\frac{d\tau}{dG} \right) \quad (3.3)$$

was assigned according to $d\tau/dG$ and the spread $\Delta G = \pm 50$ V around 650 V (Figure 3.3). This analysis assigned a systematic uncertainty of

$$\Delta\tau_{\text{syst}} = 29 \text{ ns}$$

to the measurement.

Lifetime measurements from 5 data sets acquired from Nov/2010 - Jan/2011 were averaged together in an unweighted mean, and the statistical error bar is the standard deviation of this mean

$$\Delta\tau_{\text{stat}} = 25 \text{ ns.}$$

Combing the statistical and systematic errors in quadrature, we arrive at the quoted value of

$$\tau_C = 490 \pm 40 \text{ ns.} \quad (3.4)$$

3.2 Molecular Transition Matrix Elements

Full characterization of a state in ThO requires electronic, vibrational, and rotational quantum numbers $|\alpha, \nu, J, M, \Omega\rangle$, where α is a place holder for our state labels (X, C, H, \dots). While ThO is best thought of as a Hund's case (c) molecule, decompositions exist into a Hund's case (a) basis states $|\Lambda, S, \Sigma\rangle$, giving us the ability to perform calculations in that basis [115]. The definitions of these quantum numbers may be found in Section 1.2.2, and general discussions of the preferred bases of the various Hund's cases may be found in [81, 78, 79].

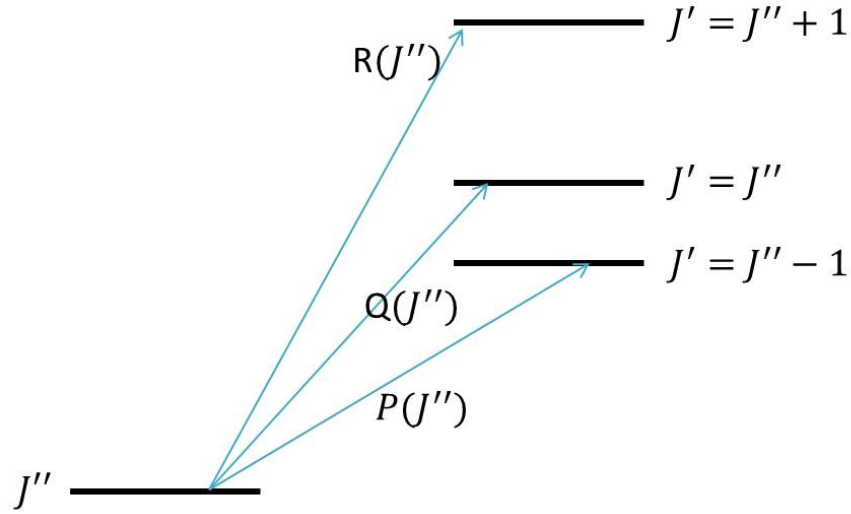


Figure 3.4: Notation diagram for state labels and rotational transition branches.

The total state wavefunction can be factorized into uncoupled basis components

$$|\text{el}\rangle |\text{vib}\rangle |\text{rot}\rangle = |\Lambda, S, \Sigma\rangle |\nu\rangle |J, M, \Omega\rangle \quad (3.5)$$

where the vibrational wavefunction $|\alpha, \nu\rangle$ is separable in the Born-Oppenheimer approximation [79]. In general, we are only considering spin allowed E1 transitions ($\Delta S = 0$, $\Delta \Sigma = 0$), so we neglect these quantum numbers in the following calculations. As is common in rotational spectroscopy, we define state labels by the convention in Figure 3.4. The lower (higher) energy state in a transition matrix element is always labeled by α'' (α') quantum numbers. Angular momentum selection rules for rotational transitions restrict ($\Delta J = J' - J'' = 0, \pm 1$), which are defined using $P(J'')$, $Q(J'')$, $R(J'')$ notation as indicated.

Observable operators exist in the lab fixed frame, while matrix elements of molecular states must be performed in the molecular dipole fixed frame. Transformation between these two frames can be performed with the rotation matrix $\mathcal{D}_{p,q}^{(k)}(\omega)$, where

$p, q = 0, \pm$ are the components of a rank-1 tensor in the lab and molecule frames respectively [78]. Vector operators in the lab frame are specified with upper case X, Y, Z spatial coordinates, while lower case x, y, z are used for the molecule frame. Note that the electronic wavefunction component $|\Lambda, S, \Sigma\rangle$ contains molecule frame quantum numbers (i.e. not good quantum numbers in the lab frame), while the total angular momentum and rotational component $|J, M, \Omega\rangle$ is represented by quantum numbers that are good in both frames.

The electric dipole operator, $\hat{\mu} = e\hat{\mathbf{r}}$, operates upon the orbital part of our electronic wavefunctions $\psi(\vec{\mathbf{r}})$. This molecule frame operator defines the leading order interaction of molecular wavefunctions with electromagnetic radiation, and is therefore at the heart of many molecular calculations. In spherical tensor form [79, 123]

$$\hat{\mu}^+ = \frac{1}{\sqrt{2}}(\hat{\mu}_x + i\hat{\mu}_y), \quad (3.6)$$

$$\hat{\mu}^- = \frac{1}{\sqrt{2}}(\hat{\mu}_x - i\hat{\mu}_y), \quad (3.7)$$

$$\hat{\mu}^0 = \hat{\mu}_z. \quad (3.8)$$

This definition is extremely useful for simplifying calculations when applied with the Wigner-Eckhart theorem. These spherical tensor operators raise and lower the values of Λ in matrix elements between electronic states ($\langle\Lambda''|\hat{\mu}|\Lambda'\rangle$). We define electronic transition moments according to these matrix elements

$$D_{\alpha'-\alpha''}^+ = \langle\alpha'', \Lambda' + 1|\hat{\mu}^+|\alpha', \Lambda'\rangle, \quad (3.9)$$

$$D_{\alpha'-\alpha''}^- = \langle\alpha'', \Lambda' - 1|\hat{\mu}^-|\alpha', \Lambda'\rangle, \quad (3.10)$$

$$D_{\alpha'-\alpha''}^0 = \langle\alpha'', \Lambda'|\hat{\mu}^0|\alpha', \Lambda'\rangle. \quad (3.11)$$

This definition preserves much of the symmetry between $\Delta\Lambda = 0$ and $\Delta\Lambda = \pm 1$ transitions, and is in close analogy to definition used for atomic linestrengths. Care must be taken when referencing older sources such as [124, 125], where a factor of 2 difference in the definitions of $D_{\alpha'-\alpha''}^{\pm}$ cause certain Hönl-London factors to change by the same factor.

The lab-frame components of transition dipole moments are typically defined by the polarization $\hat{\epsilon}$ of the absorbed or emitted radiation. The transition moments for a given polarization of light are the matrix elements of the dot product $\hat{\epsilon} \cdot \hat{\mu}$. The most general matrix elements can be simplified and separated into lab-frame and molecule-frame components

$$\begin{aligned}
 \mathcal{M}_{\alpha''-\alpha'} &= \langle \nu'' | \langle \Lambda'', S'', \Sigma'' | \langle J'', M'', \Omega'' | \hat{\epsilon} \cdot \hat{\mu} | \nu' \rangle | \Lambda', S', \Sigma' \rangle | J', M', \Omega' \rangle \\
 &= \sum_{p,q} \langle \nu'' | \nu' \rangle \underbrace{\langle S'' | S' \rangle \langle \Sigma'' | \Sigma' \rangle \langle \Lambda'' | \hat{\mu}^q | \Lambda' \rangle}_{\text{molecule-frame}} \times \dots \\
 &\quad \underbrace{(-1)^p \hat{\epsilon}^p \langle J'', M'', \Omega'' | \mathcal{D}_{-p,q}^{(1)}(\omega)^* | J', M', \Omega' \rangle}_{\text{lab-frame}} \\
 \mathcal{M}_{\alpha''-\alpha'} &= \sqrt{|q_{\nu''-\nu'}|} \delta_{S',S''} \delta_{\Sigma',\Sigma''} D^{-\Delta\Omega} (-1)^p \hat{\epsilon}^p \langle J'', M'', \Omega'' | \mathcal{D}_{-p,q}^{(1)}(\omega)^* | J', M', \Omega' \rangle.
 \end{aligned} \tag{3.12}$$

The vibrational wavefunction overlap is equal to the square root of the Franck-Condon factor $q_{\nu''-\nu'}$ between states $\alpha' \leftrightarrow \alpha''$. Here we have used the fact that the dipole matrix element only operates on the orbital part of the wavefunction. The orthonormality of spin states then enforces the spin selection rules ($\delta_{S',S''}$, $\delta_{\Sigma',\Sigma''}$) for electric dipole transitions.

We can evaluate the rotational matrix element in terms of 3-j symbols and factors

of J , M , and Ω [81, 78, 80],

$$\begin{aligned} \mathcal{M}_{\alpha''-\alpha'} &= \sqrt{|q_{\nu'-\nu''}|} (-1)^{\Delta M} (-1)^{M'-\Omega'} \hat{e}^{\Delta M} D^{-\Delta\Omega} \times \dots \\ &\sqrt{(2J'+1)(2J''+1)} \begin{pmatrix} J'' & 1 & J' \\ -\Omega'' & -\Delta\Omega & \Omega' \end{pmatrix} \begin{pmatrix} J'' & 1 & J' \\ -M'' & -\Delta M & M' \end{pmatrix}, \end{aligned} \quad (3.13)$$

The only terms for which the 3-j symbols are non-zero must satisfy

$$q = -\Delta\Omega = -(\Omega' - \Omega''), \quad (3.14)$$

$$p = \Delta M = M' - M''. \quad (3.15)$$

With Equation 3.13 and measurements of the transition dipole D^\pm , we are able to calculate many quantities useful for performing precision measurements with ThO.

3.3 Molecular Constants From *C* State Lifetime

Measurements of excited state lifetimes provide an excellent way of extracting important experimental parameters, such as absorption cross sections, saturation intensities, branching ratios, and Rabi frequencies. This is complicated in a species where multiple decay channels contribute to the total state lifetime τ . Extracting $|D^\pm|^2$ in diatomic molecules generally requires the measurement of multiple lifetimes because their extra degrees of freedom (vibration and rotation) and hybridized electronic wavefunctions open up extra decay channels. In this section I will derive expressions for several “linestrength” related quantities as a function of our measurement of τ_C . The ability to compute these values precisely is limited by our imprecise estimates of electronic and vibrational branching ratios, but the formulas contained here would be useful if these estimates are improved in the future.

3.3.1 Partial Decay Rates

The total decay rate $\gamma_e = 1/\tau_e$, where $|e\rangle$ represents all relevant quantum numbers, is directly measured for the *C* state as described in Section 3.1. For a given decay channel from $|e\rangle \rightsquigarrow |g\rangle$, the Einstein *A* coefficient $A_{e,g} \propto |\mathcal{M}_{e-g}|^2$ represents its partial decay rate. These sum to the total decay rate

$$\gamma_e = \sum_g A_{e,g} = \sum_g \xi_{e,g} \gamma_e, \quad (3.16)$$

where we have defined the fractional branching ratios

$$\begin{aligned} \xi_{e,g} &= A_{e,g}/\gamma_e, \text{ where} \\ \xi_{e,g} &< 1, \quad \sum_g \xi_{e,g} = 1. \end{aligned} \quad (3.17)$$

The lack of closed cycling transitions in diatomic molecules such as ThO means a single excited state lifetime depends on the branching ratio of all possible decay paths. Both the lifetime and branching ratios (electronic, vibrational, and rotational) must be known in order to extract each transition's partial decay rate $A_{e,g}$.

A general expression for decay between non-degenerate states $|e\rangle \rightsquigarrow |g\rangle$, separated by frequency $\omega_0 = 2\pi \times \nu_0$, is given by Fermi's Golden Rule. Per our case we assume the density of photon states is that of free space and decay is via electric dipole radiation [126, 79]. The following expression has already been integrated over solid angle and includes the necessary factor of 2 for the two-fold polarization degeneracy of radiation emitted into each wavevector \hat{k}

$$A_{e,g} = \frac{\omega_0^3}{\pi\epsilon_0\hbar c^3} |\mathcal{M}_{e-g}|^2. \quad (3.18)$$

In the absence of quantizing \mathcal{E} or \mathcal{B} fields, as is the case in our measurement of τ_C , the molecules are completely unpolarized. Due to the isotropy of space, molecules

decay in an unpolarized fashion back to the ground state, such that transitions with all values of $\Delta M = 0, \pm 1$ are equally likely. Moreover, spatial isotropy dictates that the excited state population will be evenly distributed across all $2J' + 1$ angular momentum projections (M'). This distribution of population effectively averages the individual decay rates into the observed rate of decay for the entire degenerate manifold [79], and the population decays according to

$$\frac{dN_{J'}}{dt} = - \sum_{M', M''} A_{(J'M', J''M'')} \frac{N_{J'}}{2J' + 1}. \quad (3.19)$$

The effective decay constant for all degenerate magnetic sublevels will therefore be summed over final states and averaged over initial states

$$A_{eJ'\Omega', gJ''\Omega''} = \frac{\omega_0^3}{\pi\epsilon_0\hbar c^3} \sum_{M', M''} \frac{|\langle e, J'', M'', \Omega'' | \hat{\epsilon} \cdot \hat{\mu} | g, J', M', \Omega' \rangle|^2}{2J' + 1}. \quad (3.20)$$

All these decay paths between degenerate manifolds $J' \rightsquigarrow J''$ are related to a reduced matrix element via the Wigner-Eckhart theorem [126], and the sum in Equation 3.20 can be written in an M independent form. The sum over the M dependent 3-j coefficients from Equation 3.13 can be evaluated using the orthogonality relationships for the 3-j coefficients [79]

$$\sum_{M', M''} \left(\begin{array}{ccc} J' & 1 & J'' \\ -M' & \Delta M & M'' \end{array} \right)^2 = \frac{1}{3}. \quad (3.21)$$

Therefore, the expression for the unpolarized decay between two states (in the Hund's case (a) or (c) basis, in which Ω is a good quantum number) is

$$A_{eJ'\Omega', gJ''\Omega''} = \frac{\omega_0^3}{3\pi\epsilon_0\hbar c^3} (2J'' + 1) \left(\begin{array}{ccc} J' & 1 & J'' \\ -\Omega' & -\Delta\Omega & \Omega'' \end{array} \right)^2 q_{\nu' - \nu''} \left| D_{e-g}^{-\Delta\Omega} \right|^2. \quad (3.22)$$

We have arrived at an expression that relates the partial decay rate A to a dipole matrix element for our unpolarized sample.² We note that the remaining 3-j coefficients are often written as the rotational branching ratios (Hönl-London factors) $S_{J''}^{\Delta J}(\Delta\Omega)$. The proper form given our definitions for D^\pm are tabulated in [79] and can also be expressed symbolically

$$S_{J''}^{\Delta J}(\Delta\Omega) \equiv (2J' + 1)(2J'' + 1) \begin{pmatrix} J' & 1 & J'' \\ -\Omega' & -\Delta\Omega & \Omega'' \end{pmatrix}^2. \quad (3.23)$$

If we explicitly write the rotational dependence back in, we can solve for the partial width of an arbitrary transition

$$A_{e,g} = \frac{\xi_{e,g}}{\tau_e} = \frac{\omega_0^3}{3\pi\epsilon_0\hbar c^3} \frac{q_{\nu'-\nu''} |D_{e-g}|^2}{(2J' + 1)} S_{J''}^{\Delta J}. \quad (3.24)$$

3.3.2 Branching Ratios

A caveat to evaluating Equation 3.24 is that our zero-field eigenstates are symmetric or antisymmetric combinations of $\pm\Omega$ for electronic states with $|\Omega| > 1$ such as (C , H , Q). The zero field rotational eigenstates must be eigenstates of the parity operator P . If one considers the full molecular wavefunction in a Hund's case (a) basis, the parity transformations [78] are

$$P |\Lambda, S, \Sigma\rangle |J, M, \Omega\rangle = (-1)^{J-S} |-\Lambda, S, -\Sigma\rangle |J, M, -\Omega\rangle \quad (3.25)$$

which are slightly different than the oft quoted parity relationships for only the rotational part $P |J, M, \Omega\rangle = (-1)^{J-\Omega} |J, M, -\Omega\rangle$ [78, 80]. The good eigenstates of parity

²This should not be used if the initial state is polarized by an \mathcal{E} -field and excited with a single laser polarization $\hat{\epsilon}$, as the sum over M sublevels will not be valid.

are then [79]

$$|^{2S+1}\Lambda_{\Omega, \pm}\rangle = \frac{|^{2S+1}\Lambda_{\Omega}\rangle \pm (-1)^{J-2\Sigma+S} |^{2S+1}\Lambda_{-\Omega}\rangle}{\sqrt{2}}. \quad (3.26)$$

One can check that this definition is correct according to the parity transformations of Equation 3.25, or by explicitly showing that matrix elements from Equation 3.13 vanish when evaluated between states of the same parity.

When applying Equation 3.22, we must calculate the matrix elements in the good parity basis, $|^{2S+1}\Lambda_{\Omega, \pm}\rangle$. In particular, we consider transitions from $|C, J = 1\rangle$ to all accessible states with $\Delta\Omega = 0, \pm 1$ and $\Delta J = 0, \pm 1$. Evaluating the rotational part of Equation 3.24, one can make the following substitutions in the parity basis for all relevant rotational transitions

$$\text{For } (C \rightarrow X) Q(1) : \frac{S_1^0(1)}{(2J' + 1)} \rightarrow 1, \quad (3.27)$$

$$\text{For } (C \rightarrow H) Q(1) : \frac{S_1^0(0)}{(2J' + 1)} \rightarrow 1/2, \quad (3.28)$$

$$\text{For } (C \rightarrow H) P(2) : \frac{S_2^{-1}(0)}{(2J' + 1)} \rightarrow 1/2, \quad (3.29)$$

$$\text{For } (C \rightarrow Q) P(2) : \frac{S_2^{-1}(-1)}{(2J' + 1)} \rightarrow 1. \quad (3.30)$$

Notice that summing over all rotational branches, even in the parity basis, makes the total rotational branching fractions equal. Applying the sum rule for 3-j symbols over all final rotational states,

$$\sum_{J''} \left(\begin{array}{ccc} J' & 1 & J'' \\ -|\Omega'| & |\Delta\Omega| & |\Omega''| \end{array} \right)^2 = \frac{1}{2J'' + 1}, \quad (3.31)$$

cancels the factor of $(2J'' + 1)$ in Equation 3.22 when all rotational branches are included. Therefore, the decay rate for each electronic and vibrational branch becomes

$ g\rangle$	$ \langle C \hat{D} g\rangle ^2/ D ^2$	$1/\lambda_{C-g}$ (cm ⁻¹)	$\xi_{C,g}$
X	0.75	14490	0.82
H	0.15	9173.4	0.04
Q	0.61	8362	0.13
A	0.12	3890	0.002
B	0.60	3361	0.008

Table 3.1: Estimated electronic branching ratios. The $\xi_{C,g}$ are normalized to add to unity.

rotation independent in the limit that the difference in frequency between rotational states is small compared to the transition frequency. An important consequence of these sum rules over J'' and selection rules over Ω is that for unpolarized molecules the rotational branching fraction does not depend on the rotational state. We can understand this physically, because the excited state decay rate involves an electronic transition within the molecule fixed frame. This rate cannot depend on the molecule rotation, since there is no rotation in this fixed frame.

According to Equation 3.24, each partial decay rate can be expressed using separate electronic and vibrational terms in addition to the rotational dependence discussed above. The *C* state can decay electronically to (*X*, *H*, *Q*, *A*, *B*), and estimates of branching ratios are shown in Table 3.1. We assume Hund's case (a) basis decom-

positions listed in [127, 115] are equal to amplitudes squared, such that

$$|X\rangle \approx |^1\Sigma^+\rangle, \quad (3.32)$$

$$|H\rangle \approx \sqrt{0.985} |^3\Delta_1\rangle + \sqrt{0.01} |^3\Pi_1\rangle + \sqrt{0.005} |^1\Pi_1\rangle, \quad (3.33)$$

$$|Q\rangle \approx \sqrt{0.95} |^3\Delta_2\rangle + \sqrt{0.05} |^1\Delta_2\rangle, \quad (3.34)$$

$$|A\rangle \approx \sqrt{0.95} |^3\Pi_0\rangle + \sqrt{0.05} |^1\Sigma^+\rangle, \quad (3.35)$$

$$|B\rangle \approx \sqrt{0.75} |^3\Pi_1\rangle + \sqrt{0.2} |^1\Pi_1\rangle + \sqrt{0.05} |^3\Sigma_1\rangle, \quad (3.36)$$

$$|C\rangle \approx \sqrt{0.77} |^1\Pi_1\rangle + \sqrt{0.2} |^3\Pi_1\rangle + \sqrt{0.015} |^3\Delta_1\rangle + \sqrt{0.015} |^3\Phi_2\rangle. \quad (3.37)$$

We assume that any basis states that are connected by electric dipole selection rules ($\Delta S = 0$, $\Delta \Sigma = 0$, $\Delta \Lambda = \pm 1, 0$, and $\Delta \Omega = \pm 1, 0$) have equal matrix elements. Therefore, their contribution to the total matrix element $|\langle C|\hat{D}|g\rangle|^2$ is weighted by the product of the amplitude of each connected state. These weighting factors, summed in quadrature, give the the relative state overlaps $|\langle C|\hat{D}|g\rangle|^2/|D|^2$. The branching ratios follow from Equation 3.18 and depend on both these state overlaps and the transition wavelength $\xi_{C,g} \propto 1/\lambda^3 \left(|\langle C|\hat{D}|g\rangle|^2/|D|^2 \right)$ (Table 3.1).

We consider only the decay to X , H , and Q states, because the w_0^3 factor in the decay rates makes the branching ratio to the nearby A and B states contribute a negligible amount to γ_C [81, 128]. Vibrational branching ratios $q_{\nu'-\nu''}$ (Franck-Condon factors) have been calculated for ThO using Morse potentials [129], and are in good agreement with our own calculations using harmonic wavefunction overlap based on measured rotational constants [81]. For decay from $|C, \nu' = 0\rangle$, the Franck-Condon factors $q_{0-\nu''} \lesssim 1\%$ for states $\nu'' \geq 2$, so a sum over vibrational decay channels can typically be truncated after the first or second term.

3.3.3 $X \rightarrow C$ Transition Dipole Moment

The branching ratios estimated in the previous section allow us to limit the partial decay rates which dominantly contribute to the C state lifetime τ_C . In the measurement of τ_C , the excitation laser drives the Q(1) line from $X \rightarrow C$ from the odd parity $|X, J = 1\rangle$ ground state to the even parity excited state $|C, J = 1, P = +\rangle$. The observed decay, following parity selection rules, is rotationally closed (only Q(1) transitions) from $C \rightsquigarrow X$. Decay to either of the opposite parity superpositions of H and C states allow rotational decays in the $C \rightsquigarrow H$ and $C \rightsquigarrow Q$ manifolds satisfying $\Delta J = 0, \pm 1$. The remaining non-zero terms in the C state decay are

$$\gamma_{C, \nu'=0, J'=1} \approx \sum_{\nu''} \left(A_{C \rightarrow X, Q(1)} + A_{C \rightarrow H, Q(1)} + A_{C \rightarrow H, P(1)} + A_{C \rightarrow Q, P(1)} \right). \quad (3.38)$$

Applying the rotational branching ratios in our parity basis (Equations 3.27-3.30) and summing over rotational branches, we are left with

$$\begin{aligned} \gamma_{C,0} &= \sum_{\nu''} (A_{C0, X\nu''} + A_{C0, H\nu''} + A_{C0, Q\nu''}) \\ \gamma_{C,0} &= \frac{8\pi^3}{3\pi\epsilon_0\hbar} \sum_{\nu''} \left(q_{C0-X\nu''} \frac{|D_{X-C}|^2}{\lambda_{C-X}^3} + q_{C0-H\nu''} \frac{|D_{H-C}|^2}{\lambda_{C-H}^3} + q_{C0-Q\nu''} \frac{|D_{Q-C}|^2}{\lambda_{C-Q}^3} \right). \end{aligned} \quad (3.39)$$

By applying the sum rules for the Franck-Condon factors $\sum_{\nu''} q_{\nu'-\nu''} = 1$, then we can write the decay in a vibration independent form

$$\gamma_C = \frac{8\pi^2}{3\epsilon_0\hbar} \left(\frac{|D_{X-C}|^2}{\lambda_{C \rightarrow X}^3} + \frac{|D_{H-C}|^2}{\lambda_{C \rightarrow H}^3} + \frac{|D_{Q-C}|^2}{\lambda_{C \rightarrow Q}^3} \right). \quad (3.40)$$

Note that here we assume the electronic and vibrational wavefunctions are completely separable (i.e. Born-Oppenheimer is a good approximation).

We can use our estimates of electronic branching ratios to calculate the dominant

transition moment that contributes to the *C* state decay, $|D_{X-C}|^2$,

$$|D_{X-C}| = \sqrt{\frac{\xi_{C,X}}{\tau_C} \frac{3\epsilon_0 \hbar \lambda_{C-X}^3}{8\pi^2}}. \quad (3.41)$$

Using the branching ratios as defined in Equation 3.17 and listed in Table 3.1, and our measurement of the lifetime, this dipole moment is

$$|D_{X-C}| = 1.3 \pm 0.2 \text{ D} = 0.52 \pm 0.08 \text{ ea}_0 \quad (3.42)$$

Here we have included a $\sim 15\%$ error bar which combines the quoted 10% uncertainty in the lifetime measurement and a comparable uncertainty in the branching ratio estimates.

Using estimated or measured branching ratios, various transition dipole moments with the *C* state can be computed using $|D_{X-C}|$ derived above. Of particular interest is the $H \rightarrow C$ transition used for *H* state spin preparation and probing,

$$|D_{H-C}| = \sqrt{\frac{\xi_{C,H}}{\xi_{C,X}} \frac{\lambda_{C-H}^3}{\lambda_{C-X}^3}} |D_{X-C}|. \quad (3.43)$$

There is currently a discrepancy between a calculation of $|D_{H-C}|^2$ using our estimated branching ratios and estimates from directly driving the $H \rightarrow C$ transition. This probably indicates that our estimation of $\xi_{C,H}$ is inaccurate. The dipole allowed overlap $|\langle C|\hat{D}|H\rangle|^2/|D|^2$ is computed as the sum of many terms in 3.1. We lack the knowledge of wavefunction phases in Equations 3.32-3.37, so these terms could just as easily cancel, suppressing the branching ratio and removing the discrepancy. Equation 3.43 is useful if we have other measurements of the branching ratio, including those from saturation measurements [105].

3.3.4 Optical Absorption Cross Section

As mentioned above, the transition dipole matrix element can be related to measurable quantities such as Rabi frequencies, saturation intensities, and absorption cross sections. The literature varies greatly over the definitions of some of these quantities and the assumptions that go into their derivations [126, 130]. Reference [79] presents a self consistent set of rate equations in the context of diatomic molecules, is well referenced, and is consistent with simpler results derived in the case of two level atoms [131, 132].

The optical absorption cross section is defined as the rate of photon absorption ($\Gamma_{e,g}$) per photon at a given frequency ω

$$\sigma_{e,g}(\omega) = \frac{\Gamma_{e,g}(\omega)}{\Phi(\omega)} \quad (3.44)$$

where $\Phi(\omega) = I(\omega)/(\hbar\omega)$ is the photon flux [126]. If we consider that stimulated emission from the upper state can actually amplify our signal³, then the the intensity of a laser beam passing through this molecular medium with number density $N = N_g + N_e$ is

$$I(z) = I_0 e^{-\sigma_{e,g}(N_g - N_e)z}. \quad (3.45)$$

We quote the result from [79], where the cross section is defined in terms of the transition moments

$$\sigma_{e,g}(\omega) = \frac{\omega_0}{6\epsilon_0\hbar c} \frac{q_{\nu'-\nu''} |D_{e-g}|^2 S_{J''}^{\Delta J}}{(2J'' + 1)} g(\omega - \omega_0). \quad (3.46)$$

³The effects of stimulated emission are negligible for weak excitations, so for weak probe beams the $e^{\sigma_{e,g}N_e z}$ term in Equation 3.45 can be neglected. One significant exception is in a laser, where a large population inversion is created by other pumping mechanisms.

We express the cross section in a general form that includes a normalized linewidth function $\int g(\omega - \omega_0) = 1$, which can be representative of any linewidth broadening mechanism [79]. For a homogenously broadened Lorentzian lineshape

$$g_L(\omega - \omega_0) = \frac{\gamma/2\pi}{(\gamma/2)^2 + (\omega - \omega_0)^2} \quad (3.47)$$

where the FWHM of $\Delta\omega_L = 2\pi \times \Delta\nu_L = \gamma = 1/\tau$. Also useful are Doppler broadened Gaussian lineshapes with FWHM $\Delta\omega_D$

$$g_D(\omega - \omega_0) = \frac{2}{\Delta\omega_D} \sqrt{\pi \ln(2)} e^{-4 \ln(2) ((\omega - \omega_0)/\Delta\omega_D)^2}. \quad (3.48)$$

In general, we should integrate across our laser linewidth to compute the total attenuation of the beam. When our light source has a narrow linewidth compared to other broadening mechanisms, $g(\omega - \omega_0)$ can just be evaluated at a single point, typically on resonance. It is interesting to evaluate the cross section on resonance in the limit that lifetime broadening is the dominant mechanism.⁴ Then Equation 3.46 can be combined with Equations 3.24 and 3.47 to recover the formula from [126, 81] for the resonant absorption cross section

$$\sigma_{\text{nat}} = \frac{\lambda^2 (2J' + 1)}{2\pi (2J'' + 1)} \xi_{e,g}. \quad (3.49)$$

In the ACME experiment, we are typically in the limit of $\Delta\omega_D > \Delta\omega_{\text{laser}}$, so equation so Equation 3.48 should be applied to Equation 3.46 to predict the amount of optical absorption. Laser absorption can be used to measure atom number densities in our molecular beam. If a probe laser frequency is scanned across an atomic resonance, the integrated absorption optical density will give a lineshape independent

⁴This is typically NOT the case in the ACME experiment, where our lineshapes are dominated by the Doppler broadening of our molecular beam.

measurement of the molecule number density. This technique is typically used on the $X \rightarrow C$ transition as an accurate probe of molecules in the ground state.

3.3.5 Fluorescence Saturation Intensity

Saturation intensities, which can be related to transition dipole moments, are a useful way of quantifying our ability to strongly drive transitions. We have determined the saturation intensity of various transitions in ThO by directly measuring molecule fluorescence as a function of laser power [105]. Such measurements can be defined in different ways for different transitions, depending on decay pathways and the relevant broadening mechanisms [126]. The relevant saturation condition for ACME is that we can power broaden the transition linewidth past our Doppler linewidth, so that our laser interacts with all available molecules. In this section we will use the definition of the saturation intensity as applied to a two level system to draw comparisons between $X \rightarrow C$ saturation measurements and the lifetime measurement. In Section 4.2, we consider the case of fluorescence when driving the highly off diagonal transition $H \rightarrow C$.

Typically one defines the saturation intensity for a closed two level system, in which there is a steady state solution to the rate equations [126]. If we instead consider the three level system shown in Figure 3.5, then the full set of rate equations is

$$\begin{aligned}
 \frac{dN_g}{dt} &= -\Gamma N_g + (A_{e,g} + \Gamma)N_e + A_{i,g}N_i \\
 \frac{dN_e}{dt} &= \Gamma N_g - (A_{e,g} + A_{e,i} + \Gamma)N_e \\
 \frac{dN_i}{dt} &= A_{e,i}N_e - A_{i,g}N_i
 \end{aligned}
 \tag{3.50}$$

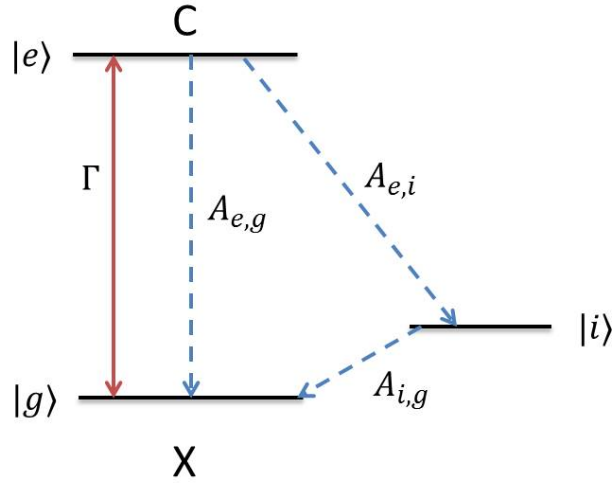


Figure 3.5: Diagram of the model used to consider saturation of the $X \rightarrow C$ transition. Γ represents the optical excitation rate, and the decay rates are assumed to have the hierarchy $A_{e,g} \gg A_{e,i} \gg A_{i,g}$. The state $|i\rangle$ represents other “off-diagonal” states to which C can decay, which is primarily the higher vibrational state $|X, \nu = 1\rangle$.

We consider the limit that $A_{e,g} \gg A_{e,i} \gg A_{i,g}$, and that the total time the molecule interacts with the laser is $T \lesssim 1/A_{e,i}$. This is the case for the $H \rightarrow C$ transition, where the fastest “off diagonal” decay rate from $|C, \nu' = 0\rangle \rightsquigarrow |X, \nu'' = 1\rangle$ is $1/A_{C0,X1} \approx 3\mu\text{s}$ is about the same as the $T \sim 5\mu\text{s}$ time it takes a 200 m/s ThO molecule to traverse the 1 mm laser beam. The population that has decayed into level $|i\rangle$ is very small, so $N_i(T) \approx 0$. In this case, the rate equations reduce to those for a two level system, and we recover the typical expression for the fluorescence intensity (I_F),

$$I_F = A_{e,g} N_e \propto \frac{\kappa}{1 + 2\kappa} \quad (3.51)$$

where

$$\kappa = I/I_{\text{sat}} = \Gamma/A_{e,g} \quad (3.52)$$

is the saturation parameter [126].

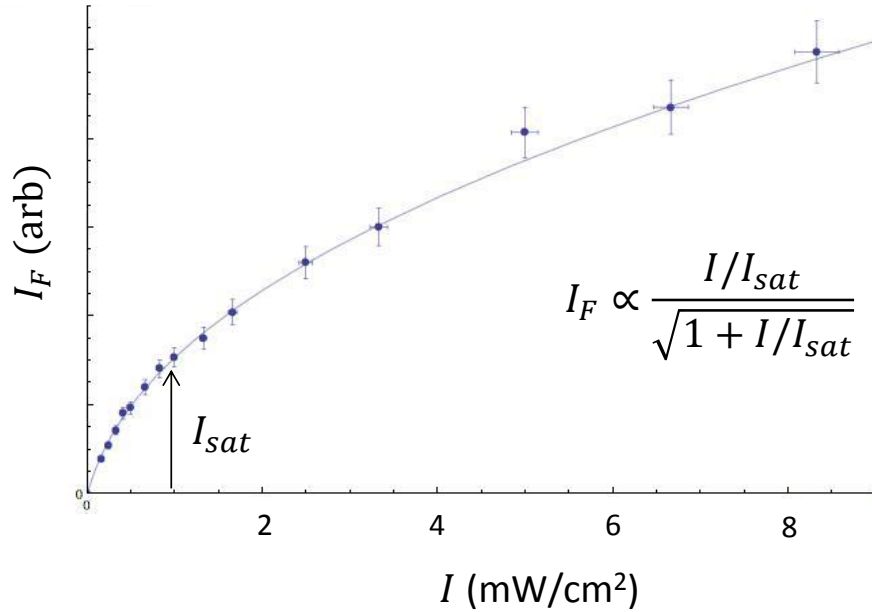


Figure 3.6: Saturation of observed fluorescence intensity from the $X \rightarrow C$ transition. The transition is driven with 690 nm light, and the intensity of 690 nm fluorescence is measured. The extracted $I_{\text{sat}} = 1 \pm 0.5$ mW/cm². This data was taken and fit to the functional form of Equation 3.55 by Ben Spaun.

The physical interpretation of the saturation intensity is that $\kappa = 1$ represents when optical excitation rate Γ equals the relaxation rate back to the ground state $A_{e,g}$. The fluorescence curve turns over at $I = I_{\text{sat}}$ because the rapid Rabi flopping between ground and excited state saturates the time averaged population in the excited state to $N_{\text{tot}}/2$. We define the saturation intensity on resonance, such that $\Gamma = \sigma_{\text{nat}}\Phi(\omega_0)$. The saturation intensity of $|X, \nu = 0\rangle \rightarrow |C, \nu = 0\rangle$ according to our definitions is

$$I_{\text{sat}} = \frac{\hbar\omega_0 A_{C0,X0}}{\sigma_{\text{nat}}}, \quad (3.53)$$

$$I_{\text{sat}} = \frac{2\pi\hbar c}{\lambda^3} \frac{(2J'' + 1)}{(2J' + 1)} \frac{1}{\tau_C}. \quad (3.54)$$

In the limit that Doppler broadening is much greater than the natural or power

broadened linewidth, one can show that the fluorescence saturates more slowly,

$$I_F(I) \propto \frac{I/I_{\text{sat}}}{\sqrt{1 + I/I_{\text{sat}}}} \quad (3.55)$$

as power broadening increases under the Doppler width, capturing more molecules and creating more fluorescence [126]. Saturation data was acquired in this regime (Figure 3.6), making measurements in MBII with a large amount of Doppler broadening. Fluorescence was monitored while driving the $|X, \nu'' = 0, J'' = 1\rangle \rightarrow |C, \nu' = 0, J'' = 1\rangle$, while varying the power in the 690 nm laser beam. Fitting this data yields a saturation parameter of $I_{\text{sat}} = 1 \pm 0.5 \text{ mW/cm}^2$, with a large error bar that takes into account uncertainties in both fluorescence and intensity measurements. Using Equation 3.54 and applying Gaussian error propagation, the measured lifetime τ_C predicts a saturation intensity of

$$I_{\text{sat}} = 0.77 \pm 0.06 \text{ mW/cm}^2, \quad (3.56)$$

in excellent agreement with the directly measured saturation intensity.

3.3.6 Optical Excitation Rate

The excitation rate Γ as defined above is an intuitive indication of the strength at which a transition is driven. We can write the excitation rate per laser intensity Γ/I in terms of parameters already measured or extracted. The excitation rate for the rotationally closed Q(1) $X \rightarrow C$ transition in zero field is

$$\frac{\Gamma_{X0-C0}}{I} = \frac{A_{X0,C0}}{\Gamma}, \quad (3.57)$$

$$= \frac{2\tau_C}{3\epsilon_0\hbar^2c} q_{0-0} |D_{X-C}|^2. \quad (3.58)$$

For this transition the optical excitation rate is

$$\frac{\Gamma_{X0-C0}}{I} \approx 2 \frac{\text{MHz}}{(\text{mW}/\text{cm}^2)}. \quad (3.59)$$

Note that the ratio of Γ/I for states with similar rotational branching ratios depends on transition dipole moments and Franck-Condon factors. In particular

$$\frac{\Gamma_{H-C}/I}{\Gamma_{X-C}/I} = \frac{q_{H0-C0}|D_{H-C}|^2}{q_{X0-C0}|D_{X-C}|^2}, \quad (3.60)$$

can be used to find the transition dipole $|D_{H-C}|^2$ of the *H* state by comparing measurements of optical excitation rates.

Chapter 4

Properties of State Preparation and Probe Lasers

The 1090 nm state preparation and probe lasers are a key element of the phase precession measurement. In analogy to a Ramsey sequence, these lasers act as our effective $\pi/2$ pulses, spatially separated regions where spin coherence is either created or measured. Their properties must be carefully controlled to ensure our data is high contrast, low noise, and free of systematics.

4.1 Optical Configuration

The state preparation and probe lasers are meant to strongly drive the $H \rightarrow C$ transition for all molecules in the ThO beam. By driving with sufficient intensity to power broaden past the Doppler width, molecules in all transverse velocity classes participate in the experiment [105]. The lasers were shaped into elongated 2D profiles,

generating light sheets that intersected the molecular beam and maximized both the signal and contrast. The properties of both lasers were dynamic. For example, the frequency was tuned to perform the $\tilde{\mathcal{N}}$ and $\tilde{\mathcal{P}}$ switches (Section 5.4.2). In addition, the polarization of the probe laser was rapidly modulated to measure the two spin quadratures used to compute a normalized asymmetry (Section 2.1). Two different schemes for polarization switching, one using two AOMs and another with a single EOM, were both rigorously tested. Ultimately we chose the former implementation, as discussed below.

4.1.1 Laser Amplification and Shaping

The state preparation and probe lasers are separated by 22 cm, and each has optical access to the molecule beam through separate window flanges in the vacuum chamber and slits in the magnetic shields. They are launched off a breadboard table (positioned next to the interaction region) that includes beam shaping and polarization control optics (Figure 4.2). On the far side of the interaction region there is a smaller optics table for beam dumps, retroreflection optics, and space for setting up auxiliary optical measurements (such as the Raman measurement described in Section 6.2.4). At one point, the position of these two breadboards was reversed in order to change the propagation direction $\hat{k} \cdot \hat{z}$ of these lasers (Section 7.1.3), which required complete realignment of both sets of optics.

Light from state preparation and probe outputs of the $\tilde{\mathcal{N}}$ and $\tilde{\mathcal{P}}$ state switching breadboards (Section 5.4.2) are seeded into two 10W fiber amplifiers (Nufern NUA-1084-PB-0010-B3) with a maximum gain of 40 dB. These amplifiers are designed for

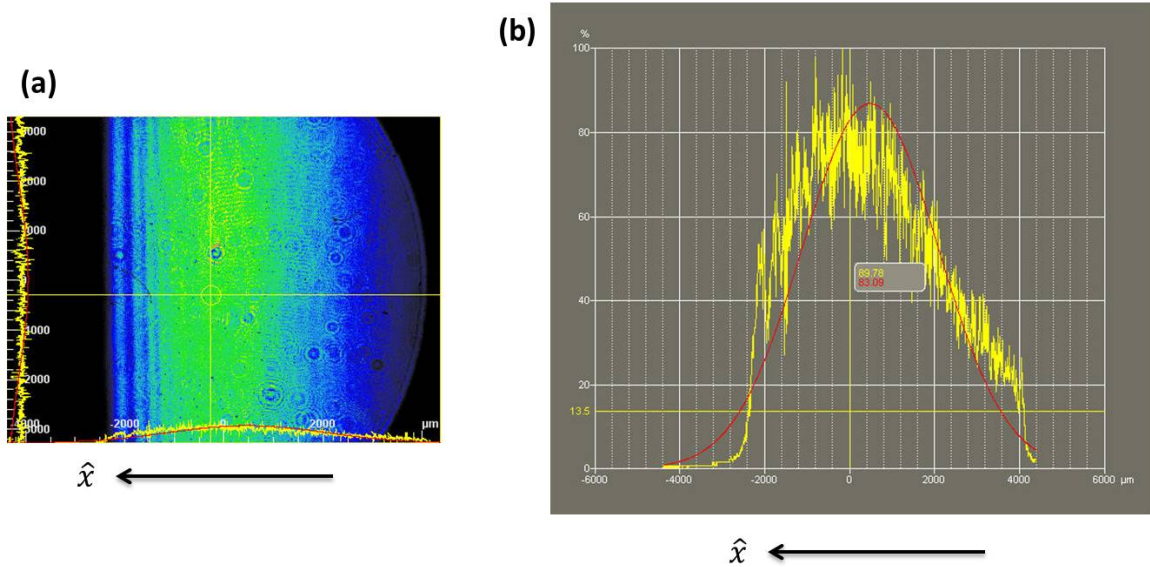


Figure 4.1: Intensity profile of the state preparation beam with intentional spherical aberration, including (a) the 2D image and (b) the profile along the \hat{x} direction. In both cases the molecules propagate along the indicated \hat{x} direction, so the steep side of the profile is the “downstream” edge.

amplification of narrow linewidth, low power (1-15 mW) seed lasers, so are well suited for generating 2-4 W of power from our ~ 1 MHz linewidth diode lasers to drive the weak $H \rightarrow C$ transition. After collimating the freespace output of the armored fiber cable, each beam is sent through a 30 dB optical isolator (Thorlabs IO-5-1090-HP) to protect the amplifier against back reflections.

The state preparation laser is first expanded using a pair of spherical lenses, which are tilted to intentionally introduce spherical aberrations into the beam. This tilt angle is optimized to create a steep reduction in the laser intensity on the downstream side of the laser profile (Figure 4.1). A chopper wheel (Terahertz Technologies C-995) with 50% duty cycle at 50 Hz reduces the prep laser’s time averaged power incident on the electric field plates (Section 4.3). Using the undiffracted output of an additional AOM in both prep and probe beam paths allows us to fine tune our laser

power for studies of power correlated systematics (Section 7.1.3). The isolators and these power modulating AOMs have $\sim 85\%$ transmission, while the AOMs used for polarization switching of the probe beam have $\sim 50\%$ transmission efficiency. The Nufern amplifiers for prep and probe are typically turned up to 60% and 45% of their max power setting, respectively¹. Including the 85% transmission through the field plates, we estimate about 2.5 W in the prep beam and 1 W of the probe beam intersect the molecule beam.

The final stretching of the prep and probe lasers into an elongated ~ 3 cm transverse (\hat{y}) by 3-5 mm (\hat{x}) Gaussian ellipse is done using cylindrical lenses. To minimize the variation in intensity across the molecule beam, the \hat{y} transverse height of the lasers is set to be twice as broad as the collimated diameter of the molecule beam. This large laser beam height would be clipped by 1" diameter optics such as mirrors or waveplates, so vertical beam expansion must happen immediately before the laser enters the interaction region. To preserve arbitrary polarization states, the laser does not reflect off any mirrors between the final half-wave plate and the interaction region (Section 5.4.3), so the cylindrical lenses must be in-line with the final clean-up polarizer (Figure 4.2).

The global polarization of each laser is controlled using a pair of half-wave plates mounted in rotation stages, allowing for slow switches of polarization orientation as described in Section 5.4.3. The signal normalization scheme requires the linear polarization of the probe laser to be switched rapidly between orthogonal directions, which we call \hat{X} and \hat{Y} . Note that these polarization directions need not align with

¹The power supply used in conjunction with the Nufern amplifiers cannot provide their maximum required current for 10 W output. Therefore, the reported percentage settings are not out of 10 W, but instead should be taken from a max power of ~ 6 W.

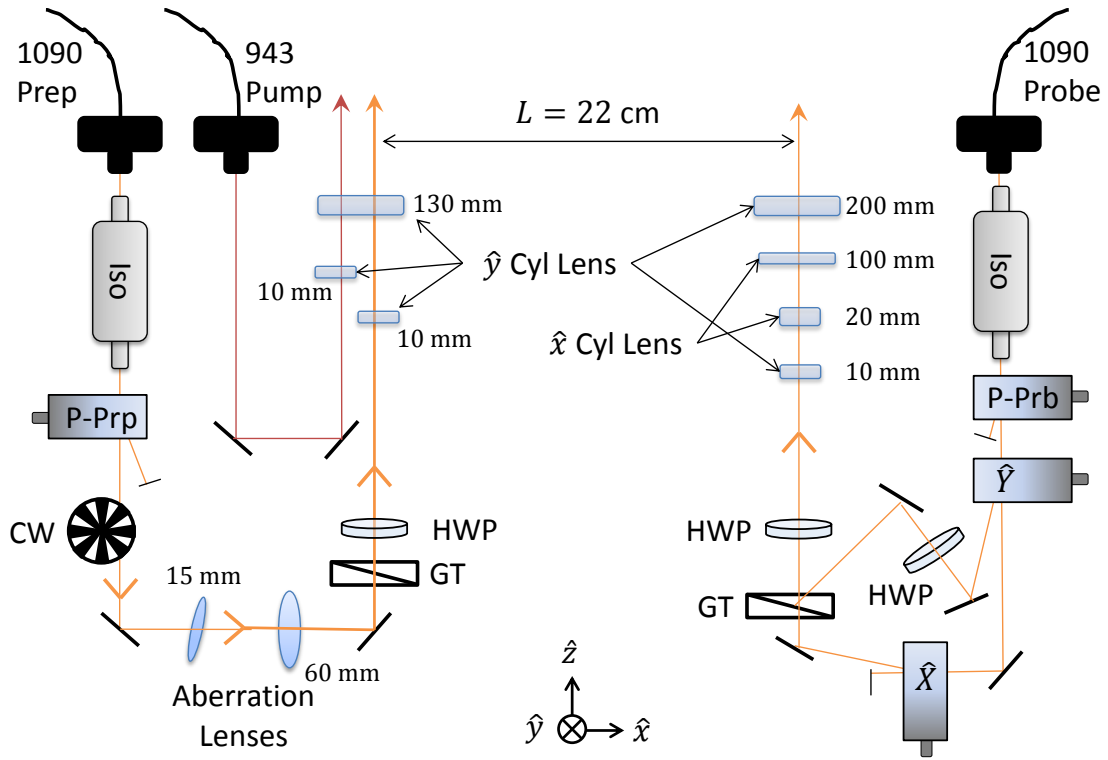


Figure 4.2: Layout of beam shaping and polarization control optics outside the interaction region. Components include cylindrical lenses (Cyl Lens) for stretching beams in the horizontal (\hat{x}) or vertical (\hat{y}) directions, half-wave plates (HWP), a chopper wheel (CW), Glan-Taylor polarizers (GT), optical isolators (Iso), tilted lenses for creating spherical aberration, and AOMs for polarization switching (\hat{X} , \hat{Y}) and power control (P-Prp, P-Prb). Spherical and cylindrical lens focal lengths are labeled in millimeters. All output fiber couplers are collimated with aspheric lenses of $f = 9 \pm 2$ mm.

the absolute spatial axes (\hat{x}, \hat{y}), with relative angle θ depending on the quarter-wave plate angle.

4.1.2 Fast Polarization Switching

The probe polarization must be rapidly modulated between orthogonal linear states to compute the asymmetry $\mathcal{A} = (S_X - S_Y)/(S_X + S_Y)$. The duration of each

polarization bin τ_{chop} was bounded from above and below by the following considerations. Efficient normalization requires that the change in signal level (S_0) in between \hat{X} and \hat{Y} polarization bins be less than the shot noise. Pulses from the final configuration of our molecular beam source can be approximated by a Gaussian with width $\Delta t_p \approx 2$ ms. The Fourier transform of such a pulse is a Gaussian in frequency space with typical width $1/\Delta t_p \sim 500$ Hz, which sets a lower limit on our polarization switching rate. The molecule pulses can occasionally have a faster rising edges than a Gaussian, so we conservatively set a lower limit of a 10 kHz chopping rate ($\tau_{\text{chop}} \leq 50 \mu\text{s}$) for polarization modulation [9].

An upper limit on the switch rate is determined by the C state lifetime, $\tau_C \approx 0.5 \mu\text{s}$. The signals from each time bin will decay exponentially at a rate of e^{-t/τ_C} after the polarization is switched. In order to remove signal correlations between opposite polarization bins, we require that $\tau_{\text{chop}} \geq 10\tau_C$. An additional $2.4 \times \tau_C = 1.2 \mu\text{s}$ of “deadtime” is inserted into the polarization switching waveform, such that both beams are simultaneously extinguished (Figure 4.3). This allows the peak fluorescence signals, which occur immediately after a polarization switch, to not be contaminated from the decay of the previous state.

Switching at the maximum rate of $1/(2\tau_{\text{chop}}) = 100$ kHz is advantageous because it allows us to double our fluorescence signal by probing 100% of the available molecules. By requiring $2\tau_{\text{chop}} < w_{\text{prb}}/v_{\text{beam}}$, then any given molecule will see both \hat{X} and \hat{Y} polarizations while crossing the probe beam of width w_{prb} . Each molecule will always emit a photon into one of the polarization bins, so long as the switch between polarization states is fast enough to prevent adiabatic following of the spin [9]. Therefore,

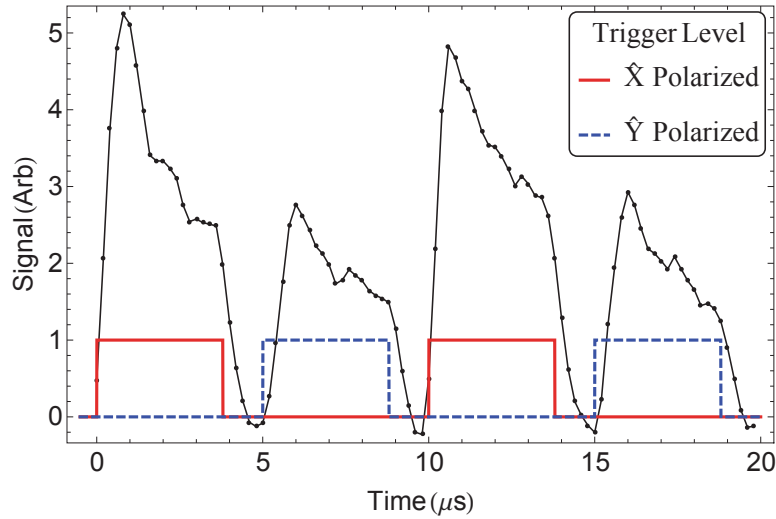


Figure 4.3: Trigger waveforms for polarization switching, plotted alongside measured fluorescence signals. The polarization is switched at 100 kHz using AOM shutters, corresponding to one full period of \hat{X} and \hat{Y} polarization, with a $2.4 \times \tau_C = 1.2 \mu s$ “deadtime” inserted. Background levels are measured for each pulse before the molecules enters the probe region. They are subtracted from the entire fluorescence trace to produce the background free signals shown here.

we chose $\tau_{\text{chop}} = 5 \mu s$, and a probe beam width of $d_{\text{prb}} \approx 4.5 \text{ mm}$ in order to satisfy this condition for maximum signal.

Probe polarization switching is implemented by splitting the probe beam into two orthogonal frequency components, passing them through AOM shutters, then recombining them on a high extinction ratio Glan-Taylor polarizing beam splitter (Thorlabs GT10-B) (Figure 4.2). Originally, an EOM configured for polarization switching (Conoptics 360-120)² was used to modulate the polarization, but the AOM

²This polarization switching EOM is configured with two stages of Lithium Tantalate (LTA) crystals with crystal orientation and electric fields rotated by 90° with respect to each other. This cancels out all phase retardation aside from the electric field dependent component, greatly reducing the temperature dependence of the output polarization. A polarizer on the input aligns the polarization at 45° to the crystal axes, and a quarter-wave plate mounted on the output ensures that the polarization is always linear, regardless of the voltage applied [133].

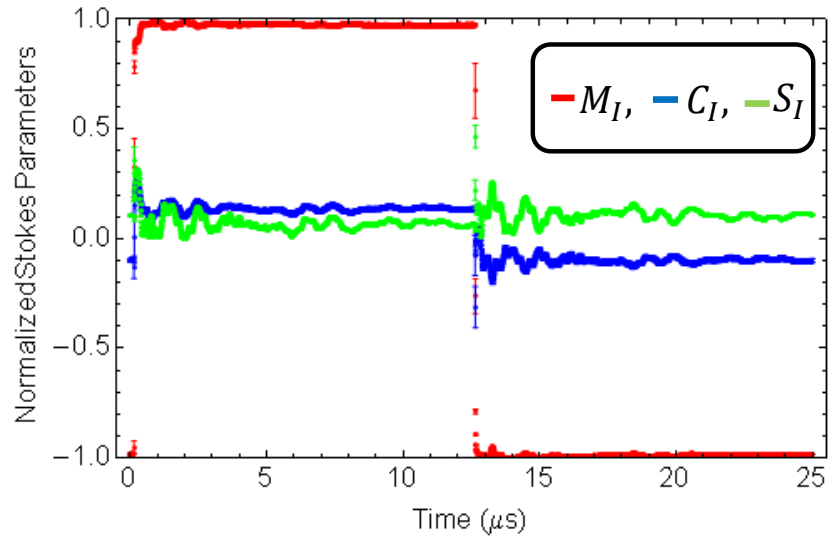


Figure 4.4: Time resolved Stokes parameters while polarization switching with an EOM, as measured with the Stokes polarimeter (Appendix B). Note that for these tests, the EOM was being driven at 40 kHz, so switches occurs at $0 \mu\text{s}$ and $12.5 \mu\text{s}$. A time bin for EDM data would correspond to the first $5 \mu\text{s}$ of this waveform. The change in the sign of M_I indicates rotation of the polarization by 90° after the switch. Ringing in the amount of circular polarization S_I is apparent.

configuration was ultimately chosen due to the following advantages:

- A much higher guaranteed level of polarization purity can be achieved with the AOMs because the GT polarizer is the last optic in the polarization switching system.
- The \hat{X} and \hat{Y} polarization components are guaranteed to be orthogonal by the high extinction ratio of the GT polarizer (100,000:1). In contrast, the EOM configuration requires careful tuning of the half-wave voltage to achieve orthogonality, and this setting can drift over time. The maximum effective “extinction ratio” of the EOM is 100:1.

- Good spatial uniformity of the GT polarizer reduces spatial polarization gradients, to which our experiment is particularly sensitive. We observed that our EOM generated a non-uniform electric fields across the retarder crystal, thus creating a spatial polarization gradient across an extended laser beam.
- AOM beam shutters can be switched rapidly with rise time of (100 ns). An EOM must be driven with high voltage ($V_{1/2} \approx 150$ V), making the necessary fast rise times of the switching pulse (5 ns with Conoptics 25D driver) hard to generate cleanly. Observed ringing of the EOM driver voltage (Figure 4.4), and therefore the polarization state, would have required special measures to suppress, which were not necessary for the AOM.

A drawback of the AOM configuration is that the two polarization components are derived from physically different beams. The power and alignment of these two beams had to be carefully monitored and adjusted to equalize them. Although IPV studies demonstrated no dependence of the EDM channel on probe \hat{X} or \hat{Y} pointing or power offsets, it simplifies data analysis to have these parameters well matched. In principle, the polarization rotation of the EOM should not affect the \hat{X}, \hat{Y} power or pointing, although this need to be tested rigorously if we ever elect to return to EOM polarization switching.

4.2 Temporal Profile: Sub-Bin Signal Dependence

The fluorescence signal has a distinctive shape after each polarization switch. In EDM data, we call each of these switches a “bin”, so this switching process leads

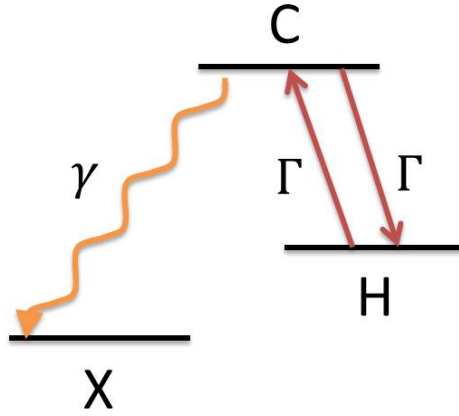


Figure 4.5: Simplified level scheme relevant for optical pumping out of the H state. Radiation at 1090 nm causes stimulated absorption/emission between $H \leftrightarrow C$ at a rate Γ . The C state decays only off diagonally to the ground state at rate γ .

to a “sub-bin” dependence of the fluorescence. It is important to understand the shape of this signal for purposes of data analysis and error bar estimation. If the background in each sub-bin was flat, one would be able to calculate noise on a fluorescence measurement by looking at the variance of the 25 points within a sub-bin. This uncertainty would get propagated into the measurement of the asymmetry, and through to the final error bar.

With a time varying fluorescence signal, one cannot directly measure the variance of the signal level using a single bin. Instead, we integrate under the sub-bin, and calculate asymmetries with respect to neighboring bins $\mathcal{A}_i = (S_{i,X} + S_{i,Y}) / (S_{i,X} - S_{i,Y})$. To compute a fundamental error bar in this case we take the variance of consecutive measurements of \mathcal{A}_i [81, 105]. The statistical error calculated in this way can be somewhat sensitive to the bounds of the sub-bin under which we integrate, so we must understand the temporal fluorescence profile for robust data analysis.

4.2.1 Saturation and Fluorescence Model

I modeled the fluorescence saturation curve classically using a system of rate equations to describe the optical pumping of population out of the H state. The relevant energy levels are H , C , and X , where H and C are coupled by the optical field of the 1090 nm probe laser, and the C state spontaneously decays at 690 nm (Figure 4.5). We define Γ as the symmetric rate of stimulated absorption and emission, equivalent to an Einstein B coefficient between $H \leftrightarrow C$ (Section 3.3.6). The estimated branching ratio $\xi_{C,H}$ is suitably small that decay back to the H state can be neglected, and population is lost from the $H \leftrightarrow C$ subsystem at rate $\gamma N_C(t)$. Since this loss rate is independent of the distribution of ground states into which C decays, the relaxation rate is $\gamma = 1/\tau_C$ where the total lifetime of the C state $\tau_C = 490 \pm 40$ ns was measured as described in Section 3.1.

Given these assumptions, we can write down the rate equations for the population of the three states in the standard way [126]

$$\dot{N}_C = \Gamma N_H - (\gamma + \Gamma)N_C, \quad (4.1)$$

$$\dot{N}_H = -\Gamma N_H + \Gamma N_C, \quad (4.2)$$

$$\dot{N}_X = \gamma N_C, \quad (4.3)$$

where $N_C(t) + N_H(t) + N_X(t) = N_{\text{tot}}$ preserves the total number density (molecules/volume).

The observed fluorescence intensity $I_F \propto N_C(t)\gamma$, so we must solve the third order differential equation for N_C ,

$$\ddot{N}_C = \gamma\Gamma^2 N_C + 2\Gamma^2 \dot{N}_C - (\gamma + \Gamma)\ddot{N}_C \quad (4.4)$$

using initial conditions $N_C(0) = 0$, $\dot{N}_C(0) = \Gamma$, and $\ddot{N}_C(0) = -\Gamma^2 - (\gamma + \Gamma)\Gamma$ which

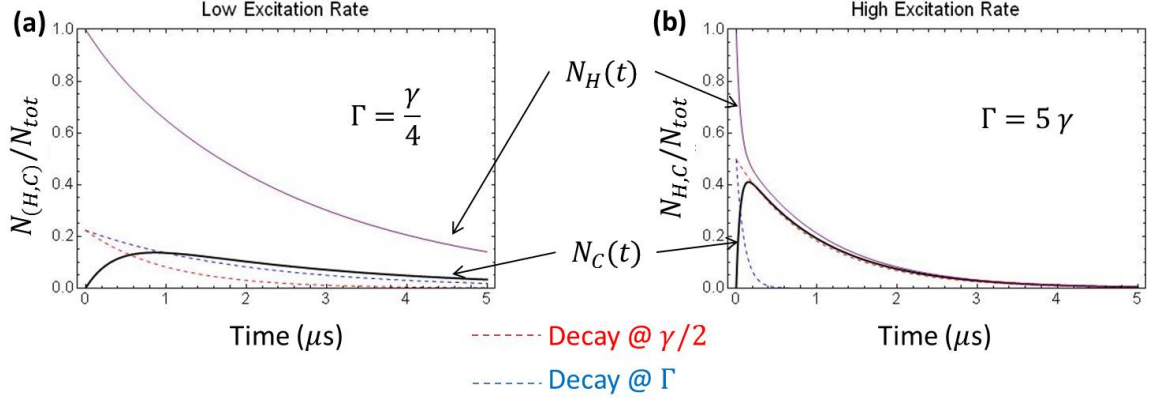


Figure 4.6: Fluorescence decay curves from $H \rightarrow C$ optical pumping. These are plots of Equation 4.5 under the conditions described in the text. A value of $\gamma = 1/\tau_C = 2$ MHz is used.

describe all the population initially in the H state when the laser is abruptly turned on at $t = 0$.

This equation has an analytic solution,

$$N_C(\eta, \kappa) = e^{-(1+2\kappa)\eta/2} \sinh\left(\frac{\eta}{2}\sqrt{1+4\kappa^2}\right) \frac{2\kappa}{\sqrt{1+4\kappa^2}} \quad (4.5)$$

where we have defined a dimensionless variable for t in units of decay time $\eta = t\gamma$ and an effective saturation parameter $\kappa = \Gamma/\gamma$. We can examine this expression in a few interesting limits, which are plotted in Figure 4.6.

If we have a very weak drive, $\kappa \ll 1$, we find that the signal initially increases linearly with rate Γ as expected. Once there is sufficient population in the C state, the fluorescence saturates, and a careful expansion for long times $\eta\kappa = \Gamma t > 1$ reveals that the fluorescence decays at the excitation rate

$$\lim_{\substack{\kappa \ll 1 \\ t \rightarrow \infty}} I_F(t) \propto \kappa e^{-\Gamma t}. \quad (4.6)$$

Operating in this limit would be interesting, because the slow decay of the fluorescence could let us make a measurement of Γ , although peak signals would be very

small because the maximum intensity $I_{\max} \propto \kappa$. We understand this limit physically, because the slow rate of optical excitation creates a bottleneck in the fluorescence decay. As soon as the laser excites a molecule, it will immediately decay to the ground state, so the signal's rate of decay is limited to Γ .

The experiment operates in the opposite limit, of $\kappa \gtrsim 1$, which is enforced in order to power broaden past the Doppler width and maximize the total fluorescence signal [105]. As expected the fluorescence initially increases with linear slope Γ to a maximum intensity given by $I_{\max} = \kappa/\sqrt{1+4\kappa^2}$. After the maximum intensity, the fluorescence decays at half the free space decay rate ($\gamma/2$)

$$\lim_{\substack{\kappa \gg 1 \\ t \rightarrow \infty}} I_F(t) \propto \frac{\kappa}{\sqrt{1+4\kappa^2}} e^{-\gamma t/2}. \quad (4.7)$$

In this limit, the large saturation parameter causes rapid Rabi flopping that time averages to distribute the population evenly between H and C , and the population is immediately equilibrated after every decay. If $N_{HC} = (N_H + N_C) = 2N_H = 2N_C$, then the observed fluorescence decays with the total population $I_F \propto N_{HC}$, but can still only leave through the C state, so the simplified rate equation in this limit is

$$\dot{N}_{HC} = -\gamma N_C = -\frac{\gamma}{2} N_{HC} \quad \rightarrow \quad I_F(t) \propto e^{-\gamma t/2}. \quad (4.8)$$

Under conditions of strong saturation, the decay profile becomes less sensitive to our laser intensity. Typically, the ACME data analysis averages over photons after the peak in fluorescence. It is then convenient that we operate in saturation, where the temporal fluorescence profile is insensitive to drifts in excitation rate from laser power or frequency fluctuations.

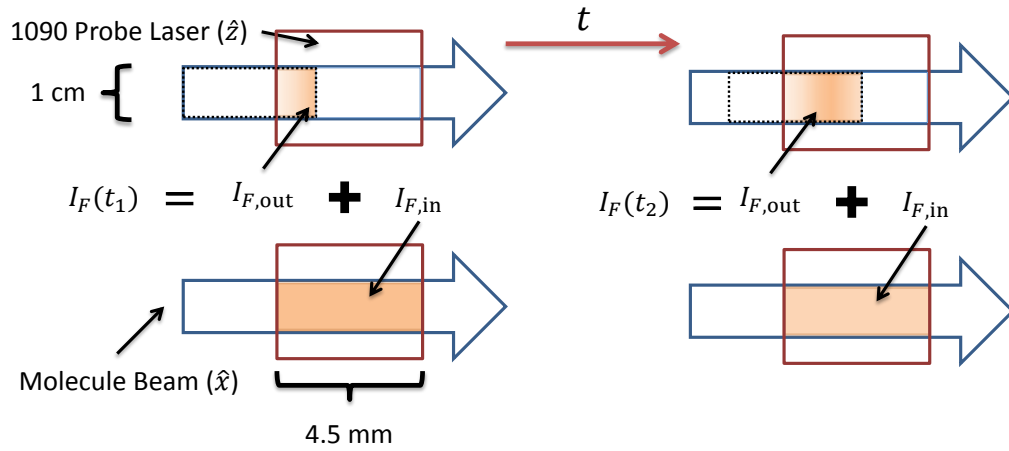
4.2.2 Fluorescence Profiles in a Molecular Beam

The discussion from the previous section describes fluorescence signals that always decay to zero for arbitrary values of κ if we excite for long enough, assuming that our total supply of molecules N_{tot} is fixed. This is not the case for a molecular beam, where the flux of molecules entering the probe laser creates a fluorescence background, such that our signals will not decay to zero even a long time after the excitation laser is switched on. On the time scale of a polarization bin, we can consider the flux to be a constant $\mathcal{F} = \lambda v_{\text{beam}}$, where $\lambda = N_{\text{tot}} A$ is the molecules per unit length in the \hat{x} direction for a molecules beam with cross sectional area A . We assume that the laser beam has a hard edge, so that a molecule moving into the laser beam sees the intensity turn on abruptly. This assumption is not strictly true for Gaussian beams, although as mentioned in Section 4.1 our probe beam is intentionally shaped to have a fast rising edge.

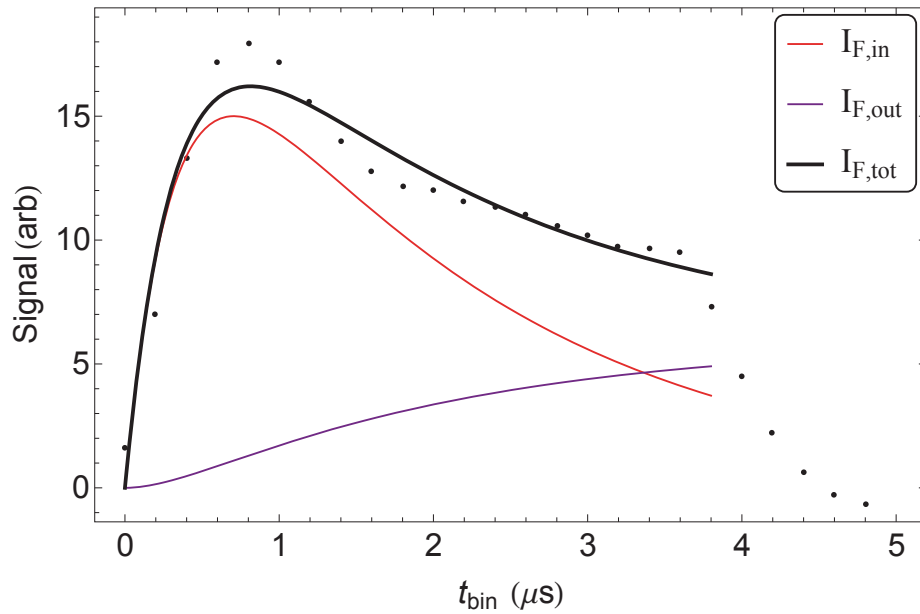
We note that because of the molecule's linear velocity v_{beam} , the temporal profile of fluorescence from Equation 4.5 is mapped into a spatial profile for molecules that have entered the laser beam since it was turned on. As molecules move into the laser after it has been switched on, this spatial profile gets “filled out” in time (Figure 4.7a: Top Case). Because our detection is not spatially resolved, the measured fluorescence profile is the integral over this spatial distribution. The fluorescence for these molecules initially outside of the laser $I_{F,\text{out}}$ as a function of time relative to the laser switch ($t_{\text{bin}} = t - t_s$) is

$$I_{F,\text{out}}(t_{\text{bin}}) \propto \lambda v_{\text{beam}} \int_0^{t_{\text{bin}}} N_C(t') dt'. \quad (4.9)$$

This integral has a closed form solution plotted in Figure 4.7b, and for $t_{\text{bin}} \gg \Gamma, \gamma$



(a)



(b)

Figure 4.7: Diagram of two components that contribute to temporal shape of observed H state probe fluorescence. (a) $I_{F,\text{in}}$ comes from the molecules that are in the probe laser when it is switched on, while $I_{F,\text{out}}$ is from molecules that enter the laser beam after the switch. (b) The two component fit (Equation 4.11) to a sample of probe laser induced fluorescence in a typical $5 \mu\text{s}$ polarization switching bin. The $I_{F,\text{out}}$ component increases to a steady state value for $t_2 > t_1$, while $I_{F,\text{in}}$ is a transient that decays as shown in Figure 4.6. For this particular fit, $\gamma = 2 \text{ MHz}$ is fixed by the C state lifetime, while the fit yields $\Gamma = 0.8 \text{ MHz}$. The data is from a single molecule pulse, averaged over the ~ 200 polarization switches during the pulse.

the signal asymptotes to a constant background fluorescence of λv_{beam} . For reference, the full form of $N_{\text{out}}(t) = \int_0^t N_C(t') dt'$ is

$$N_{\text{out}}(t, \gamma, \kappa) = \frac{1}{\gamma} - \frac{e^{-\gamma t(1+2\kappa)/2}}{\gamma\sqrt{1+4\kappa^2}} \left[(1+2\kappa) \sinh\left(\frac{\gamma t}{2}\sqrt{1+4\kappa^2}\right) + \sqrt{1+4\kappa^2} \cosh\left(\frac{\gamma t}{2}\sqrt{1+4\kappa^2}\right) \right]. \quad (4.10)$$

Therefore, our fluorescence signals can be approximated by two components, $I_{F,\text{out}}(t_{\text{bin}})$ from Equation 4.9, and the molecules that were initially within the probe beam of width w_{prb} at time t_s , which decay with a temporal profile $I_{F,\text{in}}(t_{\text{bin}}) \propto \lambda w_{\text{prb}} N_C(t_{\text{bin}})$ (Figure 4.7a). We can fit polarization chopped fluorescence signals to the functional form

$$S(t_{\text{bin}}) = A_1 N_C(t_{\text{bin}}, \gamma, \Gamma) + A_2 N_{\text{out}}(t_{\text{bin}}, \gamma, \Gamma) \quad (4.11)$$

An example fit is seen in Figure 4.7b. The fit does not accurately capture the peak of the excitation, which may be a consequence of not including the Gaussian laser beam shape.

Models that more carefully take into account the length of the probe region and polarization switching rate can accurately predict the relative amplitudes A_1/A_2 , but for the purposes of fitting it is conceptually simpler to keep these as independent fit parameters. The Gaussian shape of the probe beam can be included as a time dependent $\Gamma(t) \propto e^{-(vt/w_{\text{prb}})^2}$ when solving for N_C in Equation 4.4. This differential equation no longer has a closed form solution, so its utility in fitting to EDM data is limited. Numerical integration shows that including this Gaussian laser profile introduces only small deviations from the approximate closed form solutions of Equations 4.5 and 4.10.

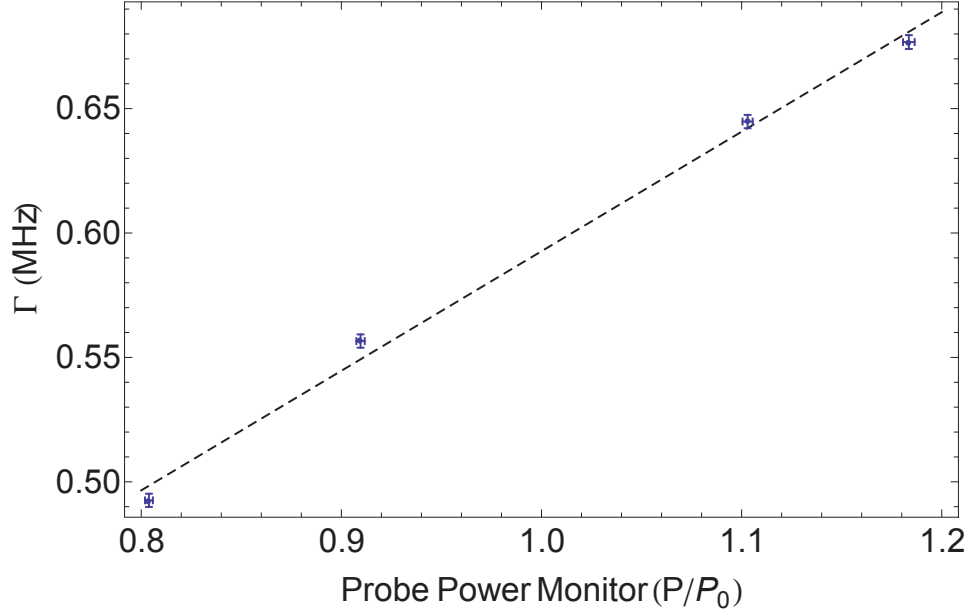


Figure 4.8: Measured linear relationship between optical excitation rate and probe laser power. Relative probe power (P/P_0) is monitored using photodiode on an irised subregion of the laser after passing through in the interaction region. The excitation rate Γ is extracted from a fit to Equation 4.11 by fixing the decay constant $\gamma = 2$ MHz. Error bars on both measurements are the standard deviation of the mean of measurements over $\sim 25,000$ ablation pulses.

By fixing the decay rate $\gamma = 1/\tau_C = 2$ MHz, these fits can be used to extract the rate of optical excitation from $H \rightarrow C$. Since $\Gamma \propto I_{prb}|D_{H-C}|^2$, these fits can be used to either monitor the laser power or extract a measurement for the transition dipole moment, assuming we know the laser intensity. Figure 4.8 compares the extracted Γ against the probe power as monitored by a photodiode signal (taken during a $P^{\mathcal{N}\mathcal{E}}$ superblock where the power was being intentionally modulated). The fit reveals the expected linear dependence, although with an unexplained offset if the fits are

extrapolated to zero power.³

Ultimately such data could be used to compensate for changes in molecule Rabi frequency in future EDM data. Absolute measurements of probe laser power incident on the molecules are imprecise because of scattering off the electric field plates. There is of order 1 W/cm^2 intensity in the laser beam, so the measurement of $\Gamma \sim 0.5 \text{ MHz}$ is consistent with our estimates of $|D_{H-C}|$ from Section 3.3.3 and from saturation intensity measurements [105].

4.3 Spatial Profile: Polarization Gradients

We discovered that polarization gradients along the trajectory of our molecules (\hat{x}) were responsible for a major source of systematic error, as described in Section 7.1. Careful studies of these gradients using the polarimeter described in Appendix B was key for diagnosing and limiting these systematics. We discovered that birefringence gradients in our glass electric field plates were created by thermally induced optic stress [134] from the absorbed laser energy of our intense $\sim 2 \text{ W}$ state preparation and probe laser beams. They were minimized by reducing the time averaged energy deposited in the field plates by inserting an optical chopper into the laser beam.

³This measurement is limited in practice by the low pass filter at 2 MHz applied to the detection circuitry. Values of $\Gamma \gg \gamma$ could not be distinguished because they would all be smoothed to the bandwidth of the filter. It is also possible that this filter could account for the imperfections in the peak fit and the offset when Figure 4.8 is extrapolated to zero power.

4.3.1 Thermally Induced Stress Birefringence

We consider our glass field plates of thickness t_G , with a single side ITO coating of thickness t_C . Both the substrate and coating contribute to heating due to absorption $I(z) = I_0 \exp(-(\alpha_G t_G + \alpha_C t_C)z)$ with respective absorption coefficients α_G, α_C [133]. In limit of small absorption $\alpha t \ll 1$, the power deposited per unit volume averaged over the substrate can be approximated as

$$Q(x) \approx \frac{I(x, t_G) - I_0(x)}{t_G} = I_0(x) \left(\alpha_G + \frac{\alpha_C t_C}{t_G} \right) \quad (4.12)$$

For a stretched laser beam, in the limit of high aspect ratio (narrow in \hat{x} , wide in \hat{y}) the heat deposited by absorption will create a gradient of the principle stress component $\sigma_{yy}(x)$ [135, 81]. The resulting stress gradient will induce a birefringence gradient according to the stress optic law [136], $\delta n = K(\sigma_{xx} - \sigma_{yy})$, where the stress optic coefficient is $K \approx (3 - 4) \times 10^{-3} \text{ GPa}^{-1}$ for commonly used optical glasses.

One arrives at a differential equation for the optical retardance gradient ($\delta\Gamma(x) = \frac{2\pi t_G}{\lambda} \delta n(x)$) in relation to the laser intensity [81],

$$\frac{d^2 \delta\Gamma(x)}{dx^2} = \frac{\beta t_G}{\lambda} I(x). \quad (4.13)$$

The factor β is almost entirely material specific,

$$\beta = \frac{2\pi K E \alpha_v}{\kappa} \left(\alpha_G + \alpha_C \frac{t_C}{t_G} \right), \quad (4.14)$$

and depends on the stress optic coefficient K , Young's modulus E , coefficient of thermal expansion α_v , and thermal conductivity κ of the substrate, as well as the absorption coefficients⁴ and thickness of the coating and substrate. For our 200 nm

⁴The *absorption coefficient* α is related to the *extinction coefficient* $\kappa = \text{Im}(n)$ by $\alpha = 4\pi\kappa/\lambda$ [133].

coating of ITO on Borosilicate glass⁵, substituting the appropriate numbers gives $\beta \approx 7 \times 10^{-5} \text{ W}^{-1}$. Notice how the stress birefringence is a property of both the substrate and the coating if there is a substantial amount of absorption in the coating.

As long as the intensity profile is suitably elongated, Equation 4.13 can be integrated to yield the optical retardance gradient $\Gamma(x)$ for a laser beam with an arbitrary intensity profile $I(x)$. A closed form solution exists for a 2D Gaussian beam $I(x, y) = P_{\text{tot}}/(2\pi w_x w_y) \exp(-(x^2/2w_x^2 + y^2/2w_y^2))$ of the form [81]

$$\Delta\Gamma(x) = -\beta \frac{t_G P_{\text{tot}}}{2\pi w_x w_y \lambda} \left[w_x^2 e^{-x^2/2w_x^2} + \sqrt{\frac{\pi}{2}} w_x x \text{erf} \left(\frac{x}{w_x \sqrt{2}} \right) \right] \quad (4.15)$$

This serves a reasonable fit function to optical retardance gradient data. Good agreement between this function and polarimetry data supports this model for thermally-generating birefringence gradients.

4.3.2 Polarization Effects of Thermal Birefringence

As discussed in Section 7.1.1, our ac Stark shift phases are sensitive to linear and circular polarization gradients in different ways. Let's analyze how the small changes in retardance Γ described in the previous section can affect our laser polarization parameters. We assume the linearly polarized input state is altered by the small retardance gradient $\Gamma(x)$. This section is an extension the analysis from [81] to include arbitrary angles between the laser polarization and birefringent axes. Here we assume familiarity with both the Jones calculus and the Stokes parameters (see [133] or Appendix B.1).

⁵The optical thickness of our coating was specified to be $\lambda/2$ at 900 nm by Custom Scientific. The index of refraction $n \approx 2.0$, so the physical thickness is $t_C \approx 450/2 = 225$ nm.

Assume our input light is propagating in the \hat{z} direction. We are free to choose a linear polarization basis of Jones vectors aligned with the \hat{x} and \hat{y} axes,

$$\mathbf{X} = \begin{pmatrix} 1 \\ 0 \end{pmatrix}, \quad \mathbf{Y} = \begin{pmatrix} 0 \\ 1 \end{pmatrix}. \quad (4.16)$$

A linear polarization in an arbitrary direction ϕ with respect to the \hat{x} axis is then

$$P(\phi) = \cos(\phi)\mathbf{X} + \sin(\phi)\mathbf{Y} = \begin{pmatrix} \cos \phi \\ \sin \phi \end{pmatrix}. \quad (4.17)$$

Consider the input linear polarization to be fixed and oriented along the $\phi = 0$ direction. In the basis described above

$$P_{in} = \begin{pmatrix} 1 \\ 0 \end{pmatrix}. \quad (4.18)$$

The polarization state can be rotated between linear bases separated by an angle ψ by applying the rotation matrix $R(\psi)$ ([133] Equation 1.9-9).

$$R(\psi) = \begin{pmatrix} \cos \psi & \sin \psi \\ -\sin \psi & \cos \psi \end{pmatrix}. \quad (4.19)$$

In the basis parallel to the fast axis of some linear retardation element with phase retardation $\Gamma = \frac{2\pi}{\lambda}(n_s - n_f)d$, the Jones matrix is

$$U(\Gamma) = \begin{pmatrix} e^{-i\Gamma/2} & 0 \\ 0 & e^{i\Gamma/2} \end{pmatrix}. \quad (4.20)$$

The Jones matrix corresponding to a waveplate oriented at an angle ψ with respect

to the input polarization follows from a simple basis transformation

$$\begin{aligned}
 U(\Gamma, \psi) &= R(-\psi)U(\Gamma)R(\psi) \\
 &= \begin{pmatrix} e^{-i\Gamma/2} \cos^2 \psi + e^{i\Gamma/2} \sin^2 \psi & -i \sin(\Gamma/2) \sin(2\psi) \\ -i \sin(\Gamma/2) \sin(2\psi) & e^{-i\Gamma/2} \sin^2 \psi + e^{i\Gamma/2} \cos^2 \psi \end{pmatrix}.
 \end{aligned} \tag{4.21}$$

The state of the output polarization is then $P_{out}(\Gamma, \psi) = U(\Gamma, \psi)P_{in}$. This formulation is mathematically equivalent to the case where the input linear polarization is rotated while the birefringent element is kept fixed. When looking for small changes in polarization, it is advantageous to operate in this fixed polarization frame, so the output state can easily be related to the static input. The output polarization is

$$P_{out}(\Gamma, \psi) = \begin{pmatrix} e^{-i\Gamma/2} \cos^2 \psi + e^{i\Gamma/2} \sin^2 \psi \\ -i \sin(\Gamma/2) \sin(2\psi) \end{pmatrix}. \tag{4.22}$$

Analysis of P_{out} in terms of Stokes parameters is a useful way to quantify small polarization deviations and compare to our polarimetry measurements. By definition, the normalized Stokes parameters can be computed as the differences in intensity in the linear basis (M_I), another linear basis at 45 degrees (C_I), and a circular basis (S_I),

$$M_I = |P \cdot \hat{x}|^2 - |P \cdot \hat{y}|^2, \tag{4.23}$$

$$C_I = 1/2(|(P \cdot \hat{x} + P \cdot \hat{y})|^2 - |(P \cdot \hat{x} - P \cdot \hat{y})|^2), \tag{4.24}$$

$$S_I = 1/2(|(P \cdot \hat{x} - iP \cdot \hat{y})|^2 - |(P \cdot \hat{x} + iP \cdot \hat{y})|^2). \tag{4.25}$$

Solving explicitly for the Stokes parameters of P_{out} in Equation 4.22

$$M_I = \cos^2(\Gamma/2) + \cos(4\psi) \sin^2(\Gamma/2), \quad (4.26)$$

$$C_I = \sin^2(\Gamma/2) \sin(4\psi) \quad (4.27)$$

$$S_I = -\sin(\Gamma) \sin(2\psi) \quad (4.28)$$

The angle of the linear polarization is simply determined by the ratio of the two linear stokes parameters, $\phi = 1/2 \arctan(C_I/M_I)$. For a small retardance ($\Gamma \ll 1$), one finds the linear polarization angle has been rotated to

$$\delta\phi \approx \frac{1}{8} \sin(4\psi) \Gamma^2 \quad (4.29)$$

Likewise, the circular polarization is quantified in terms of the ellipticity angle $\theta_e = 1/2 \arccos(S_I)$. In the Γ , $S_I \ll 1$ limit the ellipticity and circular stokes parameter differ by a factor of 2, so for small changes in the ellipticity

$$\delta\theta_e \approx -\frac{S_I}{2} \approx \frac{1}{2} \sin(2\psi) \Gamma. \quad (4.30)$$

With a small thermally induced birefringence gradient across the field plates, the spatially varying $\Gamma(x)$ will generate both linear and circular spatial polarization gradients, $\delta\phi(x), \theta_e(x)$. The circular polarization gradient has been directly observed, both through gradient polarimetry (Figure 4.10) and its coupling to the molecule phase through the \mathcal{E}^{nr} systematic (Figure 7.5). Noting a few interesting features about the linear polarization gradients from Equation 4.29

- The linear gradient is always quadratic in the small quantity Γ , suppressing it with respect to the circular polarization gradient.

- Where the circular gradient is maximized, at $\psi = \pi/4$, the linear gradient vanishes.
- Both the linear and circular gradients vanish when the input polarization is aligned with the fast or slow birefringence axes.

The linear gradient at various values of input polarization angle are

$$\delta\phi(x) \approx \begin{cases} \frac{\psi\Gamma(x)^2}{2} & \text{min at } \psi \approx 0, \pi/4 \\ \frac{1}{8}\Gamma(x)^2 & \text{max at } \psi \approx \pi/8 \end{cases} \quad (4.31)$$

If we are actively rotating the angle between the birefringent axes and the input linear polarization(ψ), we see that the induced circular and linear polarization gradients have different angular dependencies. The linear polarization gradient should exhibit half the period of the circular gradient. Our polarimetry measurements can not currently resolve a linear gradient of $\lesssim 10$ mrad. In principle, the periodicity of the $\Omega_r^{\mathcal{N}\mathcal{E}}$ systematic should have the same angular dependence as $\phi(x)$, as described in Section 7.1.3. However, by the time we realized the significance of the $\Omega_r^{\mathcal{N}\mathcal{E}}$ systematic, we had already taken measures to suppress the $\Gamma(x)$ gradient, so no statistically significant polarization dependence was observed in the $P^{\mathcal{N}\mathcal{E}}$ IPV data. Future iterations of the experiment should look closely for $\phi(x)$ gradients, either through higher resolution gradient polarimetry or $P^{\mathcal{N}\mathcal{E}}$ data with intentionally exaggerated birefringence gradients.

4.3.3 Measuring Circular Polarization Gradients

The predicted ellipticity gradients were directly observed using the polarimeter described in Appendix B [137]. The polarimeter has a spatial resolution of 0.8 mm, the size of the input aperture iris. The polarimeter was aligned perpendicular to the state preparation and probe beams, and a translation stage scanned it across each laser's wavefront to collect spatial polarization data. By using the automated waveplates to control the input polarization, the effects of the relative angle ψ between the input polarization and birefringence axes could be studied. Ellipticity gradient scans at various angles for a single probe polarization component are shown in Figure 4.9. Similar scans taken before the laser passed through the electric field plates show no polarization gradient, regardless of input angle. As mentioned in the previous section, there were never any linear polarization gradients observed, as they appear to be beyond the resolution of the polarimeter.

For ellipticity gradients caused by a space fixed birefringence gradient, Equation 4.30 predicts these gradients to have a 2ψ periodicity. By measuring amplitudes of curves like those in Figure 4.9, we can extract the angular dependence of our polarization gradients. Simply fitting each curve to a Gaussian or function in the form of Equation 4.15 provides a very large uncertainty in measurements of the gradient. The more robust and straightforward way to extract an amplitude is to take differences between points in the center and at the edges of the distribution. Figure 4.9 also shows that both the offset and amplitude of the ellipticity changes as a function of angle. Using an IPV data set where a large amount of circular polarization was added to the state preparation laser, we demonstrated that our EDM measurement

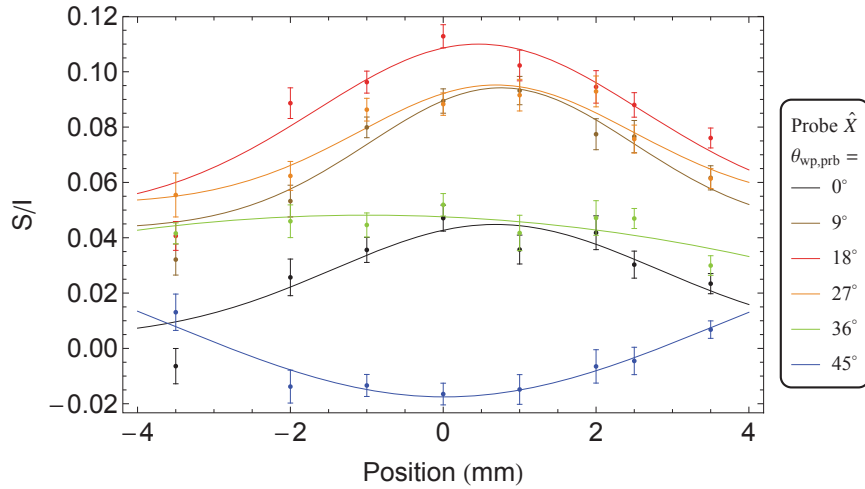


Figure 4.9: Circular polarization gradients in the probe laser beam at various input polarization angles. The y-axis is in terms of $S/I = -2\theta_e$. Input angles are relative to the home position on the rotating wave plate. Similar gradients were seen in the state preparation laser.

is not sensitive to ellipticity offsets, only spatial gradients.

The results shown Figure 4.10, for both state preparation and \hat{X} and \hat{Y} components of the probe laser, confirm the predicted periodicity. By measuring polarization relative to the polarimeter’s fixed polarizer, we can compare the phase of this angular dependence of all lasers with respect to absolute spatial coordinates. Our theory predicts that the orientation of the principle birefringent axes should depend only on the orientation of the stretched laser profile, so the gradients should vanish at $(-90^\circ, 0^\circ, 90^\circ)$. This is true in the probe laser, but the comparison shows that the prep laser gradient does not vanish at these angles, and does not have the same phase as the \mathcal{E}^{nr} systematic’s angular dependence. We note that these gradient measurements are performed after the laser has passed through two layers of electric field plates. This could account for the discrepancy in these measurements. Future polarimetry measurements should be made on a single substrate to confirm.

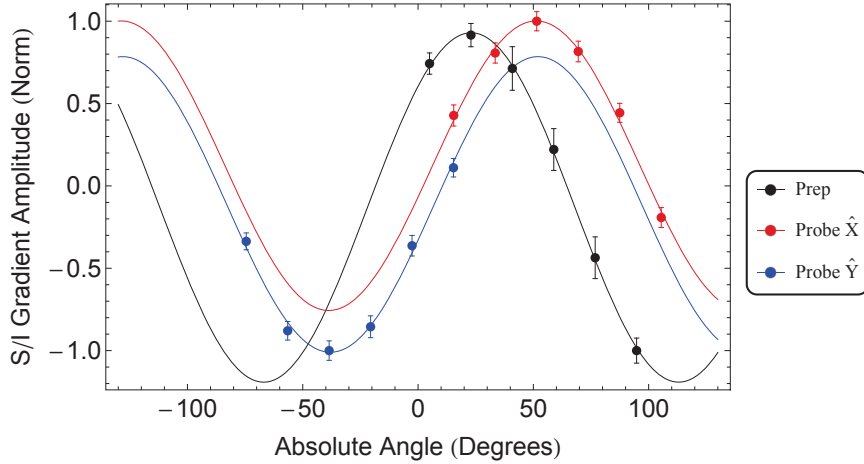


Figure 4.10: Angular dependence of thermally induced polarization gradients for both state preparation and \hat{X} and \hat{Y} components of the probe laser. The absolute linear polarization angle (for which there is no spatial gradient) was measured by the Stokes polarimeter, relative to the polarimeter’s fixed polarizer. The ellipticities have been normalized to arbitrary units so the periodicity of the various curves can be compared on the same scale.

The data presented in Figure 4.10 demonstrates that we have a birefringence gradient, while the data from Figure 4.11 confirms that the gradients are thermally induced from deposited laser power. Reducing the power of the input laser decreases the amplitude of the gradient by a comparable amount. Moreover, inserting a chopper wheel at 50 Hz with a 50% duty cycle has the same effect as turning down the instantaneous laser power by a factor of 2. This confirms that the thermal time scale in the field plates (10 s as calculated in [81]) is sufficiently long that in most cases our measurements are only sensitive to the time averaged laser power. Therefore, we were able to reduce the size of ellipticity gradients and the resulting \mathcal{E}^{nr} systematic by inserting this chopper wheel into the state preparation laser’s beam path while keeping the instantaneous power high enough to fully saturate the Doppler broadened $H \rightarrow C$ transition. Because background levels from scattered light must be constant

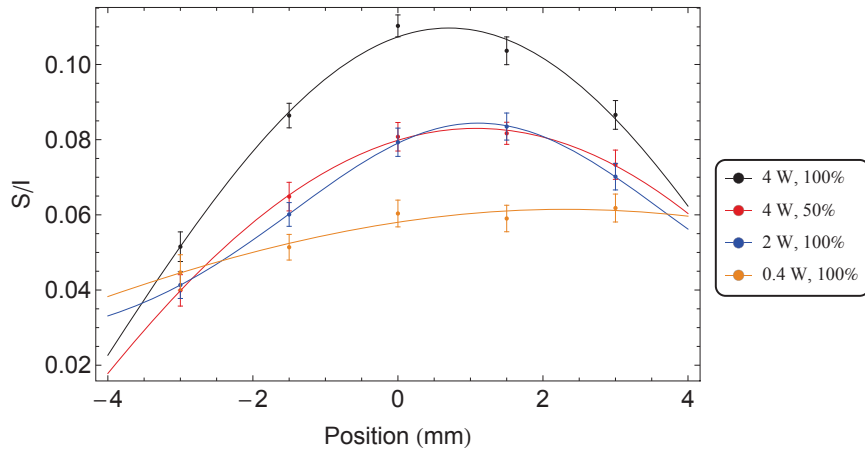


Figure 4.11: Power dependence of the thermally induced polarization gradients in the probe laser. Measured power levels are approximate, and correspond to settings of 45%, 22%, 0% on the Nufern controller for approximately 4W, 2W and 0.4W of output power, respectively. The curve with a 50% duty cycle indicates a chopper wheel was placed in the beam path. For all other data points the chopper wheel was off.

across the 9 ms long digitizer trace captured every 20 ms, a 50% duty cycle synched with our ablation pulses provided the greatest power reduction possible.

4.4 Contrast Lineshapes

By fully saturating the $H \rightarrow C$ transition, the state preparation laser will create a completely pure spin state, therefore maximizing the experiment's contrast and sensitivity to the EDM. When the frequency is scanned across the resonance, the pump beam will maximally deplete the bright state spin quadrature at zero detuning. A measurement of the contrast reveals a power broadened and flat-topped lineshape (Figure C.3b). Understanding this lineshape is important, for example, to determine how the prep laser detuning will create correlated contrasts and EDM systemat-

ics [81], or for using the contrast to calibrate an \mathcal{E} -field measurement (see [105] and Section 6.4).

The contrast lineshape can also be used as a means of returning a drifting probe laser back to the resonance frequency. This requires fitting to a simple analytic contrast lineshape that determines the center frequency. The contrast lineshapes in [81, 105] include many experimental parameters, not ideal for robust nonlinear fitting with minimal free parameters. I have found the following simplified model produces good contrast fits. In the limit of a small saturation parameter $\kappa = \Gamma/\gamma \lesssim 1$, which will be the case when the laser is off resonance, the H state population is given by Equation 4.6,

$$N_H(t) = N_0 e^{-\Gamma t}, \quad (4.32)$$

for interaction time t with the state preparation laser.

We treat N_H and Γ as quantities averaged over the entire Doppler broadened sample. Therefore, the resonance condition can be modeled as a Gaussian lineshape for Γ

$$\Gamma(\Delta, \sigma_D) = A e^{-\Delta^2/(2\sigma_D^2)} \quad (4.33)$$

where $\Delta = \nu - \nu_0$ is the detuning from resonance, and σ_D is the Doppler width (about 2 MHz for our collimated ThO beam). Assume the probe laser polarization is aligned with the spin state after precession, such that $\phi - \theta = n\pi/2$ for integer n . In this case,

$$\mathcal{A} = \mathcal{C} \cos(2(\phi - \theta)) \approx \mathcal{C}, \quad (4.34)$$

so the probe's asymmetry measurement becomes a direct measurement of our state contrast. The measurements in the \hat{X} and \hat{Y} spin quadratures are aligned with the

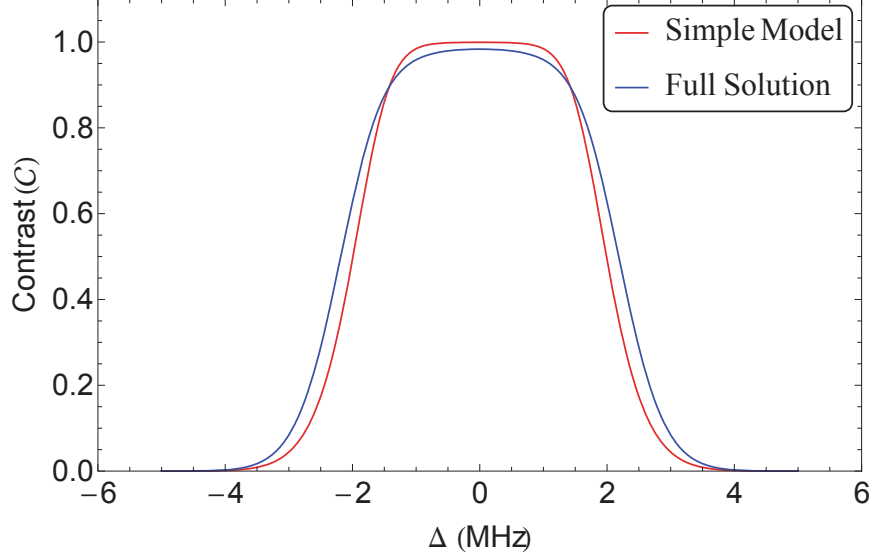


Figure 4.12: Contrast lineshape models. The simple model is from Equation 4.36 and the full solution is from Equation 4.37.

bright and dark states created by the state preparation laser. The measured populations are therefore $N_X = N_0 e^{-\Gamma t}$ and $N_Y = N_0$, leading to a measured asymmetry

$$\begin{aligned} \mathcal{A} &= \mathcal{C}_{\max} \frac{N_Y - N_X}{N_Y + N_X} \\ &= \mathcal{C}_{\max} \frac{1 - e^{-\Gamma t}}{1 + e^{-\Gamma t}} \\ \mathcal{A} &= \mathcal{C}_{\max} \tanh(\Gamma t/2). \end{aligned} \quad (4.35)$$

The factor \mathcal{C}_{\max} has been added to account for the less than 100% maximum contrast from dephasing, laser misalignment, and velocity dispersion [106].

This simple model provides us with a four parameter fit function

$$\mathcal{C}(\Delta, \sigma_D, \mathcal{C}_{\max}, A) = \mathcal{C}_{\max} \tanh(Ae^{-\Delta^2/(2\sigma_D^2)}). \quad (4.36)$$

As an alternative approach, we could have used the exact solution for the remaining population of the bright state using Equation 4.1 ($N_H = \frac{\gamma+\Gamma}{\Gamma} N_C + \frac{\dot{N}_C}{\Gamma}$), with $N_C(\eta, \kappa)$

from Equation 4.5. Solving for the asymmetry and using the excitation lineshape

$\Gamma(\Delta, \sigma_D)$

$$\mathcal{C}(\Delta, \sigma_D, \mathcal{C}_{\max}, \eta, \kappa) = \mathcal{C}_{\max} \frac{1 - N_H(\Delta, \sigma_D, \eta, \kappa)}{1 + N_H(\Delta, \sigma_D, \eta, \kappa)}. \quad (4.37)$$

This result contains an extra fit parameter, and the analytic form is also much more complicated than the approximation from Equation 4.36. The two are compared in

Figure 4.12 for physically relevant parameters, with excellent agreement in lineshape.

The latter is therefore more useful as a fitting function when the most important parameter is the linecenter.

Chapter 5

ACME Data Acquisition System

A major contribution of my thesis work was to develop the data acquisition (DAQ) system that controls the experiment. This involved developing a robust and user friendly software system that could easily interface with a wide variety of scientific equipment. This system has been designed to be easily expandable and well documented so future generations of students can add to it. The design goal for the ACME DAQ was to maximize the degree of automation, so the experiment could be run from “a beach on Tahiti”, so to speak. The desire to perform daily checks of the apparatus and maintain a constant human presence from a safety standpoint (high power lasers), meant that it was never necessary to achieve 100% remote automation. However, once a daily data run has commenced, the experiment can be run remotely, and most common experiment glitches can be diagnosed and treated remotely as well.

The data acquisition system simultaneously performs the following three functions:

1. Controlled digital modulation of experimental parameters on time scales ≥ 0.5 s, necessary for acquiring the complete set of phase and contrast measurements

required to extract the EDM.

2. Acquisition and storage of high bandwidth (5 MSa/s) fluorescence waveforms for the near shot noise limited spin precession measurement [9].
3. Logging of experimental parameters necessary for computing correlated phases.

All functions were coordinated with a LabVIEW based software system. A laboratory ethernet based local-area-network (LAN) was used to network the majority of the hardware and allowed for a unified interface to the data acquisition and storage PC. Some of the individual components were implemented by others, into the framework I developed and maintained, as will be noted in the text.

5.1 Data Acquisition Structure

The experiment is controlled as a “state machine”, where each state is specified by the configuration of a large number of binary switch parameters. Each parameter “reversal” is controlled by commands set via the LabVIEW control system. The data acquisition system was designed to allow flexible integration of additional devices and switches. Parameters are switched between pulses of the molecular beam source, and the data acquisition is paused while the switch is being actuated. Phase precession measurements are repeated at every 20 ms, synchronous with the 50 Hz pulse rate of our molecular beam source.

Four switches, $(\tilde{\mathcal{N}}, \tilde{\mathcal{E}}, \tilde{\theta}, \tilde{\mathcal{B}})$, are necessary to deduce an EDM from measurements of the correlated phase $\phi^{\mathcal{N}\mathcal{E}}$, the precession time τ , and the contrast \mathcal{C} , as discussed in Section 2.2. These four switches are modulated as quickly as possible, and a group of

phase measurements from all 2^4 switch state combinations are subdivided into a unit called a “block”. In the absence of systematic errors, these four switches would be sufficient to make an EDM measurement. Twenty five consecutive molecular beam pulses are averaged for each switch state, so the minimum time between switches is 0.5 s. Due to some repeat states (Section 5.2), a block length is typically 64 independent phase precession measurements (1600 total beam pulses), and is acquired in about 45 seconds including switch transition times.

A number of other switches, $(\tilde{\mathcal{P}}, \tilde{\mathcal{L}}, \tilde{\mathcal{R}}, \tilde{\mathcal{G}})$ were designed to suppress systematics that vary slowly with time, and therefore were modulated only between blocks, at multiples of the 45 s block acquisition period. A block of data is collected for each of the 2^4 states of these less frequent switches, where the complete cycle has been dubbed a “superblock”. The superblock length is extended past the minimum to 32 blocks long, which allows additional parameters to be inserted into the superblock cycle without altering its length (Section 5.1.2). Each superblock requires an acquisition of 51,200 beam pulses, with an average acquisition time of 27 minutes.

5.1.1 Block and Superblock Switches

The switch parity component analysis (Section 2.2) was applied to the following eight block and superblock switches to extract the EDM and analyze systematics. Brief definitions are below, with details of each switch’s properties in following sections.

- The $\tilde{\mathcal{N}}$ switch tunes the 1090 nm state preparation and probe lasers to address either the $\mathcal{N} = +1$ or $\mathcal{N} = -1$ omega doublet spin state manifold in the H

state. This is effectively a reversal of ThO's internal electric field \mathcal{E}_{eff} . The AOMs used as frequency shifters and shutters have a very fast settling time, so $\tilde{\mathcal{N}}$ was reversed every 0.5 s during the experiment.

- The \mathcal{E} -field switch ($\tilde{\mathcal{E}}$) reverses the direction of the laboratory electric field by inverting the voltage source's set output to the two sides of the \mathcal{E} -field plate assembly. The EDM is odd under the combination of $\tilde{\mathcal{N}}\tilde{\mathcal{E}}$, so this switch was modulated every ~ 2 seconds, the most frequently switched after $\tilde{\mathcal{N}}$.
- The $\tilde{\theta}$ switch is a modulation of the probe laser polarization angle by 12° using a half-wave plate mounted in an automated rotation stage. This changes the measurement basis angle θ and the measured asymmetry signal $\mathcal{A} = \mathcal{C} \cos(2(\phi - \theta))$. By stepping up and down the linear region of the Ramsey fringe, we measure the slope $d\mathcal{A}/d\theta = 2\mathcal{C}$, which allows us to convert asymmetry into phase $\phi = \mathcal{A}/2\mathcal{C}$. This is the third most frequent switch, modulated every 10 seconds in an *ABBA* sequence.
- The \mathcal{B} -field switch ($\tilde{\mathcal{B}}$) reverses the direction of the laboratory magnetic field by inverting the polarity of our current source. Although the EDM is not odd under a $\tilde{\mathcal{B}}$ switch, it does allow us to extract our spin coherence time via a measurement of the \mathcal{B} -correlated phase ($\phi^{\mathcal{B}} = g_H\mu_B|\mathcal{B}_z|\tau/\hbar$). A lengthy degauss cycle is applied with each \mathcal{B} -field change, so the $\tilde{\mathcal{B}}$ switch is modulated only once per block, every 45 seconds.
- The $\tilde{\mathcal{P}}$ switch tunes the 1090 nm probe laser by 50.4 MHz to address either of the excited state omega doublets ($|C, J = 1, M = 0, \mathcal{P} = \pm 1\rangle$). These states have

opposite parity, and therefore couple to orthogonal H state superpositions [80]. This allows us to reverse our measurement basis without rotating the laser polarization. The $\tilde{\mathcal{P}}$ state is randomly selected between blocks, every 45 s.¹

- The $\tilde{\mathcal{L}}$ switch is an alternate way of reversing the electric field direction. Using a system of TTL controlled mercury wetted relays, it physically switches the leads connecting the voltage supply channels to the field plates. This switch has an even faster settling time than the $\tilde{\mathcal{E}}$ switch, but due to lifetime concerns for the relays, the switch is modulated with a four block period, about every 200 s.
- The $\tilde{\mathcal{R}}$ switch is a rotation of the probe laser’s polarization by 90° every eight blocks or roughly 400 s.² This rotates the measurement basis, interchanging which of two overlapping probe laser beams (Section 4.1) measures in the \hat{X} or \hat{Y} direction. Along with the $\tilde{\mathcal{P}}$ switch it helps to cancel drifts in laser beam pointing or power [105].
- The $\tilde{\mathcal{G}}$ switch is a synchronous $\sim 90^\circ$ global polarization rotation of both the state preparation and probe lasers. The relative angle between prep and probe, and therefore the measured asymmetry, should be unaffected by this global switch. The two angles were chosen to fall at the two locations that minimized the \mathcal{E}^{nr} systematic slope, aligned with the induced birefringence axes of our field plates (Section 4.3).

¹The frequency detuning of the $\tilde{\mathcal{P}}$ switch is performed using AOMs, and therefore is capable of being modulated as fast as the $\tilde{\mathcal{N}}$ switch. In practice, it was only switched between blocks to reduce the total number of states required for a block cycle.

²This large polarization slew is slow, so this switch is rotated infrequently.

5.1.2 Longer Switches and Interleaved Systematic Checks

A few other switches are modulated on even slower time scales. The switch parity component analysis was not applied to the following switches, but instead the EDM measurements from superblocks generated in each configuration were directly compared, and shown to agree within experimental error bars (Figure 7.7). Because we have no evidence that any of these switches caused an EDM shift, we averaged these to determine the final result.

- The \mathcal{E} -field magnitude was set once per day to a value of either 141 V/cm or 36 V/cm. Since the molecular polarization is saturated, this should not change \mathcal{E}_{eff} (Section 1.3.1). This unique saturation in ThO provides an additional means of searching for systematics from leakage currents or $\vec{v} \times \vec{\mathcal{E}}$ motional magnetic fields [3, 41]. This switch required manual rerouting of fibers, switching BNC cables, and retuning of the prep/probe laser lock point, which is why it was performed so infrequently. These two configurations are referred to as “High- \mathcal{E} ” and “Low- \mathcal{E} ” elsewhere in this thesis.
- The \mathcal{B} -field magnitude was switched between three values (1, 19, 38 mG) between superblocks on an ~ 1 hour time scale. As a probe of any \mathcal{B} -field dependent systematic effects, this confirmed their absence at our current level of statistical precision. Switching the \mathcal{B} -field magnitude changes the amount of magnetic phase precession, and therefore requires rotating the probe laser polarization in order to satisfy $\phi - \theta \approx \frac{\pi}{4}(2n + 1)$. This basis rotation was fully automated along with the change in the magnitude $|\mathcal{B}_z|$. This data is often referred to as $0\mathcal{B}$, $1\mathcal{B}$, and $2\mathcal{B}$ because the specific $|\mathcal{B}_z|$ values applied required

daily adjustment to account for velocity drifts in the ThO beam. Acquiring at $0\mathcal{B}$ and $2\mathcal{B}$ require the same probe angles, so those measurements were actually acquired in the same superblock structure. We define the “ \mathcal{B} -field parity” as either even ($0\mathcal{B}$ and $2\mathcal{B}$) or odd ($1\mathcal{B}$).

- An additional switch was performed only once, which reversed the propagation direction of our state preparation and probe lasers (\hat{k}) with respect to our laboratory axis (\hat{z}). The laser preparation breadboard (Figure 4.2) was moved to the other side of the interaction region, where it then had to be realigned. This so-called ($\hat{k} \cdot \hat{z}$) switch confirmed the existence of the $\tilde{\mathcal{N}}\tilde{\mathcal{E}}$ odd Rabi frequency $\Omega_r^{\mathcal{N}\mathcal{E}}$ (see Section 7.1.3), and allowed us to place model-dependent bounds on it in our error budget. Although it is not strictly necessary to repeat this switch now that we understand the systematic, future generations should consider building two copies of the state preparation optics, and switching between them with MEMS fiber switches.

Our approach to quantify systematic error involved acquiring “intentional parameter variation” (IPV) data sets, where the conditions were varied so as to be inappropriate for an EDM measurement (e.g. a large magnetic field gradient). Most of these IPV parameters were implemented as automated switches (for the full list see Tables E.1 and E.2) and inserted into the usual superblock structure. The IPV was inserted as the most frequent superblock switch between every 45 s block, with a maximum superblock length of 32 blocks.

Three IPV data superblocks were interleaved with the final data sets, and were used to constrain the dominant \mathcal{E}^{nr} and $\Omega_r^{\mathcal{N}\mathcal{E}}$ systematics. Unlike the approach taken

by the YbF experiment, where they chose to constantly interleave systematic monitoring switches within their data set [4, 7], we interrupted our “ideal conditions” data acquisition with these IPV superblocs. This approach allowed us to greatly exaggerate the IPV parameter and rapidly acquire a statistically significant systematic error limit (see Section 7.2), which minimized the time spent only limiting systematics.

A complete cycle of all IPV and $0\mathcal{B}$, $1\mathcal{B}$, $2\mathcal{B}$ ideal data superblocs is affectionately dubbed an “uberblock”. An uberblock has a typical period of ~ 400 blocks (640,000 beam pulses over an average of 6.5 hours) and included the following IPV superblocs:

- A large \mathcal{E}^{nr} of up to 200 mV/cm was applied to the field plates by modifying the $\tilde{\mathcal{E}}$ switch to include a $|V|^{\mathcal{E}}$ component from the voltage source. Monitoring the \mathcal{E}^{nr} sensitivity ($S_{\mathcal{E}^{\text{nr}}} = \partial\omega^{\mathcal{N}\mathcal{E}}/\partial\mathcal{E}^{\text{nr}}$) interleaved within the published final data set was necessary to apply a daily systematic correction. Because the \mathcal{E}^{nr} systematic depends on the probe laser angles, which are different for the two \mathcal{B} -field parities, we acquired two \mathcal{E}^{nr} IPV superblocs per uberblock, one for each \mathcal{B} -field parity.
- Once per uberblock, the frequency of the state preparation laser was detuned by $\Delta_{\text{prp}} \pm 2$ MHz from resonance. This puts the phase measurement on the linear region of the contrast curve, where it is sensitive to shifts in the resonance frequency. In particular, the $C^{\mathcal{E}}$ contrast channel provides a measurement of the \mathcal{E}^{nr} via the dc Stark shift (Section 6.4).
- In order to simulate a $\Omega_r^{\mathcal{N}\mathcal{E}}$, which can cause a light shift induced EDM systematic, a prep and probe laser power correlation ($P^{\mathcal{N}\mathcal{E}}$) was added by inserting an

extra AOM into each beam path (Section 4.1). The optical power in the undiffracted beam depends on the RF power to the AOM, which was modulated using commands to the DDS. In this way, we could monitor $S_{\Omega_r^{\mathcal{N}\mathcal{E}}} = \partial\omega^{\mathcal{N}\mathcal{E}}/\partial\Omega_r^{\mathcal{N}\mathcal{E}}$ using two superblocks per uberblock, one for each \mathcal{B} -field parity, and determine a shift associated with this systematic.

5.2 Switching Timescales

There are two relevant timescales for all of the switches in the ACME data sets. The time required to perform some switch $\tilde{s} \in \{\tilde{\mathcal{N}}, \tilde{\mathcal{E}}, \tilde{\theta}, \tilde{\mathcal{B}}, \tilde{\mathcal{P}}, \tilde{\mathcal{L}}, \tilde{\mathcal{R}}, \tilde{\mathcal{G}}\}$, during which the acquisition of spin precession data is paused, is the transition time Δt_s . The characteristic period over which \tilde{s} is reversed defines the switching period T_s . These timescales together determine the duty cycle of the experiment, the percentage of ablation pulses that are saved by the DAQ and useful for post-processing as EDM data. The switching period is also important for determining the extent to which different phase parity sums will be susceptible to drifts and noise in measured precession phases.

In order to understand these timescales, we introduce the waveform patterns used to program the four switches within a block. The waveform generation algorithm is input a fundamental switch cycle for each parameter, and the parameter switches are ordered by relative switch frequency (see Section C.1). The full waveform is composed by repeating these units, nesting them from fastest to slowest switch period, until all switch state combinations are included in the waveform (Figure 5.1). For a switch with binary states $\{A, B\}$, the fundamental switch cycles used are either AB or $ABBA$.

An AB sequence is the minimum required to form all $2^4 = 16$ state permutations within the block. The $ABBA$ sequence has one fewer state transition as compared to an $ABAB$ sequence, and therefore is applied for switches with long transition times (Δt_s) in order to minimize the reduction in duty cycle. It also allows for the additional cancelation of certain linear drifts, as described in Section 5.2.2.

The $\tilde{\mathcal{E}}$ and $\tilde{\theta}$ switches are programmed with an $ABBA$ switch cycle. For switch \tilde{s} , let n_s equal the number of states per fundamental cycle, where $n_s = 2(4)$ for $AB(ABBA)$ configurations respectively. The total number of phase measurements per block in ACME data is $N_{\text{tot}} = 64$, given by $N_{\text{tot}} = n_{\mathcal{N}}n_{\mathcal{E}}n_{\theta}n_{\mathcal{B}}$. The number of transitions of \tilde{s} per block (N_s) depends on the type of fundamental cycle and the switch ordering. For the ACME waveform generation algorithm

$$N_s = \begin{cases} 2N_{\text{tot}} \left(\prod_{i=0}^{i=\tilde{s}} n_i \right)^{-1} - 1 & \tilde{s} \in \{\tilde{\mathcal{N}}, \tilde{\mathcal{B}}\} \quad \text{for } (AB) \\ 2N_{\text{tot}} \left(\prod_{i=0}^{i=\tilde{s}} n_i \right)^{-1} & \tilde{s} \in \{\tilde{\mathcal{E}}, \tilde{\theta}\} \quad \text{for } (ABBA) \end{cases} \quad (5.1)$$

where the index $i = (0, 1, 2, 3) = (\tilde{\mathcal{N}}, \tilde{\mathcal{E}}, \tilde{\theta}, \tilde{\mathcal{B}})$ is the switch ordering.

5.2.1 Duty Cycle

The DAQ duty cycle per block (χ) is defined as the ratio of the minimum possible acquisition time $0.5 \times N_{\text{tot}}$ seconds, divided by the actual time required to measure a block. This definition of the duty cycle does not take into account the time lost between successive ablation pulses, which is accounted for in the beam source duty cycle. An improvement in either duty cycle would increase the measurement rate \dot{N} and therefore our EDM sensitivity per root day. The limits to either duty cycle are determined by separate considerations, so it is useful to conceptually separate

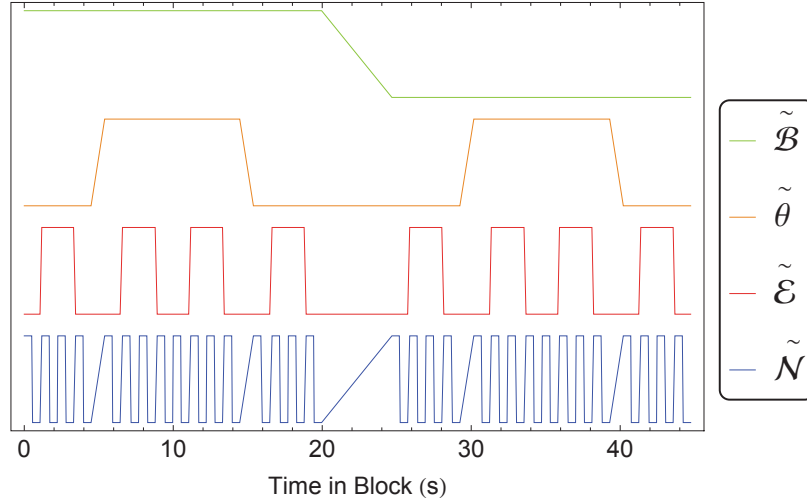


Figure 5.1: An example of the digital switching waveform from a typical block of EDM data. The $\tilde{\mathcal{N}}$ and $\tilde{\mathcal{B}}$ switches follow an AB pattern, while $\tilde{\mathcal{E}}$ and $\tilde{\theta}$ follow an $ABBA$ pattern. The switch ordering (AB or BA) is reversed or randomly selected for each block. Data is being acquired in regions where all switch levels are horizontal, while a slanted line indicates the data acquisition is paused during a switch transition time. This plot is an accurate representation of switching timescales, generated from timing information in the data header.

the two. Molecule pulses are produced at a rate of $\nu_{\text{YAG}} = 50$ Hz, and $N_{\text{avg}} = 25$ sequential pulses are averaged per state. Therefore, the time to collect a single phase precession measurement is $\tau_{\text{avg}} = N_{\text{avg}}/\nu_{\text{YAG}} = 0.5$ s. A lower bound on the DAQ duty cycle is

$$\chi \geq \frac{N_{\text{tot}}\tau_{\text{tot}}}{N_{\text{tot}}\tau_{\text{tot}} + \sum_s N_s \Delta t_s}. \quad (5.2)$$

In practice, the measured duty cycle is always greater than that calculated using Equation 5.2. The DAQ system enforces a fixed pause given by the pre-set settling time for each parameter switch. When the control software performs multiple switches, the data acquisition only needs to be paused for the greatest Δt_s amongst simultaneous switches, which is less than the sum of Δt_s for all switches.

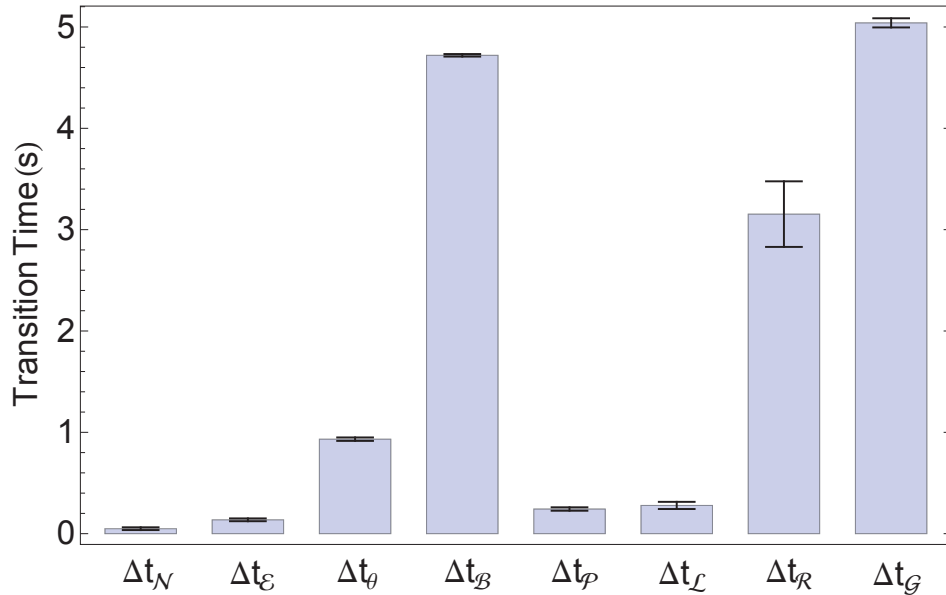


Figure 5.2: Dead-time required to actuate each block and superblock switch (Δt_s). The data is derived from the header of Run 401 in the published data set. The switches are ordered in terms of increasing period T_s from left to right. There are large uncertainties in the slew time for the polarization rotation switches ($\tilde{\theta}$, $\tilde{\mathcal{R}}$, $\tilde{\mathcal{G}}$) because their setpoints rely on open loop feedback. The $\tilde{\mathcal{P}}$ and $\tilde{\mathcal{L}}$ switches should have transition times as fast as the $\tilde{\mathcal{N}}$ and $\tilde{\mathcal{E}}$ switches, respectively. The extra time recorded in the data is due to interblock reinitialization code, which could be eliminated to improve the duty cycle in the future.

Measured values of Δt_s for each block and superblock switch are shown in Figure 5.2. Using these values, the computed lower bound to the in-block duty cycle is $\chi_{\text{lim}} \approx 70\%$, while the actual in-block duty cycle is $\chi_{\text{bk}} \approx 72 \pm 0.5\%$. The timing of block level switches is very stable, corresponding to a duty cycle and block length with only small variations. However, the data acquisition is often manually paused between blocks to either optimize the ablation yield or recenter the prep/probe laser frequency. Therefore, the superblock duty cycle is reduced and has larger variation, $\chi_{\text{sb}} = 63 \pm 6\%$. These same manual parameter checks are performed between al-

most every superblock, which further reduces the duty cycle per day to $\chi_{\text{run}} \approx 55\%$. In future ACME generations, automating these few remaining manual checks would stabilize and increase the superblock duty cycle, therefore boosting our overall data acquisition rate.

5.2.2 Switch Rates and Noise Filtering

The frequency of a particular switch determines how effectively the parity sum data analysis can cancel out noise and linear drifts in correlated phase channels. With a short switching period, the noise or drift between successive phase measurement will be more correlated, allowing a higher degree of rejection by the data analysis. As shown in Figure 5.3, all block level switches have periods less than the block length (45 s), while all superblock switches are switched only between blocks (> 45 s). Although the switching frequencies contain several components, the waveforms are composed in a periodic fashion so most frequent switching component will be

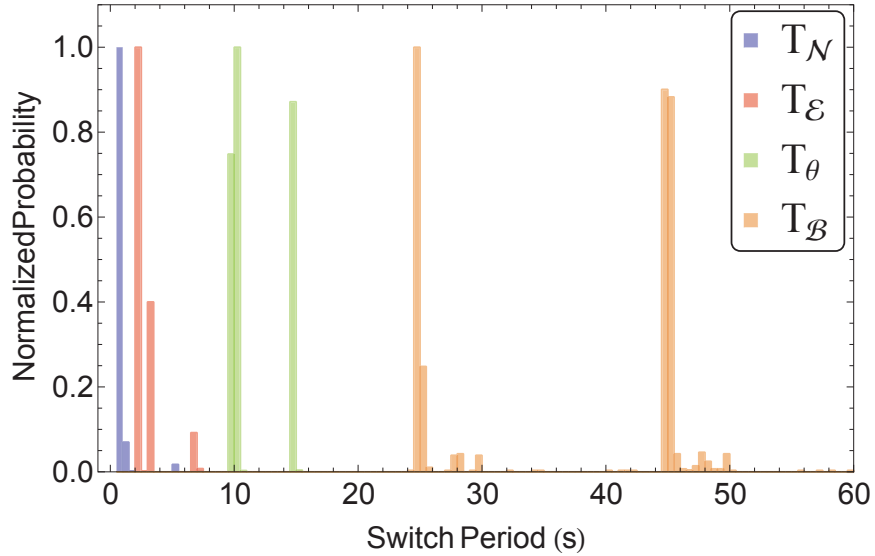
$$T_s = \frac{T_{\text{tot}}}{N_s} = \frac{N_{\text{tot}} \tau_{\text{avg}}}{\chi} \frac{1}{N_s}. \quad (5.3)$$

To demonstrate the beneficial effects of a fast switch, consider a model for our measured phases ($\phi_{m,(s_1 s_2)}$) that includes both the ideally switched component and some drifting component,

$$\begin{aligned} \phi_{m,(s_1 s_2)}(t) &= \phi_{s_1 s_2} + \phi(t), \\ \phi_{m,(s_1 s_2)}(t) &\approx \phi_{s_1 s_2} + \phi' t, \end{aligned} \quad (5.4)$$

where $\tilde{s}_1, \tilde{s}_2 \in \{+, -\}$ represent the signed states of the switch parameters. We linearize the temporal phase dependence $\phi(t)$ around small drifts (ϕ') and short times,

(a) Block Switch Periods



(b) Superblock Switch Periods

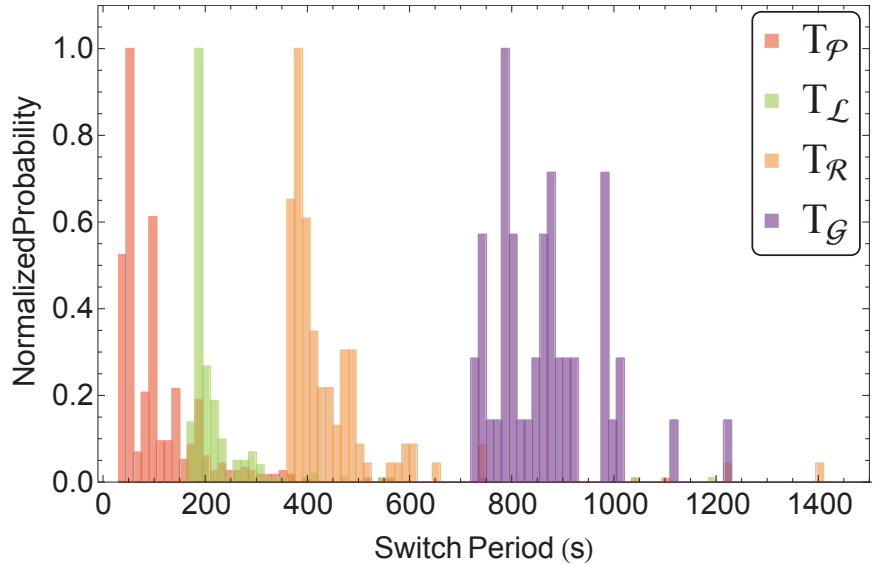


Figure 5.3: Histogram of switching periods for block (a) and superblock (b) switches. Block switch $\{\tilde{\mathcal{N}}, \tilde{\mathcal{E}}, \tilde{\theta}, \tilde{\mathcal{B}}\}$ rates are sharply peaked near their ideal fundamental switch timescales of $\{0.5, 2, 8, 32\}$ seconds, with some variation due to intervening switch times Δt_s . The superblock switches $\{\tilde{\mathcal{P}}, \tilde{\mathcal{L}}, \tilde{\mathcal{R}}, \tilde{\mathcal{G}}\}$ show more variation, related to the frequent pausing of the experimental acquisition between blocks. The heights of the bins in each series has been normalized to their maximum to allow clear comparison between the frequency components of each switch.

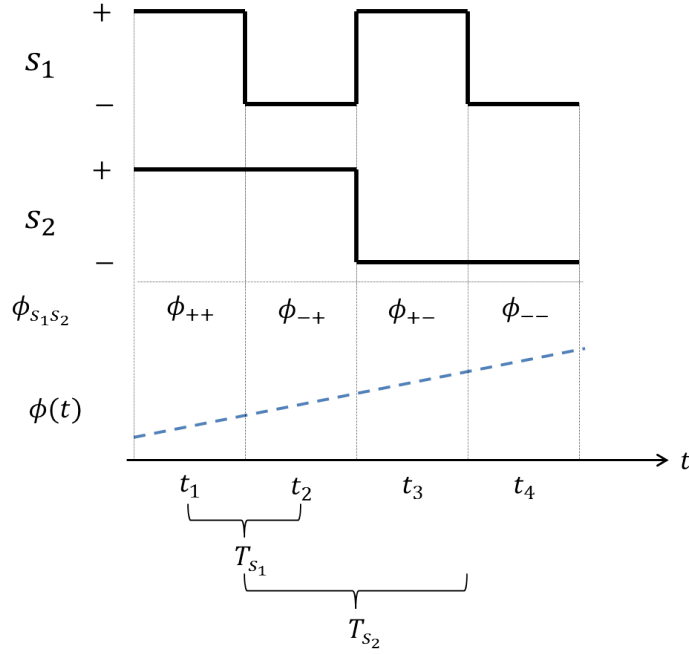


Figure 5.4: Model waveform described in the text. The effect of phase drift $\phi(t)$ on a measured phase components depends upon the correlated parameter with the shortest switch period (T_s). For the discussion in the text $s_1 = \mathcal{N}$ and $s_2 = \mathcal{B}$.

neglecting the constant component that will cancel out of interesting parity sums. For the sake of discussion, let $\tilde{s}_1 = \tilde{\mathcal{N}}$ and $\tilde{s}_2 = \tilde{\mathcal{B}}$, respectively the fastest and slowest block level switches, and we restrict ourselves to a two switch model, ignoring $(\tilde{\mathcal{E}}, \tilde{\theta})$ for the time being. Assume the ordering of switch states and measurement times as shown in Figure 5.4. The switching periods, $T_{\mathcal{B}} > T_{\mathcal{N}}$ are therefore

$$\begin{aligned} T_{\mathcal{N}} &= t_2 - t_1 = t_4 - t_3, \\ T_{\mathcal{B}} &= t_3 - t_1 = t_4 - t_2. \end{aligned} \tag{5.5}$$

The relevant parity sums are then

$$\begin{aligned}
 \phi^{\mathcal{NB}} &= \frac{1}{4} [(\phi_{m,++}(t_1) - \phi_{m,-+}(t_2)) - (\phi_{m,+-(t_3)} - \phi_{m,--}(t_4))] \\
 &= \frac{1}{4} (\Delta\phi_{\mathcal{N}+} - \phi'T_{\mathcal{N}} - \Delta\phi_{\mathcal{N}-} + \phi'T_{\mathcal{N}}) \\
 &= \frac{\Delta\phi_{\mathcal{NB}}}{4} + \mathcal{O}(t^2)
 \end{aligned} \tag{5.6}$$

$$\begin{aligned}
 \phi^{\mathcal{N}} &= \frac{1}{4} [(\phi_{m,++}(t_1) - \phi_{m,-+}(t_2)) + (\phi_{m,+-(t_3)} - \phi_{m,--}(t_4))] \\
 &= \frac{1}{4} (\Delta\phi_{\mathcal{N}+} - \phi'T_{\mathcal{N}} + \Delta\phi_{\mathcal{N}-} + \phi'T_{\mathcal{N}}) \\
 &= \frac{\Delta\phi_{\mathcal{N}}}{4} - \frac{\phi'T_{\mathcal{N}}}{2}
 \end{aligned} \tag{5.7}$$

$$\begin{aligned}
 \phi^{\mathcal{B}} &= \frac{1}{4} [(\phi_{m,++}(t_1) + \phi_{m,-+}(t_2)) - (\phi_{m,+-(t_3)} + \phi_{m,--}(t_4))] \\
 &= \frac{1}{4} ((\phi_{\mathcal{N}+} + \phi'(t_1 + t_2)) - (\phi_{\mathcal{N}-} + \phi'(t_3 + t_4))) \\
 &= \frac{\Delta\phi_{\mathcal{B}}}{4} - \frac{\phi'T_{\mathcal{B}}}{2}
 \end{aligned} \tag{5.8}$$

$$\begin{aligned}
 \phi^0 &= \frac{1}{4} [(\phi_{m,++}(t_1) + \phi_{m,-+}(t_2)) + (\phi_{m,+-(t_3)} + \phi_{m,--}(t_4))] \\
 &= \frac{1}{4} ((\phi_{\mathcal{N}+} + \phi'(t_1 + t_2)) + (\phi_{\mathcal{N}-} + \phi'(t_3 + t_4))) \\
 &= \frac{\Delta\phi_0}{4} - \frac{\phi'(t_1 + t_2 + t_3 + t_4)}{4}
 \end{aligned} \tag{5.9}$$

Notice that the susceptibility of the measurement to the drift or noise parameter ϕ' is dependent on the timescale of the shortest switch. This means that important parity sums such as $\phi^{\mathcal{NB}}$ will be well behaved even though they contain a slow switch. The fact that the drift canceled out entirely in the $\phi^{\mathcal{NB}}$ parity sum is an artifact of our noise model that was uncorrelated with any switch. In general, the ϕ' dependence in a parity sum will depend on the drift's switch correlations, but the effect will always be limited by the smallest switch timescale associated with that parity sum.

For example, there are large drifts in the precession time τ due to an unsta-

ble beam velocity. This leads to a drifting \mathcal{B} odd magnetic precession phase $\phi^{\mathcal{B}} = \tilde{\mathcal{B}}g_H\mu_B|\mathcal{B}_z|(\tau + \delta\tau(t))/\hbar$, which in the notation of this model creates a term with a large \mathcal{B} odd phase $\phi_{m,(s_1s_2)}(t) \approx \phi_{s_1s_2} + \tilde{\mathcal{B}}\phi't$. In that case, the terms with dominant noise sensitivity would be reversed with respect to their \mathcal{B} symmetry:

$$\phi^{\mathcal{NB}} = \frac{\Delta\phi_{\mathcal{NB}}}{4} - \frac{\phi'T_{\mathcal{N}}}{2}, \quad (5.10)$$

$$\phi^{\mathcal{N}} = \frac{\Delta\phi_{\mathcal{N}}}{4} + \mathcal{O}(t^2), \quad (5.11)$$

$$\phi^{\mathcal{B}} = \frac{\Delta\phi_{\mathcal{B}}}{4} - \frac{\phi'(t_1 + t_2 + t_3 + t_4)}{4}, \quad (5.12)$$

$$\phi^0 = \frac{\Delta\phi_0}{4} - \frac{\phi'T_{\mathcal{B}}}{2}. \quad (5.13)$$

An *ABBA* switch pattern is also a useful method for canceling sources of linear phase drift. In the example above, an *ABAB* switch pattern was employed for simplicity. Consider an uncorrelated linear phase drift model with a single switch, such that $\phi_{m,s} = \phi_s + \phi't$. The relevant parity sums are computed in the standard way,

ABAB

$$\begin{aligned} \phi^s &= \frac{\Delta\phi_s}{2} + \frac{\phi'}{4}((t_1 - t_2) + (t_3 - t_4)) \\ &= \frac{\Delta\phi_s}{2} - \frac{\phi'T_s}{2} \end{aligned} \quad (5.14)$$

$$\phi^0 = \frac{\Delta\phi_0}{2} + \frac{\phi'((t_1 + t_2 + t_3 + t_4))}{4} \quad (5.15)$$

ABBA

$$\begin{aligned} \phi^s &= \frac{\Delta\phi_s}{2} + \frac{\phi'}{4}((t_1 - t_2) + (t_4 - t_3)) \\ &= \frac{\Delta\phi_s}{2} + \mathcal{O}(t^2) \end{aligned} \quad (5.16)$$

$$\phi^0 = \frac{\Delta\phi_0}{2} + \frac{\phi'((t_1 + t_2 + t_3 + t_4))}{4} \quad (5.17)$$

The *ABBA* pattern has canceled out linear phase drifts in the odd parity sums, although the sequence does not improve the even parity sums. Therefore, a parity sum that is solely odd under a slow switch and is modulated in an *AB* pattern will be particularly sensitive to noise and drifts. We have found that the noisiest asymmetry channels are \mathcal{A}^B and \mathcal{A}^0 [81], which satisfy both of these criteria.

5.3 \mathcal{E}^{nr} Suppression Through Lead Switching

As is discussed in Section 7.1.2, the presence of a non-reversing electric field (\mathcal{E}^{nr}) causes systematic errors in the EDM measurement. The application of both $\tilde{\mathcal{E}}$ and $\tilde{\mathcal{L}}$ switches allows for the suppression of \mathcal{E}^{nr} effects from externally applied offset voltages.

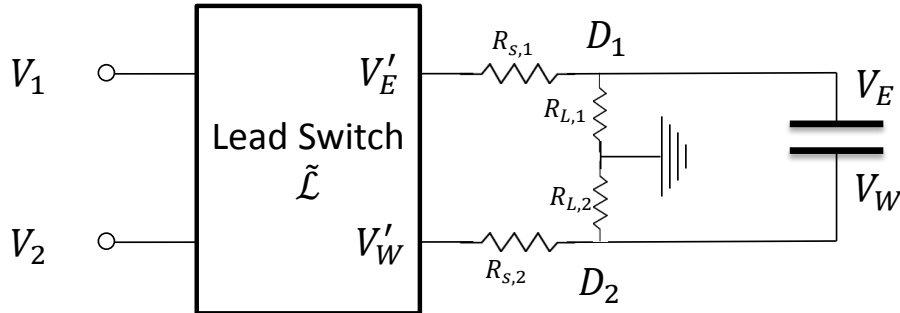


Figure 5.5: A wiring schematic of the voltage applied to the field plates with two switches, to accompany the model presented in Section 5.3. Voltages (V_1, V_2) from the source pass through a lead switching device. A combination of lead and leakage resistances create voltage dividers (D_1, D_2) that reduce the voltage on the field plates (V_E, V_W).

Consider the following model, illustrated in Figure 5.5, which describes how the voltage difference $\Delta V = V_E - V_W$ depends on offsets from the voltage source and

lead wiring. The voltages from separate channels on the voltage source (V_1, V_2) can be decomposed into an amplitude component ($V_1^\mathcal{E}, V_2^\mathcal{E}$) that reverses with $\tilde{\mathcal{E}}$, and a constant offset component ($V_1^{\text{nr}}, V_2^{\text{nr}}$),

$$\begin{aligned} V_1 &= V_1^\mathcal{E} \tilde{\mathcal{E}} + V_1^{\text{nr}}, \\ V_2 &= -V_2^\mathcal{E} \tilde{\mathcal{E}} + V_2^{\text{nr}}. \end{aligned} \tag{5.18}$$

We assume that $V_1^\mathcal{E} \approx V_2^\mathcal{E} > 0$ and that the offsets are small, such that the potential difference between the channels is $V_1 - V_2 \approx (V_1^\mathcal{E} + V_2^\mathcal{E}) \approx 2V_1^\mathcal{E}$. These voltages are applied on the inputs of the relay box which switches the input and output leads, where the voltages at the output terminals (V'_E, V'_W) are connected to the (East, West) field plate respectively. The output of this lead switching box can be expressed in terms of the $\tilde{\mathcal{L}} = \pm 1$ state as

$$\begin{aligned} V'_E &= \left(\frac{(1 + \tilde{\mathcal{L}})}{2} V_1 + \frac{(1 - \tilde{\mathcal{L}})}{2} V_2 \right), \\ V'_W &= \left(\frac{(1 + \tilde{\mathcal{L}})}{2} V_2 + \frac{(1 - \tilde{\mathcal{L}})}{2} V_1 \right). \end{aligned} \tag{5.19}$$

We allow for an additional source of voltage offset due to finite series resistances ($R_{s,1}, R_{s,2}$) in conjunction with leakage resistances to ground ($R_{L,1}, R_{L,2}$). These resistances will act like voltage dividers $D_{1/2} \approx R_{L,1/2} / (R_{L,1/2} + R_{s,1/2})$, which reduce the voltage applied to either field plate,

$$\begin{aligned} V_E &= D_1 V'_E, \\ V_W &= D_2 V'_W, \end{aligned} \tag{5.20}$$

Typically, series resistances, say from the mercury relays themselves, are $R_s < 1 \Omega$, while overall leakage resistances are very large, $R_L > 1 \text{ T}\Omega$. Therefore, we expect $D_1 \approx D_2 \lesssim 1$, and the effects from these equivalent voltage dividers will be small.

Putting all these elements together and grouping terms by switch parity, we arrive at the following expression for the electric field across the field plates. Assuming a fixed field plate spacing d , the electric field $\mathcal{E}_z = \Delta V/d$

$$\mathcal{E}_z = \frac{(V_E - V_W)}{d} + \mathcal{E}_{\text{int}}(x) \quad (5.21)$$

$$\begin{aligned} &= \tilde{\mathcal{L}}\tilde{\mathcal{E}} \left[\frac{D_1 + D_2}{2} (V_1^\mathcal{E} + V_2^\mathcal{E}) \right] \frac{1}{d} + \tilde{\mathcal{L}} \left[\frac{D_1 + D_2}{2} (V_1^{\text{nr}} - V_2^{\text{nr}}) \right] \frac{1}{d} \\ &\quad + \tilde{\mathcal{E}} \left[\frac{D_1 - D_2}{2} (V_1^\mathcal{E} - V_2^\mathcal{E}) \right] \frac{1}{d} + \left[\frac{D_1 - D_2}{2} (V_1^{\text{nr}} + V_2^{\text{nr}}) \right] \frac{1}{d} + \mathcal{E}_{\text{int}}(x) \end{aligned} \quad (5.22)$$

Here we have included the effects from the position dependent internal patch potentials which generate stray non-reversing electric fields $\mathcal{E}_{\text{int}}(x)$. These cannot be controlled via the external supplies, and add as an offset to the electric field generated by the applied external voltages.

The \mathcal{E}^{nr} systematic is caused by $\tilde{\mathcal{N}}\tilde{\mathcal{E}}$ correlated changes in the dc Stark shift $\Delta_{\text{st}} = 2D_H|\mathcal{E}_z|$ (Section 7.1.2). The systematic will therefore be caused by the EDM correlated term in the magnitude $|\mathcal{E}_z|$, in the switch parity notation

$$|\mathcal{E}_z| = |\mathcal{E}_z^0| + \mathcal{E}_z^\mathcal{E}\tilde{\mathcal{E}} + \mathcal{E}_z^\mathcal{L}\tilde{\mathcal{L}} + \mathcal{E}_z^{\mathcal{E}\mathcal{L}}\tilde{\mathcal{E}}\tilde{\mathcal{L}}. \quad (5.23)$$

In Equation 5.22, the term with the greatest magnitude is the $\tilde{\mathcal{L}}\tilde{\mathcal{E}}$ -odd term proportional to ΔV . When taking the absolute value this term will always be positive, and we can find the signs of all other terms by multiplying the equation by $\tilde{\mathcal{L}}\tilde{\mathcal{E}}$. Therefore, the parity of terms in Equation 5.22 are reversed with respect to $\tilde{\mathcal{L}}\tilde{\mathcal{E}}$, and as defined

in Equation 5.23

$$|\mathcal{E}_z^0| = \left[\frac{D_1 + D_2}{2} \frac{(V_1^\mathcal{E} + V_2^\mathcal{E})}{d} \right], \quad (5.24)$$

$$\mathcal{E}_z^\mathcal{E} = \left[\frac{D_1 + D_2}{2} \frac{(V_1^{\text{nr}} - V_2^{\text{nr}})}{d} \right], \quad (5.25)$$

$$\mathcal{E}_z^\mathcal{L} = \left[\frac{D_1 - D_2}{2} \frac{(V_1^\mathcal{E} - V_2^\mathcal{E})}{d} \right], \quad (5.26)$$

$$\mathcal{E}_z^{\mathcal{E}\mathcal{L}} = \left[\frac{D_1 - D_2}{2} \frac{(V_1^{\text{nr}} + V_2^{\text{nr}})}{d} \right] + \mathcal{E}_{\text{int}}(x). \quad (5.27)$$

We assume the voltage supply is operated in the linear regime, so that the offsets are small and $V_1 \approx V_2$. Given that we do not know the signs of $V_{1/2}^{\text{nr}}$, we assume that the sums and differences ($V_1^{\text{nr}} \pm V_2^{\text{nr}}$) are of approximately the same size. Therefore, neglecting the contribution from $\mathcal{E}_{\text{int}}(x)$, the hierarchy of terms is

$$|\mathcal{E}_z^0| \gg \mathcal{E}_z^\mathcal{E} > (\mathcal{E}_z^{\mathcal{E}\mathcal{L}} - \mathcal{E}_{\text{int}}) \approx \mathcal{E}_z^\mathcal{L}. \quad (5.28)$$

The reversal of the laboratory \mathcal{E} -field direction is $\tilde{\mathcal{E}}\tilde{\mathcal{L}}$ -odd, and therefore the term $\mathcal{E}^{\text{nr}} = \mathcal{E}_z^{\mathcal{E}\mathcal{L}}$ will cause an EDM correlated detuning and the associated ac Stark shift systematic. The effect of voltage offsets is suppressed by the $\tilde{\mathcal{L}}$ switch for the case $D_1 \approx D_2$, such that the term is dominated by the patch potentials $\mathcal{E}_{\text{int}}(x)$. If we neglected the $\tilde{\mathcal{E}}$ or $\tilde{\mathcal{L}}$ switches, respectively the $\mathcal{E}_z^\mathcal{L}$ or $\mathcal{E}_z^\mathcal{E}$ terms would contribute to an \mathcal{E}^{nr} systematic. Turning off $\tilde{\mathcal{E}}$ is of little consequence due to the smallness of the extra term, but disabling $\tilde{\mathcal{L}}$ could be problematic if the supply's offset voltages are not carefully compensated. In practice, it is useful to modulate both switches on different timescales. The finite lifetime of the mechanical $\tilde{\mathcal{L}}$ switch restricts us from switching it frequently. By configuring $\tilde{\mathcal{E}}$ as a rapid *ABBA* switch, it helps to eliminate phase drifts in the $\tilde{\mathcal{E}}$ correlated phase channels (Section 5.2). The $\tilde{\mathcal{L}}$ switch will then be

effective at canceling out uncompensated offsets from the voltage source, so long as those offsets are stable over the switch timescale ($T_{\mathcal{L}}$).

5.4 Experimental Switches

5.4.1 Electric Field Control

The electric field in the interaction region was controlled by the voltage applied to the transparent indium tin oxide (ITO) coated electric field plates. The potential difference is generated by a digitally controlled voltage source, which outputs up to $\sim \pm 200$ V. Equal and opposite voltages (relative to instrument ground) were applied to each side of the floating field plate assembly. The direction of the laboratory \mathcal{E} -field was reversed in two ways: on fast time scales (2 s) by reprogramming the output of the DAC channels to reverse their polarity (the $\tilde{\mathcal{E}}$ switch), and less frequently (every 3.3 minutes) by reversing the electrical connections via a pair of mercury whetted relays (the $\tilde{\mathcal{L}}$ switch).

The voltage source was designed and built in-house by Jim MacArthur, based around his 20-bit BabyDAC board. The BabyDAC output is amplified by a PA98A Power OpAmp to operate at a maximum of ± 200 V, which provides a setpoint resolution of 0.4 mV. In practice, the output of the power supplies begins to sag at around ± 180 V, and the output becomes non-linear with respect to the setpoint. The supplies were designed to have a very good repeatability upon reversal, a key parameter for avoiding non-reversing electric fields. Any DC offsets also need to be very stable over time, as these will show up directly as a drifting \mathcal{E}^{nr} . Over the course of a run, we

measured the voltage difference ΔV between opposite polarity channels to be stable to < 3 mV.

The voltage source is sent commands over a fiberring serial connection in the binary encoding common to all BabyDACs used in the Gabrielse lab. A fiber converter box allows the electronic RS-232 signals to be connected to the over which all the BabyDAC based devices in the ACME lab are connected.

The lead switch ($\tilde{\mathcal{L}}$) is composed of several double pole, single throw (DPST) mercury whetted relays switches (Pickering 101-2-A-12/6D). An single logic level plus inverter can be used to perform a lead switch using the wiring show in Figure 5.6, although in practice two separate computer controlled digital outputs with opposite polarities are used. This allows the first relay to be opened before the second is closed, ensuring that oppositely polarized outputs are never tied together. The mercury whetted reeds reduce contact resistances, and decrease switching chatter while increasing the lifetime of the switches. These relays are also magnetically shielded, which helps to eliminate potential $\mathcal{B}^{\mathcal{L}}$ fields which could mimic an EDM. The circuitry for the lead switching device was designed and built by Brendon O’Leary.

The full wiring diagram for the field plate assembly is shown in Figure 5.6. Voltage monitoring for all for \mathcal{E} -field channels is performed on a 6.5 digit multiplexed digital multimeter (Keithly 2701 with 7702 multiplexer module), specified to have an accuracy of ± 20 mV. The eight leads enter the interaction region vacuum chamber through a vacuum feedthrough. A lead is mechanically attached with an indium pad at both the bottom north and south corners of each field plate and guard ring. One set of contact leads was wired to the voltage supply, while the other was left uncon-

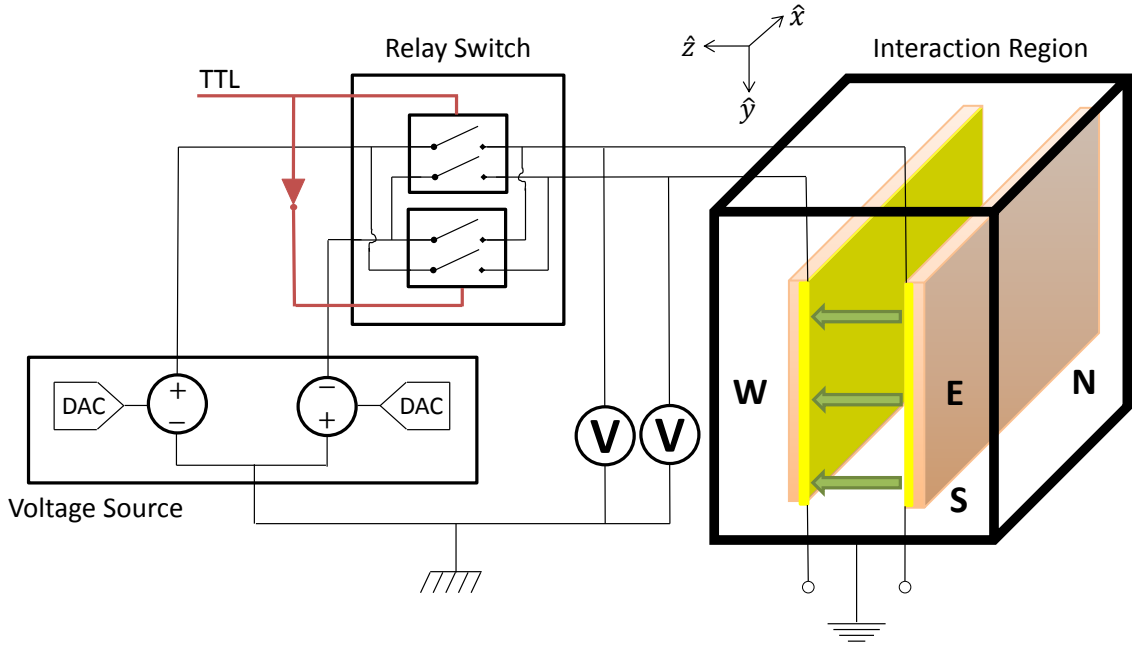


Figure 5.6: The wiring diagram for the electric field plates. Two amplified DAC channels apply voltages to the ITO coated glass field plates. The voltage source and relay switch control the $\tilde{\mathcal{E}}$ and $\tilde{\mathcal{L}}$ switches respectively (see text). Not shown are two additional voltage source and relay channels with identical wirings connected to the East and West guard rings. A common grounding point across the entire system was not enforced, indicated by the unconnected grounds in the diagram. The extra set of leads on each field plate and guard ring was left unconnected in this experiment. Voltage taps after the relay switch monitored all four voltages on a DMM. For reference, the molecular beam’s velocity is in the \hat{x} direction, from South to North.

nected. This backup connection was used occasionally for measurements of leakage resistances and currents.

The ground of the voltage source is not directly connected to the interaction region chassis or field plate assembly ground. It was found that doing so caused large leakage currents to be driven through the interaction region due to dissimilar ground potentials between the voltage source and powered vacuum equipment attached to the interaction region. Consolidating and equalizing all ground potentials in the room

would have been difficult given the layout of our equipment and the lab’s electrical wiring. We instead isolated the grounds, thereby floating the field plates and guard rings with respect to the interaction region. We exaggerated the ground offset in an IPV run, which revealed no systemic caused by the floating field plates.

The programmability of the supply provided the means of applying \mathcal{E} -field related IPVs. For example, an \mathcal{E}^{nr} was applied by setting the applied voltage to have a large non-reversing offset, so that the \mathcal{E} -field magnitude changes along with its sign (eg, for $\mathcal{E}^{\text{nr}} = 200 \text{ mV/cm}$, $V_+ = 2 \times 177.25 \text{ V}$, and $V_- = 2 \times -176.75 \text{ V}$). The floating ground offset IPV was performed by increasing the voltage on the east and west field plates by an equal amount.

5.4.2 Frequency Switching for \mathcal{N} and \mathcal{P} State Selection

The internal molecule direction $\tilde{\mathcal{N}}$ and the readout parity $\tilde{\mathcal{P}}$ are selected by choosing one of the four transitions in the

$$|H, J = 1, |M| = 1, \mathcal{N} = \pm 1\rangle \rightarrow |C, J = 1, M = 0, \mathcal{P} = \pm 1\rangle$$

manifold. A system of three cascaded AOMs acting as frequency shifters and shutters selects the proper 1090 nm state preparation and probe laser frequency as required by the H state Stark shift $\Delta_{st} = 2D_H\mathcal{E}$ (74 MHz (292 MHz) for Low- \mathcal{E} (High- \mathcal{E})) and the C state zero-field omega doublet splitting (50.4 MHz). The AOM states are modulated using either digital logic controlled RF switches (Mini-Circuits ZYSWA-2-50DR) or frequency tuning of the DDS synthesizer (Novatech 409B). Of these two switch methods, the former has a shorter transition time Δt , while the latter requires fewer resources (DDS channels). The $\tilde{\mathcal{N}}$ and $\tilde{\mathcal{P}}$ states can be changed frequently with

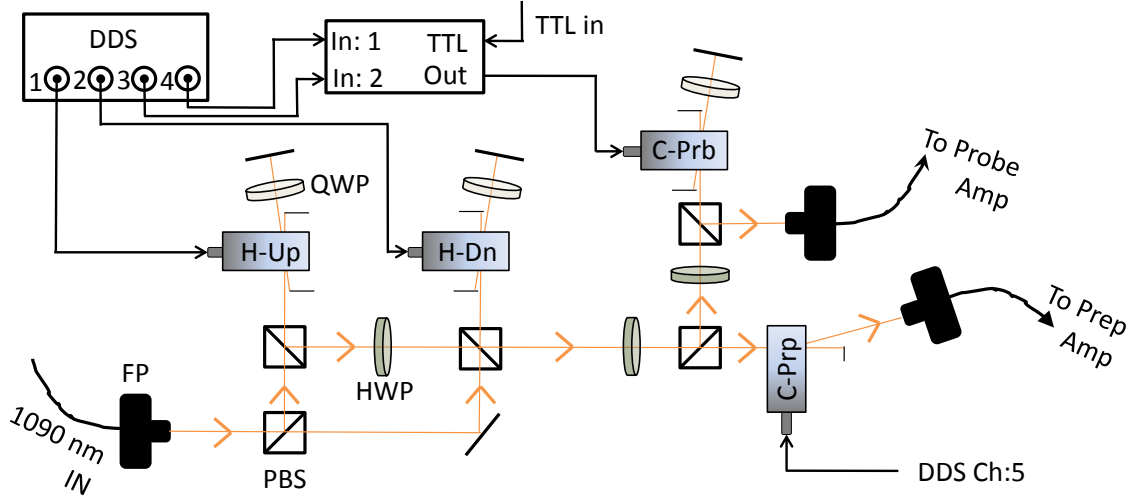


Figure 5.7: Frequency switching layout for \mathcal{N} and \mathcal{P} state selection. This is layout of essential components of both the High and Low \mathcal{E} -field breadboards. Elements include: Fiber Ports (FP), Half-Wave Plates (HWP), Quarter-Wave Plates (QWP), Polarizing Beam Splitters (PBS), Acousto Optic Modulators (H -Up, H -Dn, C -Prb, C -Prp), Direct Digital Synthesizer (DDS), and TTL driven RF switch.

little reduction in duty cycle, so the $\tilde{\mathcal{N}}$ switch is reversed every 0.5 s. In practice, the reversal of $\tilde{\mathcal{P}}$ is randomized with a typical switch period of 45 s, much slower than $\tilde{\mathcal{N}}$ because it suppresses systematics with lower frequency drift rates [105].

The optical system for frequency selection is shown in Figure 5.7, and is similar to that described in [9]. The optical system was first designed and built by Emil Kirilov, and later improved by Brendon O’Leary. The entire setup is on a single breadboard, with light coupled in and out using polarization maintaining fibers. The two double-passed AOMs H -Up and H -Dn shift the frequency by an amount $2(\nu_{H\uparrow} - \nu_{H\downarrow}) = 2D_H\mathcal{E}$, and therefore act as our $\tilde{\mathcal{N}}$ switch. These AOMs are operated as shutters, 50% of the input light goes into either AOM, and the output is extinguished by removing the RF drive to either AOM. In practice, an AOM is switched off by shifting the

DDS output by ~ 40 MHz, which alters the Bragg diffraction angle enough such that the 1st order beam becomes blocked. This technique is preferable to setting the RF amplitude to zero, because keeping the AOM “warm” is necessary to eliminate the long switch transients between infrequent $\tilde{\mathcal{N}}$ switches. The fiber amplifiers will be damaged if the seed power output of the breadboard falls below 1 mW. To avoid a time when both H -Up and H -Dn are off (zero output power), the $\tilde{\mathcal{N}}$ switch is operated in the following sequence:

1. The current off-resonant AOM is switched on.
2. The on-resonant AOM is switched off.

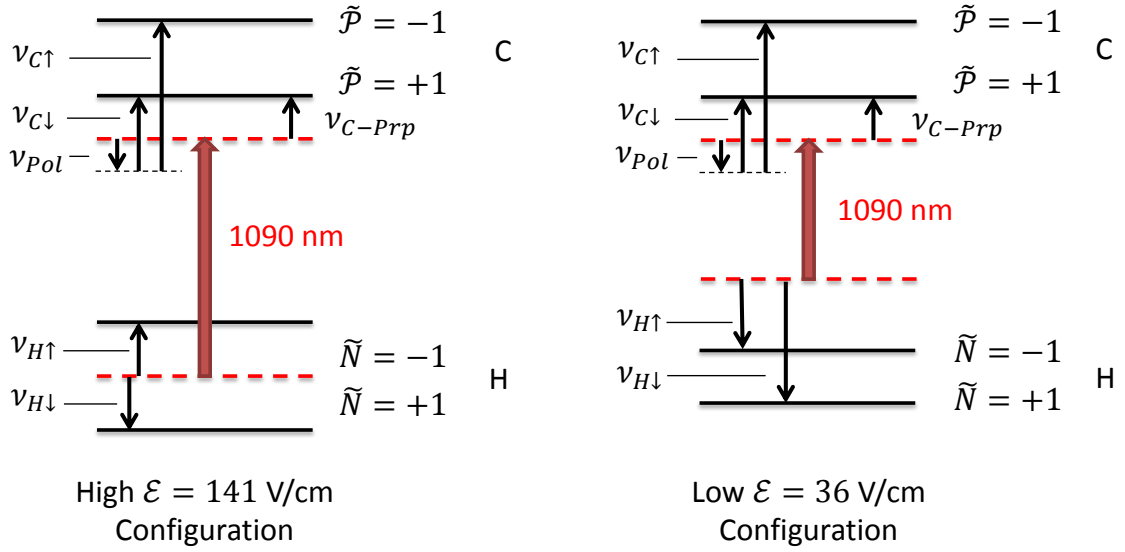
This leads to a short period when both H -Up and H -Dn are on and the output from the switching breadboard is doubled. We are well below the maximum seed power threshold of the amplifiers, so a momentary increase does no damage.

The output of the $\tilde{\mathcal{N}}$ shutter system is split for delivery to state preparation and probe laser output couplers. The single-passed AOM C -Prp increases the frequency of the state preparation laser to address the $\mathcal{P} = +1$ state³. This AOM does not perform any block or superblock switches, but it is used for the detuning Δ_{prp} IPV, interleaved with the final published data set. The probe laser frequency is shifted by a double-passed AOM labeled C -Prb in Figure 5.7. This AOM is carefully tuned such that its frequency can be switched between $\nu_{C\uparrow}$ and $\nu_{C\downarrow}$ without changing the fiber coupling into the probe output port. The frequency shift $2(\nu_{C\uparrow} - \nu_{C\downarrow}) = 50.4$ MHz, so this allows selection of the proper \mathcal{P} state in C (the $\tilde{\mathcal{P}}$ switch).

³State preparation is always performed by pumping population out of H through the lower C state omega doublet.

Drive frequencies $\nu_{C\uparrow}$ and $\nu_{C\downarrow}$ are fixed on two separate DDS channels, then the output is chosen via a TTL driven RF switch. Actuating $\tilde{\mathcal{P}}$ with an RF switch, instead of reprogramming the DDS, allows a much faster switch rate (100 ns vs. 40 ms), at the cost of needing an extra DDS channel per AOM. A drawback of this technique is if the RF amplitude is different between the $\nu_{C\uparrow}$ and $\nu_{C\downarrow}$ DDS channels, this will lead to a $\tilde{\mathcal{P}}$ odd laser power ($P^{\mathcal{P}}$). We measure both a $P^{\mathcal{P}}$ and $P^{\mathcal{N}}$ on photodiode power monitors. We performed IPV studies where these effects were greatly exaggerated, and found no resulting EDM systematics. Therefore, I recommend that future generations implement all binary frequency switches using the fast technique involving TTL switches.

Two versions of this AOM switching breadboard have been built for High and Low \mathcal{E} -field run configurations, with drive frequencies appropriately adjusted for the H state dc Stark shift (Table 5.1). The change in Stark shift by a factor of four is beyond the tunable bandwidth of available AOMs, so each breadboard required selecting AOMs with different center frequencies. Not shown in Figure 5.7 are the probe polarization switching AOMs (Section 4.1), which impart an extra 90 MHz frequency shift on the probe beam. Switching between the High and Low \mathcal{E} -field breadboards was accomplished by manually swapping breadboard input and output fibers and swapping DDS output channels. This process could be made more efficient by using MEMS fiber optic multiplexers and additional dedicated DDS units to avoid the physical switching of cables.



	$\nu_{H\uparrow}/2$	$\nu_{H\downarrow}/2$	$\nu_{C\uparrow}/2$	$\nu_{C\downarrow}/2$	ν_{C-Prp}	ν_{Pol}	$\Delta\nu_{X\rightarrow C}$
High \mathcal{E}	73.015	73.015	110.7	85.5	91.05	80	0
Low \mathcal{E}	78.005	115	92.7	67.5	55.005	80	-156.955

Table 5.1: The frequency shifts provided by AOMs for the High and Low \mathcal{E} -field \mathcal{N} and \mathcal{P} state switching. Where the shift is divided by 2, the AOM is double-passed.

5.4.3 Polarization Control

Polarization control of the state preparation and probe lasers is accomplished via $\lambda/2$ plates mounted in a high resolution rotation stage (Newport URS50BCC). Because our phase and contrast measurements are sensitive to the relative polarization angle of these two lasers, rotation stages with closed-loop encoder feedback are required. Along each beam path, the lasers do not reflect off any mirrors between the rotation stage and molecule beam, allowing us to prepare states with arbitrary linear polarization angle⁴. The waveplates control the state of the $\tilde{\theta}$, $\tilde{\mathcal{R}}$, and $\tilde{\mathcal{G}}$ switches with an accuracy of 0.04° and a uni-repeatability of 0.002° . Similar rotation stages (Newport SR50CC) were used to precisely set the position of a quarter-wave plate used for an IPV in which circular polarization was inserted into the pump beam.

These stages must be accurate enough to be able to repeatedly nullify the zero crossings in the polarization dependence of the \mathcal{E}^{nr} systematic. Measurements and of the \mathcal{E}^{nr} zero-crossing were limited by our averaging time to a statistical precision at the $\sim 1^\circ$ level (Figure 7.5). In a future generation of the experiment, a 10x better phase measurement may be required to limit the \mathcal{E}^{nr} systematic, assuming the systematic slope remained constant. This means we could relax our requirements on stage accuracy to 0.1° for a stable EDM measurement, which makes a large array of faster rotation stages available for use.

The rotation stages are driven at their rotation speed limit of $20^\circ/\text{s}$. The measured transition times $\Delta t_\theta \approx 1$ s and $\Delta t_{\mathcal{R}} \approx 3$ s are longer than what one would expect

⁴Reflection off a mirrored surface can perturb a polarization state when S and P polarization components have different reflection coefficients. Where a mirror must be inserted in a path requiring critical polarization control, data from Thorlabs indicates protected silver mirrors should be used, which have S and P reflection coefficients differing by $< 0.15\%$ for $\text{AOI} \leq 45^\circ$.

from the 6° and 45° waveplate slews required respectively for the $\tilde{\theta}$ and $\tilde{\mathcal{R}}$ switches. Therefore, the closed loop encoder feedback must be contributing to the switch time. While a faster rotation stage with similar accuracy (eg, Newport's URS75BCC with $80^\circ/\text{s}$) would in principle improve the duty cycle, the speed of the feedback would also have to be increased. The more frequent Δt_θ might be dominated by encoder feedback time, but the larger slews required for $\tilde{\mathcal{R}}$ and $\tilde{\mathcal{G}}$ could be significantly sped up by a faster rotation stage.

5.4.4 Magnetic Field Control

The magnetic field is controlled via several remotely programmable current supplies. A DC current calibration source (Krohn-Hite 521/522) drives the main cosine theta coil generating the \hat{z} bias field, while shim and gradient coils in the $\hat{x}, \hat{y}, \hat{z}$ directions were powered by a Harvard-built current supply based on the BabyDAC architecture. The reversal of the \mathcal{B} -field is always accompanied by a degauss cycle to eliminate hysteresis from to magnetization of the magnetic shields. The current is first reduced to zero, then the shields are demagnetized by applying up to ~ 1 A of current as an exponentially chirped 200 Hz sine wave, with an envelope duration of 1 second. To cycle through all layers of magnetic shields, the full degauss cycle requires about 4.5 seconds. For this reason, we chose to switch $\tilde{\mathcal{B}}$ every 25 or 45 seconds, which limits the impact on the duty cycle while still allowing frequent measurements of the $\tilde{\mathcal{B}}$ correlated precession phases.

Careful flux gate magnetometry revealed that large magnetic field gradients of 0.4-0.7 mG in the \hat{y} direction were present while acquiring all of our EDM data [138].

We determined that the somewhat jarring process of assembling the shields pins in magnetic domains which require an especially high current degauss cycle to eliminate [2]. By doubling the current to 2-2.5 A, we were able to eliminate this magnetization. IPV studies revealed that transverse \mathcal{B} -fields and gradients do not cause EDM systematics. However, in future generations of the experiment it would be desirable to implement a higher current degauss cycle, preventing this permanent magnetization from developing over time.

5.5 Acquisition of Phase Precession Data

Within a single ablation pulse, data acquisition timing is controlled by a digital delay generator (SRS DG645). Every 20 ms, the ablation YAG Q-switch is fired, creating a pulse of molecules. Molecule fluorescence signals, measured as a PMT photocurrent, are captured on a 22-bit digital oscilloscope (National Instruments PXI-5922), which is triggered 6-7 ms after the ablation pulse. The scope trigger delay is adjusted to compensate for the drifting molecule velocity, allowing the detection window to remain centered around the arrival of the molecule pulse at the probe region. The sequence is triggered off the 100 kHz square wave synchronized to the \hat{X} and \hat{Y} probe polarization switches (Section 4.1). The phase of the polarization switching waveform is fixed relative to the scope trigger, which allows for reliable digital demodulation of the captured fluorescence signal in post processing.

The scope acquires a point every 200 ns, which allows us to easily resolve the time dependent structure within each 5 μ s polarization bin. Data was stored and analyzed as a function of time after ablation and time within a polarization switch state. Due

to the 10% longitudinal velocity dispersion of our molecule beam, the arrival time at our detectors is correlated with different longitudinal velocity classes, and therefore different precession times τ . Being able to temporally resolve these velocity classes across the 1 ms wide molecule pulse allows us to calculate precession phases for each velocity class. This improved the contrast \mathcal{C} by effectively narrowing the velocity distribution for the precession measurement performed in each (\hat{X}, \hat{Y}) polarization switch pair.

Signal waveforms captured on the oscilloscopes are transferred to the control PC every ablation pulse (50 Hz). The waveforms from each PMT are digitally averaged over 25 pulses (2 Hz), then stored on disk in a binary file format. This has the advantage of significantly reducing the data storage requirements and the time necessary for post processing. It also allows a file containing a number of auxiliary measurements to be recorded synchronously with the fluorescence waveforms. This “header” file includes the programmed set values of all binary switches, as well as measurements of these parameters, including \mathcal{E} -field voltages, \mathcal{B} -field currents, laser power and polarization, and magnetic field readings from flux gate magnetometers. We also log (and record in the header) slowly drifting parameters such as molecular beam buffer gas flow rates and cell temperatures, as well as temperature, pressure and humidity in our lab. All of this data has proved useful in searching for systematics described in Chapter 7.

In summary, the data acquisition system has been a flexible tool for acquiring EDM data, and studying EDM systematics. The ability to apply various types of switching waveforms for a wide variety of experimental parameters helps to suppress

unwanted effects. Simultaneously digitizing fast waveforms and measuring auxiliary parameters created a richly structured data set for error detection and rejection. The ability to rapidly integrate and program new switches, as described in Appendix C, allowed us to isolate systematics and improve the EDM limit by an order of magnitude in a first generation experiment.

Chapter 6

Measuring Electric Fields with ThO

In order to compute shifts and uncertainties associated with the \mathcal{E}^{nr} systematic, we had to set limits on the size of $\mathcal{E}^{\text{nr}}\hat{z}$ in the interaction region (Section 7.1.2). Using our pulsed molecular beam source, we were able to adapt the apparatus to perform several electric field measurements in our precession region, using ThO as an electric field probe. Similar precision measurements with atomic or molecular beams have used their species of interest to study the magnetic or electric fields in their apparatus [139, 140]. States with large magnetic (μ) or electric (D) dipole moments are used as sensitive field probes, measuring the shift in resonances from Zeeman or Stark interactions.

In ThO, the polarized electric dipole moment of the $|H, J = 1\rangle$ state

$$D_{H,1} = 1.0315 \pm 0.0008 \text{ MHz}/(\text{V}/\text{cm})^1 \quad (6.1)$$

provides linear dc Stark shifts

$$\Delta_{\text{st}} = 2D_{H,1}|\mathcal{E}_z| \quad (6.2)$$

that are sufficiently sensitive to measure \mathcal{E} -fields at the mV/cm level when probing narrow, ~ 10 kHz wide resonances. We measured the electric field along the molecular beam path in three ways. The first used a stimulated Raman transition to directly drive population between the Stark shifted H state omega doublets, $|\mathcal{N} = +1\rangle \leftrightarrow |\mathcal{N} = -1\rangle$. This transition had the narrowest linewidth and the best sensitivity, but could only be measured near the state preparation and probe lasers, where we had optical access. The second technique used microwaves to drive the Stark shift sensitive $|H, J = 1\rangle \rightarrow |H, J = 2\rangle$ rotational transition. Microwaves could be injected longitudinally down the beamline, so this technique can map the electric field over the entire precession distance. It had the drawback of less sensitivity in both frequency and position than the Raman measurement. A third technique measured \mathcal{E}^{nr} only via contrast correlations in the state preparation laser. It had the worst sensitivity and could not measure the absolute \mathcal{E} -field, but it could be easily integrated in with other data acquisition to measure the \mathcal{E}^{nr} at regular intervals.

The magnetic moment in the H state,

$$\mu_{H,1} = 0.0044\mu_B = 6.2 \text{ Hz/mG},$$

¹The value used for $D_{H,1}$ differs slightly from that reported in reference [97]. It was determined through a combination of measurements described in Section 6.5. Additional sources of uncertainty in the frequency calibration of the previous measurement were discovered after publication.

is too small to allow \mathcal{B} -field mapping using these same techniques. Maximum fields achievable in our apparatus are ~ 100 mG, which cannot split the spin states beyond the ~ 10 kHz linewidth of the Raman and microwave measurements. The metastable Q state has both a large magnetic moment of $\sim 1\mu_B$ and a long lifetime, and therefore would be ideal for \mathcal{B} -field mapping. We have yet to directly observe the Q state, and developing the necessary optical systems to locate the state would have been a major disruption to our EDM experiments. We detected no statistically significant EDM systematics under applied transverse $\vec{\mathcal{B}}$ or $\vec{\mathcal{B}}^{\text{nr}}$ fields, so it was not necessary to measure these fields with a high degree of spatial or temporal precision. We measured the magnetic field using a minimally invasive 3-axis flux gate magnetometer probe inserted between our electric field plates upon completion of the data acquisition [138].

6.1 Relevant Field Components

Being able to fully characterize $\vec{\mathcal{E}}$ and $\vec{\mathcal{B}}$ fields is important for quantifying many systematics common to electron EDM experiments. An ideal beam type eEDM experiment would have perfectly uniform $\vec{\mathcal{E}}$ and $\vec{\mathcal{B}}$ fields along the entire phase precession region [3, 4]. A variation in the magnitude of the quantizing field (e.g. $\vec{\mathcal{E}} \cdot \hat{z}$) for a single molecule with trajectory ($\vec{v} = \bar{v}\hat{x}$) is averaged out by the phase precession measurement [10]

$$\phi = -\frac{1}{\hbar} \int_{x=0}^{x=L} (\mu_B g \tilde{\mathcal{B}} |\mathcal{B}_z(x)| + \tilde{\mathcal{N}} \tilde{\mathcal{E}} d_e \mathcal{E}_{\text{eff}}) dx / \bar{v}. \quad (6.3)$$

However, Maxwell's equations in free space ($\vec{\nabla} \times \vec{\mathcal{E}} = 0$) imply that gradients in the field strength along the beamline ($\partial \mathcal{E}_z / \partial x$) must be accompanied by other non-

zero gradients ($\partial\mathcal{E}_x/\partial z$) and fields in other directions. Transverse \mathcal{E} and \mathcal{B} fields can cause systematics such as geometric phases [141, 106, 142], so we desire the fields to be completely uniform in all directions when the molecules are undergoing phase precession.

Another idealized requirement is that fields reverse perfectly under switch operations $\tilde{\mathcal{E}}$, $\tilde{\mathcal{B}}$, and $\tilde{\mathcal{L}}$. This means that when the \mathcal{E} or \mathcal{B} field direction is inverted, its magnitude is preserved. For example, if $\vec{\mathcal{E}} = (|\mathcal{E}_z^0|\tilde{\mathcal{E}} + \mathcal{E}^{\text{nr}})\hat{z}$, ideally $\mathcal{E}^{\text{nr}} = 0$. A non-reversing field in a transverse direction (e.g. $\mathcal{E}^{\text{nr}}\hat{x}$) will cause the field vector to tip because $\vec{\mathcal{E}} \approx |\mathcal{E}_z^0|\tilde{\mathcal{E}}\hat{z} + \mathcal{E}^{\text{nr}}\hat{x}$. A wobble in the field direction is the classic example of source of geometric phase, but an advantage of the ThO molecule is that such systematics should be highly suppressed [10].

DC Stark or Zeeman shifts caused by non-reversing components \mathcal{E}^{nr} and \mathcal{B}^{nr} can cause correlated shifts of atomic resonances with $\tilde{\mathcal{N}}$, $\tilde{\mathcal{E}}$, and $\tilde{\mathcal{B}}$ switches. We have demonstrated that our phase measurements are sensitive to the detuning of the state preparation and probe lasers from resonance (Section 7.1.1), an effect which couples energy level shifts to the preparation of the spin state. In particular, we discovered $\mathcal{E}^{\text{nr}}\hat{z}$ causes a large EDM systematic by creating an $\tilde{\mathcal{N}}\tilde{\mathcal{E}}$ correlated detuning (Section 7.1.2).

Our measurement relies on sensitive cancellation of magnetic phase components upon reversal, and having non-zero \mathcal{B}^{nr} can also contribute an EDM systematic by coupling to other experimental imperfections. For example, a combination of the electric field dependence of the g factor (η), with an \mathcal{E}^{nr} and a \mathcal{B}^{nr} will generate a

systematic shift

$$\hbar\omega^{\mathcal{N}\mathcal{E}} = -\eta\mu_B\mathcal{E}^{\text{nr}}\mathcal{B}^{\text{nr}} \quad (6.4)$$

from the second term of Equation 1.9. The measured values of \mathcal{E}^{nr} and \mathcal{B}^{nr} are sufficiently small such that this higher order systematic is much less ($\sim 10^{-36} e\cdot\text{cm}$) than our statistical uncertainty.

6.2 Raman Measurement

The first technique used to probe a Stark shift sensitive transition utilized a two-photon stimulated Raman transition to directly drive population between the H state's $\mathcal{N} = \pm 1$ omega doublets. These transitions are analogous to a direct drive of Δ_{st} using RF radiation. The two-photon resonance has a sensitivity of $d\nu/d\mathcal{E} = 2D_{H,1}/h$ and a less than 100 kHz linewidth limited by transit time broadening. The scheme requires additional optical access for a \hat{z} propagating laser beam, but otherwise utilizes the same optics setup as our normal EDM measurement. This technique has the advantage of the greatest \mathcal{E} -field sensitivity and spatial resolution (~ 1 mm). Therefore, \mathcal{E}^{nr} can be determined very close to either prep or probe laser positions, which are the only two locations where the measurement of d_e is sensitive to the \mathcal{E}^{nr} coupling to the ac Stark shift systematic. The need for optical access was the primary drawback of this technique, which restricted the spatial measurement range.

6.2.1 Stimulated Raman Transitions and Measurement Procedure

Stimulated Raman transitions can occur in a Λ -type 3 level system between “ground states” $|1\rangle \leftrightarrow |2\rangle$ via a virtual excitation to state $|e\rangle$ (Figure 6.1). In our case, the “ground states” are omega doublet sublevels of the H state which are each two fold degenerate. In a basis that is “bright” and “dark” with respect to our linearly polarized laser beams, the relevant sublevels of $|H, J = 1, |M| = 1\rangle$ are

$$\begin{aligned} |X\rangle &= \frac{|M = +1, \mathcal{N}\rangle + |M = -1, \mathcal{N}\rangle}{\sqrt{2}}, \\ |Y\rangle &= \frac{|M = +1, \mathcal{N}\rangle - |M = -1, \mathcal{N}\rangle}{\sqrt{2}}. \end{aligned} \quad (6.5)$$

The states $|X\rangle, |Y\rangle$ couple to either the \hat{X} or \hat{Y} polarized light of the state preparation, probe, and Raman lasers.

The subspace of our “3-level system” is

$$|1, X/Y\rangle = |H, J = 1, X/Y, N = +1\rangle, \quad (6.6)$$

$$|2, X/Y\rangle = |H, J = 1, X/Y, N = -1\rangle, \quad (6.7)$$

$$|e\rangle = |C, J = 1, M = 0, \mathcal{P} = +1\rangle, \quad (6.8)$$

where $|1, X/Y\rangle$ and $|2, X/Y\rangle$ are each connected to $|e\rangle$ by optical radiation at 1090 nm with one-photon Rabi frequencies Ω_1 and Ω_2 , respectively. The detuning of the laser frequencies ω_{L1} and ω_{L2} from the transition frequencies ω_1 and ω_2 can be written in terms of one-photon (Δ_R) and two-photon (δ_R) components

$$\Delta_R = \omega_{L1} - \omega_1, \quad (6.9)$$

$$\delta_R = \omega_{L1} - \omega_{L2} - \Delta_{\text{st}}. \quad (6.10)$$

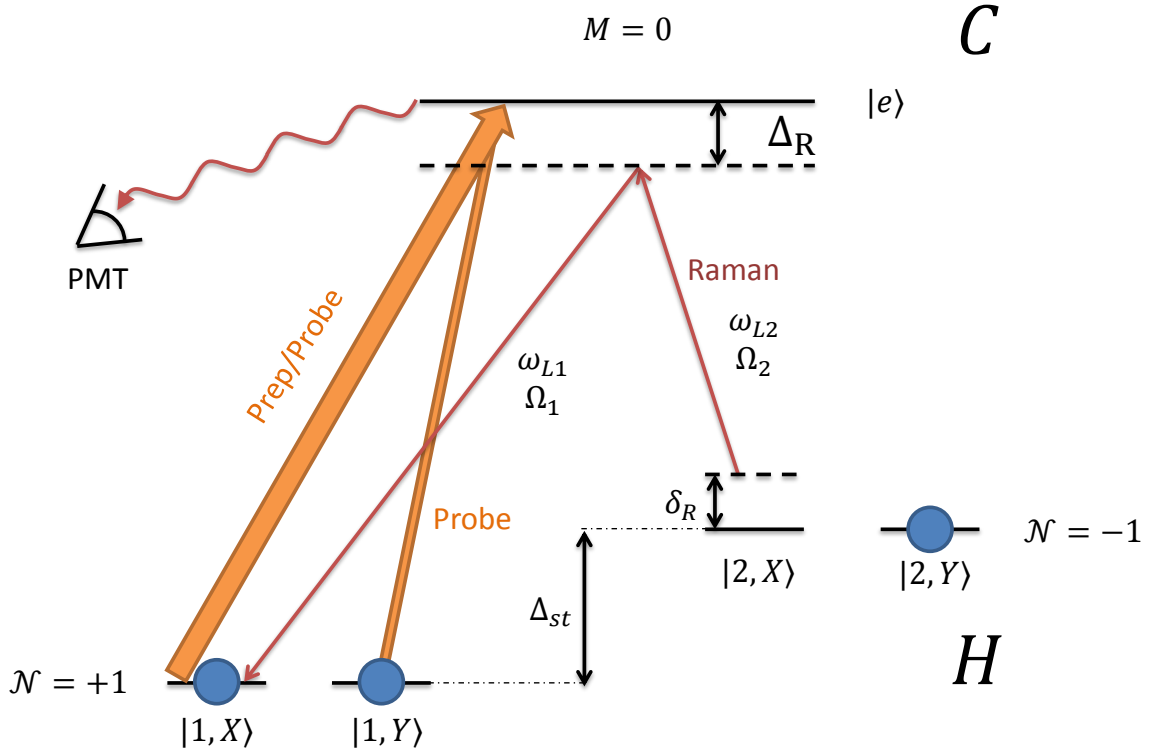


Figure 6.1: Relevant energy levels for the Raman electric field measurement scheme. In this examples, a stimulated Raman transition transfers population from $|2, X\rangle \rightarrow |1, X\rangle$ after depletion of the population using the state preparation laser. The probe laser measures both quadratures $|1, X/Y\rangle$ by rapidly switching polarizations between \hat{X} and \hat{Y} .

The individual Rabi frequencies

$$\Omega_{1/2} = \frac{D_{H-C} E_{1/2}}{\hbar} = \frac{D_{H-C}}{\hbar} \sqrt{2 \frac{I_{1/2}}{\epsilon_0 c}} \quad (6.11)$$

depend upon the $H \rightarrow C$ dipole matrix element D_{H-C} and the laser intensities [130, 108, 143]

$$I_{1/2} = \frac{\epsilon_0 c E_{1/2}^2}{2}. \quad (6.12)$$

In the limit of a large one-photon detuning with respect to the Doppler broadened one-photon linewidth ($\Delta_R \gtrsim 1.5$ MHz), we can adiabatically eliminate the excited

state population, treating $|e\rangle$ as a virtual state. In the limit that $|\Delta_R| \gg |\delta_R|$, the dynamics become identical to those for a two level system, and the Raman beam coherently couples states $|1, X/Y\rangle$ to $|2, X/Y\rangle$ [130, 144]. If we choose both frequency components of our Raman beam to be polarized along the \hat{X} direction, then we can restrict ourselves to transitions between $|2, X\rangle \leftrightarrow |1, X\rangle$. The equivalent two level dynamics have an effective Rabi frequency

$$\Omega_{\text{eff}} = \frac{\Omega_1 \Omega_2}{2\Delta_R}, \quad (6.13)$$

leading to oscillations of the atomic population

$$P_{2,X} = \frac{\Omega_{\text{eff}}^2}{\Omega_{\text{eff}}^2 + \delta_R^2} \sin^2 \left(\frac{\sqrt{\Omega_{\text{eff}}^2 + \delta_R^2}}{2} t \right). \quad (6.14)$$

The scheme for measuring \mathcal{E} -fields with this Raman resonance is as follows:

1. Transfer ground state population to all H state sublevels by optically pumping through the A state.
2. Deplete the population from a single spin quadrature (e.g. $|1, X\rangle$) using the state preparation laser ($X \rightarrow C$ transition).
3. Coherently transfer population from $|2, X\rangle \rightarrow |1, X\rangle$ using a ‘‘Raman beam’’ with two frequency components separated by the Stark shift $\Delta_{\text{st}} = 2D_{H,1}|\mathcal{E}_z|$.
4. Measure the population transferred back into $|1, X\rangle$ using the probe laser and collection optics. Due to polarization chopping of the probe beam, the population of the $|1, Y\rangle$ state is also measured. This state has not been affected by the Raman laser, and therefore provides a means of normalizing out molecule beam flux variations.

5. Change the two-photon detuning δ_R and repeat steps 1-4 on subsequent ablation pulses, therefore building up a lineshape of transferred population as a function of δ_R .

The ThO beam's forward velocity maps the arrangement of lasers shown in Figure 6.2 into the time sequence described above. The stimulated Raman transfer of population depends on $|\mathcal{E}_z(x)|$ locally at the position of the Raman beam, allowing us to gather spatially measure the electric fields within our limits of optical access.

6.2.2 Experimental Configuration

The setup for this measurement was meant to minimally disturb the fully configured ACME optics setup. A component of the 1090 nm seed laser for prep and probe beams is picked off and sent to the breadboard shown in Figure 6.2b. Two AOMs split the input, and create frequency components near the $|1\rangle \leftrightarrow |e\rangle$ and $|2\rangle \leftrightarrow |e\rangle$ transition frequencies. Only two 80 MHz AOMs were available for use, which meant that only transitions to the $\mathcal{P} = +1$ (lower) C state at High- \mathcal{E} could be driven efficiently given the required shifts (Table 5.1).

The two frequency components are recombined and fiber coupled into a Keopsys amplifier (Keopsys KPS-BT2-YFA-1083-SLM-PM-05-FA) to pre-amplify the power from 4 mW to ~ 50 mW. The Keopsys output is sent to a homemade fiber amplifier [105], which is operated with the pre-amplified seed safely above its 25 mW minimum. The homemade amplifier had power output between 500 and 800 mW after an isolator, which drifted due to thermal effects rotating the polarization in the doped fiber. When coupled back into free space, the fiber amplifier output contains

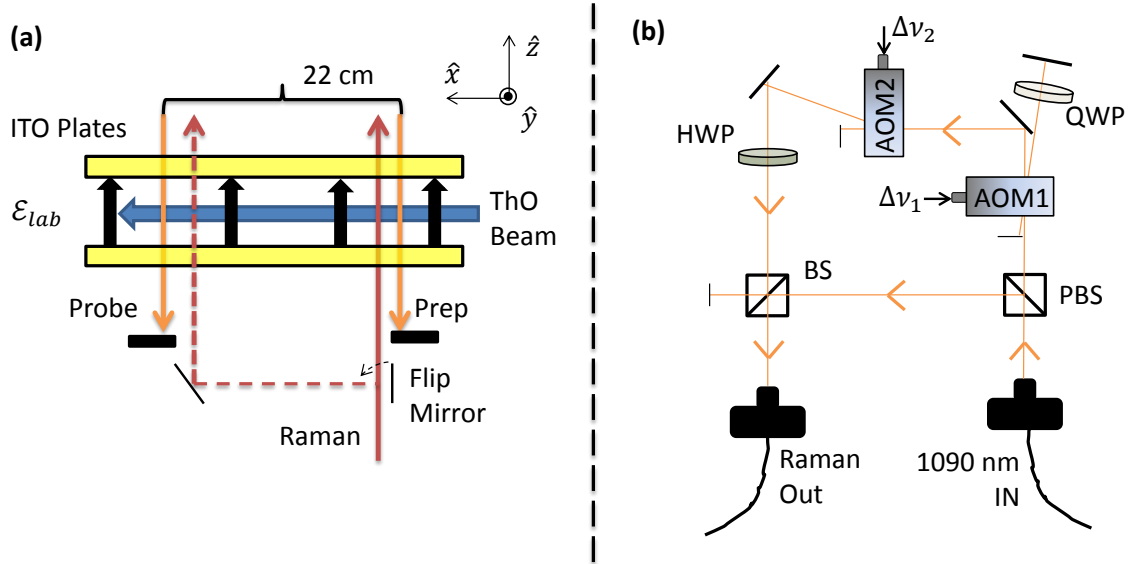


Figure 6.2: Optical configuration for Raman \mathcal{E} -field probe measurement. (a) A flipper mirror allows optical access of the Raman beam to either a region near the prep laser or probe laser. (b) Two cascaded AOMs create frequency components to drive the stimulated Raman transition. Components include Polarizing Beam Splitter (PBS), 50:50 Beam Splitter (BS), Fiber Ports, Half Wave Plate (HWP), Quarter Wave Plate (QWP), and AOMs.

both Raman frequency components amplified into the same spatial mode.

The Raman beam is counter-propagating with the prep and probe lasers, allowing it to be shaped on the less crowded optics table. The only available optical access is at the prep and probe window ports, so the Raman beam was positioned either just to the $+\hat{x}$ (downstream) side of the prep laser, or the $-\hat{x}$ (upstream) side of the probe. A flipper mirror allowed rapid switching between these two positions (Figure 6.2a). The Raman beam was shaped using cylindrical lenses into a stretched Gaussian with 1 mm width and 1 cm height.

The Raman beam's two frequency components are generated by a double passed AOM (AOM1) followed by a single passed AOM (AOM2), which shifts the 0th

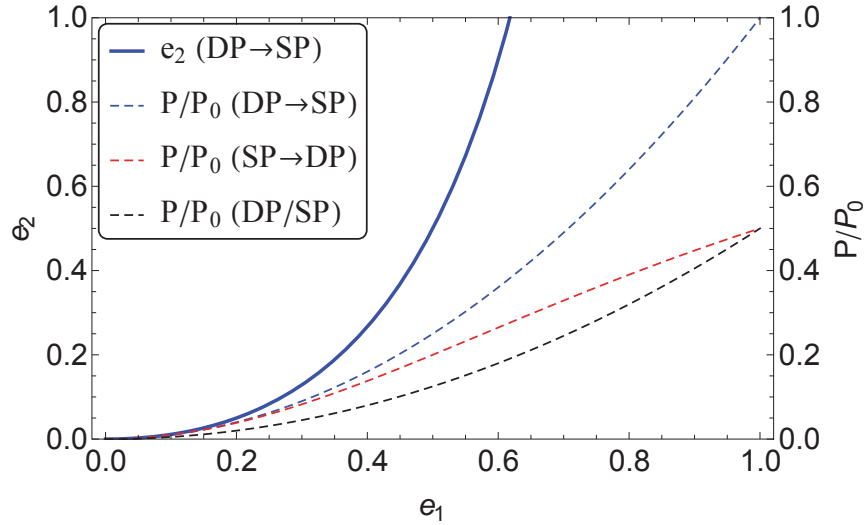


Figure 6.3: Efficiency relationship of cascaded AOMs for balancing power (solid blue line, left axis). The output power in each Raman beam $P = P_1 = P_2$ is plotted on the right axis for several configurations (dashed curves): Blue plots Equation 6.15 representing Figure 6.2(b); Red corresponds to the single passed AOM (e_2) coming first in the cascade; Black is if the power is first split on a 50/50 beamsplitter, then sent to each AOM.

order output of the **AOM1** (Figure 6.2). If these AOMs have 1st order single pass efficiencies of e_1, e_2 respectively, then for input power P_0 the power in the two Raman beams before recombination is $P_1 = P_0 e_1^2$ and $P_2 = P_0(1 - e_1)e_2$. In order to balance the power of the two Raman beams, the following relationship between the AOM efficiencies must be satisfied

$$e_2 = \frac{e_1^2}{(1 - e_1)} \quad (6.15)$$

In a similar fashion, one can compute the power and efficiency requirements if the cascade order of single and double passed AOMs is reversed.

As seen in Figure 6.3, the AOM with the lower intrinsic efficiency should be chosen as the first in the cascade. For properly chosen cascade order, this configuration will always outperform a simple 50/50 split of the input power, although the latter

configuration is easier to align. The frequency settings for our AOMs must satisfy

$$\Delta\nu_1 = (\nu_{H\downarrow} + \nu_{C-Prp} + \Delta_R)/2 = (118.5 + \Delta_R/2) \text{ MHz} \quad (6.16)$$

$$\Delta\nu_2 = (-\nu_{H\uparrow} + \nu_{C-Prp} + \Delta_R) = (-55 + \Delta_R) \text{ MHz} \quad (6.17)$$

where the additional detunings must satisfy those from Table 5.1 because of the common 1090 nm seed between prep, probe, and Raman lasers. The double passed AOM must be driven with $\Delta\nu_1$, far from the optimal drive frequency of 80 MHz, so we chose the DP \rightarrow SP cascaded configuration to maximize the output power.

Detunings are chosen such that $\Delta_R = -2.5$ MHz is just outside of the Doppler width of ~ 1.5 MHz. This maximized the two-photon Rabi frequency Ω_{eff} , but did not cause noticeable loss in signal due to one-photon scattering. Because $H \rightarrow C$ resonant excitations tend to decay back to the ground state, such events will appear mainly as a loss in transfer efficiency, as opposed to a decrease in contrast. The two-photon detuning was typically scanned around $\delta_R = \pm 150$ kHz, which captures the entire lineshape. Typically, $\Delta\nu_2$ was scanned while $\Delta\nu_1$ was kept fixed. $\Delta\nu_2$ has a larger effective tuning range because it is closer to the output fiber couple.

6.2.3 Raman Lineshape

In the procedure outlined above, the maximum transfer efficiency will occur when the effective Rabi dynamics undergo a π oscillation on resonance. If the molecules experience the Raman pulse for duration τ_R , then the π pulse is achieved for $\Omega_{\text{eff}}\tau_R \approx \pi$. The Raman pulse timescale τ_R is determined by the transit time of the molecules through the Raman beam. For a time varying Rabi frequency $\Omega_{\text{eff}}(t)$, the two state dynamics can be solved exactly, and now depend on the complete history of the Rabi

function. For complete population transfer, we require [145]

$$\int \Omega_R(t') dt' = \pi. \quad (6.18)$$

The Raman beam has a Gaussian spatial intensity profile in the \hat{x} direction, which looks like a time dependent intensity in the molecule's frame

$$I(t) = I_0 e^{-2(vt)^2/w^2} = I_0 e^{-8t^2/\tau_R^2}. \quad (6.19)$$

For our $\bar{v} \approx 200$ m/s ThO beam crossing a Raman laser with $1/e^2$ half width $w \sim 1$ mm, the characteristic interaction time is $\tau_R = 2w/\bar{v}$. For Raman frequency components derived from the same laser such that they have a common spatial profile, Equations 6.11 and 6.13 imply that $\Omega_{\text{eff}}(t) \propto I(t)$. Therefore, the Rabi frequency can be written

$$\Omega_{\text{eff}}(t) = \Omega_0 e^{-8t^2/\tau_R^2}. \quad (6.20)$$

There are several ways to demonstrate that Raman resonance is transit time broadened to a Gaussian frequency profile. The approach taken in [126] is to Fourier transform the sinusoidal time dependence of the laser's electric field with the Gaussian intensity envelope. This results in a Gaussian intensity spectrum for the laser $I(\omega_L)$ which can be composed with the lineshape of the Rabi resonance for monochromatic radiation (Equation 6.14). This approach gives linewidths with the proper order of magnitude, but the approach is unphysical in the limit of a single Rabi oscillation. As an alternative, one can numerically integrate the two state Schrodinger equations of motion in the rotating wave approximation under the influence of the time dependent

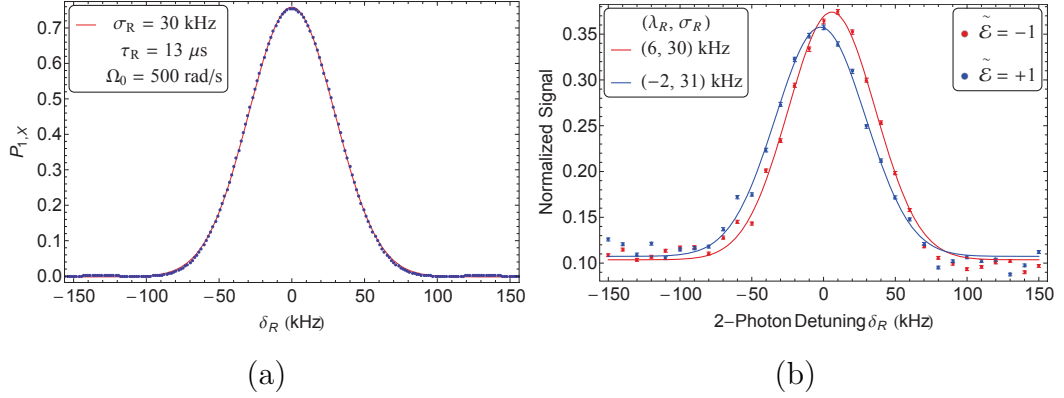


Figure 6.4: Simulated and measured Raman lineshapes. **(a)** The simulations predict lineshapes of very similar shape and width to those observed for input τ_R and Ω_0 within the uncertainty of experimental parameters. **(b)** Measured resonances with fit centers $\lambda_R = \delta_R - \Delta_{st}$ and Gaussian widths σ_R . Resonances for different $\tilde{\mathcal{E}}$ states illustrate the size of the line shifts being resolved. This data has been normalized to the unperturbed quadrature $P_{1,Y}$. Error bars are given by the standard deviation in repeated measurements.

Rabi frequency

$$\begin{aligned} -i\dot{c}_1(t) &= c_2(t) \frac{\Omega_{\text{eff}}(t)}{2} e^{i\delta_R t}, \\ -i\dot{c}_2(t) &= c_1(t) \frac{\Omega_{\text{eff}}(t)}{2} e^{-i\delta_R t}. \end{aligned} \quad (6.21)$$

Such an approach correctly reproduces the quasi-static prediction of Equation 6.18, whereby integrating over Equation 6.20 correctly predicts

$$\tau_R = \frac{2\sqrt{2\pi}}{\Omega_0} \quad (6.22)$$

for a full π pulse.

The results for this simulation are shown in Figure 6.4a and compared with measured Raman resonance lineshapes of 6.4b. The smooth Gaussian excitation has eliminated the additional oscillations expected from the $\text{sinc}()$ shape of a sharper edge boxcar excitation. The width of the lineshape depends as expected upon τ_R , demonstrating that transit time broadening is defining the lineshape. The Fourier

	$ \mathcal{E}_z^0 $ (mV/cm)	$\mathcal{E}_z^{\mathcal{E}}$ (mV/cm)	$\mathcal{E}_z^{\mathcal{E}\mathcal{L}}$ (mV/cm)	$\mathcal{E}_z^{\mathcal{L}}$ (mV/cm)
	Avg Magnitude	Supply	Patch	Leads
Prep	$141,573. \pm 0.2$	1.6 ± 0.2	-6.5 ± 0.3	-0.14 ± 0.2
Probe	$141,585. \pm 0.2$	1.6 ± 0.2	-5.5 ± 0.3	0.15 ± 0.2

Table 6.1: \mathcal{E}^{nr} components from Raman data set on 7/2/2013. Measurements were alternated between the prep and probe regions using a flipper mirror. The error bars are purely statistical. Assumes $2D_{H,1} = 2.06315$ kHz/(mV/cm), within the error bars of the measured value (Equation 6.38).

transform of $\Omega_{\text{eff}}(t)$ yield an $I(\omega)$ with frequency width $\sigma_R = \sqrt{2}/\pi\tau_R$, which agrees with the width fit to the numerical simulations to within 10%. The height of the resonance curve depends upon Ω_0 and the laser intensity. Some unexplained processes create a background of residual population even when δ_R was far off resonance, and also appears to be independent of Δ_R . This background makes extracting an absolute quantity for Ω_{eff} from the resonances inaccurate, but does not adversely affect line-center fits to a simple Gaussian, as is discussed in the following section.

6.2.4 Data Acquisition and Results

For each scan of the Raman laser across resonance, the line-center was extracted from a Gaussian fit. Data collected under varying $\tilde{\mathcal{E}}$ and $\tilde{\mathcal{L}}$ switch states allowed measurement of all four components of the reversing and non-reversing \mathcal{E} -fields. The difference in frequencies between the two AOMs is used to extract the electric field

$$|\mathcal{E}_z| = \frac{2\Delta\nu_1 - \Delta\nu_2}{2D_{H,1}}. \quad (6.23)$$

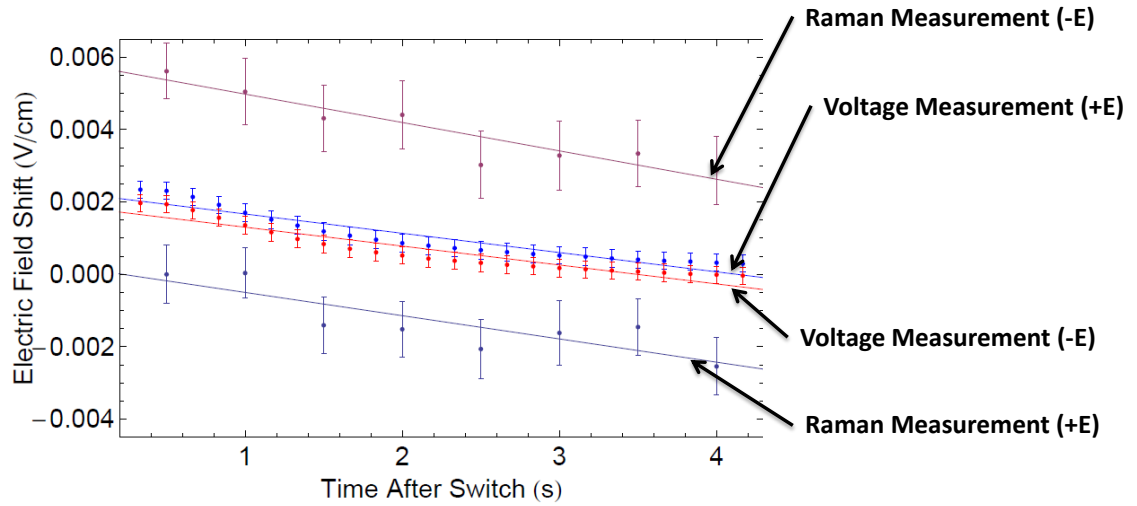
The extracted \mathcal{E} -field parity components for measurements made on 7/2/2013 are

shown in Table 6.1. This data was acquired between the two longer runs averaged together into our final error bar (6/4/2013 - 6/11/2013 and 8/22/2013 - 9/3/2013). It can therefore be compared to \mathcal{E}^{nr} measurements made with microwaves and contrast correlation measurements close in time to either of these runs.

Using Equation 5.23, the parity sums of $|\mathcal{E}_z|$ extracted from Equation 6.23 can be related to the internal and external components of \mathcal{E}^{nr} . The $\mathcal{E}_z^{\mathcal{L}}$ term is consistent with zero, confirming that the \mathcal{E}^{nr} due to lead switching ($(D_1 - D_2)/2$ in the model of Section 5.3) is negligible. Therefore, $\mathcal{E}_z^{\mathcal{E}\mathcal{L}} = \mathcal{E}_{\text{int}}^{\text{nr}}$, and this term is a direct measurement of the non-reversing patch potentials on the field plates themselves. The $\mathcal{E}_z^{\mathcal{E}}$ term represents the voltage offsets from the imperfectly set voltage supply.

This measurement was checked for several sources of systematics. There was no effect from probing through either $\mathcal{P} = \pm 1$ state, or from transferring population in the opposite direction (depleting $|2, X\rangle$ then transferring from $|1, X\rangle$ with the Raman laser). The spatial dependence $|\mathcal{E}_z(x)|$ was studied by translating the Raman beams in the \hat{x} direction. The optical access was limited to a small range, but the maximum translation of 5 mm revealed no statistically significant changes in the \mathcal{E} -field. An interesting effect was discovered whereby the measured internal \mathcal{E}_{int} was dependent on a change in the adjustable collimator position. This collimator adjustment shifted the spatial distribution of the molecule beam in the \hat{z} direction, thus sampling a slightly different patch potential \mathcal{E}^{nr} on each field plate. While the effect did not cause a systematic in the current generation, it is worth further exploration in the future.

This same setup was also used to take data in the “side of fringe” (SOF) mode. By setting a fixed δ_R to sit on the steep slope of the Raman resonance, one can



Raman Measured Drift (+/-) = $0.64/0.78 \pm 0.25$ mV/cm*sec⁻¹
Voltage Measured Drift (+/-) = $0.53/0.52 \pm 0.04$ mV/cm*sec⁻¹

Figure 6.5: Drifts in electric field measured with Raman side-of-fringe measurements and voltage monitors. The latter were acquired with a 6.5 digit multimeter with acquisition triggered to an $\tilde{\mathcal{E}}$ switch. The large $\tilde{\mathcal{E}}$ odd offset in the Raman data absent from the voltage monitor is indicative of the $\mathcal{E}_{\text{int}}^{\text{nr}}$.

infer shifts in this narrow line-center ($\Delta\nu$) from small correlated signal changes (ΔS). This technique has the advantage of much better temporal resolution than a full frequency scan, allowing us to measure electric field changes with resolution better than one second. A disadvantage of this technique is that $\tilde{\mathcal{E}}$ or $\tilde{\mathcal{L}}$ correlated changes in the amplitude or width of the lineshape cannot be distinguished from changes in the line-center. This would cause a false \mathcal{E}^{nr} if, for example the Raman laser power was correlated with $\tilde{\mathcal{E}}$ or $\tilde{\mathcal{L}}$. This is an unlikely scenario, and generally good agreement between SOF data and full resonance scans proves that this systematic is not present.

In order to convert ΔS measurements into $\Delta\nu$ shifts, we must know the slope of the curve $\Delta S/\Delta\nu$. The simplest way to do this is to step the laser frequency by a small amount up and down the fluorescence curve. This provides a direct measurement of

$\Delta S/\Delta\nu$, and is conceptually similar to how we measure our EDM contrast. We did not collect data with this additional frequency step, so we instead calibrate the slope using a lineshape function.

In principle, the slope can be calculated from the Gaussian fits to frequency scans acquired during the same run as the SOF data. However, the drifting laser power meant the excitation efficiency could vary between frequency scans and SOF data. We can normalize out the slope of the curve by assuming a drifting power affects only the amplitude of our lineshape. Then if our analytic lineshape is well described by a Gaussian plus background $G(\nu) + B$,

$$S(\nu) = A(G(\nu) + B) \quad (6.24)$$

The amplitude scaling factor A can be found by taking the ratio of the average signal and calculated lineshape on the side (ν_s) of the fringe,

$$A = \frac{\bar{S}(\nu_s)}{(G(\nu_s) + B)} \quad (6.25)$$

Then a signal change can be related to the slope of this lineshape $dG(\nu)/d\nu$

$$\Delta\nu = \Delta S \left(A \frac{dG(\nu)}{d\nu} \Big|_{\nu_s} \right)^{-1} \quad (6.26)$$

This lineshape calibration model was found to reproduce the \mathcal{E}^{nr} extracted from full scans across resonance. The results of this technique are shown in Figure 6.5, where we confirmed that the bandwidth of the voltage source creates a drift for many seconds after an $\tilde{\mathcal{E}}$ switch. This drift of a few mV/cm over the $\Delta t_{\mathcal{E}} = 2$ s between $\tilde{\mathcal{E}}$ switches is another good motivation for the randomized *ABBA* or *BAAB* selection of the $\tilde{\mathcal{E}}$ switch pattern (Section 5.2.2).

6.3 Microwave Measurement

Using microwaves to drive the Stark shift sensitive $|H, J = 1\rangle \rightarrow |H, J = 2\rangle$ rotational transition provides a second means of using ThO to probe the \mathcal{E} -field. Microwaves could be injected longitudinally down the beamline, so this technique maps the electric field over the entire precession distance. An additional advantage is the broad tunability of the microwave source frequency, so \mathcal{E} -field measurements can be made in both High and Low \mathcal{E} -field configurations. A Low- \mathcal{E} version of the Raman measurement could not be performed because it would have required building a second breadboard, as was required for the $\tilde{\mathcal{N}}$ and $\tilde{\mathcal{P}}$ state switching breadboard. The microwave measurement has the drawback of less sensitivity in both frequency and position compared to the the Raman measurement.

Diatomic molecules such as ThO have conveniently accessible microwave transitions between neighboring rotational levels. With a rotational constant of $B_{H,\nu=0} = 9765$ MHz [93], the rotational splitting between $|H, \nu = 0, J = 1\rangle$ and $|H, \nu = 0, J = 2\rangle$ in the H state is $4B_{H,\nu=0} = 39.06$ GHz. These transitions are accessible using the doubled output of a 20 GHz microwave frequency generator. A high gain horn beams microwave radiation through a window in the “dump region”, counter-propagating against the ThO beam velocity (Figure 6.6a). Sufficient microwave power is accessible to penetrate into the field plate assembly and drive π pulses from $|H, J = 1\rangle \rightarrow |H, J = 2\rangle$ for molecules previous transferred into the H state. The microwave source configuration and power coupling studies were performed by Adam West, and detailed microwave spectroscopy and measurement of rotational constants were performed by Adam West and Nick Hutzler.

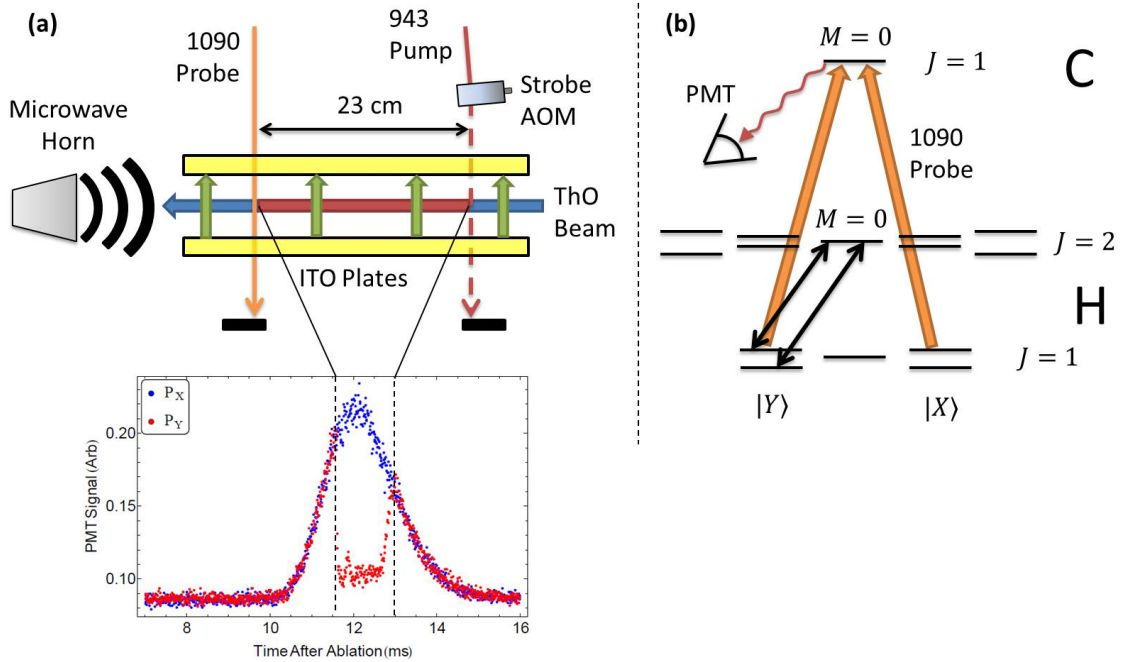


Figure 6.6: Apparatus and relevant energy levels for the microwave \mathcal{E} -field measurement. (a) A \hat{y} polarized pulse of microwaves is broadcast down the beamline with power and duration adjusted to drive π -pulses $|H, J = 1, Y, \mathcal{N}\rangle \rightarrow |H, J = 2, M = 0\rangle$. Molecules are only in the H state between the pump and probe beams. Therefore, the observed signal (inset) shows depletion only for molecules between these lasers when the microwave pulse arrives. (b) The relevant levels for the \mathcal{E} -field measurement scheme. States in the $(|X\rangle, |Y\rangle)$ basis couple to (\hat{x}, \hat{y}) laser and microwave polarizations.

The procedure to measure \mathcal{E} -fields is similar to that for the Raman measurement, using a Stark shift sensitive transition to deplete a single spin quadrature. Again, we write the $|H, J = 1, |M| = 1, \mathcal{N}\rangle$ states in the same $|X\rangle, |Y\rangle$ basis introduced in Equation 6.5. The procedure is as follows:

1. Ground state population is transferred to the $|H, J = 1\rangle$ state by optically pumping with 943 pump laser. An AOM is added to the beam path which allows strobing the 943 laser, creating packets of H state molecules at precisely

defined times.

2. A pulse of \hat{y} polarized microwaves transfers population from $|H, J = 1, Y, \mathcal{N}\rangle$ to the Stark shift insensitive $|H, J = 2, M = 0\rangle$ state if the microwave frequency is near resonance ($\nu_\mu \approx 4B$). These transitions exhibit \mathcal{E} -field dependence $d\nu/d\mathcal{E} = D_{H,1}/h$ due to the differential Stark shift between the states (Figure 6.6b).
3. The probe (with modulated polarization) measures population in both the $|X\rangle$ and $|Y\rangle$ quadratures in the usual way. Therefore, the undisturbed population in the $|X\rangle$ quadrature provides normalization for the depletion signal in $|Y\rangle$ when we compute the asymmetry.
4. The microwave frequency is changed, and the experiment is repeated on successive beam pulses. An asymmetry versus frequency resonance is built up, and repeated for different $\tilde{\mathcal{N}}$ and $\tilde{\mathcal{L}}$ states.

The molecule pulse is spatially about twice as long as the $d = 23$ cm distance between the pump and probe lasers, the only region where molecules are actually in the H state. Therefore, the fluorescence trace exhibits a “burned out” hole, with a rising edge at the microwave pulse trigger time and observed duration $\sim \bar{v}d$ (Figure 6.6a). The microwave pulse traverses the interaction region in a fraction of a millisecond, so all molecules in the region are simultaneously excited to $|J = 2\rangle$. The local Stark shift $\Delta_{\text{st}}(x)$ is imprinted on the transferred population, which is then temporally resolved as the molecules transit the probe laser. The resulting scans of frequency and field plates can be visualized as a contour plot (Figure 6.7).

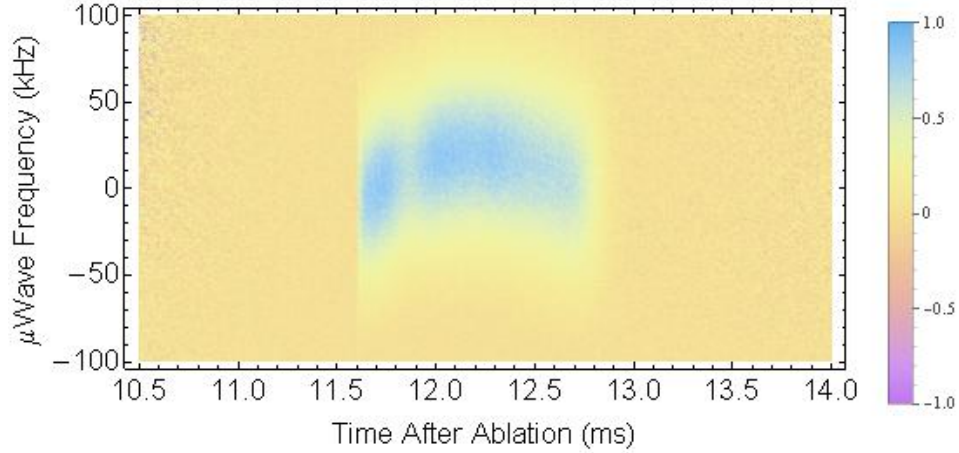


Figure 6.7: Measurements of asymmetry (color scale) versus microwave frequency (ν_μ) and time after ablation. Grouping the data by arrival time at the probe laser provides information about the spatial dependency of the \mathcal{E} -field.

Prior knowledge of the molecule pulse’s velocity profile can be used to back out the position dependence of each point. For a short excitation pulse, the spatial resolution depends on the width σ_v of the velocity distribution, which is typically $\sigma_v/\bar{v} \approx 10\%$. For the slowest molecules excited close to the state preparation lasers, the resulting spatial resolution is $d(\sigma_v/\bar{v}) \approx 1$ cm. We chose a microwave pulse width $\delta t_\mu = 40 \mu\text{s}$, which sets a uniform spatial resolution of $\delta t_\mu \bar{v} \approx 1$ cm across the precession region.

By strobing the pump laser (Figure 6.8), more precise timing information could be used as an independent determination of the excitation position of the molecules. The time difference between creation and detection of a molecule packet is inversely proportional to its velocity, which determines its relative position within the field plates. This technique was also utilized for extracting precise precession timing for the g -factor measurements in [9, 80]. By scanning the relative delay of the pump laser and microwave pulses, we can excite the molecule packets at arbitrary positions

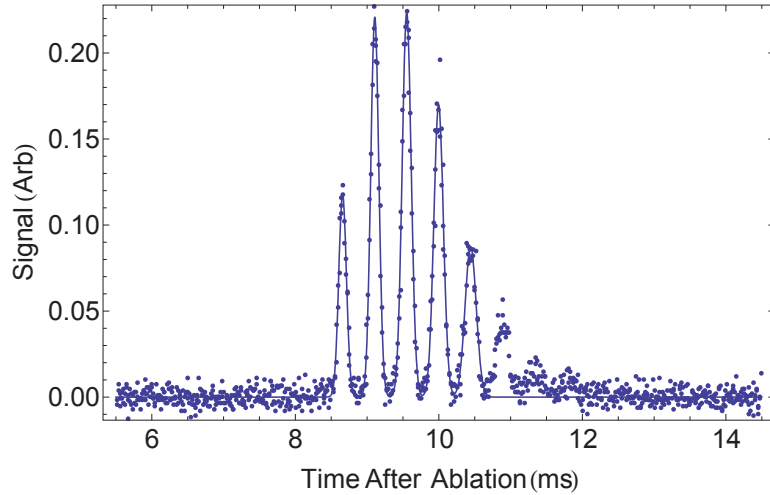


Figure 6.8: Strobed fluorescence signal used for extracting molecule velocity distributions. The first five pulses were fit to Gaussians, and line-centers were extracted to precisely measure precession times and beam velocity.

within the field plates. This technique confirmed the data taken with continuous pump lasers, but had worse signal to noise because many molecules were “thrown away” between laser pulses. Therefore, the CW technique proved a more versatile for mapping the \mathcal{E} -fields with minimal averaging.

A parity sum analysis allows us to extract all \mathcal{E} -field correlations of interest from microwave resonance scans. The microwave transition frequencies are

$$\nu_\mu = f_0 + \frac{D_{H,1}}{h} |\mathcal{E}| \tilde{\mathcal{N}}. \quad (6.27)$$

As the Raman data confirmed, $\mathcal{E}_z^\mathcal{E} \ll |\mathcal{E}_z^0|$ and $\mathcal{E}_z^\mathcal{L} \approx 0$, which requires that $\mathcal{E}_{\text{int}}^{\text{nr}} = \mathcal{E}_z^{\mathcal{E}\mathcal{L}}$. If we are only interested in measuring patch potentials $\mathcal{E}_{\text{int}}^{\text{nr}}(x)$ it is sufficient to only use the $\tilde{\mathcal{L}}$ switch. Eliminating the $\tilde{\mathcal{E}}$ switch from our data set, Equation 6.28 should be rewritten as

$$|\mathcal{E}_z| = |\mathcal{E}_z^0| + \mathcal{E}_{\text{int}}^{\text{nr}} \tilde{\mathcal{L}}. \quad (6.28)$$

The parity sum components then yield the interesting quantities

$$\nu_{\mu}^0 = f_0 = 4B \quad (6.29)$$

$$\nu_{\mu}^{\mathcal{N}} = \frac{D_{H,1}}{h} |\mathcal{E}_z^0| \quad (6.30)$$

$$\nu_{\mu}^{\mathcal{L}} = 0 \quad (6.31)$$

$$\nu_{\mu}^{\mathcal{NL}} = \frac{D_{H,1}}{h} \mathcal{E}_{\text{int}}^{\text{nr}} \quad (6.32)$$

The data confirmed that Equation 6.31 holds, and therefore the model of Equation 6.28 is consistent with the Raman data. The results from Equations 6.30 and 6.32 are discussed and plotted in Section 6.4.

6.4 A Comparison of \mathcal{E} -Field Maps

Ultimately, these various techniques allow us to generate self-consistent maps of the \mathcal{E} -field distribution. In addition to Raman and microwave measurements, additional data about the electric field distribution can be gleaned from interferometric studies of the field plate spacing. A Michelson interferometer remote gauge (MIRG) can determine the distance between partially reflective surfaces by detecting interference as one arm of the interferometer is scanned by a distance equal to the plate spacing [146]. The linewidth of the measurement is roughly equal to the the coherence length of the light source. Our light source was a diode (QPhotonics QSDM-620-2) that produced $\sim 20 \mu\text{m}$ wide interference maxima, but with ample signal to noise to allow line-center fitting to $< 1 \mu\text{m}$. The ultimate resolution is determined by the step accuracy of the translation stage, which allowed us to make spacing measurements to accuracies of $\sim 1 \mu\text{m}$. This system was built by Ivan Kozyryev, and measurements of

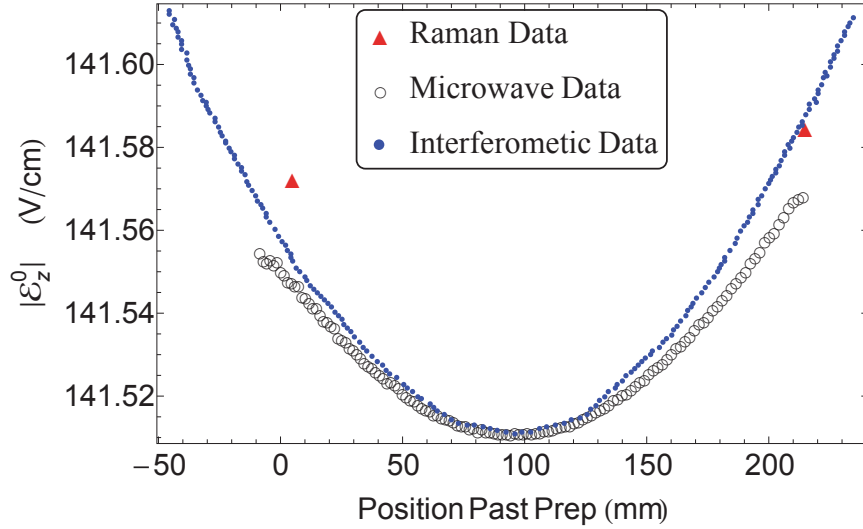


Figure 6.9: Map of \mathcal{E} -field magnitude in the interaction region. Errors bars are not shown. Statistical error bars are a part in a million of Δ_{st} , but the 0.1% uncertainty in $D_{H,1}$ would make the error bars greater than the scale of this plot.

the spacing between ACME’s ITO coated field plates were performed by Ben Spaun.

Reflection off the ITO coated surfaces provides a strong signal for measurement of the absolute plate separation. By placing the interferometer and light source on translation stages in the \hat{x}, \hat{y} directions, scans of the field plate spacings allowed us to optimize the parallelism of the electric field plates. It was discovered that there was a permanent bow of $\sim 20 \mu\text{m}$ across the surface of one or both plates. The field plates’s orientation was tuned such that a maximum in the plate spacing was centered on the ThO beamline. This made the electric field at the prep and probe regions as similar as possible, which was important for eliminating any potential systematics due to omega doublet detunings ($\Delta^{\mathcal{N}}$). These measurements were made before pumping down the interaction region, with the assumption that the field plate assembly would not be affected by the change in pressure [106].

This map of the field plate spacing can then be converted to an electric field magnitude by

$$|\mathcal{E}_z^0|(x) = \frac{|V_E - V_W|}{d(x)} = \frac{|\Delta V|}{d(x)} \quad (6.33)$$

Figure 6.9 shows this $|\mathcal{E}_z^0|(x)$ map as compared to the values extracted from the microwave and Raman measurements in the High- \mathcal{E} field configuration. The electric field values V_E, V_W are those recorded by the data acquisition system, which agreed for all data sets analyzed with $\Delta V = 353.635 \pm 0.003$ V. The bow in the field plates is apparent, but the electric field at prep/probe regions (0 and 22 cm) does agree to within ~ 10 mV/cm. Raman and microwave frequency splitting measurements are converted to \mathcal{E} -field values by dividing by $2D_{H,1}/h$ and $D_{H,1}/h$ respectively. The value of $2D_{H,1}/h = 2.06315$ MHz/(V/cm) (within the statistical error of Equation 6.38) has been fine tuned to eliminate frequency shifts between the interferometric and microwave data in Figure 6.9. The velocity profile was calibrated so the figure reproduced the known 23 cm distance between pump and probe.

The Raman and microwave measurements of $|\mathcal{E}_z^0|(x)$ agree to within ~ 20 mV/cm, or a part in 10^4 . A potential systematic in this measurement could come from $\tilde{\mathcal{N}}$ odd ac Stark shifts from the microwaves or Raman lasers. The ac Stark shift for upper/lower states coupled by a dipole radiation field with Rabi frequency Ω and detuning Δ is $\delta\nu_{U/L} = \pm\Omega^2/(4\Delta)$ [126, 130]. Since the microwaves are driven on resonance, there should be no related ac Stark shift. However, the non-zero one-photon detuning Δ_R of the Raman beams will cause a Stark shift for each H state omega doublet, $|1, X\rangle$ and $|2, X\rangle$. This shift will be common mode, but different intensities of each Raman frequency component will create an imbalance in Rabi

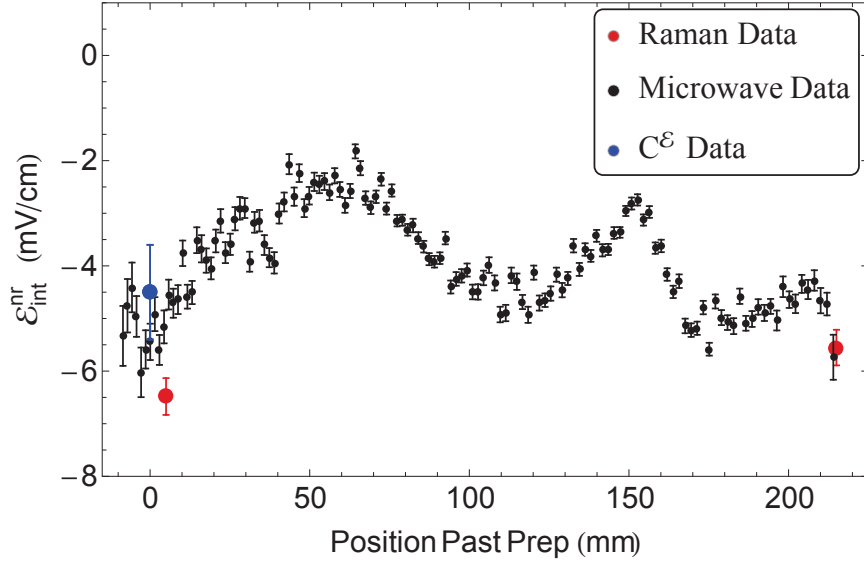


Figure 6.10: Map of \mathcal{E}^{nr} in the interaction region. Identical calibrations are applied to the data as the $|\mathcal{E}_z^0|(x)$ map (Figure 6.9). The state preparation and probe lasers are centered at 0 mm and 220 mm respectively.

frequencies $\Delta\Omega = \Omega_1 - \Omega_2$. Differential ac Stark shifts would contribute an offset to the omega double frequency splitting

$$\delta\Delta_{\text{st}} = \frac{\Omega_{\text{avg}}\Delta\Omega}{\Delta_R}. \quad (6.34)$$

For sufficiently large Rabi frequencies of $\Omega_{\text{avg}} \sim 1$ MHz and $\Delta_R = 2.5$ MHz, poor power balance between our Raman AOMs would lead to shifts of order 100 kHz, comparable to the observed offset between Raman and microwave measurements. While a measurement of $\delta\Delta_{\text{st}}$ as a function of Δ_R should have revealed such a systematic, studies of this effect were inconclusive, perhaps because the output power of the fiber amplifier and therefore Ω_{avg} was poorly controlled. Future studies should be made with a better stabilized Ω_{avg} and $\Delta\Omega$ in order to explore this systematic effect.

While the $|\mathcal{E}_z^0|(x)$ map provides an important calibration of these measurements, it is ultimately the $\mathcal{E}_{\text{int}}^{\text{nr}}$ values at the prep and probe regions that will determine the

\mathcal{E}^{nr} dependent systematics. Figure 6.10 compares these measurements with the $\mathcal{C}^{\mathcal{E}\mathcal{L}}$ contrast channel of the Δ_{prp} IPV superblocks, acquired in an interleaved fashion with the final data set (Section 5.1.2). An analysis similar to that discussed in Section 6.2.4 for side-of-fringe data was used to convert these measurements to contrast line-center shifts, and the corresponding \mathcal{E}^{nr} was calculated using $D_{H,1}$ [105]. The small magnitude ($\mathcal{E}_{\text{int}}^{\text{nr}} < 10 \text{ mV/cm}$) and small difference between the prep and probe regions meant the shifts associated with \mathcal{E}^{nr} systematics were limited to the $\delta d_e < 10^{-29} \text{ e}\cdot\text{cm}$ level (see Table 7.1).

Ultimately, all these measurements provided a wide range of independent consistency checks. The Raman technique has the advantage of having higher \mathcal{E} -field sensitivity and spatial resolution ($\sim 1 \text{ mm}$). On the other hand, the microwave map of $|\mathcal{E}_z|(x)$ eliminates the possibility of large geometric phases caused by rapidly changing \mathcal{E}^{nr} in regions that the Raman measurement cannot probe. Each measurement has its own systematics; microwave resonances are sensitive to “ghost resonances” due to Doppler shifted reflections of microwave pulses, while Raman measurements are more sensitive to ac Stark shift systematics as discussed above. The fact that all these measurements agree to within a few mV/cm gives us confidence in our prescribed \mathcal{E}^{nr} error bar.

6.5 Measuring H and C State Molecule Fixed Dipole Moments

The precise spacing measurements and careful voltage monitoring of the field plate allows us to extract the molecule fixed dipole moments for the H and C states much more accurately than before [97]. We measure the dipole moment $D_J = \frac{D_{\parallel}}{J(J+1)}$ via the dc Stark splitting between the omega doublet states

$$\Delta_{\text{st}} = \sqrt{\Delta_{\Omega}^2 + \left(2D \frac{\Delta V}{d}\right)^2} \quad (6.35)$$

for field plate voltage difference ΔV and spacing d . Stark splittings are measured where there is optical access, in the state preparation and probe regions of the electric field plates. Interferometer measurements indicate the field plate spacing $d = 2.498 \pm 0.001$ cm is almost identical in these two areas, but I include a conservative uncertainty estimate equal to the 10 μm amplitude of the plate spacing bow. The voltage is measured by a 6.5 digit multimeter, but we assume a conservative error of $\delta V = 0.1$ V because the DMM has not been recently calibrated.

The C state Stark splitting was measured by driving the $|H, J = 1, M = 0\rangle \rightarrow |C, J = 1, M = \pm 1\rangle$ optical resonance over a wide range of electric fields. The shift was monitored by taking scans across the Doppler broadened resonance as ΔV was increased. The frequency shift was measured by the voltage to frequency conversion of our laser locking transfer cavities [80], and agreed with the coarser measurement from our WSU-30 wavelength meter (10 MHz resolution). By fitting to Equation 6.35 (Figure 6.11), we could extract both the Δ_{Ω} and D_J for the C state. The extracted value of Δ_{Ω} differs from other measurements [147, 9] by 3%, so we apply a conservative

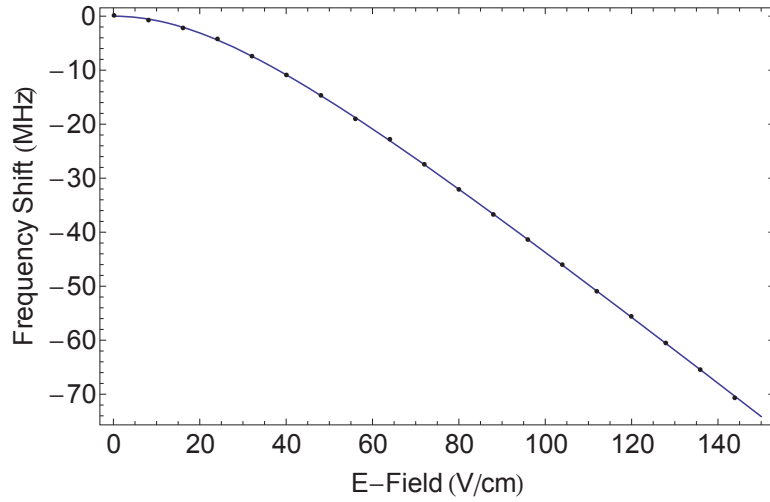


Figure 6.11: Fit to determine the dipole moment of the $|C, J = 1, M = \pm 1\rangle$ states from dc Stark shift data.

error bar with the same relative uncertainty to $D_{H,1}$. We find that

$$D_{\parallel,C} = 2.53(7) D = 1.00(3) e \cdot a_0, \quad (6.36)$$

so that in the $J = 1$ state

$$D_{C,1} = 0.63 \pm 0.02 \text{ MHz}/(\text{V}/\text{cm}). \quad (6.37)$$

The H state Stark splittings were measured most accurately from the Raman and microwave data discussed above. Both techniques restricted the probe laser's frequency to the normal values for either High- \mathcal{E} or Low- \mathcal{E} data acquisition. Therefore, we measured Stark splittings only at $\mathcal{E} = 141, 36 \text{ V}/\text{cm}$, but the $< 100 \text{ kHz}$ precision of these frequency measurements still allows us measure D_H with 0.1% precision. Comparing Raman data taken in the state preparation and probe regions, and microwave data taken at High- \mathcal{E} and Low- \mathcal{E} , all measurements are consistent with a H state $J = 1$ dipole moment of

$$D_{H,1} = 1.0315 \pm 0.0008 \text{ MHz}/(\text{V}/\text{cm}) \quad (6.38)$$

or a molecule fixed dipole moment

$$D_{\parallel,H} = 4.098(3) \text{ D} = 1.612(1) e \cdot a_0. \quad (6.39)$$

The measurement error includes the quadrature sum of the fractional uncertainty on d and ΔV in addition to a conservative systematic measurement uncertainty of $\delta\nu = 100$ kHz. This $\delta\nu$ accounts for the systematics on the Raman and microwave measurements discussed in Section 6.4. Note that this value is $> 3\sigma$ from the measurement reported in [97]. The error bar in the previous measurement was likely underestimated for the several reasons. The laser frequency was calibrated with the transfer cavity lock, and we now know that the calibration could be worse than the 1% quoted. Moreover, it is likely that the uncertainty in the measured field plate spacing was greater than the quoted 0.05 mm given their lack of interferometric measurements. Also, there no uncertainty was quoted for the applied voltage.

Chapter 7

Systematic and Statistical Limits

After completing assembly of the ACME apparatus and implementation of the software control system, the following 20 month period was dedicated to the diagnosis of systematics in the experiment. Testing for systematics involved performing “intentional parameter variations” (IPVs), where the measured values of $\omega^{\mathcal{N}\mathcal{E}}$ were correlated with controlled adjustment of various experimental “knobs”. Typically an IPV study was run for one day’s worth of data, and only explored further if correlations with the EDM measurement, or other interesting phase parity channels, were observed. As a result of these studies, we were able to continually adjust the optical system and data acquisition interface in order to reduce unwanted effects, without ever being forced to open the vacuum chamber. Our blinded data analysis removed the dangers of experimental bias during this process. All measured EDM systematics were demonstrated to be consistent with the model described in this chapter, and were reduced to below the final statistical precision.

The statistical error bar reported in our final result of $d_e = (-2.1 \pm 3.7_{\text{stat}} \pm$

$2.5_{\text{sys}}) \times 10^{-29} e \cdot \text{cm}$ was extracted from approximately 16 million ablation pulses¹ measured over the course of 2 weeks of nearly round the clock operation of the experiment. Data acquisition was subdivided into $\sim 10^4$ “blocks” of independent EDM measurements and ~ 300 longer “superblock” cycles for systematic suppression, as described in Chapter 5. The systematic error budget was a combination of the results of selected IPV studies performed actively during this final data set, and uncertainty upper bounds based on a longer list of IPV measurements acquired before the published data set (Appendix E). Data taken during IPV superblocks was used only for evaluating systematic shifts and uncertainties.

7.1 The \mathcal{E}^{nr} and $\Omega_r^{\mathcal{N}\mathcal{E}}$ Systematics

We identified two parameters that systematically shift the value of $\omega^{\mathcal{N}\mathcal{E}}$ within our experimental resolution, both of which couple to the ac Stark shift induced by the lasers. AC Stark shifts are of course unavoidable in a system where a transition is being strongly driven towards saturation, as is the case for our 1090 nm state preparation and probe lasers on the $H \rightarrow C$ transition. However, the light shifts must have some unique properties in order to mimic an EDM. There must be a relative shift between the $|M = +1\rangle$ and $|M = -1\rangle$ sublevels in order to generate a phase. Such an effect is not hard to imagine if the laser has a non-zero circular polarization component, so that one M sublevel is light shifted more strongly than another. Circular polarization gradients capable to generating a differential phase have been observed in both state preparation and probe lasers (Section 4.3).

¹About 8 billion detected photoelectrons.

In order to appear like an EDM phase in our analysis, this differential shift must reverse sign with changes in either the external electric field $\tilde{\mathcal{E}}$ or the optically selected molecule orientation $\tilde{\mathcal{N}}$. The ac Stark shift for the $H \rightarrow C$ transition is the ratio of the square of Ω_r , the Rabi frequency for this transition, divided by Δ , the detuning of the laser from resonance for this transition [126, 130]

$$\delta E_{ac} \propto \frac{\Omega_r^2}{\Delta}. \quad (7.1)$$

Therefore either a detuning Δ or Rabi frequency Ω_r that switch with $\tilde{\mathcal{N}}\tilde{\mathcal{E}}$ are capable of causing a systematic, and in fact we have observed both. We shall see that the former can be caused by the dc Stark shifts from a non-reversing electric field \mathcal{E}^{nr} , and the latter from a component of the Rabi frequency dependent on the molecule's orientation

$$\Omega_r = \Omega_r^0 + \Omega_r^{\mathcal{N}\mathcal{E}} \tilde{\mathcal{N}}\tilde{\mathcal{E}}. \quad (7.2)$$

The subtlety in these effects is that they are generated by coupling multiple experimental imperfections (e.g. \mathcal{E}^{nr} and circular polarization gradient) into a “higher order” EDM correlated systematic; a connection which took some time to deduce. Modeling of these systematics was lead by B. O’Leary and N.R. Hutzler [81], and the fundamental results are summarized below.

7.1.1 Modeling the AC Stark Shift Phases

As described above, the ac Stark shift phases are generated by differential coupling of the $|M = +1\rangle$ and $|M = -1\rangle$ states to the C state, which is best analyzed in the

circular basis (LHC = $\hat{\epsilon}_+$, RHC = $\hat{\epsilon}_-$)

$$\hat{\epsilon}_{\pm} = \frac{\hat{x} \pm i\hat{y}}{\sqrt{2}}. \quad (7.3)$$

The general polarization state of our lasers is

$$\hat{\epsilon} = -\cos(\epsilon)e^{-i\theta}\hat{\epsilon}_+ + \sin(\epsilon)e^{i\theta}\hat{\epsilon}_- \quad (7.4)$$

where θ and ϵ are respectively the laser's linear and circular polarization angles (see Appendix B.1 for definitions). We consider the system of the $|C, J = 1, M = 0\rangle$ state coupled to the $|H, J = 1, M = \pm 1\rangle$ states by the 1090 nm laser as in Figure 7.1, which we will abbreviate to $|C\rangle$, $|+1\rangle$, and $|-1\rangle$ respectively. The $\hat{\epsilon}_{\pm}$ polarization component will drive the transition $|C\rangle \leftrightarrow |\pm 1\rangle$ with Rabi frequency $\Omega_{r,\pm}$. We then parameterize in terms of the total Rabi frequency $\Omega_r = \sqrt{\Omega_{r,+}^2 + \Omega_{r,-}^2}$, and in the proper rotating frame we can write the Hamiltonian for our 3 state system as

$$H = \begin{pmatrix} & |C\rangle & |+1\rangle & |-1\rangle \\ \Delta & -\frac{\Omega_r}{2}e^{-i\theta}\cos\epsilon & \frac{\Omega_r}{2}e^{i\theta}\sin\epsilon \\ -\frac{\Omega_r}{2}e^{i\theta}\cos\epsilon & \kappa & 0 \\ \frac{\Omega_r}{2}e^{-i\theta}\sin\epsilon & 0 & 0 \end{pmatrix}, \quad (7.5)$$

where Δ is the detuning from resonance, and $\kappa = 2\mu_B g_H \mathcal{B}_z / \hbar$ is the Zeeman shift. Here we have ignored any tiny energy level shift associated with the EDM since it is too small to affect our conclusion.

It is useful to operate in the dressed state picture, where we can diagonalize the Hamiltonian into dark ($|D\rangle$) and bright ($|B\rangle$) state eigenvectors. By definition, the laser does not connect the dark states to the C state $\langle C|\hat{\epsilon}|D\rangle = 0$. Therefore, the dark

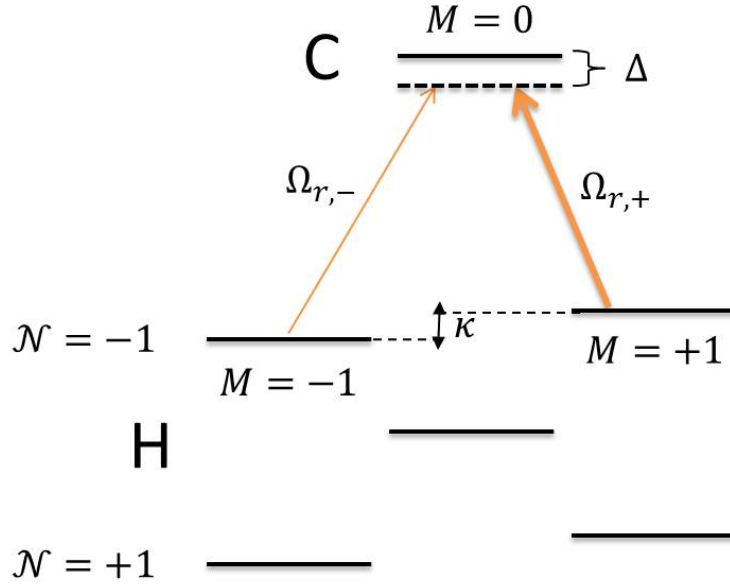


Figure 7.1: Relevant energy levels for prep and probe laser ac Stark shifts model, corresponding to the Hamiltonian in Equation 7.5. This diagram shows the coupling between $|C\rangle$ and the upper \mathcal{N} omega doublet manifold, but the equation applies to either \mathcal{N} state. Selecting the opposite \mathcal{P} state in C is equivalent to reversing our measurement basis $\theta \rightarrow -\theta$.

state eigenvector has no admixed $|C\rangle$ state amplitude, and also experiences zero ac Stark shift. For example, in the case of zero magnetic field $\kappa = 0$ and zero detuning $\Delta = 0$, the dark and bright states are

$$|D\rangle = \begin{pmatrix} 0, & e^{i\theta} \sin \epsilon, & e^{-i\theta} \cos \epsilon \end{pmatrix}, \quad (7.6)$$

$$|B_{\pm}\rangle = \frac{1}{\sqrt{2}} \begin{pmatrix} \pm 1, & -e^{i\theta} \cos \epsilon, & e^{-i\theta} \sin \epsilon \end{pmatrix}, \quad (7.7)$$

and the bright states have energy eigenvalues $E_{B_{\pm}} = \pm\Omega_r/2$. The C state decays off diagonally back down to the ground state at rate $\gamma = 2$ MHz, dumping population out of the three state system. Then for optical excitation rate $\Gamma \propto \Omega_r^2$, if a molecule interacts with the laser for time $\delta t \gg 1/\Gamma$, the bright state population will be completely depleted and we are left with a pure dark state.

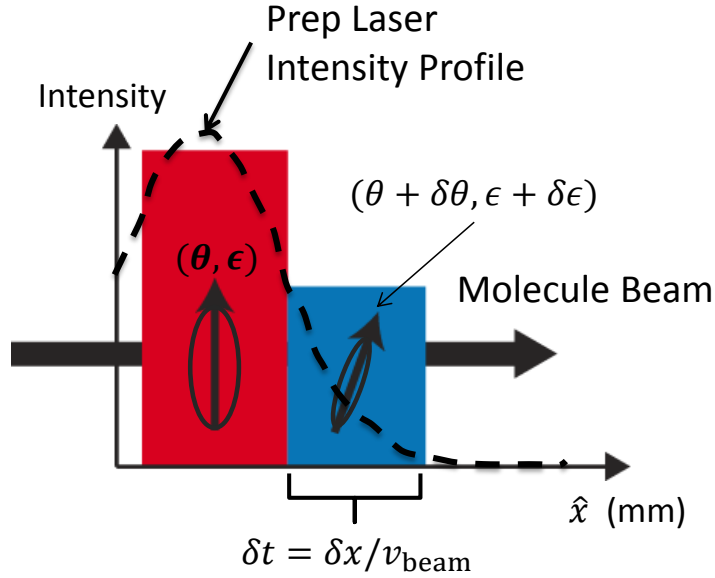


Figure 7.2: Diagram of intensity and polarization gradients in the state preparation laser beam. The intensity profile in our model is approximated as a step function. The polarization experiences both a linear angle and ellipticity angle gradient across the beam, depicted as a different polarization ellipse in each region.

We consider the effects of the ac Stark shift given two discrete regions with different laser intensities, and therefore different Rabi frequencies, as an approximation to our Gaussian beam shapes (Figure 7.2). The molecules first pass through the higher intensity region, where the laser has linear and circular polarization angles θ and ϵ . The thermal birefringence in the field plates creates a polarization gradient across the laser wave front, which rotates the polarization in the less intense region to $\theta + \delta\theta$ and $\epsilon + \delta\epsilon$. Notice that the polarization rotation $\delta\theta = (\partial\theta/\partial x)\delta x$ and $\delta\epsilon = (\partial\epsilon/\partial x)\delta x$ depends on both these gradients and the width of the less intense region δx . The spatial intensity and polarization gradients in the state preparation and probe lasers have been thoroughly characterized as discussed in Chapter 4.

The first region has intensity large enough to saturate the $H \rightarrow C$ transition, so the bright states decay away and we are left with a pure dark state as described above. In the second region $\delta t \Gamma \ll 1$, so the intensity is not sufficient to prepare a dark state. Since the polarization in this region is different, our initial dark state will be projected into a new bright and dark state basis of $|B'_{\pm}\rangle$ and $|D'\rangle$. The dark state and bright state terms in the resulting superposition interact differently with the light, the latter experiencing a Δ and Ω_r dependent ac Stark shift to its energy ($E_{B'_{\pm}} = \delta E_{ac}$). Our initial dark state will evolve under the influence of these shifts according to

$$|D(\delta t)\rangle = \sum_{j=D',B'_{\pm}} e^{-iE_j\delta t} \langle j|D\rangle |D\rangle. \quad (7.8)$$

To calculate the evolution of $|D(\delta t)\rangle$, we must diagonalize the general Hamiltonian in Equation 7.5 to find the bright energy eigenvalues and compute the overlap between rotated bright and dark state eigenvectors. We emphasize that the evaluation of Equation 7.8 will depend on experimentally controllable parameters $(\Delta, \Omega_r, \mathcal{B}_z, \delta\theta, \delta\epsilon, \delta t)^2$, where $\delta t = \delta x/v_{\text{beam}}$ is the fly-through interaction time with the weak laser field. There will be no evolution of $|D(\delta t)\rangle$, and therefore no ac Stark shift systematics, if all of these parameters are small. By reducing the size of polarization gradients $(\partial\theta/\partial x, \partial\epsilon/\partial x)$ and by shaping the lasers to decrease the interaction time δt , we are able to largely eliminate our sensitivity to light shift induced phases (see Chapter 4). Likewise, our ability to measure the EDM correlated detuning $\Delta^{\mathcal{N}\mathcal{E}}$ and Rabi frequency $\Omega_r^{\mathcal{N}\mathcal{E}}$ allows us to place limits on phase evolution that contributes to systematic errors.

²The energy of the bright states largely depends on the first three parameters, $E_{B'_{\pm}}(\Delta, \Omega_r, \mathcal{B}_z)$ while the overlap between the two polarization bases mostly depends upon of $(\delta\theta, \delta\epsilon)$.

To determine the particular functional dependence on these parameters, we must continue to evolve the state after it exits the state preparation laser. The phase ϕ of the $|M = \pm 1\rangle$ states evolves through the interaction region according to Zeeman and EDM interactions, and at the probe laser we measure in a $\pi/4$ rotated basis for maximal sensitivity (Section 2.1). We then calculate the asymmetry \mathcal{A} , and divide by the contrast $\mathcal{C} = d\mathcal{A}/d\phi$ to compute the phase $\phi = \mathcal{A}/2\mathcal{C}$, which yields the following expression [81, 148, 107]

$$\begin{aligned} \phi_{ac} = & \cos\left(\frac{\Omega_e \delta t}{2}\right) (\delta\theta \cos(\Delta\delta t/2) - \delta\epsilon \sin(\Delta\delta t/2)) + \frac{\delta\epsilon\Delta}{\Omega_e} \cos(\delta\delta t/2) \sin(\Omega_e \delta t/2) \\ & - \frac{\kappa}{\Omega_e} \left[\left(1 + 2\frac{\Delta^2}{\Omega_e^2}\right) \cos(\Delta\delta t/2) \sin(\Omega_e \delta t/2) - 2\frac{\Delta\Omega_e}{\Omega_r^2} \cos(\Omega_e \delta t/2) \sin(\Delta\delta t/2) \right], \end{aligned} \quad (7.9)$$

where $\Omega_e = \sqrt{\Delta^2 + \Omega_r^2}$.

This result can be analyzed in a few limits relevant for the systematics observed in the ACME experiment. In particular, we are interested in how the measured phase changes with respect to the detuning Δ and deviations in the Rabi frequency $\Omega_r = \Omega_r^0 + \delta\Omega_r$. Expanding around small $\Delta \ll \Omega_r$ and $\delta\Omega_r \ll \Omega_r^0$, we find the ac Stark shift induced phase shifts can be parameterized as

$$\phi_{ac} = \alpha\Delta + \alpha^{\mathcal{B}}\mathcal{B}_z\Delta^2 + \beta\delta\Omega_r + \beta^{\mathcal{B}}\mathcal{B}_z\delta\Omega_r. \quad (7.10)$$

The first and third terms are what cause the \mathcal{E}^{nr} and $\Omega_r^{\mathcal{N}\mathcal{E}}$ systematics. We separate the \mathcal{B} odd components into separate terms because they will not appear as EDM systematics, except at higher order [81].

The coefficients α and β we leave as parameters to measure in experimental IPV data sets. The model predicts them to have the following dependence on Δ , Ω_r^0 , $\delta\epsilon$,

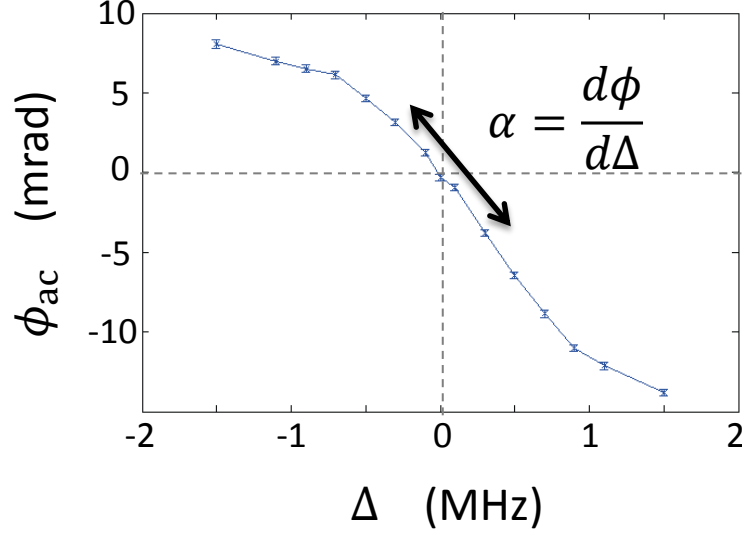


Figure 7.3: AC Stark shift induced phase as a function of detuning. For this particular set of experimental parameters, the laser polarization is aligned to maximize the circular gradients $\partial\epsilon/\partial x$, generating a light shift phase parameter $\alpha = 10$ mrad/MHz. Considering our $\mathcal{E}^{\text{nr}} \approx 5$ mV/cm induces a $\Delta^{\mathcal{N}\mathcal{E}} \approx 5$ kHz, this would have led to a systematic $10\times$ greater than our final error bar.

and $\delta\theta$ to leading order in δt

$$\alpha \propto \delta\epsilon (\Omega_r^0 \delta t)^2 \delta t, \quad (7.11)$$

$$\alpha^{\mathcal{B}} \propto \frac{g_H \mu_B}{\hbar} \frac{\delta t^3}{(\Omega_r^0 \delta t)^2}, \quad (7.12)$$

$$\beta \propto \delta\theta (\Omega_r^0 \delta t) \delta t + \delta\epsilon \Delta (\Omega_r^0 \delta t) \delta t^2, \quad (7.13)$$

$$\beta^{\mathcal{B}} \propto \frac{g_H \mu_B}{\hbar} (\Omega_r^0 \delta t) \delta t^2. \quad (7.14)$$

We have observed all of these terms in the experiment. For example, in Figure 7.3 we observe the linear dependence of the measured phase on detuning near resonance, from which we can determine α . In addition, the ellipticity dependence of $\alpha(\delta\epsilon)$ has been carefully measured (Figure 7.5). Under our experimental conditions we expect $\delta\epsilon \gg \delta\theta$ (Section 4.3.2), from which the model correctly predicts $\alpha \gg \beta$ and that the

$\Omega_r^{\mathcal{N}\mathcal{E}}$ systematic is suppressed with respect to the \mathcal{E}^{nr} systematic. It is worth noting the strong dependence of all terms on the weak field interaction time δt . Specialized optics such as diffractive “flat-toppers” could potentially make the edge of our laser very sharp, thereby reducing the δt , and might prove very useful in reducing these ac Stark shift systematics.

7.1.2 Measurement of \mathcal{E}^{nr} Correlations

The first term of Equation 7.10 gives the detuning dependence of the ac Stark shift phase ϕ_{ac} . If this term is dominant, then a detuning correlated with $\tilde{\mathcal{N}}\tilde{\mathcal{E}}$ switches ($\Delta^{\mathcal{N}\mathcal{E}}$) would lead directly to a EDM-mimicking systematic,

$$\omega^{\mathcal{N}\mathcal{E}} = \frac{\alpha\Delta^{\mathcal{N}\mathcal{E}}}{\tau}. \quad (7.15)$$

Such a detuning can arise from a non-reversing electric field \mathcal{E}^{nr} due to patch potentials or voltage offsets (see Section 5.3), as illustrated in Figure 7.4. Our electric field measurements (Section 6.2.4)³ indicate that we can express the electric field magnitude as the sum of the average field magnitude $|\mathcal{E}_z^0|$ and the \mathcal{E}^{nr}

$$|\mathcal{E}_z| = |\mathcal{E}_z^0| + \mathcal{E}^{\text{nr}}\tilde{\mathcal{E}}. \quad (7.16)$$

Expressing the detuning in terms of the laser frequency (ω_l) and the molecular transition frequency (ω_m)

$$\begin{aligned} \Delta &= \omega_l(\tilde{\mathcal{N}}) - \omega_m(\tilde{\mathcal{N}}) = (\omega_{H-C} - \Delta_{\text{AOM}}\tilde{\mathcal{N}}) - (\omega_{H-C} - D_H|\mathcal{E}_z|\tilde{\mathcal{N}}) \\ &= (D_H|\mathcal{E}_z^0| - \Delta_{\text{AOM}})\tilde{\mathcal{N}} + D_H\mathcal{E}^{\text{nr}}\tilde{\mathcal{N}}\tilde{\mathcal{E}}, \end{aligned} \quad (7.17)$$

³The most general expression for the electric field is given by Equation 5.23. For the discussion in this chapter, the odd parity under the $\tilde{\mathcal{L}}$ switch will be implied and our notation modified such that $\mathcal{E}^{\mathcal{E}\mathcal{L}}\tilde{\mathcal{E}}\tilde{\mathcal{L}} \rightarrow \mathcal{E}^{\text{nr}}\tilde{\mathcal{E}}$. We adopt this notation because $\tilde{\mathcal{L}}$ is a superblock switch.

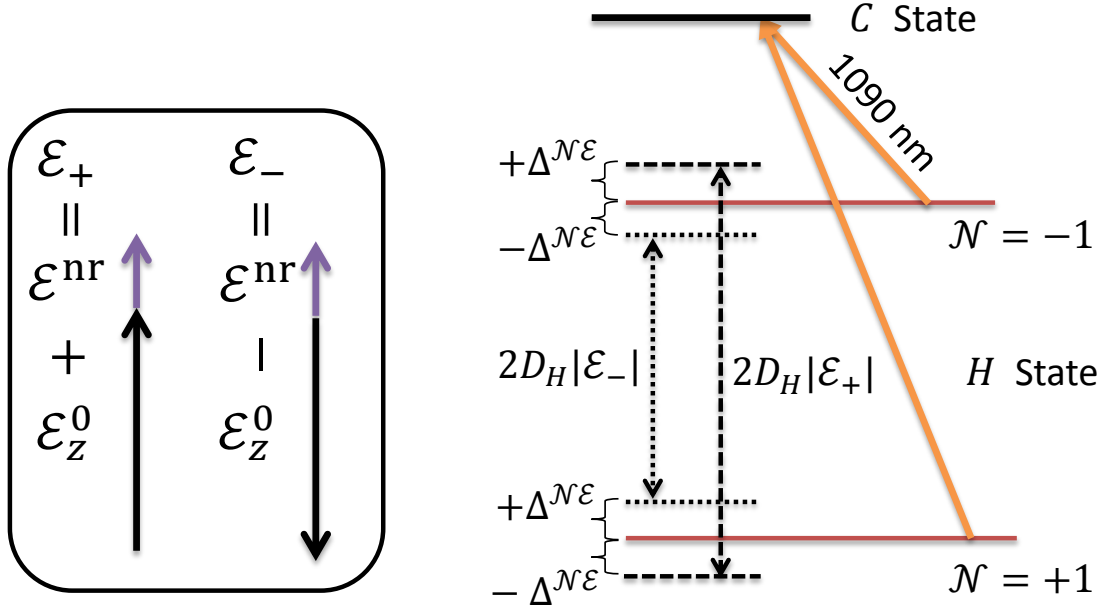


Figure 7.4: Diagram depicting how a non-reversing electric field \mathcal{E}^{nr} can generate an EDM correlated detuning $\Delta^{\mathcal{N}\mathcal{E}}$. At left we show how patch potentials \mathcal{E}^{nr} add to an ideally reversing field component $|\mathcal{E}_z^0|\tilde{\mathcal{E}}$ to produce state dependent electric field magnitudes $|\mathcal{E}_+| > |\mathcal{E}_-|$. At right, an energy level diagram of H and C states shows how the detuning reverses sign when either the $\tilde{\mathcal{E}}$ switch changes the dc Stark shift, or when the $\tilde{\mathcal{N}}$ switch tunes the state preparation or probe laser to the opposite omega doublet state.

and we see that $\Delta^{\mathcal{N}\mathcal{E}} = D_H \mathcal{E}^{\text{nr}}$. Note that the $\Delta^{\mathcal{N}\mathcal{E}}$ in Equation 7.17, could be corrected if we allow the frequency of the AOMs setting the $\tilde{\mathcal{N}}$ switch to be $\tilde{\mathcal{N}}\tilde{\mathcal{E}}$ correlated. This is in some sense equivalent to subtracting the known systematic shift from the EDM data, which was the approach we adopted in our data analysis [2, 105].

The “smoking gun” evidence supporting our model for the $\phi_{ac} = \alpha\Delta$ term was that it matched the functional dependence on laser power and polarization predicted by the thermal polarization gradients in the \mathcal{E} -field plates. Our light shift model predicts that α will be linearly proportional the circular polarization gradient according to Equation 7.11. The results of Section 4.3 demonstrate that the magnitude of circular

polarization gradients $\partial\epsilon/\partial x$ should be proportional to the laser power (P_l) and have a sinusoidal dependence on the input polarization angle

$$\frac{\partial\epsilon}{\partial x} \propto P_l \sin(2\theta). \quad (7.18)$$

By measuring detuning scans as in Figure 7.3, the phase sensitivity $d\phi/d\Delta$ as a function of detuning was extracted from linear fits. The state preparation laser detuning (Δ_{prp}) and the probe laser detuning (Δ_{prb}) could be independently controlled, allowing us to measure $d\phi/d\Delta$ for either laser. Assuming this slope is caused entirely from ac Stark shift induced phases, then $d\phi/d\Delta = \alpha(\theta_{\text{prp}}) \propto \partial\epsilon/\partial x$. The proper angular dependence is clear, as is the dependence on the prep power in the red and blue curves in Figure 7.5.

To first order, the ϕ_{ac} induced by the probe laser should cancel out in our calculation of the asymmetry.

$$\begin{aligned} \mathcal{A} &= \frac{S_X - S_Y}{S_X + S_Y} = \sin^2(\phi_0 + \phi_{ac,X}) - \cos^2(\phi_0 + \phi_{ac,Y}) \\ &\approx \phi_0 + \phi_{ac,X} + \phi_0 + \phi_{ac,Y} \\ \mathcal{A} &= 2\phi_0, \end{aligned} \quad (7.19)$$

where we have expanded the phase about $\phi_0 \approx \pi/4$, and used the fact that $\phi_{ac,Y} \propto \sin(2(\theta_X + \pi/2)) = -\phi_{ac,X}$. However, as shown in the black curve in Figure 7.5, we observed that the probe's detuning slope $d\phi/d\Delta_{\text{prb}}$ depends sinusoidally on the angle of the state preparation laser, but with a smaller amplitude and opposite sign than $d\phi/d\Delta_{\text{prp}}$. This was confirmed by tuning the $|\mathcal{B}_z|$ field magnitude and acquiring data with different amounts of magnetic phase precession ϕ . Our measurement always has a fixed relationship between the prep and probe angles such that $\phi - (\theta_{\text{prb}} - \theta_{\text{prp}}) \approx$

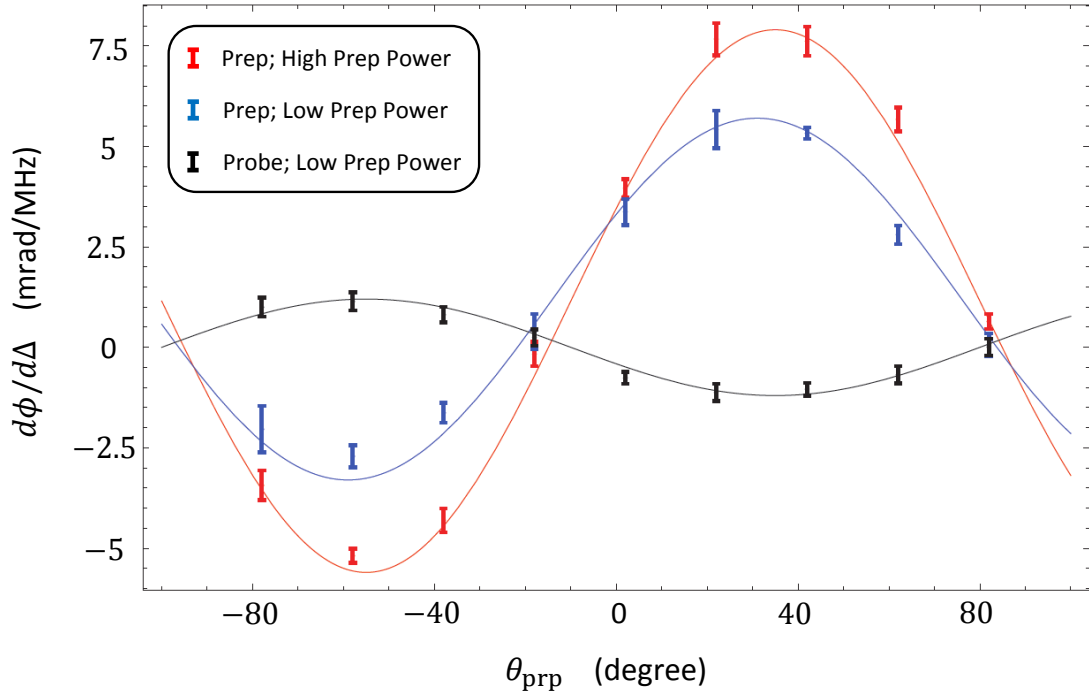


Figure 7.5: Sensitivity of ac Stark shift phases to prep laser angle. By rotating the polarization of the state preparation laser (θ_{prp}), the thermal birefringence generates polarization gradients with periodicity as predicted in Section 4.3.2. The sensitivity of ϕ_{ac} is measured with respect to detuning of either the prep laser (Δ_{prp}) or probe laser (Δ_{prb}).

$\pi/4(2n+1)$. For any value of $\theta_{\text{prb}} - \theta_{\text{prp}}$, the slope $d\phi/d\Delta_{\text{prb}}$ could always be predicted by θ_{prp} alone.

This effect is likely caused by a residual prep detuning phase imprinted on the Doppler distribution of our molecule beam. The molecule beam's transverse velocity distribution δv_z creates a transverse (\hat{z}) gradient of $\phi_{\text{ac}}(v_z)$ because each velocity class v_z sees a Doppler shifted prep laser detuning $\Delta(v_z)$. Depending on the detuning of the probe laser, subsets of the full distribution $\phi_{\text{ac}}(\delta v_z)$ are sampled, shifting the values of $\bar{\phi}_{\text{ac}}$ and generating the observed $d\bar{\phi}/d\Delta_{\text{prb}}$ effect. Measurements of $d\phi/d\Delta_{\text{prb}}$ were much noisier than $d\phi/d\Delta_{\text{prp}}$, which supports this hypothesis because the molecule

beam velocity distribution drifts by $\sim 10\%$ over the times scales necessary for these measurements. Additional details may be found in [105, 107].

7.1.3 Measurement of $\Omega_r^{\mathcal{N}\mathcal{E}}$ Correlations

The third term of Equation 7.10 can generate an EDM systematic correlated with a $\Omega_r^{\mathcal{N}\mathcal{E}}$ if the β coefficient is non-zero. The Rabi frequency for the $H \rightarrow C$ transition is defined as

$$\Omega_r = \frac{D_{H-C}}{\hbar} \sqrt{\frac{2I}{\epsilon_0 c}} \quad (7.20)$$

for laser intensity $I = P/A = \epsilon_0 c E^2/2$ and transition dipole moment D_{H-C} . The Rabi frequency Ω_r is proportional to $D_{H-C} \sqrt{P}$, so either an EDM correlated laser power $P^{\mathcal{N}\mathcal{E}}$ or transition dipole moment $D_{H-C}^{\mathcal{N}\mathcal{E}}$ could lead to a systematic. Photodiode monitors measured the $P^{\mathcal{N}\mathcal{E}}$ during the final data set, and the result was consistent with zero to within 1% of P^0 , small enough to not contribute to the systematic error bar at a significant level.

There is evidence that our molecule exhibits an inherent $D_{H-C}^{\mathcal{N}\mathcal{E}}$ large enough to cause an EDM systematic. Physically, this means the transition dipole moment depends on the orientation of the molecule, $\hat{n} = \tilde{\mathcal{N}}\tilde{\mathcal{E}}\hat{z}$, relative to the propagation direction of the laser \hat{k} . Measurements of a nonzero $\tilde{\mathcal{N}}\tilde{\mathcal{E}}$ -correlated fluorescence signal, $S^{\mathcal{N}\mathcal{E}}$, and an $\tilde{\mathcal{N}}\tilde{\mathcal{E}}\tilde{\mathcal{B}}$ -correlated phase, $\phi^{\mathcal{N}\mathcal{E}\mathcal{B}}$, both of which changed sign when we reversed \hat{k} , provided evidence for a nonzero $\hat{k} \cdot \hat{z}$ dependent $\Omega_r^{\mathcal{N}\mathcal{E}}$ (see details below). We hypothesize that this \hat{n} odd Rabi frequency is generated by interference between the electric and magnetic (E1 and M1) dipole transition amplitudes.

We can make a qualitative argument for the origin of $D_{H-C}^{\mathcal{N}\mathcal{E}}$ based on the form of

the operators [149, 150, 151]

$$\hat{O}_{E1} = k_E(\hat{\epsilon} \cdot \vec{r}), \quad (7.21)$$

$$\hat{O}_{M1} = k_M(\hat{k} \times \hat{\epsilon}) \cdot \vec{L}. \quad (7.22)$$

The E1 operator describes the coupling of the laser's electric field with polarization $\hat{\epsilon}$ to the electron's position \vec{r} (electric dipole moment), while the M1 operator couples the laser's magnetic field with polarization $(\hat{k} \times \hat{\epsilon})$ to the orbital angular momentum \vec{L} (magnetic dipole moment). The E1 and M1 operators have odd and even parity, respectively.

Both the H and C states have mixed parities in an electric field, so it plausible that the matrix elements $\langle C|\hat{O}|H, \mathcal{N} = +1\rangle$ and $\langle C|\hat{O}|H, \mathcal{N} = -1\rangle$ might have opposite sign, dependent on the parity of the operators. The transition dipole matrix element

$$D_{H-C} = \langle C|\hat{O}_{E1} + \hat{O}_{M1}|H, \mathcal{N}\rangle \quad (7.23)$$

will have a cross term that depends on this relative \mathcal{N} sign. This matrix element has been calculated in detail in [81, 148], and the authors conclude that this effect can generate a $D_{H-C}^{\mathcal{N}\mathcal{E}}$ given the proper phases between the E1 and M1 transition matrix elements. The ratio of the size of allowed E1 and M2 matrix elements is the fine structure constant, $\alpha \approx 1/137$, so a $D_{H-C}^{\mathcal{N}\mathcal{E}}$ generated by their interference is expected to be small [150].

We studied this effect directly by applying a $P^{\mathcal{N}\mathcal{E}}$ component to each of our laser beams, such that

$$P = P^0 + P^{\mathcal{N}\mathcal{E}}\tilde{\mathcal{N}}\tilde{\mathcal{E}}. \quad (7.24)$$

The EDM correlated phase sensitivity $d\phi^{\mathcal{N}\mathcal{E}}/dP^{\mathcal{N}\mathcal{E}} \propto \beta$ was generally consistent with

zero. The coefficient β is non-zero in the presence of a linear polarization gradient ($\partial\theta/\partial x$) or combined detuning and circular gradient $\Delta(\partial\epsilon/\partial x)$ according to Equation 7.13. Both effects are small, and we expect that $\beta \ll \alpha$, so the $\Omega_r^{\mathcal{N}\mathcal{E}}$ systematic is suppressed compared to \mathcal{E}^{nr} . It was difficult to measure this effect because we could only modulate the state preparation or probe laser's power by up to $\pm 20\%$ without degrading the signal or contrast. For comparison, in measurements of the \mathcal{E}^{nr} systematic the intentionally applied \mathcal{E}^{nr} was ~ 100 times the 5 mV/cm background value, which allowed us to quickly measure non-zero EDM sensitivity slopes $d\phi^{\mathcal{N}\mathcal{E}}/d\mathcal{E}^{\text{nr}}$.

Regardless of the mechanism that generated the $D_{H-C}^{\mathcal{N}\mathcal{E}}$, we were able to measure it using auxiliary measurements. The $\phi^{\mathcal{N}\mathcal{E}\mathcal{B}}$ phase will be correlated with a $\Omega_r^{\mathcal{N}\mathcal{E}}$ in a non-zero magnetic field (fourth term in Equation 7.10). Because $\beta^{\mathcal{B}} \gg \beta$ we could clearly observe an orientation dependent Rabi frequency in the $\phi^{\mathcal{N}\mathcal{E}\mathcal{B}}$ channel even when $d\phi^{\mathcal{N}\mathcal{E}}/dP^{\mathcal{N}\mathcal{E}}$ was consistent with zero. When applying a $P^{\mathcal{N}\mathcal{E}}$ with no detuning Δ and negligible amounts of \mathcal{E}^{nr} , the ac Stark shift dependence is

$$\begin{aligned}\phi_{ac} &= (\beta + \beta^{\mathcal{B}}|\mathcal{B}_z|\tilde{\mathcal{B}}) \left(D_{H-C}^0 + D_{H-C}^{\mathcal{N}\mathcal{E}}\tilde{\mathcal{N}}\tilde{\mathcal{E}} \right) \sqrt{P^0 + P^{\mathcal{N}\mathcal{E}}\tilde{\mathcal{N}}\tilde{\mathcal{E}}} \\ \phi_{ac} &\approx (\beta + \beta^{\mathcal{B}}|\mathcal{B}_z|\tilde{\mathcal{B}})\sqrt{P^0} \left(D_{H-C}^0 + D_{H-C}^{\mathcal{N}\mathcal{E}}\tilde{\mathcal{N}}\tilde{\mathcal{E}} \right) \left(1 + \frac{1}{2} \frac{P^{\mathcal{N}\mathcal{E}}}{P^0} \tilde{\mathcal{N}}\tilde{\mathcal{E}} \right),\end{aligned}\quad (7.25)$$

such that

$$\phi_{ac}^{\mathcal{N}\mathcal{E}\mathcal{B}} = \beta^{\mathcal{B}}|\mathcal{B}_z|\sqrt{P^0} \left(D_{H-C}^{\mathcal{N}\mathcal{E}} + \frac{D_{H-C}^0}{2} \frac{P^{\mathcal{N}\mathcal{E}}}{P^0} \right), \quad (7.26)$$

$$\phi_{ac}^{\mathcal{N}\mathcal{E}} = \beta\sqrt{P^0} \left(D_{H-C}^{\mathcal{N}\mathcal{E}} + \frac{D_{H-C}^0}{2} \frac{P^{\mathcal{N}\mathcal{E}}}{P^0} \right). \quad (7.27)$$

By using a fit to measurements of $\phi^{\mathcal{N}\mathcal{E}\mathcal{B}}$ as a function of $P^{\mathcal{N}\mathcal{E}}$, we can measure the value of $P^{\mathcal{N}\mathcal{E}}$ where $\phi_{ac}^{\mathcal{N}\mathcal{E}\mathcal{B}} = 0$, which occurs when

$$\frac{P_{eff}^{\mathcal{N}\mathcal{E}}}{P^0} = -2 \frac{D_{H-C}^{\mathcal{N}\mathcal{E}}}{D_{H-C}^0}. \quad (7.28)$$

The sensitivity slope of the EDM channel (S_P) is

$$S_P = \frac{d\phi^{\mathcal{N}\mathcal{E}}}{(dP^{\mathcal{N}\mathcal{E}}/P^0)} = \frac{\beta D_{H-C}^0 \sqrt{P^0}}{2} \quad (7.29)$$

Using these two measurements, we can calculate the shift to the EDM caused by the $\Omega_r^{\mathcal{N}\mathcal{E}}$ using

$$\Delta\phi^{\mathcal{N}\mathcal{E}} = S_P P_{eff}^{\mathcal{N}\mathcal{E}} = -\beta D_{H-C}^{\mathcal{N}\mathcal{E}} \sqrt{P_0}. \quad (7.30)$$

Using a measured value of $P_{eff}^{\mathcal{N}\mathcal{E}}/P^0 = -0.0158 \pm 0.002$, we were able to limit the systematic uncertainty in d_e from the $\Omega_r^{\mathcal{N}\mathcal{E}}$ systematic to the 10^{-29} e·cm level.⁴

7.2 Systematic Error Budget

To search for possible sources of systematic error, we varied more than 40 separate parameters and observed their effects on $\omega^{\mathcal{N}\mathcal{E}}$ and many other components of the phase correlated with $\tilde{\mathcal{N}}$, $\tilde{\mathcal{E}}$, or $\tilde{\mathcal{B}}$. These parameters were intentionally applied tunable imperfections, such as transverse magnetic fields or laser detunings (for a complete list see Appendix E). These tuned imperfections were applied concurrently with the 8 block and superblock switches, so that all the parity components were measured as a function of the imperfection. We typically weren't satisfied until we understood the behavior of $\omega^{\mathcal{N}}$, $\omega^{\mathcal{E}}$, $\omega^{\mathcal{N}\mathcal{E}\mathcal{B}}$, $\omega^{\mathcal{N}\mathcal{B}}$ and $\omega^{\mathcal{E}\mathcal{B}}$ with the varied parameter.

We assume that $\omega^{\mathcal{N}\mathcal{E}}$ depends linearly on each parameter Q , such that we may calculate the slope $S_Q = \partial\omega^{\mathcal{N}\mathcal{E}}/\partial Q$ and uncertainty δS_Q using a linear regression fit. Using auxiliary measurements we obtain the mean Q_0 and uncertainty δQ_0 of

⁴According to Equation 7.20, $P_{eff}^{\mathcal{N}\mathcal{E}}/P^0 = 2\Omega_r^{\mathcal{N}\mathcal{E}}/\Omega_r^0$, which is how the result was quoted in [2]: $\Omega_r^{\mathcal{N}\mathcal{E}}/\Omega_r^0 = (-8.0 \pm 0.8) \times 10^{-3}(\hat{k} \cdot \hat{z})$.

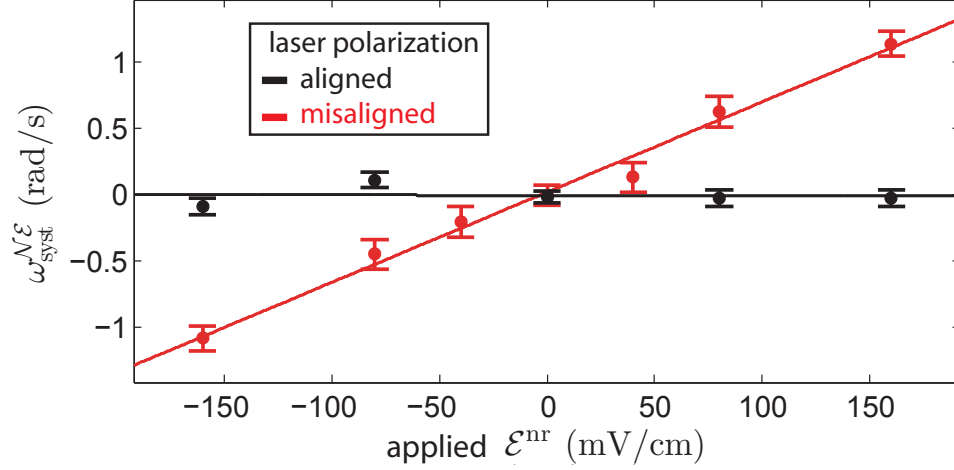


Figure 7.6: Eliminating the \mathcal{E}^{nr} systematic (Ref [2] Figure 3A). Red and black data points were taken with the prep laser polarization misaligned and aligned, respectively, with the birefringence axes of the electric field plates. This figure illustrates how we performed general IPV searches for systematics, applying an exaggerated parameter imperfection and assuming a linear response to $\omega^{\mathcal{N}\mathcal{E}}$. The slope of these curves $S_{\mathcal{E}^{\text{nr}}} = \partial\omega^{\mathcal{N}\mathcal{E}}/\partial\mathcal{E}^{\text{nr}}$ represent the sensitivity of our EDM measurement to \mathcal{E}^{nr} imperfections.

this parameter under ideal operating conditions. The systematic shift in $\omega^{\mathcal{N}\mathcal{E}}$ is $\Delta\omega^{\mathcal{N}\mathcal{E}} = S_Q Q_0$ and the uncertainty follows from Gaussian error propagation.

Figure 7.6 shows an example of the linearized fitting to determine the slope $S_{\mathcal{E}^{\text{nr}}}$ in the case of the \mathcal{E}^{nr} systematic. We chose to apply the systematic shift for a parameter if; (i) the slope S_Q was monitored throughout the data set, (ii) at some point there was an observed non-zero slope S_Q , and (iii) we have a physical model describing the systematic shift. If any of these conditions do not apply, we instead include an upper limit uncertainty

$$\delta\omega^{\mathcal{N}\mathcal{E}} = Q_0 \sqrt{(\delta S_Q)^2 + S_Q^2} \quad (7.31)$$

in our systematic error budget.

Given these assumptions, if we have good control over our IPV parameter, then

for maximum parameter imperfection ΔQ

$$\delta S_Q \approx \frac{\delta\omega_{\text{stat}}^{\mathcal{N}\mathcal{E}}}{\Delta Q}. \quad (7.32)$$

When there is no observed correlation with $\omega^{\mathcal{N}\mathcal{E}}$, it is advantageous to increase the size of the imperfection as much as possible to drive down δS_Q and therefore decrease $\delta\omega_{\text{syst}}^{\mathcal{N}\mathcal{E}}$. Therefore, there were a broad class of parameters that we could check at the 10^{-29} e-cm level after only one day of averaging by applying $\Delta Q > 10Q_0$. Other parameters we could not tune as broadly, and the uncertainty as calculated by Equation 7.31 would have been larger than the final statistical error bar. Without a justifiable model, observed correlation, or historical precedent for inclusion in our error budget, all of these less careful systematic studies were excluded. I note that uncertainty on the measurement of a slope parameter depends on our statistical precision per root day. Therefore, adopting these same systematic error analysis techniques in future ACME generations, we expect most systematic error limits should be decreased by improved statistics alone.

7.2.1 Observed EDM Correlated Systematics

There were only three IPV studies for which we observed a systematic slope S_Q that was greater than zero to statistical significance 3σ . For all three, we have a well understood model for the existence of the EDM correlation. Two are due to the ac Stark shifts, discussed in detail in Section 7.1. By intentionally exaggerating these parameters, we verified that both \mathcal{E}^{nr} and $\Omega_r^{\mathcal{N}\mathcal{E}}$ couple to ac Stark shift effects to produce a false EDM. For the published data set, we tuned the laser polarization for each $\tilde{\mathcal{G}}$ state to minimize the magnitude of the systematic slope $S_{\mathcal{E}^{\text{nr}}} = \partial\omega^{\mathcal{N}\mathcal{E}}/\partial\mathcal{E}^{\text{nr}}$

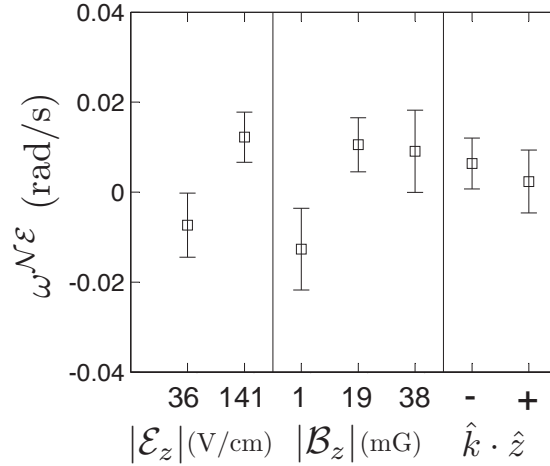


Figure 7.7: Comparison of EDM values under changing field magnitudes $|\mathcal{E}_z|$, $|\mathcal{B}_z|$, and laser pointing $\hat{k} \cdot \hat{z}$. The same data set is represented in each category, it has just been grouped and averaged according to the labeled switch.

(Figure 7.6).

The EDM correlated phase sensitivities $S_{\mathcal{E}^{\text{nr}}}$ and $S_{\Omega_r^{\mathcal{N}\mathcal{E}}}$ were monitored at regular intervals throughout data collection. The values for $(\mathcal{E}^{\text{nr}})_0$ in the prep and probe lasers are extracted from the measurements described in Chapter 6, and $(\Omega_r^{\mathcal{N}\mathcal{E}})_0$ intrinsic to the molecules was measured using the $\phi^{\mathcal{N}\mathcal{E}\mathcal{B}}$ channel as described in Section 7.1.3. The resulting systematic corrections to $\omega^{\mathcal{N}\mathcal{E}}$ were all < 1 mrad/s. Only for the \mathcal{E}^{nr} systematic did we apply a correction term that was larger than the associated systematic uncertainty (Table 7.1). The steps taken to eliminate these systematics made the $S_{\Omega_r^{\mathcal{N}\mathcal{E}}}$ consistent with zero for the final data sets.

The third observed EDM correlation was caused by an $\tilde{\mathcal{E}}$ -correlated magnetic phase, $\phi^{\mathcal{E}}$, which leaks into the EDM channel because the \mathcal{N} states have slightly different g factors [83, 86]. If the molecules experience an effective magnetic field $\mathcal{B}^{\mathcal{E}}$

correlated with $\tilde{\mathcal{E}}$, the magnetic phase will be

$$\phi = \mu_B(g + \Delta g \tilde{\mathcal{N}}) \mathcal{B}^{\mathcal{E}} \tilde{\mathcal{E}}. \quad (7.33)$$

This gives rise to the EDM correlated term $\phi^{\mathcal{N}\mathcal{E}} = \mu_B \Delta g \mathcal{B}^{\mathcal{E}}$. Notice that the same imperfections cause phases to appear in the $\phi^{\mathcal{E}}$ channel as well, and that $\phi^{\mathcal{N}\mathcal{E}}/\phi^{\mathcal{E}} = \Delta g/g \approx 0.3\%$ [83]. Comparison of these two phase channels provides us with a method to detect the presence of systematic errors due to a wide range of physical sources for $\mathcal{B}^{\mathcal{E}}$.

The ratio $\Delta g/g$ represents the limits of the ability of the \mathcal{N} states to act as an internal comagnetometer [5]. We experimentally simulated the effects that contribute to $\phi^{\mathcal{E}}$ by deliberately correlating $|\mathcal{B}_z|$ with $\tilde{\mathcal{E}}$, which allowed us to place a $\sim 10^{-2}$ mrad/s limit on their combined effect. The suppression factor $\Delta g/g \approx 0.07\%$ is improved at Low- \mathcal{E} fields, so the good agreement between High- and Low- \mathcal{E} EDM measurements (left panel in Figure 7.7) also demonstrates our insensitivity to $\mathcal{B}^{\mathcal{E}}$ effects.

Although the $\phi^{\mathcal{E}}$ channel was used to directly put systematic limits on $\tilde{\mathcal{E}}$ -correlated magnetic phases, it is useful to consider the sources and sizes of possible effects. In order to keep $B^{\mathcal{E}}$ systematics below the 10^{-29} e·cm level, we require $|\mathcal{B}_z|^{\mathcal{E}} < 3 \mu\text{G}$. Leakage currents can create $|\mathcal{B}_z|^{\mathcal{E}}$ fields, and were a limiting systematic for the ^{199}Hg EDM experiment [41]. A limit was set on our leakage currents by quickly disconnecting the field plates when fully charged, and monitoring the drift in the Stark shift sensitive $H \rightarrow C$ transition frequency by taking Doppler scans across the resonance.⁵

Considering the field plate capacitance C and leakage resistance R_L , for times

⁵Rapid Doppler scans were taken using the ‘‘Doppler Scan VI’’ described in Appendix C.2.

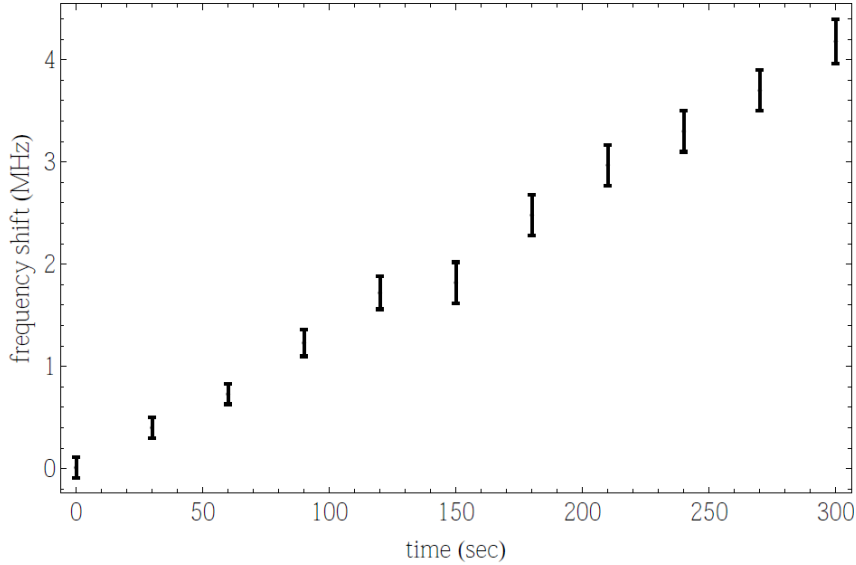


Figure 7.8: Measurement of leakage currents by monitoring the dc Stark Shift dependent $|H, \mathcal{N} = -1\rangle \rightarrow |C, M = 0\rangle$ transition frequency. This plot represents a decaying electric field; as charge drains off the field plates the $|H, \mathcal{N} = -1\rangle$ state decreases in energy and the transition frequency will increase. The dipole moment $D_H \approx 1 \text{ MHz}/(\text{V}/\text{cm})$ allows conversion to a linear voltage decrease of $dV/dt = 0.03 \text{ V/s}$.

$t \ll R_L C$ the voltage should decrease linearly $V(t) \approx V_0 - tV_0/R_L C$. Fitting to the slope $dV/dt = -I_L/C$ allow us to measure the leakage current $I_l = V_0/R_L$ under normal operating conditions. The field plates form a parallel plate capacitor of 35 pF, although using a commercial impedance meter (ESI 252) plate capacitances including vacuum feedthrough were typically $C \sim 350 \text{ pF}$. This data put a limit of $I_L < 10 \text{ pA}$ at High- \mathcal{E} field, where leakage currents are largest. The closest realistic leakage current path we could imagine that would generate a $|B_z|^\mathcal{E}$ would come from a loop around the edges of the 17" \times 9" field plates. This would result in a completely inconsequential $|B_z|^\mathcal{E} < 1 \text{ pG}$.

Motional magnetic fields and geometric phase effects were the limiting systematic for other beam type EDM experiments, such as the thallium EDM [3]. In a moving

reference frame the ThO molecules experience a motional magnetic field $\vec{B}^\mathcal{E} \approx \vec{v}_{\text{beam}} \times \vec{\mathcal{E}}/c^2$ [108]. Although $|\vec{B}^\mathcal{E}| \approx 0.3 \mu\text{G}$, a $|B_z|^\mathcal{E}$ field is additionally suppressed because $\vec{v}_{\text{beam}} \approx |v_{\text{beam}}|\hat{x}$ and $\vec{\mathcal{E}} = |\mathcal{E}|\hat{z}$, so we predominately have a transverse field $|\mathcal{B}_y|^\mathcal{E}\hat{y}$. Systematics due to transverse \mathcal{B} -fields are suppressed by the large dc Stark shift [10], which was directly checked with a transverse $|\mathcal{B}_{x,y}|^\mathcal{E}$ IPV study.

Geometric phases due to magnetic fields are generated in a similar fashion as motional magnetic fields [141, 10]. They are also suppressed by the Stark splitting, and would appear in the $\phi^\mathcal{E}$ term if present. Geometric phases due to electric fields will not have this same behavior [106], but should scale with the \mathcal{E} -field magnitude. The agreement between data at High- and Low- \mathcal{E} field therefore excludes the presence of these effects at our current level of sensitivity.

7.2.2 Systematic Errors without Observed Correlations

The rest of the IPV studies revealed no correlations with the EDM. To be cautious, we included in our systematic error budget possible contributions from the following parameters that caused a nonzero EDM shift in experiments similar to ours, with direct $\omega^{\mathcal{N}\mathcal{E}}$ systematic limits of $\lesssim 1$ mrad/s for each. Stray \mathcal{B} -fields and \mathcal{B} -field gradients were the dominant source of systematic error in the final result of the PbO experiment [6]. We applied transverse fields $\mathcal{B}_{x,y,z}^{\text{nr}}$ and gradients $\left(\frac{\partial\mathcal{B}_x}{\partial x}, \frac{\partial\mathcal{B}_y}{\partial x}, \frac{\partial\mathcal{B}_y}{\partial y}, \frac{\partial\mathcal{B}_y}{\partial z}, \frac{\partial\mathcal{B}_z}{\partial x}, \frac{\partial\mathcal{B}_z}{\partial z}\right)$ to demonstrate that we were not susceptible to the same effect. Although there are only 5 independent gradients (from $\nabla \cdot \vec{B} = 0$ and $\nabla \times \vec{B} = 0$), these extra gradients define a more conservative error bar.

The YbF experiment discovered the detuning of their rf pulses were a leading

source of systematic error [4, 7]. In analogy, our state preparation and probe lasers cause phase shifts when detuned from resonance, but EDM systematics are only observed in the presence of an \mathcal{E}^{nr} , already accounted for above. Nevertheless, we included a systematic uncertainty due to uncorrelated laser detunings in prep and probe Δ_{prp}^0 and Δ_{prb}^0 , in addition to the $\tilde{\mathcal{N}}$ correlated detunings $\Delta^{\mathcal{N}}$ and $(\Delta^{\mathcal{N}} \times \Delta^0)$, which cause offsets to the $\omega^{\mathcal{N}}$ or $\omega^{\mathcal{N}\mathcal{B}}$ parity correlations if α or $\alpha^{\mathcal{B}}$ are non-zero (see Equation 7.10). Finally, the YbF experiment also suffered from an unexplained systematic due to \mathcal{E} -field ground offsets [4]. We measured the ground offset to be 5 mV using a handheld multimeter, and an applied ground offset a hundred times larger revealed no $\omega^{\mathcal{N}\mathcal{E}}$ correlation.

For a subset of our data, the $\tilde{\mathcal{N}}$ -correlated phase $\phi^{\mathcal{N}}$ was nonzero and drifted with time. We determined that the cause of this behavior was an $\tilde{\mathcal{N}}$ -correlated laser pointing $\hat{k}^{\mathcal{N}} \cdot \hat{x} = 5 \mu\text{rad}$ present in our optical frequency switching setup (Section 5.4.2). If not well aligned, the beams exiting the AOMs for $\tilde{\mathcal{N}}$ switching would have different coupling angles into the output fiber coupler. After amplification by the fiber amplifier and coupling back into free space, this pointing dependence seemed to persist, as monitored on a beam profiler. We eliminated the effect with improved alignment of the $\tilde{\mathcal{N}}\tilde{\mathcal{P}}$ switching breadboard, although the observed effect is not well understood. In addition, we were not able to determine the precise mechanism by which $\hat{k}^{\mathcal{N}}$ coupled to $\phi^{\mathcal{N}}$, and so we chose to include $\phi^{\mathcal{N}}$ variations in our systematic error budget. The slope $\partial\omega^{\mathcal{N}\mathcal{E}}/\partial\phi^{\mathcal{N}}$ (consistent with zero) and the mean value of $\phi^{\mathcal{N}}$ established a systematic uncertainty limit of $\sim 1 \text{ mrad/s}$ on $\omega^{\mathcal{N}\mathcal{E}}$.

7.3 Statistical Analysis

A careful statistical analysis and series of well motivated cuts were performed on the EDM measurements in our final data set [81, 105]. This resulted in a distribution of EDM measurements that were extremely Gaussian, as can be seen in a histogram of all final data set measurements (Figure 7.9). In parallel, the statistical uncertainty was computed using standard Gaussian error propagation of the 1σ standard-error-in-the-mean of groups of individual EDM measurements. The asymmetry \mathcal{A} obeys a ratio distribution, which has large non-Gaussian tails in the limit of low-signal-noise ratio [152, 81]. We applied a photon count rate threshold cut so that we included only data with a large signal-to-noise ratio, resulting in a statistical distribution that closely approximates a Gaussian. When the EDM measurements are fit to a constant value, the reduced χ^2 is 0.996 ± 0.006 . In this case, a $\chi^2 \approx 1$ indicates that our EDM uncertainty extracted from Gaussian error propagation agrees with that from a Gaussian fit to the histogram of Figure 7.9. The result was a statistical uncertainty of $\delta\omega_{\text{stat}}^{\mathcal{N}\mathcal{E}} = 4.80$ mrad/sec. On the basis of the total number of detected photoelectrons (~ 1000 per pulse) that contributed to the measurement, the statistical uncertainty is 1.15 times that from shot noise [9].

The reported upper limit was computed using the Feldman-Cousins prescription [153] applied to a folded normal distribution. The folded normal distribution for $|x|$

$$P(|x||\mu) = \frac{1}{\sigma\sqrt{2\pi}} \left(e^{-\frac{(|x|-\mu)^2}{2\sigma^2}} + e^{-\frac{-(|x|+\mu)^2}{2\sigma^2}} \right) \quad (7.34)$$

assumes Gaussian distributed measurements of x with variance σ^2 about a central value μ , where values of $\mu < 0$ are physically valid. This is appropriate for calculating

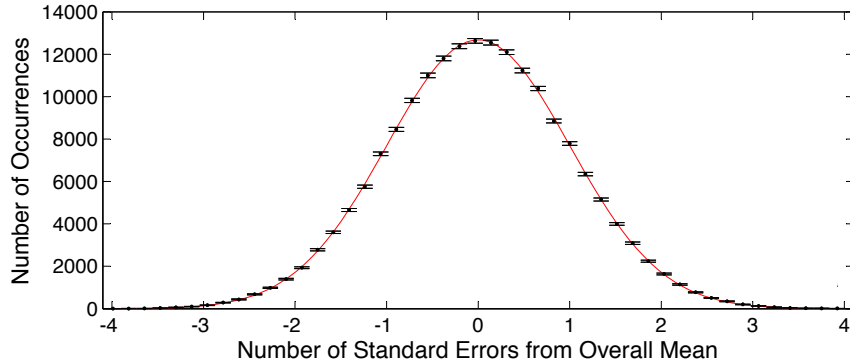


Figure 7.9: Histogram of $\omega^{\mathcal{N}\mathcal{E}}$ measurements from published data set (Ref [2] Figure 2A). There are several $\omega^{\mathcal{N}\mathcal{E}}$ measurements per block, divided up as a function of time across the molecule pulse. We did not see any variation in $\omega^{\mathcal{N}\mathcal{E}}$ as a function of time after ablation. Error bars represent expected Poissonian fluctuations in each histogram bin.

EDM upper limits, where the EDM itself may be negative, but an upper limit should only reflect the magnitude of d_e . In reporting our result, for $|d_e| \ll \sigma$ we wish to report a traditional upper limit, but for $|d_e| \gg \sigma$ a double sided confidence interval is appropriate to announce the discovery of an EDM. The Feldman-Cousins maximum likelihood prescription avoids the misquoting of confidence intervals in the region between these limits by algorithmically handling the crossover from single to double sided confidence intervals [107]. Note that this prescription differs from those used to set previous EDM limits. For the Tl experiment, Regan *et. al.* [3] applied a standard 90% confidence level upper limit for the mean of a half Gaussian distribution (see [153] Figure 2). For the YbF result Hudson *et. al.* [4] applied the 90% confidence bound for the folded normal distribution $CL = \int_0^{d_{e,\text{lim}}} P(x, d_e) dx$. If we applied the same prescription as [4], our EDM upper limit would be lowered to $|d_e| < 8.12 \times 10^{-29} e \cdot \text{cm}$.

To prevent any experimental bias, we preformed a blind analysis by adding an unknown offset to $\omega^{\mathcal{N}\mathcal{E}}$. The mean, statistical error, systematics shifts, and procedure

Parameter	Shift	Uncertainty
\mathcal{E}^{nr} correction	-0.81	0.66
$\Omega_{\text{r}}^{\mathcal{N}\mathcal{E}}$ correction	-0.03	1.58
$\phi^{\mathcal{E}}$ correlated effects	-0.01	0.01
$\phi^{\mathcal{N}}$ correlation		1.25
Non-Reversing \mathcal{B} -field ($\mathcal{B}_z^{\text{nr}}$)		0.86
Transverse \mathcal{B} -fields ($\mathcal{B}_x^{\text{nr}}, \mathcal{B}_y^{\text{nr}}$)		0.85
\mathcal{B} -Field Gradients		1.24
Prep./Read Laser Detunings		1.31
$\tilde{\mathcal{N}}$ Correlated Detuning		0.90
\mathcal{E} -field Ground Offset		0.16
Total Systematic	-0.85	3.24
Statistical		4.80
Total Uncertainty		5.79

Table 7.1: Systematic and statistical errors for $\omega^{\mathcal{N}\mathcal{E}}$, in units of mrad/s. All errors are added in quadrature, and are derived from Gaussian 1σ (68%) confidence intervals. In EDM units, $1.3 \text{ mrad/s} \approx 10^{-29} e \text{ cm}$.

for calculating the systematic error were determined before unblinding. Such hidden offset blinding techniques are inspired by those used in the nuclear and particle physics community [154]. Previous EDM searches in atomic and molecular systems have employed blinds with varying degrees of complexity [41, 4]. We chose a simple approach of adding a single offset value to the value of $\omega^{\mathcal{N}\mathcal{E}}$ as the last step in data analysis.⁶

7.4 Results and Interpretation

The result of this first-generation ThO measurement,

$$d_e = (-2.1 \pm 3.7_{\text{stat}} \pm 2.5_{\text{syst}}) \times 10^{-29} e \cdot \text{cm} \quad (7.35)$$

⁶The goal of blinding was not to produce an “uncrackable” blind, but one that could be easily applied by any member of the collaboration wishing to perform data analysis. It was assumed that there were no adversaries trying to reveal the unblinded value before the appropriate time.

comes from $d_e = -\hbar\omega^{\mathcal{N}\mathcal{E}}/\mathcal{E}_{\text{eff}}$ using $\mathcal{E}_{\text{eff}} = 84$ GV/cm [88] and $\omega^{\mathcal{N}\mathcal{E}} = (2.6 \pm 4.8_{\text{stat}} \pm 3.2_{\text{syst}})$ mrad/s. This sets a 90% confidence limit,

$$|d_e| < 8.7 \times 10^{-29} e \cdot \text{cm} \quad (7.36)$$

that is smaller than the previous limit by a factor of 12 [3, 4] - an improvement made possible by the use the ThO molecule and of a cryogenic source of cold molecules for this purpose. In addition to the included systematic error bars, the result is robust under large changes of $|\mathcal{E}_z|$ and $|\mathcal{B}_z|$ (Figure 7.7).

A recent calculation of \mathcal{E}_{eff} has been performed by another group yielding 75.2 GV/cm with an estimated uncertainty of 3% [155]. A useful experimental check for \mathcal{E}_{eff} calculations is the hyperfine structure constant A_{\parallel} , which depends on the same wavefunctions of valence electrons near the nucleus [156]. $^{232}\text{Th}^{16}\text{O}$ has zero nuclear spin, so we are unable to observe any hyperfine structure. Calculating observables such as transitions energies (T_e) and magnetic [83] and electric dipole moments depend less sensitively on these short range wavefunctions, but can serve as reasonable proxy measurements. The calculations by Fleig *et. al.* [155] show better agreement with T_e , but those of Skripnikov *et. al.* [88] have calculated a wider variety of parameters to within 15%. We chose the 84 GV/cm result because it has a more conservative error bar, and lies in between the 75 GV/cm calculation and the 104 GV/cm semi-empirical estimate [89]. If we were to take into account the roughly estimated 15% uncertainty on the calculated \mathcal{E}_{eff} [88] and assume that this represents a 1σ Gaussian distribution width, the d_e limit stated above would increase by about 5%. We hope that the recent interest in ^{229}Th spectroscopy [157, 158, 159] will make new measurements of A_{\parallel} feasible in ^{229}ThO for verification of \mathcal{E}_{eff} calculations.

Because paramagnetic molecules are sensitive to multiple T-violating effects [160, 38], our measurement should be interpreted as $\hbar\omega^{\mathcal{N}\mathcal{E}} = -d_e\mathcal{E}_{\text{eff}} - W_S C_S$, where C_S is a T-violating electron-nucleon coupling and W_S is a molecule-specific constant determined by the molecular calculations [88, 161]. For the d_e limit above, we assume $C_S = 0$. Assuming instead that $d_e = 0$ yields $C_S = (-1.3 \pm 3.0) \times 10^{-9}$, corresponding to a 90% confidence limit $|C_S| < 5.9 \times 10^{-9}$ that is smaller than the previous limit by a factor of 9 [41].

Chapter 8

Conclusion and Future Steps

The first generation of the ACME experiment has improved the limit on the electron EDM by over an order of magnitude. Despite our much higher sensitivity, an electron EDM has not materialized, consistent with the prediction of the Standard Model. Our result further emphasises the unnaturalness of certain supersymmetric models that must be fine tuned to predict electron EDMs close to zero [25]. However, some models predict d_e to be just below our current sensitivity [162]. Therefore, more sensitive searches for an electron EDM continue to be useful for testing Standard Model extensions, while the discovery of a nonzero eEDM would be a clear indication of physics beyond the Standard Model.

Many of the extensions to the Standard Model that predict an electron EDM could be within the sensitivity range of our second generation experiment. Moreover, many major systematics will only enter our measurement at the 10^{-32} $e\cdot\text{cm}$ level [10], so improvements in ACME's statistical precision will likewise improve our limit on the electron EDM. The experiment was operated in the regime of saturated \mathcal{E}_{eff} , and

the lifetime of the metastable H state limits improvements from increased interaction length to 15% of the current sensitivity (Figure 5 from [10]). Therefore, future improvements rely upon the increase in beam flux (\dot{N}) improving the measurement's signal to noise and reducing the statistical uncertainty by $1/\sqrt{N}$. Several upgrades, already demonstrated in proof-of-principle experiments, could increase our fluorescence by a total factor of ~ 100 , therefore improving the statistical sensitivity by an order of magnitude. All entries in our systematic error budget were limited by the precision with which we could measure the phase offsets. Therefore, improvement of statistical sensitivity should also improve the systematic error estimate as well, and increase the speed at which we can diagnose and eliminate new systematics.

Currently, observe the spin precession of only a small fraction of the molecules produced by our beam source. Molecules emerge from the beam source with a wide divergence half angle of $\sim 40^\circ$ [8], but the final collimator has an acceptance angle of only $\sim 0.6^\circ$. Using an electrostatic lens to “focus” the divergent molecular beam would increase the fraction of molecules which travel through the interaction region. In a separate apparatus we have demonstrated that the $M = 0$ ground states can be guided by an magnetic quadrupole field. Simulations of a new electrostatic lens indicate that the beam flux can be increased by up to a factor of 40 without depositing ThO on the field plates. This will modify the velocity profile of the molecule beam in the interaction region. Therefore, the \mathcal{E}^{nr} systematic, which couples to the velocity dependent Doppler profile, should be carefully reexamined.

The EDM state preparation efficiency could be increased by up to a factor of 10 by utilizing Stimulated Raman Adiabatic Passage (STIRAP) [163] on the $X \rightarrow C \rightarrow H$

Lambda transition. Currently, only 12% of available ground state molecules are prepared in an H state spin superposition. This is a combination of the $A \rightsquigarrow H$ branching ratio and the incoherent decay leading to population distributed across 5 sublevels in the H state. STIRAP could directly move population from a single ground state sublevel to a spin superposition with transfer efficiency of up to 100%. The narrow two-photon linewidth [164] requires the 690 nm and 1090 nm lasers be stabilized to within ~ 100 kHz. Both lasers have already been locked to a high finesse ultra-low expansion (ULE) glass cavity (Advanced Thin Films) within a thermally stabilized vacuum chamber [165].¹

In addition, a thermochemical beam source may increase our molecule flux by a factor of ~ 10 . ThO can be produced chemically by heating samples of Th and ThO₂ metal powder to temperatures of $\sim 1600^\circ$ K [166]. We have already demonstrated that a focused laser can locally heat a pressed Th + ThO₂ target to produce buffer gas beams of ThO with higher peak fluxes than ablation. However, this technique produced larger heat loads than the cooling power provided by our current cryogenic beam source, and the thermochemical beams were not stable. A beam source is being constructed with improved cooling power, which should allow for the continued development of this new beam technology in parallel with other experimental upgrades.

The dominant ac Stark shift systematic errors can further be suppressed by implementing electric field plates with improved thermal and optical properties. As derived in Equation 4.14, the size of our thermal birefringence gradients depends on both the optical properties of the field plates substrates and ITO coatings. The cur-

¹Transfer efficiencies of up to 70% have been demonstrated previously by E. Kirilov, but we are actively trying to improve this figure.

rent field plates are made of borosilicate float glass, which can be manufactured into large flat sheets rather inexpensively, but doesn't have ideal optical properties. Fused silica (such as Corning 7980) has optical properties that minimize thermal stress in the material and reduce gradients by a factor of 10. Moreover, a thinner coating of ITO will decrease the $\sim 4\%$ absorption of laser light linearly with the reduction in thickness. Coatings down to 100\AA seem feasible, and would reduce the heat deposited by a factor of 10.

The aforementioned statistical improvements have all been previously demonstrated to increase the useful molecule flux in auxiliary experiments. Their combined effect should increase the number of molecules participating in a second generation experiment by a factor of 100 or more, resulting in an improved statistical precision of at least an order of magnitude. The improved electric field plates should decrease the polarization gradients and resulting ac Stark shift systematics by more than a factor of 10. Therefore, the next generation of ACME is poised to strike out yet again in search of the elusive electron EDM. Regardless of the result, a discovery of a tiny EDM or an improved upper bound, this data will help steer us towards the extensions to the Standard Model which best describe our universe.

Appendix A

ACME PMTs

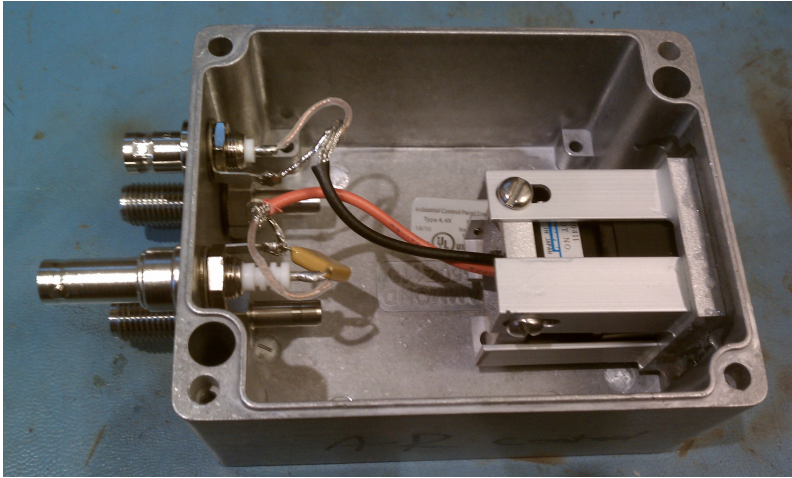
The ACME experiment required a low noise detector in order to perform spin precession measurements at the shot noise limit [9, 2]. For detection of $C \rightsquigarrow X$ fluorescence photons at 690 nm, we chose a multi-anode photomultiplier (PMT) with a multialkali photocathode (Hamamatsu R8900U-20) [167, 168]. This PMT model was selected because of its large effective area of $23.5 \times 23.5 \text{ mm}^2$ and its extended sensitivity into the near infrared ($\sim 10\%$ quantum efficiency at 690 nm). Although silicon photodiodes or avalanche photodiodes have much higher quantum efficiencies, they lack the noise-free gain of PMTs [169]. Signal levels must be ~ 10 times greater than those in the current generation ACME experiment for shot noise to dominate over photodiode and amplifier noise [105]. A cooled avalanche photodiode [170] would be the best choice for a next generation photodetector.

A.1 PMT Enclosure Assembly and Operation

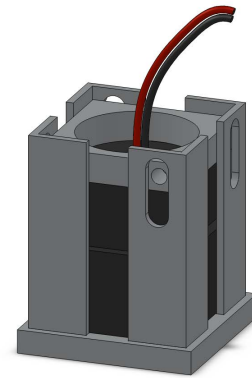
The degradation of PMT performance caused by a slow increase of the pressure inside the vacuum tube is well documented [171, 122]. In particular, helium gas permeates through the glass surface on the front of the PMT, causing afterpulsing and a reduction in tube lifetime. This problem could be exacerbated in a setting such as the LISE laboratory, where there is higher partial pressure of helium in the air.

Care was taken to house our PMTs in an enclosure that could be constantly purged with dry nitrogen gas, thus increasing the lifetime of the detectors. Two Swagelock bulkhead feedthroughs allow nitrogen to be continually flowed in and out of the enclosure, so multiple PMTs can be daisy chained on one nitrogen line. The air-tight enclosures and hermetically sealed electrical feedthroughs provide a low leak rate when pressurized. A thin AR coated window was epoxied in place to provide a good seal. All joints were leak tested using a pressure test appropriate for gas fittings; the enclosure was pressurized and no gas bubbles were observed when “liquid Snoop” was applied to the joints. The parts list for these inclosures is recorded in Table A.1, and the assembly is shown in Figure A.1a.

The high voltage (HV) is supplied from an external source to the voltage divider socket through a SHV connector, and the PMT output signals are returned through a BNC connector. The input HV was filtered by a $0.22 \mu\text{F}$ capacitor in parallel with three surface mount 220 pF capacitors, all rated to 1 kV . These smaller capacitors from ATC have a self resonance frequency above the 100 MHz maximum frequency component in the fourier transform of the $\sim 10 \text{ ns}$ single photon pulses. Three in parallel have a total capacitance that matches the ideal impedance of a $0.22 \mu\text{F}$



(a) Assembled PMT Enclosure



(b) Solidworks model of PMT mounting rails

Figure A.1: PMT Enclosure Assembly

capacitor at 100 MHz. The four capacitors in parallel therefore provide filtering from DC to 100 MHz, up to frequencies where the large capacitor behaves inductively.

Light diverges rapidly after exiting the light pipes abutted to the front face of these PMT enclosures [81]. Therefore, the enclosure was designed to position the PMT's photocathode as close to the exterior surface as possible. The PMT itself is mounted inside a cage mount type enclosure, shown as a Solidworks model in Figure A.1b. The rails are glued into the cage base plate with 5 minute epoxy. The cage mount is centered on the window aperture using an alignment tool, then attached to the inside of the enclosure with epoxy. The PMT can slide all the way to be flush with the inside surface, and is fixed in place with the clamp and screws on top of the rail assembly. In practice, a few turns of electrical tape are applied to the base of the PMT to ensure a snug fit. The window on the front face is as thin as possible (1 mm), and filters are mounted flush with this window in a 1" diameter lens tube epoxied to the exterior of the assembly.

Component	Part No.	Comment
PMT	Hamamatsu R8900U-20	
Voltage Divider and Socket	Hamamatsu E10411	
Enclosure	Hammond 1550Z113	Hermetically Sealed
BNC Feedthrough	Amphenol 31-102	O-Ring Sealed (Grounding Tab on Inside)
SHV Feedthrough	Pasternack 4500	O-Ring Sealed (Grounding Tab on Inside)
Nitrogen Feedthrough	Swagelock SS-400-R1-4	Seal with #110 O-Ring on inside surface
Filtering Capacitor	Digi-Key 399-3514-ND	0.22 μ F with 1 kV limit
High Frequency Filtering Capacitor	ATC 100B221JT1000 X 10	220 pF @ 1 kV ($\times 3$ wired in parallel)
1" Diameter Window	Edmund Optics 48924	1 mm thick, AR Coated 425-700 nm
Filter Holder	Thorlabs SM1M10	Epoxy lens tube to exterior
Angle Bracket Stock	McMaster 4630T12	Clear Anodized Aluminium
Epoxy	5-Minute Epoxy	

Table A.1: Components for sealed ACME PMT enclosure

In order to make the assembly as compact as possible, all electronics besides a few filtering capacitors were housed in a separate rack mountable power supply, designed and assembled by the MacArthur electronics lab. This supply contains 8 channels, each of which has an independently tunable output voltage between 0 – 900 V, produced by a compact high voltage power module (Hamamatsu C4900). Each channel has a display of the HV setting, and a monitor port for logging the control voltage ($V = 250 \times V_{\text{ctrl}}$). The max output of the power module is -1250 V, but the control voltage has been limited to 3.6 V so they cannot supply more than the -900 V recommended maximum supply voltage to the R8900U-20 PMT modules.

The PMTs are typically operated at -675 V, where they were observed to have well behaved noise spectra in both current and photon counting mode. The gain of

theses PMTs depends on the voltage as a power law [122]

$$G = kV^\alpha, \tag{A.1}$$

where $k = 9.5 \times 10^{-17}$ and $\alpha = 7.75$, as extracted from gain curves on the PMT datasheet. This corresponds to a gain of $G \approx 8 \times 10^5$ at our operating voltage, although there is some indication that this underestimates the real gain (see 3/27/2012 EDM Experiment lablog). The gain has never been carefully measured over a wide range of supply voltages. In principle, measurements of average photocurrent (I) and noise (σ_I) can be used to calculate the gain ($G = \sigma_I^2/I$), since the photoelectron emissions are a Poissonian process [172, 173]. This measurement should be made in the future, especially when characterizing new PMT modules.

A.2 Setting Discriminator Level for Photon Counting

Single photon counting is an excellent technique for recording very low noise fluorescence signals at low light levels [121]. For example, in the lifetime measurement described in Section 3.1, we counted $\bar{n} \leq 0.1$ photons per time bin. The SR430 multichannel scaler (MCS) used in the measurement contains an amplifier, discriminator, and time bin clock necessary for a time resolved photon counting measurement. The MCS rapidly identifies single photon pulses with heights above the discriminator threshold, and counts them in time bins relative to a trigger signal, averaging over multiple triggered acquisitions to build up statistics when counting rates are low.

In order to optimize signal to noise, we must set the discriminator level based

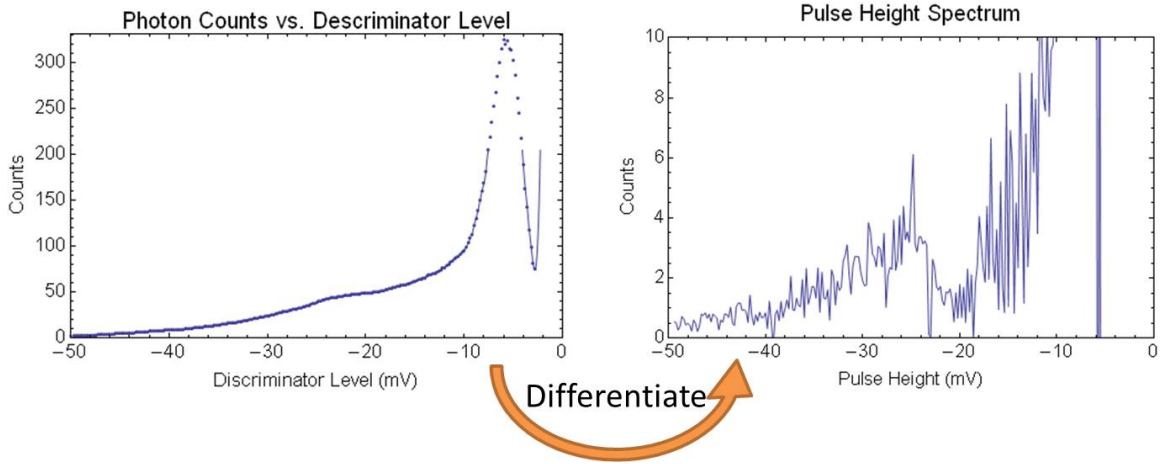


Figure A.2: Integrating a sweep of the MCS discriminator level to measure a pulse height spectrum. Some smoothing is applied to the $I(p_D)$ curve at left to reduce the noise in its numerical derivative.

on the pulse height spectrum of our PMTs. The pulse height spectrum contains two peaks; the signal peak and dark current peak, each of which have a width characterized by gain fluctuations at the dynodes [122]. The dark peak is caused by thermal electron emission from both the photocathode and later dynode stages, and therefore doesn't experience as much gain and is shifted towards the low end of the pulse height spectrum. The discriminator level should be set at the minimum between these two curves, in order to reject the most dark pulses without cutting out significant signal pulses (Figure A.3).

Many applications of single photon counting, for example monitoring scintillation signals in nuclear physics, have very low counting rates of < 1 MHz. In these cases, a class of devices called Multi-channel Analyzers (MCA) are available, which can rapidly measure pulse heights and bin them into histograms to produce pulse height spectra. Ideally, a pulse height spectrum should be measured using signal levels that are comparable to those in the experiment. Lowering(Raising) the signal level would

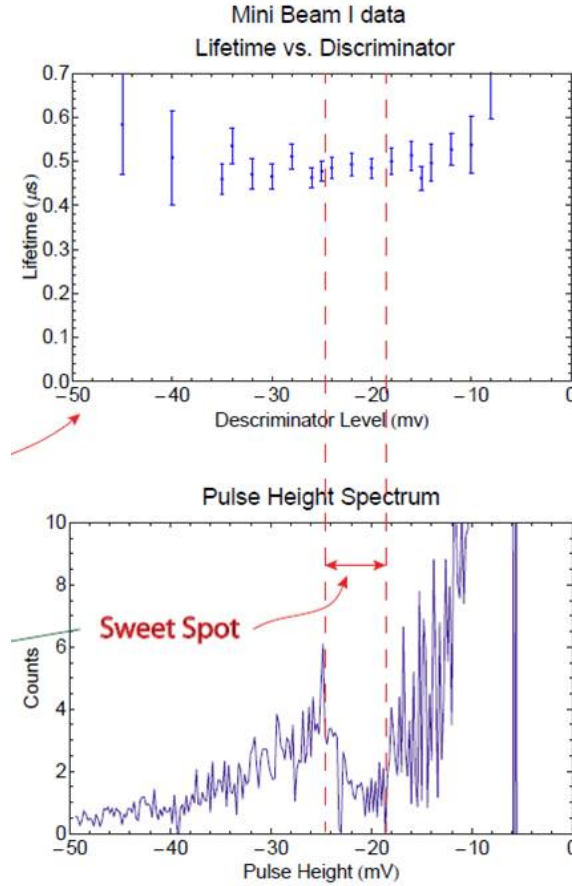


Figure A.3: Discriminator level settings and associated lifetime measurements.

decrease(increase) the height of the signal peak and shift the spectrum's minimum towards larger(smaller) pulse heights. In our measurement, count rates were typically in the range of 1 – 5 MHz,¹ so a MCA could not be used to measure the pulse height spectrum.

Here I describe the technique used to measure the pulse height spectrum using only the MCS. The MCS counts the number of photon pulses below the discriminator level p_D , and by sweeping this level we can measure the integrated spectrum $I(p_D)$.

¹The MCS response was found to become non-linear at count rates of ~ 10 MHz (see Section 3.1).

We can apply the second fundamental theorem of calculus to recover the pulse height spectrum $S(p)$,

$$I(p_D) = \int_0^{p_D} S(p) dp \quad (\text{A.2})$$

$$I'(p_D) = S(p_D) \quad (\text{A.3})$$

Figure A.2 shows the results of applying numerical differentiation to an integrated pulse height spectrum measured with the MCS. The signal and dark pulse distributions become immediately apparent. The signal is generated with a 690 nm laser light source attenuated to mimic the light levels measured in the lifetime experiment. To minimize the noise on the spectrum, the discriminator sweep should be made faster than intensity drifts in this signal laser. It helps to increase the MCS bin size and record length to collect more total photons per discriminator setpoint.

In the comparison to lifetime data taken as a function of discriminator level (Figure A.3), it is clear that setting the discriminator around the minimum yields measurements with the fastest decay rate and smallest uncertainty. Setting the discriminator level too low will cause issues of pulse pile up, where overlapping pulses are counted as one, suppressing the measured count rates at the highest signal levels. This non-linear signal suppression will make the decay appear slower, and therefore exponential fits produce a longer fit lifetime, in agreement with the data. The uncertainty increases if the discriminator is set too low because the rejection of signal photons produces very low measurement statistics.

Appendix B

Stokes Polarimeter System

In order to fully characterize the polarization state of our lasers, a polarimeter was constructed based on the Rotatable Retarder Fixed Polarizer (RRFP) design [137]. This polarimeter uses a movable retardation plate to modulate the light polarization, which is measured in a fixed polarization basis by a static polarizer. Many variations exist on this basic design, and it is possible to optimize the retarder's measurement angles and retardance value [174, 175] given imperfections in calibration [176] or various noise models of the light being measured [177, 178]. Many RRFP based commercial polarimeter systems (e.g. Thorlabs PAX5720) are now available, with state of polarization (SOP) accuracies of up to $\sim 0.25^\circ$ on the Poincaré sphere. An advantage of our system is that it allows us to measure both polarization components of the probe beam simultaneously by digitally demodulating the signals. This has proved important in measuring the degree of orthogonality of the \hat{X} and \hat{Y} probe polarization components.

B.1 Useful Definitions in Polarimetry

The Stokes parameters (I, M, C, S) ¹ can be fully defined using six intensity measurements

$$I = I(0^\circ) + I(90^\circ) \quad (\text{B.1})$$

$$M = I(0^\circ) - I(90^\circ) \quad (\text{B.2})$$

$$C = I(45^\circ) - I(135^\circ) \quad (\text{B.3})$$

$$S = I_{\text{RHC}} - I_{\text{LHC}} \quad (\text{B.4})$$

For the coherent laser light we wish to characterize, complete polarization requires that the equality

$$M^2 + C^2 + S^2 = I^2 \quad (\text{B.5})$$

is strictly true. The relative Stokes parameters, $M_I = M/I$, $C_I = C/I$, and $S_I = S/I$ completely define the polarization state of the laser. Physically, S_I represents the degree of circular polarization, and we define $L_I = \sqrt{M_I^2 + C_I^2}$ as the analogous degree of linear polarization. Using Equation B.5, the polarization state can be written in terms of two variables, making the Stokes formulation equivalent to the Jones calculus for laser polarization [133].

Two very useful concepts for graphically representing polarization states are the polarization ellipse and the Poincaré sphere (Figure B.1). The polarization ellipse is defined with an inclination angle ϕ ,

$$\tan(2\phi) = \frac{C_I}{M_I}, \quad (\text{B.6})$$

¹Here we use the notation consistent with [137] for the Stokes parameters. A common alternate notation is (S_0, S_1, S_2, S_3) [133].

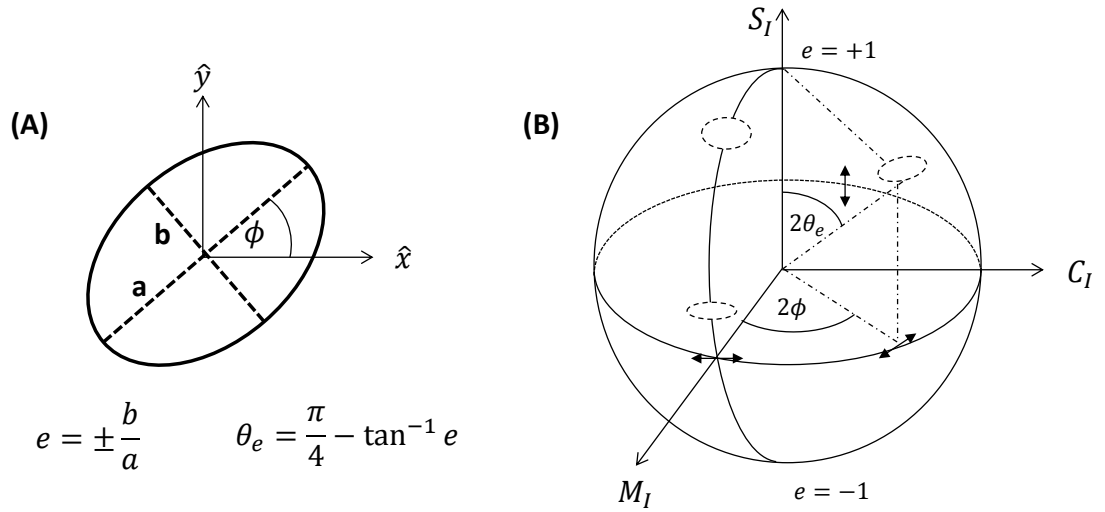


Figure B.1: The polarization ellipse and Poincaré sphere. **(A)** The polarization ellipse is drawn with major and minor axes a and b respectively. The inclination angle ϕ is with respect to the \hat{x} axis, and ellipticity $e = +1(-1)$ for RHC(LHC) polarized light, respectively. **(B)** The Poincaré sphere, with a few representative polarization ellipses drawn on for reference.

which represents the angle of linear polarization, and an ellipticity e , which defines the degree of circular polarization. The Poincaré sphere is a unit sphere in 3D space where the (x, y, z) coordinates on the sphere correspond to the (M_I, C_I, S_I) Stokes parameter values. Each meridian line represents polarization states with the same inclination angle ϕ , but with ellipticity increasing towards $e = \pm 1$ at the poles. Likewise, circles parallel to the equator have constant ellipticity but a rotating linear polarization angle. In a spherical polar basis, the position on the Poincaré sphere is given by the azimuth and polar coordinates $(2\phi, 2\theta_e)$, where

$$\theta_e = \frac{\pi}{4} - \arctan(e) \quad (\text{B.7})$$

is the ellipticity angle.

People often cavalierly use the term “ellipticity” when they truly mean S_I . These

quantities are not the same,

$$S_I = \frac{2e}{e^2 + 1} \quad \text{and} \quad S_I = \cos(2\theta_e). \quad (\text{B.8})$$

In the limit of small amounts of circular polarization, $S_I \approx \pi/2 - 2\theta_e \approx 2e$, so I encourage people to use the correct term and mind their factors of 2. For simplicity, I will use the term “ellipticity” to refer to θ_e , since it is more useful than e for describing molecule/photon interactions (Equation 7.4). Note, our definition of the ellipticity angle differs from that in reference [133]. We chose this convention to be consistent with the generalized formula for polarization used in the analysis of ac Stark shift systematics (Section 7.1.1 and [81, 179]).

An often quoted property of real linear polarizers or other optical elements is an extinction ratio $R_e = I_{\min}/I_{\max} < 1$. Here we have defined R_e in terms of measured intensities, I_{\min} and I_{\max} , when an ideal polarizer is used to analyze the light after passing through the optical element under test. Measurements of I_{\min} and I_{\max} occur when the analysis polarizer is aligned with the major and minor axes of the polarization ellipse. We are free to define these directions to be vertical (\updownarrow) and horizontal (\leftrightarrow) so that $C_I = 0$ and

$$\begin{aligned} |M_I| &= \frac{|I_{\updownarrow} - I_{\leftrightarrow}|}{I_{\updownarrow} + I_{\leftrightarrow}} \simeq \frac{I_{\max} - I_{\min}}{I_{\max}}, \\ |M_I| &= 1 - R_e, \end{aligned} \quad (\text{B.9})$$

where we have assumed the extinction ratio is high $I_{\max} \gg I_{\min}$. From the summation rule for Stokes parameters, we know the remaining circular polarization must be

$$|S_I| = \sqrt{1 - (1 - R_e)^2}. \quad (\text{B.10})$$

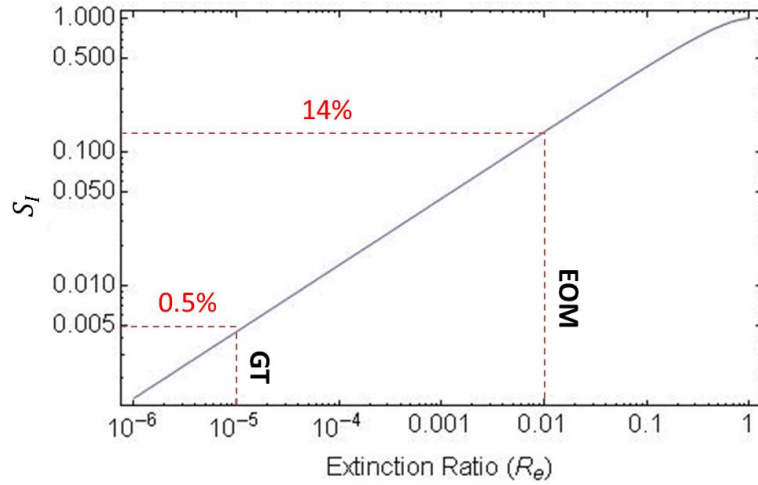


Figure B.2: Residual S_I for polarization optics with extinction ratio R_e , according to Equation B.10. Here the polarization switching EOM (Conoptics 360-120) and the frequently used Glan Taylor polarizer (GT) are marked for comparison.

Figure B.2 shows what limits certain polarization optics, such as a Glan-Taylor polarizer ($R_e = 10^{-5}$) or the polarization rotating EOM ($R_e = 10^{-2}$), would place on the amount of remaining circular polarization. It is interesting to note that according to Equation B.10, there is still $S_I = 0.5\%$ circular polarization even for the highest extinction ratio polarizers. This also sets a limit on how well our Stokes polarimeter can perform, meaning it will always measure a small offset in S_I from the Glan-Taylor analysis polarizer.

B.2 Polarimeter Fundamentals of Operation

The polarimeter consists of a rotatable quarter-wave plate with retardation $\delta \approx \pi/2$ and fast axis angle β relative to the fixed polarizer transmission axis. The

transmitted intensity of a source laser with Stokes parameters (I, M, C, S) is [137]

$$I_T(\beta, \delta) = \frac{1}{2} \left[I + \frac{M}{2}(1 + \cos(\delta)) \right] - \frac{1}{2} S \sin(\delta) \sin(2\beta) + \frac{1}{4} [M \cos(4\beta) + C \sin(4\beta)] (1 - \cos(\delta)). \quad (\text{B.11})$$

The waveplate is rotated by a discrete set of angles over 360° , and an intensity measurement $I_T(\tilde{\beta})$ is made at each step. Let $\tilde{\beta}$ be the angle recorded by the rotation stage's encoder, relative to the polarizer transmission axis. The measured intensity is fit to a linear combination of sine and cosine functions

$$I_T(\tilde{\beta}) = C_0 + C_2 \cos(2\tilde{\beta}) + C_4 \cos(4\tilde{\beta}) + S_2 \sin(2\tilde{\beta}) + S_4 \sin(4\tilde{\beta}) \quad (\text{B.12})$$

where the linear fit coefficients $(C_0, C_2, C_4, S_2, S_4)$ determine the amplitude and phase of the frequency components in this signal.

We define all our measurements relative to the polarizer transmission axis. When mounting the quarter-wave plate in the rotation stage, its fast axis cannot be perfectly aligned with the home position of the encoder, $\tilde{\beta} = 0$. The offset angle is $\beta_0 = \beta - \tilde{\beta}$. Solving for the Stokes parameters by substituting $\beta = \tilde{\beta} + \beta_0$ and comparing Equations B.11 and B.12²,

$$M = \frac{2}{1 - \cos(\delta)} [C_4 \cos(4\beta_0) - S_4 \sin(4\beta_0)], \quad (\text{B.13})$$

$$C = \frac{2}{1 - \cos(\delta)} [S_4 \cos(4\beta_0) + C_4 \sin(4\beta_0)], \quad (\text{B.14})$$

$$S = \frac{-C_2}{\sin(\delta) \sin(2\beta_0)} = \frac{-S_2}{\sin(\delta) \cos(2\beta_0)}, \quad (\text{B.15})$$

$$I = C_0 - \frac{1 + \cos(\delta)}{1 - \cos(\delta)} [C_4 \cos(4\beta_0) - S_4 \sin(4\beta_0)]. \quad (\text{B.16})$$

²These solutions are adapted from [137] equation (16), with $\alpha = 0$, $\beta_0 \rightarrow -\beta_0$. Note that [137] contains an error in the denominator of the S equations (it should be $2\beta_0$, not $4\beta_0$) which is corrected here.

Prior knowledge of δ, β_0 (through calibration techniques discussed in Section B.4) allows one to extract all the Stokes parameters. Uncertainties in calibration measurements $\sigma_\delta, \sigma_{\beta_0}$ and in the linear fit coefficients $\sigma_{C_0}, \sigma_{C_2}, \dots$ contribute to the uncertainty of the extracted Stokes parameters according to the standard equations for Gaussian error propagation [180, 181]. Typically, $\tilde{\beta}$ is rotated over a single 360° rotation, in increments of 8° (45 points). This proves to be a good compromise between the speed of acquisition and measurement precision.

B.3 Assembly and Alignment

The fully assembled polarimeter, as used for gradient polarimetry tests is shown in Figure B.3. For a full list of parts, see Table B.1. The retardation plate and polarizer are the highest quality optics that could be easily acquired. In particular, the retardation plate, designed for 1090 nm, has very close to $\pi/2$ phase retardance. CVI no longer manufactures this model of zero-order quarter-wave plate at 1090 nm. The best available off-the-shelf alternatives are broadband achromatic waveplates (e.g. Thorlabs AQWP05M-980). So long as the waveplate's retardation is properly measured, variation in retardance values is acceptable, and more non-standard retardation plates may even optimize the polarimeter's performance [174].

Unlike polaroid disks, a polarizing beam splitter cube, such as a high extinction ratio Glan-Taylor polarizer (GT10), will have a transmission axis that can be precisely referenced mechanically to its exterior geometry. Currently, the GT10 analysis polarizer is in a rotatable mount and the transmission axis has been aligned to the horizontal by eye. This should be replaced with a mount that fixes the polarizer

Component	Part No.	Comment
Irises	Thorlabs SM12D12	0.8 mm min aperture, Ring-Activated best in cage mount system
Rotation Stage	Newport URS50BCC	20°/s rotation rate
Quarter-Wave Plate	CVI QWPO-1090-08-4-R10	No longer available
Linear Polarizer	Thorlabs GT10-B	100,000:1 extinction ratio
Polarizer Mount	Thorlabs SM1PM10	Replace with non-rotatable mount
Photodetector	Thorlabs PDA10A	Si Transimpedance Amplified Photodetector, 150 MHz Bandwidth
Translation Stage	Zaber TSB28E	28mm Stage with 1/4-20 tapped holes
Translation Stage Actuator	Zaber T-NA08A25	25 mm travel, 15 μm accuracy

Table B.1: Components for ACME Stokes Polarimeter

orientation to the polarimeter’s cage system.

A spatial non-uniformity in the retardance or transmission across the waveplate face can cause systematic errors in the measurement of $I_T(\tilde{\beta})$ if the polarimeter is not properly aligned. Two apertures spaced by $\sim 4''$ ensure that the light is well centered on the rotating quarter-wave plate so that the laser samples the same region of the waveplate regardless of its rotation angle $\tilde{\beta}$. A silicon transimpedance amplified photodetector with a fast bandwidth is used to measure both polarization components of our 100 kHz polarization chopped probe beam. High bandwidths necessitate small sensor areas (0.78 mm) in such detectors. An $F = 1''$ focal length lens focuses the light onto the detector area, which both improves the signal size and makes the $I_T(\tilde{\beta})$ measurements less susceptible to laser pointing wobble from the rotation stage.

The polarimeter has three positional degrees of freedom; horizontal and vertical

translation and horizontal (azimuth) angle. The laser beam must be parallel to the polarimeter's horizontal transmission axis, which is satisfied if it is also parallel to the optics table. Alignment should proceed as follows:

1. Position the polarimeter in front of the laser beam to measure, with both apertures fully open. Make sure you can see the beam with an IR card between the second aperture and the detector. Close the front aperture until the signal starts to disappear, then adjust the stage positioning (or laser pointing if possible) such that it continues to pass through all components. Repeat until the front iris is completely closed. If the laser beam is much larger than the aperture, this step is unnecessary.
2. Begin closing the second aperture, and optimize the signal as before. At this point, only the horizontal position and angle need to be adjusted. If the laser is much larger than the aperture, tilting the azimuth angle of the stage should be sufficient.
3. With the apertures fully closed, fine tune the alignment by maximizing the photodiode signal.

B.4 Calibration

Extracting the Stokes parameters from Equations B.13-B.16 requires a calibration of the quarter-wave plate's retardation δ and offset β_0 . In the design presented above, the polarizer transmission axis (α in [137]) is parallel to our lab \hat{x} axis, so all polarizations are defined relative to this fixed polarizer. Analyzing linearly polarized light at

known angles allows elimination of terms from Equations B.13-B.16, and solutions for δ and β_0 can be found. Linearly polarized light is generated by a calibration polarizer with transmission axis at angle γ . Several calibration techniques that are variations on this theme are listed below, in order of preference.

B.4.1 Fixed Calibration and Analysis Polarizer

Using another GT10 polarizer, the polarization axis can be mechanically fixed relative to horizontal using a beamsplitter mount. Therefore $\gamma = \alpha = 0$ and the light being analyzed has Stokes parameters $(1, 1, 0, 0)$. If we define the fringe amplitude $|\eta|$ to be

$$|\eta| = \frac{1}{C_0} \sqrt{S_4^2 + C_4^2} \quad (\text{B.17})$$

then one can show that the retardation in this case is equal to

$$\cos(\delta) = \frac{1 - 3|\eta|}{1 + |\eta|}. \quad (\text{B.18})$$

By taking normal $I_T(\tilde{\beta})$ curves under these conditions, Equation B.18 can be used to solve for δ . Taking the standard deviation of many measurements of δ , one usually arrives at a retardation angle uncertainty of $\sigma_\delta < 1^\circ$ using this method.

The peak of the $I_T(\tilde{\beta})$ curve from the same data set occurs at angle $\tilde{\beta} = -\beta_0$, when the input polarization is aligned through either the fast or slow waveplate axis. The polarization is unchanged by the waveplate, and we observe maximum transmission as the light passes through both aligned polarizers. From the same data set as above, one can calibrate the waveplate offset angle using

$$\beta_0 = 1/4 \arctan(-S_4/C_4). \quad (\text{B.19})$$

Repeating this measurement multiple times the scatter reveals an uncertainty of $\sigma_{\beta_0} < 0.1^\circ$. One does not know if this axis is the fast or slow axis (and one cannot figure this out without using a circularly polarized calibration laser), but such an ambiguity is generally irrelevant for our experiment.

B.4.2 Removing the Quarter-Wave Plate

If one is not confident that the calibration and analysis polarizers have the same angle, as is required for calibration B.4.1, the offset can be determined by rotating the input polarization state. Remove the quarter-wave plate and its rotation mount from the polarimeter assembly. This can be achieved without disturbing the analysis polarizer's orientation or the polarimeter's alignment. Place the calibration polarizer in a rotation stage, and acquire transmission data through the two polarizers as a function of $\tilde{\gamma} = \gamma - \gamma_0$. The intensity follows Malus's Law for crossed polarizers,

$$I_T(\tilde{\gamma}) = I_0 \cos^2(\tilde{\gamma} + \gamma_0)$$

$$I_T(\tilde{\gamma}) = I_0 (1 + \cos(2\gamma_0) \cos(2\tilde{\gamma}) - \sin(2\gamma_0) \sin(2\tilde{\gamma})). \quad (\text{B.20})$$

By fitting to a sum of sine and cosines as normal, the peak intensity signal, when the two polarizers are aligned occurs at $\tilde{\gamma} = -\gamma_0$, and can be calculated using

$$\gamma_0 = \frac{1}{2} \arcsin(-S_2/C_2). \quad (\text{B.21})$$

After the calibration polarizer is aligned, mount the quarter-wave plate's rotation stage back into the polarimeter. Proceed as described in calibration B.4.1 to determine δ and β_0 for the waveplate.

B.4.3 Full 2D Fit

If we don't trust that we can remove the waveplate to recalibrate γ_0 without disturbing our system (as is required in calibration B.4.2), we can rotate both $\tilde{\gamma}$ and $\tilde{\beta}$ to acquire a 2D dataset and fit to all parameters simultaneously. The Stokes parameters of the calibration light will be $M = I \cos(2(\tilde{\gamma} - \gamma_0))$ and $C = I \sin(2(\tilde{\gamma} - \gamma_0))$, so the full form of Equation B.11 will become

$$I_T(\tilde{\gamma}, \tilde{\beta}, \gamma_0, \beta_0, \delta) = \frac{I}{2} \left[1 + \frac{\cos(2(\tilde{\gamma} - \gamma_0))}{2} (1 + \cos \delta) + \frac{1}{4} \left(\cos(2(\tilde{\gamma} - \gamma_0)) \cos(4(\tilde{\beta} - \beta_0)) + \sin(2(\tilde{\gamma} - \gamma_0)) \sin(4(\tilde{\beta} - \beta_0)) \right) (1 - \cos \delta) \right]. \quad (\text{B.22})$$

If we acquire a data set with an equal number of points $\tilde{\gamma}, \tilde{\beta}$, then we can write $I_T(\tilde{\gamma}, \tilde{\beta}, \gamma_0, \beta_0, \delta)$ as a linear sum of sines and cosines, and fit to extract γ_0, β_0 and δ .

In fits to data sets acquired over 8 hours, convergence of the linear fit never failed, but reproducibility of results was worse when compared to the calibration techniques in Sections B.4.1 or B.4.2. This is because all of these techniques required a stable laser intensity over the course of a rotation scan. Methods B.4.1 and B.4.2 require only a single rotation of n steps, while method B.4.3 will take n^2 steps to gather the required data set. It seems that the laser power drift on these longer time scales makes the 2D fits noisier than quicker calibration techniques. Normalization of laser power via some other means, or a reduction in the total acquisition time, could make this technique competitive with the other two.

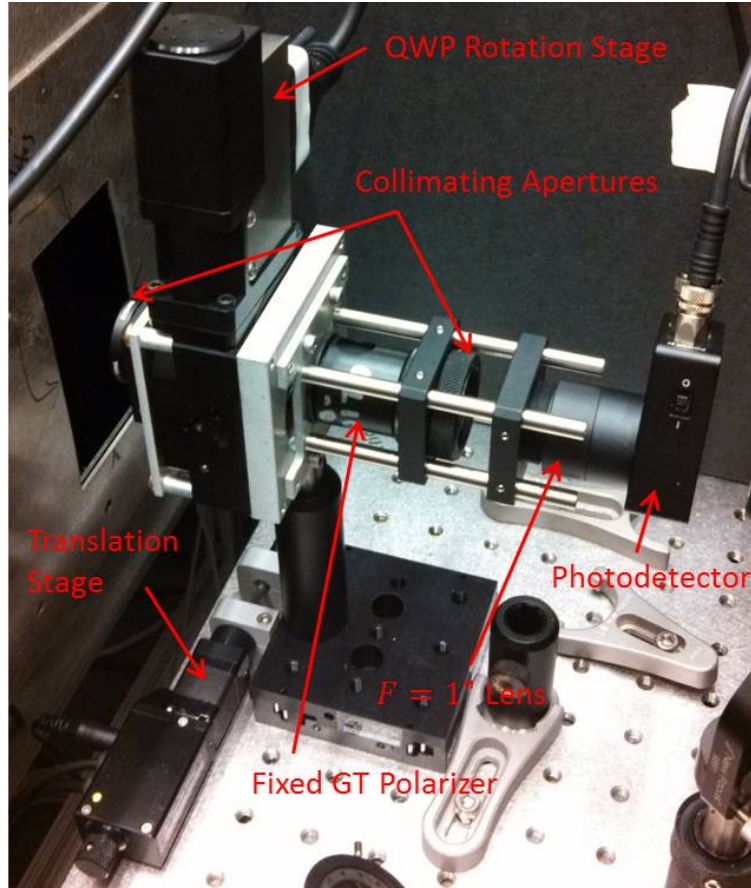


Figure B.3: Stokes polarimeter photograph with annotated components. Essential polarimeter components include irises with 0.8 mm minimum aperture, rotation stage with mounted quarter-wave plate, fixed linear polarizer, $F = 1''$ lens, and high bandwidth amplified photodetector. The whole assembly is placed on an automated translation stage when acquiring polarization gradient data. Component part numbers are listed in Table B.1.

Appendix C

Running the ACME Experiment: VI Operation Specifics

The suite of LabVIEW VIs used to control the ACME experiment has become quite extensive during my tenure. It was founded upon a library of VIs originally written for antihydrogen experiments in our group. Andrew Speck, who wrote much of the code for logging and database access, provided great assistance in initially getting the system underway. The library interfaces LabVIEW based device control with a Microsoft SQL server database structure. There are two fundamental types of databases; a device configuration database and a logging storage database. At the heart of almost every low-level VI, the generic communication VI retrieves device configuration data from the database, and sends commands to devices in a protocol independent way¹. VIs with more complexity are built upon these generic device

¹Specific devices with RS-232, RS-485, or GPIB interfaces are converted to ethernet using dedicated adapter devices. The generic communication VI “GPIB Send+Recieve” automatically parses commands in the format required for each communication protocol.

calls. Some of the most important of these are described in further detail below.

C.1 Programming a Run

The creation of switching waveforms and the flow of EDM data acquisition is controlled via two VIs. At the block and superblock level, the state waveforms are programmed using the “Generated Block Sequence” (GBS) VI, shown in Figure C.1. Each entry in the configuration arrays correspond to a particular switch parameter. Switches performed within a block should be input from least frequent ($\tilde{\mathcal{B}}$) at the top of the array to most frequent ($\tilde{\mathcal{N}}$) at the bottom. State values are input into the *Possible Parameter Sets* array, where each row consists of blocks level switches, and multiple rows can be used to change this configuration between blocks, thus creating a superblock. When multiple rows are used, the *How Many Blocks Before Cycling to Next Set?* field indicates the number of blocks per row, while a value of 0 will randomly chose one of the rows, with probability given by the corresponding value in the *Probability to Select* array. The *Counter Offset* field allows superblock switch phases to be offset with respect to each other. Using the *Random Permute Chosen Set?* boolean, a random permutation of switch states will be generated, as shown in the $\tilde{\mathcal{N}}$ switch configuration on the top of Figure C.1b.

Blocks where one parameter is correlated with another ($\mathcal{B}^{\mathcal{E}}$ or $P^{\mathcal{N}\mathcal{E}}$) can be generated in multiple ways. Figure C.1a shows an older format of configuration array where unique values of some parameter are correlated one-to-one with the *Parameter to Correlate With* state, which means both parameters must have the same number of elements. For example, this structure was used to program a prep laser detuning

scan correlated with a change in the \mathcal{E} -field magnitude, allowing us to identify our $\phi_{ac}(\Delta)$ ac Stark shift systematic (Figure 7.3). For generating parity correlations with multiple parameters, the format shown in Figure C.1b should be used. The state of the parameter is correlated with product of the sign of all parameters listed in the *Parameter Parity to Correlate* array. For example, here the probe power AOM is correlated with $\tilde{\mathcal{N}}$ and $\tilde{\mathcal{E}}$ switches, generating the $P^{\mathcal{N}\mathcal{E}}$ necessary for one of our IPV superblocks. Because the switch's parity is defined as $\text{sign}(s)$, this format cannot create correlation with parameters that do not switch signs, or have more than two states. All final data set superblocks could have been programmed using the latter format, but for historical reasons some were programmed using the latter.

Once a superblock is programmed in GBS, it can be exported to a LabVIEW specific text file. The “Master Run VI” (MRVI) processes these waveforms and determines the locations where parameter states should be switched, as show in Figure 5.1. It executes the necessary subroutines for performing switches and saves phase precession traces and header files after switches are complete. The structure of the uberblocks used in the final data sets is configured in the MRVI. Several saved GBS sequences can be loaded sequentially, and executed for a duration input to the *Number of Blocks per Configuration* field. The current superblock is referenced to the *Current Block #* index, so the uberblock cycle can be manually reset by starting a *New Run*. The data acquisition is paused automatically after *Pause After # of Blocks*, or manually after acquisition of the current block using the *Pause* button. The location within a superblock is referenced to the *Block Cnt* index, which is reset after the automatic cycle pause, so the *Pause After # of Blocks* field should always

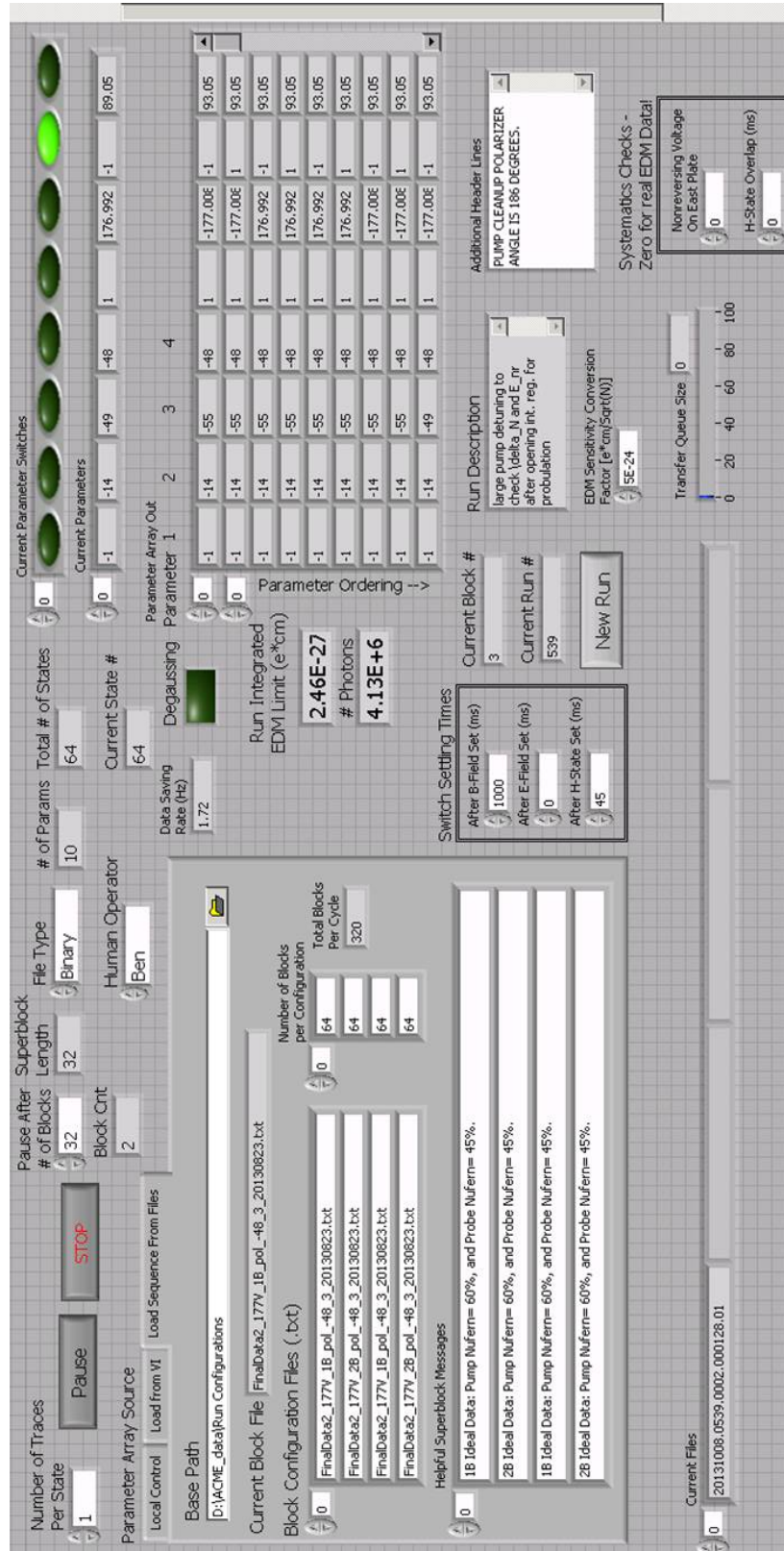


Figure C.2: The “Master Run VI” used for executing block waveform switches, it also allows the concatenating of multiple superblocks in an uberblock.

be longer than the superblock length in order to measure all superblock states. The current experimental state, a summary of the block, and the most recent switches are indicated at right, along with diagnostic timing measurements and photon counts downloaded from signal monitor VI (Demodulate and Plot).

C.2 Doppler Scans of Pump and Probe Lasers

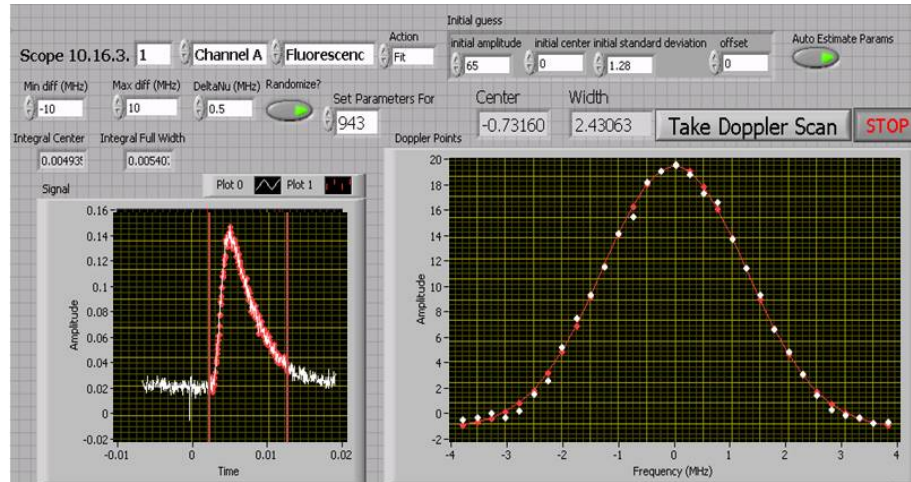
The experiment’s lasers were locked using the transfer cavity stabilization system constructed by Yulia Gurevich [80]. This locking system is able to stabilize the lasers to ~ 1 MHz over several hours, and has proven to be extremely robust, allowing lasers with good temperature regulation and low drift to stay locked for a week or longer. The full Doppler width of the molecular beam at the probe region is ~ 2 MHz, so lasers will stay on resonance despite the drift. A drift in the probe laser frequency will be translated into a reduction of the fluorescence signal sizes, while a drifting state preparation laser will likewise reduce the contrast. By optimizing contrast/signal one can manually recenter the prep/probe lasers onto the $H \rightarrow C$ resonance. Because our experiment is sensitive to detuning dependent phases ($\phi_{ac}(\Delta)$), we decided to automate this process and remove operator bias from the frequent recentering procedure.

Two VIs were developed to tackle this problem, one that fit a signal curve to a Gaussian, and other other that fit the contrast to a flat topped Gaussian line-shape [105, 81]. The software chooses a random array of frequency detunings, pausing to measure an averaged molecular fluorescence signal for each detuning point. The signal monitoring “Doppler Scan VI” (DSVI), is the most general and can be configured to monitor either fluorescence or absorption signals. It tunes the probe

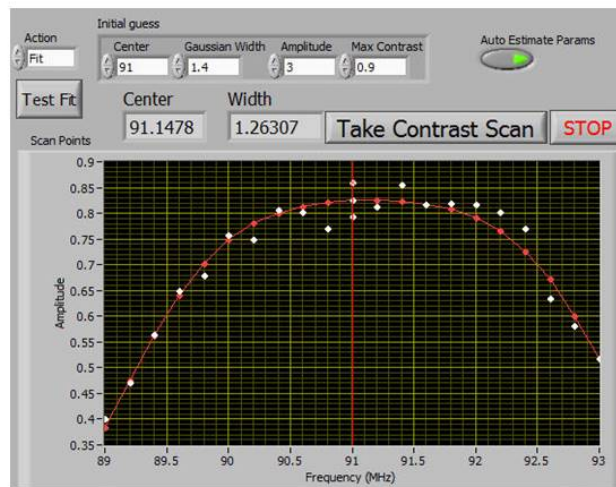
frequency by sending lock point step commands to the laser locking VI, and is capable of broadly tuning the EDCL's peizo over the entire mode hop free tuning range. The downside of this approach is that it detunes both prep and probe lasers, which are derived from the same seed laser (see Section 5.4.2). Therefore, the prep laser is first blocked using an automated beam block so the measurement is sensitive only to the probe's detuning. This VI is also used to center the 943 nm and 690 nm lasers using the same procedure.

A complementary VI, the "Contrast Scan VI" (CSVI) tunes only the state preparation laser by means of the *C*-Prp AOM (Figure 5.7). Monitoring depletion of the bright state quadrature will allow tuning this laser onto resonance using only the fluorescence in the probe region. Since both quadratures are constantly being measured by the polarization modulated probe, the contrast provides a noise-free resonance curve. For our laser parameters, the contrast lineshape is described the by the flat top shape described in Section 4.4. The CSVI fits to the simplest lineshape (least fit parameters), which provides a good fit to the center of the contrast scan.

Given typical signal to noise levels, the center of the signal or contrast lineshapes can typically be determined to within 0.1 MHz. The probe laser detuning is typically recentered at least once per superblock, which also compensates for the prep laser offsets from laser lock drift. Therefore, we only need to be able center the pump resonance with respect to the probe, which may experience differential Doppler shifts due to small beam misalignments. The CSVI is is used to center the pump/probe detuning only after events that have significantly altered the pointing of either beam.



(a)



(b)

Figure C.3: The scan VIs used to center the pump and probe laser frequencies on resonance. **(a)** The DSVI steps through a range of input values, and at each point: 1) adjusts the appropriate lock point, 2) captures a waveform off a Cleverscope, 3) integrates between the selected bounds. The series of measurements is fit to a Gaussian, and the central value is manually fed back into the laser lock VI to correct the detuning. **(b)** The CSVI captures a waveform in a similar way, fitting to a flat top contrast curve to extract the center. The computed contrast at each point is calculated by the “Demodulate and Plot” VI, from which it is fed into the CSVI.

Appendix D

Linearized Decay Fitting

Traditionally, a preferred way of fitting exponential decay $S = A \exp(-t/\tau)$ was by taking $S' = \ln(S)$. If there is no background S' exhibits a linear decay with slope $-1/\tau$, and can be fit using linear regression with no dependence on any initial guesses. The photon counting is Poissonian distributed, so the standard deviation of a measurement S_i in time bin i is $\sigma_i = \sqrt{S_i}$. For $S'_i = \ln(S_i)$, according to error propagation formulas, the uncertainty becomes $\sigma'_i = 1/\sqrt{S_i}$. Weighted linear fits weight by the inverse of the standard deviation, and therefore our weighting function to S'_i data should be $w'_i = e^{S'_i/2}$ [180, 181].

The presence of background B makes the log of

$$S = A \exp(-t/\tau) + B \tag{D.1}$$

nonlinear in τ . Expanding in orders of B/A

$$\ln(S) \approx \ln A - \frac{t}{\tau} + \frac{B}{A} e^{t/\tau} + \dots \tag{D.2}$$

which is valid out until $t/\tau \approx -\ln(B/A)$. Linear fitting can no longer be used when

a decay curve decays into a background. A solution to this problem is to measure and subtract a background from each curve, then linearize and fit. This requires careful treatment of noise in the background, because the $\ln()$ function cannot be applied to any differences $S_i - B \leq 0$. These values are set to zero in order to avoid divergences in the data, and the linear fit is performed only on the subset of data before these noisy values begin to appear. Non-linear fitting routines that directly perform a three parameter fit to Equation D.1 converge to values with comparable uncertainties to linearized fits, but don't suffer from the systematic shifts associated with the uncertainty in background subtraction.

Appendix E

Complete List of Systematic Checks

Category I Parameters
Magnetic Fields
- Non-Reversing \mathcal{B} -Field: $\mathcal{B}_z^{\text{nr}}$
- Transverse \mathcal{B} -Fields: $\mathcal{B}_x, \mathcal{B}_y$ (even and odd under $\tilde{\mathcal{B}}$)
- Magnetic \mathcal{B} -Field Gradients: $\frac{\partial \mathcal{B}_x}{\partial x}, \frac{\partial \mathcal{B}_y}{\partial x}, \frac{\partial \mathcal{B}_y}{\partial y}, \frac{\partial \mathcal{B}_y}{\partial z}, \frac{\partial \mathcal{B}_z}{\partial x}, \frac{\partial \mathcal{B}_z}{\partial z}$ (even and odd under $\tilde{\mathcal{B}}$)
- $\tilde{\mathcal{E}}$ correlated \mathcal{B} -field: $\mathcal{B}^{\tilde{\mathcal{E}}}$ (to simulate $\vec{v} \times \vec{\mathcal{E}}$ /geometric phase/leakage current effects)
Electric Fields
- Non-Reversing \mathcal{E} -Field: \mathcal{E}^{nr}
- \mathcal{E} -Field Ground Offset
Laser Detunings
- Detuning of the Prep/Read Lasers: $\Delta_{\text{prep}}, \Delta_{\text{read}}$
- $\tilde{\mathcal{P}}$ correlated Detuning: $\Delta^{\mathcal{P}}$
- $\tilde{\mathcal{N}}$ correlated Detunings: $\Delta^{\mathcal{N}}, \Delta\Delta^{\mathcal{N}}$
Laser Pointings along \hat{x}
- Change in Pointing of Prep/Read Lasers
- Readout laser \hat{X}/\hat{Y} dependent pointing
- $\tilde{\mathcal{N}}$ correlated laser pointing
- $\tilde{\mathcal{N}}$ and \hat{X}/\hat{Y} dependent laser pointing
Laser Powers
- Power of Prep/Read Lasers: $P_{\text{prep}}, P_{\text{read}}$
- $\tilde{\mathcal{N}}\tilde{\mathcal{E}}$ correlated power, $P^{\mathcal{N}\mathcal{E}}$ (simulating $\Omega_r^{\mathcal{N}\mathcal{E}}$)
- $\tilde{\mathcal{N}}$ correlated power, $P^{\mathcal{N}}$
- \hat{X}/\hat{Y} dependent Readout laser power
Laser Polarization
- Preparation Laser Ellipticity
Molecular Beam Clipping
- Molecule Beam Clipping along the \hat{y} and \hat{z} (changes $\langle v_y \rangle, \langle v_z \rangle, \langle y \rangle, \langle z \rangle$ for molecule ensemble)

Table E.1: Category 1 IPVs: Parameters that were varied far from their values under normal conditions of the experiment. For each of these parameters, direct measurements or limits were placed on possible systematic errors that could couple linearly to each by the method described in the main text. From reference [2].

Category II Parameters
Experiment Timing
- \hat{X}/\hat{Y} Polarization Switching Rate
- Number of Molecule Pulse Averages contributing to an Experiment State
Analysis
- Signal size cuts, Asymmetry magnitude cuts, Contrast cuts
- Difference between two PMT detectors (checking spatial fluorescence region dependence)
- Variation with time within molecule pulse (serves to check v_x dependence)
- Variation with time within polarization switching cycle
- Variation with time throughout the full dataset (autocorrelation)
- Search for correlations with all ϕ , \mathcal{C} , and S switch-parity components
- Search for correlations with auxiliary measurements of \mathcal{B} -fields, laser powers, and vacuum pressure
- 3 individuals performed independent analyses of the data

Table E.2: Category 2 IPVs: Parameters for which all values are considered consistent with normal conditions of the experiment. Although direct limits on systematic errors cannot be derived, these served as checks for the presence of unanticipated systematic errors. From reference [2].

Bibliography

- [1] Purcell, E. M. & Ramsey, N. F. On the Possibility of Electric Dipole Moments for Elementary Particles and Nuclei. *Phys. Rev.* 78, 807 (1950).
- [2] The ACME Collaboration, Baron, J., Campbell, W. C., DeMille, D., Doyle, J. M., Gabrielse, G., Gurevich, Y. V., Hess, P. W., Hutzler, N. R., Kirilov, E., Kozyryev, I., O’Leary, B. R., Panda, C. D., Parsons, M. F., Petrik, E. S., Spaun, B., Vutha, A. C. & West, A. D. Order of magnitude smaller limit on the electric dipole moment of the electron. *Science* 343, 269-272 (2014).
- [3] Regan, B., Commins, E., Schmidt, C. & DeMille, D. New Limit on the Electron Electric Dipole Moment. *Physical Review Letters* 88, 18–21 (2002).
- [4] Hudson, J. J., Kara, D. M., Smallman, I. J., Sauer, B. E., Tarbutt, M. R. & Hinds, E. A. Improved measurement of the shape of the electron. *Nature* 473, 493–496 (2011).
- [5] DeMille, D., Bay, F., Bickman, S., Kawall, D., Hunter, L., Krause, D., Maxwell, S. & Ulmer, K. Search for the electric dipole moment of the electron using metastable PbO. In *AIP Conference Proceedings*, vol. 596, 72–83 (AIP, 2001).
- [6] Eckel, S., Hamilton, P., Kirilov, E., Smith, H. W. & DeMille, D. Search for the electron electric dipole moment using Ω -doublet levels in PbO. *Physical Review A* 87, 52130 (2013).
- [7] Kara, D. M., Smallman, I. J., Hudson, J. J., Sauer, B. E., Tarbutt, M. R. & Hinds, E. A. Measurement of the electron’s electric dipole moment using YbF molecules: methods and data analysis. *New Journal of Physics* 14, 103051 (2012).
- [8] Hutzler, N. R., Parsons, M. F., Gurevich, Y. V., Hess, P. W., Petrik, E., Spaun, B., Vutha, A. C., DeMille, D., Gabrielse, G. & Doyle, J. M. A cryogenic beam of refractory, chemically reactive molecules with expansion cooling. *Physical chemistry chemical physics : PCCP* 13, 18976–18985 (2011).

- [9] Kirilov, E., Campbell, W. C., Doyle, J. M., Gabrielse, G., Gurevich, Y. V., Hess, P. W., Hutzler, N. R., O’Leary, B. R., Petrik, E., Spaun, B., Vutha, A. C. & DeMille, D. Shot-noise-limited spin measurements in a pulsed molecular beam. *Physical Review A* 88, 013844 (2013).
- [10] Vutha, A. C., Campbell, W. C., Gurevich, Y. V., Hutzler, N. R., Parsons, M., Patterson, D., Petrik, E., Spaun, B., Doyle, J. M., Gabrielse, G. & DeMille, D. Search for the electric dipole moment of the electron with thorium monoxide. *Journal of Physics B: Atomic, Molecular and Optical Physics* 43, 74007 (2010).
- [11] Pospelov, M. & Ritz, A. Electric dipole moments as probes of new physics. *Ann. Phys.* 318, 119–169 (2005).
- [12] Bernreuther, W. & Suzuki, M. The electric dipole moment of the electron. *Reviews of Modern Physics* 63, 313 (1991).
- [13] Gabrielse, G. The standard model’s greatest triumph. *Physics Today* 66, 64 (2013).
- [14] The ATLAS Collaboration. A particle consistent with the Higgs boson observed with the ATLAS detector at the Large Hadron Collider. *Science* 338, 1576-1582 (2012).
- [15] The CMS Collaboration. A new boson with a mass of 125 GeV observed with the CMS experiment at the Large Hadron Collider. *Science* 338, 1569-1575 (2012).
- [16] Englert, F. & Brout, R. Broken symmetry and the mass of gauge vector mesons. *Phys. Rev. Lett.* 13, 321–323 (1964).
- [17] Higgs, P. W. Broken symmetries and the masses of gauge bosons. *Phys. Rev. Lett.* 13, 508–509 (1964).
- [18] Chiu, H.-Y. Symmetry between particle and antiparticle populations in the universe. *Phys. Rev. Lett.* 17, 712–714 (1966).
- [19] Sozzi, M. *Discrete Symmetries and CP Violation: From Experiment to Theory*. Oxford Graduate Texts (OUP Oxford, 2008).
- [20] Drees, M. An Introduction to Supersymmetry. *hep-ph/9611409* (1996).
- [21] Beringer, J. *et al.* Status of Higgs boson physics. *Phys. Rev. D* 86, 010001 (2012).
- [22] The LUX Collaboration. First results from the LUX dark matter experiment at the Sanford Underground Research Facility. *Phys. Rev. Lett.* 112, 091303 (2014).

- [23] Beringer, J. *et al.* The CKM quark-mixing matrix. *Phys. Rev. D* 86, 010001 (2012).
- [24] Sakharov, A. Violation of CP Invariance, C Asymmetry, and Baryon Asymmetry of the Universe. *Pisma Zh.Eksp.Teor.Fiz.* 5, 32-35 (1967).
- [25] Cirigliano, V., Li, Y., Profumo, S. & Ramsey-Musolf, M. MSSM baryogenesis and electric dipole moments: an update on the phenomenology. *Journal of High Energy Physics* 2010, 1-23 (2010).
- [26] Fortson, N., Sandars, P. & Barr, S. The search for a permanent electric dipole moment. *Physics Today* 56, 33–39 (2003).
- [27] Engel, J., Ramsey-Musolf, M. J. & van Kolck, U. Electric dipole moments of nucleons, nuclei, and atoms: The standard model and beyond. *Progress in Particle and Nuclear Physics* 71, 21 - 74 (2013).
- [28] Baker, C., Doyle, D. D., Geltenbort, P., Green, K., van der Grinten, M. G. D., Harris, P. G., Iaydjiev, P., Ivanov, S. N., May, D. J. R., Pendlebury, J. M., Richardson, J. D., Shiers, D. & Smith, K. F. Improved Experimental Limit on the Electric Dipole Moment of the Neutron. *Physical Review Letters* 97, 131801 (2006).
- [29] Bennett, G., Bousquet, B., Brown, H., Bunce, G., Carey, R., Cushman, P., Danby, G., Debevec, P., Deile, M., Deng, H., Deninger, W., Dhawan, S., Druzhinin, V., Duong, L., Efstathiadis, E., Farley, F., Fedotovitch, G., Giron, S., Gray, F., Grigoriev, D., Grosse-Perdekamp, M., Grossmann, A., Hare, M., Hertzog, D., Huang, X., Hughes, V., Iwasaki, M., Jungmann, K., Kawall, D., Kawamura, M., Khazin, B., Kindem, J., Krienen, F., Kronkvist, I., Lam, A., Larsen, R., Lee, Y., Logashenko, I., McNabb, R., Meng, W., Mi, J., Miller, J., Mizumachi, Y., Morse, W., Nikas, D., Onderwater, C., Orlov, Y., Özben, C., Paley, J., Peng, Q., Polly, C., Pretz, J., Prigl, R., zu Putlitz, G., Qian, T., Redin, S., Rind, O., Roberts, B., Ryskulov, N., Sedykh, S., Semertzidis, Y., Shagin, P., Shatunov, Y., Sichtermann, E., Solodov, E., Sossong, M., Steinmetz, A., Sulak, L., Timmermans, C., Trofimov, A., Urner, D., von Walter, P., Warburton, D., Winn, D., Yamamoto, A. & Zimmerman, D. Improved limit on the muon electric dipole moment. *Physical Review D* 80, 052008 (2009).
- [30] Adelmann, A., Kirch, K., Onderwater, C. J. G. & Schietinger, T. Compact storage ring to search for the muon electric dipole moment. *Journal of Physics G: Nuclear and Particle Physics* 37, 085001 (2010).
- [31] Landau, L. *Sov. Phys. JETP* 5, 336 (1957).

- [32] Hanneke, D., Fogwell, S. & Gabrielse, G. New Measurement of the Electron Magnetic Moment and the Fine Structure Constant. *Physical Review Letters* 100, 120801 (2008).
- [33] Orzel, C. Searching for new physics through atomic, molecular and optical precision measurements. *Physica Scripta* 86, 068101 (2012).
- [34] Ramsey-Musolf, M. & Su, S. Low-energy precision tests of supersymmetry. *Physics Reports* 456, 1–88 (2008).
- [35] Barr, S. A review of cp violation in atoms. *International Journal of Modern Physics A* 08, 209-236 (1993).
- [36] Sandars, P. G. H. The Electric Dipole Moment of an Atom. *Physics Letters* 14, 194 (1965).
- [37] Khriplovich, I. & Lamoreaux, S. *CP Violation Without Strangeness* (Springer, 1997).
- [38] Commins, E. & DeMille, D. *Probing CP violation with electric dipole moments*, vol. 20 of *Advance Series on Directions in High Energy Physics Series*, chap. 14, 519–581 (World Scientific, Singapore, 2010).
- [39] Pospelov, M. & Ritz, A. CKM benchmarks for electron EDM experiments (2013).
- [40] Murthy, S. A., Krause, D., Li, Z. L. & Hunter, L. R. New limits on the electron electric dipole moment from cesium. *Phys. Rev. Lett.* 63, 965–968 (1989).
- [41] Griffith, W., Swallows, M., Loftus, T., Romalis, M., Heckel, B. & Fortson, E. Improved Limit on the Permanent Electric Dipole Moment of ^{199}Hg . *Physical Review Letters* 102, 101601 (2009).
- [42] Cho, D., Sangster, K. & Hinds, E. A. Tenfold improvement of limits on T violation in thallium fluoride. *Phys. Rev. Lett.* 63, 2559–2562 (1989).
- [43] Loh, H., Cossel, K. C., Grau, M. C., Ni, K.-K., Meyer, E. R., Bohn, J. L., Ye, J. & Cornell, E. A. Precision spectroscopy of polarized molecules in an ion trap. *Science* 342, 1220-1222 (2013).
- [44] Eckel, S., Sushkov, A. O. & Lamoreaux, S. K. Limit on the electron electric dipole moment using paramagnetic ferroelectric $\text{Eu}_{0.5}\text{Ba}_{0.5}\text{TiO}_3$. *Phys. Rev. Lett.* 109, 193003 (2012).
- [45] Salpeter, E. E. Some atomic effects of an electronic electric dipole moment. *Phys. Rev.* 112, 1642–1648 (1958).

- [46] Nelson, D. F., Schupp, A. A., Pidd, R. W. & Crane, H. R. Search for an electric dipole moment of the electron. *Phys. Rev. Lett.* 2, 492–495 (1959).
- [47] Wilkinson, D. T. & Crane, H. R. Precision measurement of the g factor of the free electron. *Phys. Rev.* 130, 852–863 (1963).
- [48] Goldemberg, J. & Torizuka, Y. Upper limit of the electric dipole moment of the electron. *Phys. Rev.* 129, 2580–2581 (1963).
- [49] Ensberg, E. S. *Bull. Am. Phys. Soc.* 7, 534 (1962).
- [50] Ensberg, E. S. Experimental upper limit for the permanent electric dipole moment of ^{85}Rb by optical-pumping techniques. *Phys. Rev.* 153, 36–43 (1967).
- [51] Sandars, P. G. H. & Lipworth, E. Electric dipole moment of the cesium atom. A new upper limit to the electric dipole moment of the free electron. *Phys. Rev. Lett.* 13, 718–720 (1964).
- [52] Lipworth, E., Adler, A., Carrico, J. P., Stein, T. S. & Sandars, T. S. *Bull. Am. Phys. Soc.* 11, 403 (1966).
- [53] Carrico, J. P., Lipworth, E., Sandars, P. G. H., Stein, T. S. & Weisskopf, M. C. Electric dipole moments of alkali atoms. A limit to the electric dipole moment of the free electron. *Phys. Rev.* 174, 125–138 (1968).
- [54] Stein, T. S., Carrico, J. P., Lipworth, E. & Weisskopf, M. C. Electric dipole moment of the cesium atom. A new upper limit to the electric dipole moment of the free electron. *Phys. Rev. Lett.* 19, 741–743 (1967).
- [55] Angel, J., Sandars, P. & Tinker, M. Observation of a $v \times E$ effect in an electric dipole moment experiment using a reversible atomic beam machine. *Physics Letters A* 25, 160 - 161 (1967).
- [56] Weisskopf, M. C., Carrico, J. P., Gould, H., Lipworth, E. & Stein, T. S. Electric dipole moment of the cesium atom. A new upper limit to the electric dipole moment of the electron. *Phys. Rev. Lett.* 21, 1645–1648 (1968).
- [57] Gould, H. Search for an electric dipole moment in thallium. *Phys. Rev. Lett.* 24, 1091–1093 (1970).
- [58] Abdullah, K., Carlberg, C., Commins, E. D., Gould, H. & Ross, S. B. New experimental limit on the electron electric dipole moment. *Phys. Rev. Lett.* 65, 2347–2350 (1990).
- [59] Commins, E., Ross, S., DeMille, D. & Regan, B. Improved experimental limit on the electric dipole moment of the electron. *Physical Review A* 50, 2960–2977 (1994).

- [60] Player, M. A. & Sandars, P. G. H. An experiment to search for an electric dipole moment in the 3P_2 metastable state of xenon. *J. Phys. B* 3, 1620–1635 (1970).
- [61] Vold, T. G., Raab, F. J., Heckel, B. & Fortson, E. N. Search for a permanent electric dipole moment on the ^{129}Xe atom. *Phys. Rev. Lett.* 52, 2229–2232 (1984).
- [62] Rosenberry, M. A. & Chupp, T. E. Atomic electric dipole moment measurement using spin exchange pumped masers of ^{199}Hg and ^3He . *Phys. Rev. Lett.* 86, 22–25 (2001).
- [63] Lamoreaux, S. K., Jacobs, J. P., Heckel, B. R., Raab, F. J. & Fortson, N. New constraints on time-reversal asymmetry from a search for a permanent electric dipole moment of ^{199}Hg . *Phys. Rev. Lett.* 59, 2275–2278 (1987).
- [64] Jacobs, J. P., Klipstein, W. M., Lamoreaux, S. K., Heckel, B. R. & Fortson, E. N. Testing time-reversal symmetry using ^{199}Hg . *Phys. Rev. Lett.* 71, 3782–3785 (1993).
- [65] Jacobs, J. P., Klipstein, W. M., Lamoreaux, S. K., Heckel, B. R. & Fortson, E. N. Limit on the electric-dipole moment of ^{199}Hg using synchronous optical pumping. *Phys. Rev. A* 52, 3521–3540 (1995).
- [66] Romalis, M. V., Griffith, W. C., Jacobs, J. P. & Fortson, E. N. New limit on the permanent electric dipole moment of ^{199}Hg . *Phys. Rev. Lett.* 86, 2505–2508 (2001).
- [67] Hinds, E. A. & Sandars, P. G. H. Experiment to search for P - and T -violating interactions in the hyperfine structure of thallium fluoride. *Phys. Rev. A* 21, 480–487 (1980).
- [68] Wilkening, D. A., Ramsey, N. F. & Larson, D. J. Search for P and T violations in the hyperfine structure of thallium fluoride. *Phys. Rev. A* 29, 425–438 (1984).
- [69] Schropp, D., Cho, D., Vold, T. & Hinds, E. A. New limits on time-reversal invariance from the hyperfine structure of thallium fluoride. *Phys. Rev. Lett.* 59, 991–994 (1987).
- [70] Hudson, J., Sauer, B., Tarbutt, M. & Hinds, E. Measurement of the Electron Electric Dipole Moment Using YbF Molecules. *Physical Review Letters* 89, 8–11 (2002).
- [71] Vasil'ev, B. V. & Kolycheva, E. V. Measurement of the electric dipole moment of the electron with a quantum interferometer. *JETP* 47, 243 (1978).

- [72] Heidenreich, B. J., Elliott, O. T., Charney, N. D., Virgien, K. A., Bridges, A. W., McKeon, M. A., Peck, S. K., Krause, D., Gordon, J. E., Hunter, L. R. & Lamoreaux, S. K. Limit on the electron electric dipole moment in gadolinium-iron garnet. *Phys. Rev. Lett.* 95, 253004 (2005).
- [73] Kim, Y. J., Liu, C.-Y., Lamoreaux, S. K. & Reddy, G. Experimental search for the electron electric dipole moment using solid state techniques. *Journal of Physics: Conference Series* 312, 102009 (2011).
- [74] Hamilton, P. *Preliminary results in the search for the electron electric dipole moment in PbO**. Ph.D. thesis, Yale University (2010).
- [75] Bollinger, J. J., Itano, W. M., Wineland, D. J. & Heinzen, D. J. Optimal frequency measurements with maximally correlated states. *Phys. Rev. A* 54, R4649–R4652 (1996).
- [76] Leibfried, D., Barrett, M. D., Schaetz, T., Britton, J., Chiaverini, J., Itano, W. M., Jost, J. D., Langer, C. & Wineland, D. J. Toward Heisenberg-limited spectroscopy with multiparticle entangled states. *Science* 304, 1476–1478 (2004).
- [77] Leanhardt, A. E., Bohn, J. L., Loh, H., Maletinsky, P., Meyer, E. R., Sinclair, L. C., Stutz, R. P. & Cornell, E. A. High-resolution spectroscopy on trapped molecular ions in rotating electric fields : A new approach for measuring the electron electric dipole moment. *Journal of Molecular Spectroscopy* 270, 1–25 (2011).
- [78] Brown, J. & Carrington, A. *Rotational Spectroscopy of Diatomic Molecules* (Cambridge University Press, 2003).
- [79] Bernath, P. *Spectra of Atoms and Molecules* (Oxford University Press, 2005), 2nd edn.
- [80] Gurevich, Y. V. *Preliminary Measurements for an Electron EDM Experiment in ThO*. Ph.D. thesis, Harvard University (2012).
- [81] Hutzler, N. R. *A New Limit on the Electron Electric Dipole Moment: Beam Production, Data Interpretation, and Systematics*. Ph.D. thesis, Harvard University (2014).
- [82] Brown, J. M., Cheung, A. S.-C. & Merer, A. J. Λ -Type doubling parameters for molecules in Δ electronic states. *Journal of Molecular Spectroscopy* 124, 464–475 (1987).

- [83] Petrov, A. N., Skripnikov, L. V., Titov, A. V., Hutzler, N. R., Hess, P. W., O’Leary, B. R., Spaun, B., DeMille, D., Gabrielse, G. & Doyle, J. M. Zeeman interaction in ThO $H^3\Delta_1$ for the electron EDM search. *arXiv*: 1404.4024 [physics.atom-ph] (2014).
- [84] DeMille, D., Bay, F., Bickman, S., Kawall, D., Krause, D., Maxwell, S. & Hunter, L. Investigation of PbO as a system for measuring the electric dipole moment of the electron. *Physical Review A* 61, 52507 (2000).
- [85] Kozlov, M. & DeMille, D. Enhancement of the Electric Dipole Moment of the Electron in PbO. *Physical Review Letters* 89, 133001 (2002).
- [86] Bickman, S., Hamilton, P., Jiang, Y. & DeMille, D. Preparation and detection of states with simultaneous spin alignment and selectable molecular orientation in PbO. *Physical Review A* 80, 23418 (2009).
- [87] Lee, J., Meyer, E. R., Paudel, R., Bohn, J. L. & Leanhardt, A. E. An electron electric dipole moment search in the X $^3\Delta_1$ ground state of tungsten carbide molecules. *Journal of Modern Optics* 56, 2005–2012 (2009).
- [88] Skripnikov, L. V., Petrov, A. N. & Titov, A. V. Communication: theoretical study of ThO for the electron electric dipole moment search. *The Journal of Chemical Physics* 139, 221103 (2013).
- [89] Meyer, E. R. & Bohn, J. L. Prospects for an electron electric-dipole moment search in metastable ThO and ThF⁺. *Phys. Rev. A* 78, 10502 (2008).
- [90] Commins, E. D., Jackson, J. D. & DeMille, D. P. The electric dipole moment of the electron: An intuitive explanation for the evasion of Schiff’s theorem. *American Journal of Physics* 75, 532 (2007).
- [91] Hinds, E. A. Testing time reversal symmetry using molecules. *Phys. Scr.* T70, 34–41 (1997).
- [92] Schiff, L. I. Measurability of Nuclear Electric Dipole Moments. *Physical Review* 132, 2194 (1963).
- [93] Edvinsson, G. & Lagerqvist, A. Rotational analysis of yellow and near infrared bands in ThO. *Physica Scripta* 30, 309–320 (1984).
- [94] Edvinsson, G. & Lagerqvist, A. Rotational analysis of some violet and green bands in the ThO spectrum. *Journal of Molecular Spectroscopy* 122, 428–439 (1987).
- [95] Sushkov, O. P. & Flambaum, V. V. Parity breaking effects in diatomic molecules. *Sov. Phys. JETP* 48, 608–611 (1978).

- [96] Amini, J. M., Munger, C. T. & Gould, H. Electron electric-dipole-moment experiment using electric-field quantized slow cesium atoms. *Phys. Rev. A* 75, 063416 (2007).
- [97] Vutha, A. C., Spaun, B., Gurevich, Y. V., Hutzler, N. R., Kirilov, E., Doyle, J. M., Gabrielse, G. & DeMille, D. Magnetic and electric dipole moments of the $H\ ^3\Delta_1$ state in ThO. *Phys. Rev. A* 84, 034502 (2011).
- [98] Munger, C. T. Magnetic Johnson noise constraints on electron electric dipole moment experiments. *Phys. Rev. A* 72, 012506 (2005).
- [99] Rosenband, T., Schmidt, P. O., Hume, D. B., Itano, W. M., Fortier, T. M., Stalnaker, J. E., Kim, K., Diddams, S. A., Koelemeij, J. C. J., Bergquist, J. C. & Wineland, D. J. Observation of the $^1S_0 \rightarrow ^3P_0$ clock transition in $^{27}\text{Al}^+$. *Phys. Rev. Lett.* 98, 220801 (2007).
- [100] Ramsey, N. F. A Molecular Beam Resonance Method with Separated Oscillating Fields. *Physical Review* 78, 695 (1950).
- [101] Campbell, W. C., Chan, C., DeMille, D., Doyle, J. M., Gabrielse, G., Gurevich, Y. V., Hess, P. W., Hutzler, N. R., Kirilov, E., O’Leary, B., Petrik, E. S., Spaun, B. & Vutha, A. C. Advanced cold molecule electron EDM. *EPJ Web of Conferences* 57, 02004 (2013).
- [102] Maxwell, S. E., Brahms, N., DeCarvalho, R., Glenn, D. R., Helton, J. S., Nguyen, S. V., Patterson, D., Petricka, J., DeMille, D. & Doyle, J. M. High-Flux Beam Source for Cold, Slow Atoms or Molecules. *Physical Review Letters* 95, 173201 (2005).
- [103] Hutzler, N. R., Lu, H.-I. & Doyle, J. M. The buffer gas beam: an intense, cold, and slow source for atoms and molecules. *Chemical reviews* 112, 4803–4827 (2012).
- [104] Gray, H. R., Whitley, R. M. & Stroud, C. R. Coherent trapping of atomic populations. *Opt. Lett.* 3, 218–220 (1978).
- [105] Spaun, B. *A Ten-Fold Improvement to the Limit of the Electron Electric Dipole Moment*. Ph.D. thesis, Harvard University (2014).
- [106] Vutha, A. C. *A search for the electric dipole moment of the electron using thorium monoxide*. Ph.D. thesis, Yale University (2011).
- [107] The ACME Collaboration. New limit on the electric dipole moment of the electron: data analysis and systematics (2014).
- [108] Griffiths, D. J. *Introduction to Electrodynamics* (Prentice-Hall, 1999), 3rd edn.

- [109] Budker, D., Rochester, S. M. & Yashchuk, V. V. Obtaining frequency markers of variable separation with a spherical mirror fabry-perot interferometer. *Review of Scientific Instruments* 71, 2984-2987 (2000).
- [110] Hall, J., Ma, L.-S., Taubman, M., Tiemann, B., Hong, F., Pfister, O. & Ye, J. Stabilization and frequency measurement of the I₂-stabilized Nd:YAG laser. *IEEE Transactions On Instrumentation And Measurement* 48, 583-586 (1998).
- [111] Farkas, D. *An Optical Reference and Frequency Comb for Improved Spectroscopy of Helium*. Ph.D. thesis, Harvard University (2006).
- [112] Zhao, W. Z., Simsarian, J. E., Orozco, L. A. & Sprouse, G. D. A computer-based digital feedback control of frequency drift of multiple lasers. *Review of Scientific Instruments* 69, 3737-3740 (1998).
- [113] Edvinsson, G., Bornstedt, A. & Nylén, P. Rotational Analysis for a Perturbed ¹Π state in ThO. *Ark. Phys.* 38, 193 (1968).
- [114] Edvinsson, G. & Lagerqvist, A. Two new band systems in ThO. *Physica Scripta* 41, 316-320 (1990).
- [115] Paulovič, J., Nakajima, T., Hirao, K., Lindh, R. & Malmqvist, P. Å. Relativistic and correlated calculations on the ground and excited states of ThO. *J. Chem. Phys.* 119, 798-805 (2003).
- [116] Au, Y. S. *Inelastic Collisions of Atomic Thorium and Molecular Thorium Monoxide with Cold Helium-3*. Ph.D. thesis, Harvard University (2013).
- [117] Andrä, H. J., Gaupp, A. & Wittmann, W. New method for precision lifetime measurements by laser excitation of fast-moving atoms. *Phys. Rev. Lett.* 31, 501-504 (1973).
- [118] Tanner, C., Livingston, A., Rafac, R., Kukla, K., Berry, H. & Kurtz, C. Precision lifetime measurements using laser excitation of a fast atomic beam. *Nuclear Instruments and Methods in Physics Research Section B: Beam Interactions with Materials and Atoms* 99, 117 - 120 (1995).
- [119] Tanner, C. E., Livingston, A. E., Rafac, R. J., Serpa, F. G., Kukla, K. W., Berry, H. G., Young, L. & Kurtz, C. A. Measurement of the 6p²p_{3/2} state lifetime in atomic cesium. *Phys. Rev. Lett.* 69, 2765-2767 (1992).
- [120] DiBerardino, D., Rafac, R. J., Boone, S., Gerginov, V. P. & Tanner, C. E. Construction of fiber-optic bundle light-collection systems and calculations of collection efficiency. *Optics Communications* 210, 233 - 243 (2002).

- [121] Becker, W. *Advanced Time-Correlated Single Photon Counting Techniques*. Springer Series in Chemical Physics (Springer, 2005).
- [122] Hamamatsu Photonics K.K. Editorial Committee. *Photomultiplier Tubes: Basics and Applications*. Hamamatsu Photonics K.K. Electron Tube Division, 3rd edn. (2006).
- [123] Whiting, E. E., Schadee, A., Tatum, J. B., Hougen, J. T. & Nicholls, R. W. Recommended conventions for defining transition moments and intensity factors in diatomic molecular spectra. *Journal of Molecular Spectroscopy* 80, 249 - 256 (1980).
- [124] Herzberg, G. *Molecular Spectra and Molecular Structure: Spectra of Diatomic Molecules* (D. Van Nostrand, 1950).
- [125] Zare, R. N. *Angular Momentum* (John Wiley & Sons, New York, 1988).
- [126] Budker, D., Kimball, D. & DeMille, D. *Atomic physics: An exploration through problems and solutions* (Oxford University Press, USA, 2008).
- [127] Kuchle, W., Dolg, M., Stoll, H., Preuss, H., Kihle, W. & Stall, H. Energy-adjusted pseudopotentials for the actinides. Parameter sets and test calculations for thorium and thorium monoxide. *J. Chem. Phys.* 100, 7535–7542 (1994).
- [128] O’Leary, B. Rotational cooling in the next generation. Tech. Rep., ACME Collaboration (2014).
- [129] Wentink, T. & Spindler, R. J. The isoelectronic series ScF through ThO: Notes on the band spectra of TiO, HfO and ThO. *Journal of Quantitative Spectroscopy and Radiative Transfer* 12, 1569 - 1590 (1972).
- [130] Foot, C. *Atomic Physics*. Oxford Master Series in Atomic, Optical and Laser Physics (Oxford University Press, New York, 2005).
- [131] Hilborn, R. C. Einstein coefficients, cross sections, f values, dipole moments, and all that. *arxiv: physics/0202029* (2002).
- [132] Steck, D. A. *Quantum and Atom Optics* (available online at <http://steck.us/teaching>, 2007).
- [133] Yariv, A. & Yeh, P. *Photonics: Optical Electronics in Modern Communications* (Oxford University Press, 2007), 6th edn.
- [134] Eisenbach, S., Lotem, H., Horvitz, Z., Miron, G., Lando, M. & Gabay, S. Thermally induced window birefringence in high-power copper vapor laser. *Proc. SPIE* 1972, 13-26 (1993).

- [135] Barber, J. *Elasticity*, chap. Thermoelasticity, 201–205 (Kluwer Academic Publishers, 2002), 2nd edn.
- [136] Dally, J. W. & Riley, W. F. *Experimental Stress Analysis*, chap. Theory of Photoelasticity, 406–412 (McGraw-Hill, 1978), 2nd edn.
- [137] Berry, H. G., Gabrielse, G. & Livingston, A. E. Measurement of the stokes parameters of light. *Appl. Opt.* 16, 3200–3205 (1977).
- [138] O’Leary, B. Insertion magnetometry with probulator. Tech. Rep., ACME Collaboration (2013).
- [139] Jefferts, S. R., Shirley, J., Parker, T. E., Heavner, T. P., Meekhof, D. M., Nelson, C., Levi, F., Costanzo, G., Marchi, A. D., Drullinger, R., Hollberg, L., Lee, W. D. & Walls, F. L. Accuracy evaluation of NIST-F1. *Metrologia* 39, 321 (2002).
- [140] Hudson, J. J., Ashworth, H. T., Kara, D. M., Tarbutt, M. R., Sauer, B. E. & Hinds, E. A. Pulsed beams as field probes for precision measurement. *Phys. Rev. A* 76, 033410 (2007).
- [141] Vutha, A. & DeMille, D. Geometric phases without geometry. *arXiv*: 0907.5116 (2009).
- [142] Commins, E. D. Berry’s geometric phase and motional fields. *American Journal of Physics* 59, 1077 (1991).
- [143] Griffiths, D. J. *Introduction to Quantum Mechanics* (Pearson Prentice Hall, 2005), 2nd edn.
- [144] Shore, B. W. *Multilevel Atoms and Incoherence*, vol. 2 of *The Theory of Coherent Atomic Excitation* (John Wiley & Sons, New York, 1990).
- [145] Allen, L. & Eberly, J. *Optical resonance and two-level atoms* (Wiley, 1975).
- [146] Patten, R. A. Michelson Interferometer as a Remote Gauge. *Applied Optics* 10, 2717–2721 (1971).
- [147] Edvinsson, G., Selin, L.-E. & Aslund, N. On the band spectrum of ThO. *Ark. Phys.* 30, 283–319 (1965).
- [148] O’Leary, B. Rabi frequency correlations coupling to resonant light shifts. Tech. Rep., ACME Collaboration (2013).
- [149] Sobelman, I. I. *Atomic Spectra and Radiative Transitions* (Springer Berlin Heidelberg, 1992).

- [150] Shore, B. W. *Simple Atoms and Fields*, vol. 1 of *The Theory of Coherent Atomic Excitation* (John Wiley & Sons, New York, 1990).
- [151] Condon, E. & Shortley, G. *The Theory of Atomic Spectra* (Cambridge University Press, 1951).
- [152] Curtiss, J. H. On the Distribution of the Quotient of Two Chance Variables. *The Annals of Mathematical Statistics* 12, 409–421 (1941).
- [153] Feldman, G. J. & Cousins, R. D. Unified approach to the classical statistical analysis of small signals. *Phys. Rev. D* 57, 3873–3889 (1998).
- [154] Klein, J. R. & Roodman, A. Blind Analysis in Nuclear and Particle Physics. *Annual Review of Nuclear and Particle Science* 55, 141–163 (2005).
- [155] Fleig, T. & Nayak, M. K. Electron electric dipole moment and hyperfine interaction constants for ThO. *Journal of Molecular Spectroscopy* Available Online (2014).
- [156] Kozlov, M. G., Titov, A. V., Mosyagin, N. S. & Souchko, P. V. Enhancement of the electric dipole moment of the electron in the BaF molecule. *Phys. Rev. A* 56, R3326–R3329 (1997).
- [157] Rellergert, W. G., DeMille, D., Greco, R. R., Hehlen, M. P., Torgerson, J. R. & Hudson, E. R. Constraining the evolution of the fundamental constants with a solid-state optical frequency reference based on the ^{229}Th nucleus. *Phys. Rev. Lett.* 104, 200802 (2010).
- [158] Safronova, M. S., Safronova, U. I., Radnaev, A. G., Campbell, C. J. & Kuzmich, A. Magnetic dipole and electric quadrupole moments of the ^{229}Th nucleus. *Phys. Rev. A* 88, 060501 (2013).
- [159] Campbell, C. J., Radnaev, A. G. & Kuzmich, A. Wigner crystals of ^{229}Th for optical excitation of the nuclear isomer. *Phys. Rev. Lett.* 106, 223001 (2011).
- [160] Kozlov, M. G. & Labzowsky, L. N. Parity violation effects in diatomics. *Journal of Physics B: Atomic, Molecular and Optical Physics* 28, 1933–1961 (1995).
- [161] Dzuba, V. A., Flambaum, V. V. & Harabati, C. Relations between matrix elements of different weak interactions and interpretation of the parity-nonconserving and electron electric-dipole-moment measurements in atoms and molecules. *Phys. Rev. A* 84, 052108 (2011).
- [162] Ilakovac, A., Pilaftsis, A. & Popov, L. Lepton dipole moments in supersymmetric low-scale seesaw models. *Phys. Rev. D* 89, 015001 (2014).

- [163] Bergmann, K., Theuer, H. & Shore, B. W. Coherent population transfer among quantum states of atoms and molecules. *Rev. Mod. Phys.* 70, 1003–1025 (1998).
- [164] Romanenko, V. & Yatsenko, L. Adiabatic population transfer in the three-level Λ -system: two-photon lineshape. *Optics Communications* 140, 231 - 236 (1997).
- [165] Alnis, J., Matveev, A., Kolachevsky, N., Wilken, T., Holzwarth, R. & Hänsch, T. W. Stable diode lasers for hydrogen precision spectroscopy. *The European Physical Journal Special Topics* 163, 89-94 (2008).
- [166] Darnell, A. J., McCollum, W. A. & Milne, T. A. Vapor Pressure of Thorium. *Journal of Physical Chemistry* 64, 341–346 (1960).
- [167] Kawasaki, Y., Bertaina, M., Sakaki, N., Shimizu, H., Inoue, N., Hasegawa, S., Ohtsu, I., Adachi, T., Ebisuzaki, T., Hirota, K., Ikeda, K., Kajino, F., Morishima, T., Nagano, M., Sato, M., Sawabe, T., Shibata, T., Shinohara, T., Takeda, M., Takizawa, Y., Uchihori, Y. & Wada, Y. Performance of a multi-anode photomultiplier employing a weak electrostatic focusing system (Hamamatsu R8900 series). *Nuclear Instruments and Methods in Physics Research Section A: Accelerators, Spectrometers, Detectors and Associated Equipment* 564, 378 - 394 (2006).
- [168] Toizumi, T., Inagawa, S., Nakamori, T., Kataoka, J., Tsubuku, Y., Yatsu, Y., Shimokawabe, T., Kawai, N., Okada, T. & Ohtsu, I. Performance of a multi-anode photomultiplier employing an ultra bi-alkali photo-cathode and rugged dynodes. *Nuclear Instruments and Methods in Physics Research Section A: Accelerators, Spectrometers, Detectors and Associated Equipment* 604, 168 - 173 (2009).
- [169] Bickman, S. & DeMille, D. Large-area, low-noise, high-speed, photodiode-based fluorescence detectors with fast overdrive recovery. *Review of Scientific Instruments* 76, 113101 (2005).
- [170] Fox, J. J., Woodard, N. & Lafyatis, G. P. Characterization of cooled large-area silicon avalanche photodiodes. *Review of Scientific Instruments* 70, 1951 (1999).
- [171] Incandela, J., Ahlen, S., Beatty, J., Ciocio, A., Felcini, M., Ficenec, D., Hazen, E., Levin, D., Marin, A., Stone, J., Sulak, L. & Worstell, W. The performance of photomultipliers exposed to helium. *Nuclear Instruments and Methods in Physics Research Section A: Accelerators, Spectrometers, Detectors and Associated Equipment* 269, 237 - 245 (1988).

- [172] Lombard, F. J. & Martin, F. Statistics of electron multiplication. *Review of Scientific Instruments* 32, 200-201 (1961).
- [173] MacLeod, A. *Measuring the gain of a photomultiplier tube*. Master's thesis, McGill University (2007).
- [174] Sabatke, D. S., Descour, M. R., Dereniak, E. L., Sweatt, W. C., Kemme, S. A. & Phipps, G. S. Optimization of retardance for a complete Stokes polarimeter. *Opt. Lett.* 25, 802-804 (2000).
- [175] Ambirajan, A. & Look, D. C. Optimum angles for a polarimeter: part I. *Optical Engineering* 34, 1651-1655 (1995).
- [176] Dlugunovich, V., Snopko, V. & Tsaryuk, O. Allowance for the imperfection of optical elements and inaccuracy in the initial adjustment of the rotating phase plate in a Stokes polarimeter. *Journal of Applied Spectroscopy* 67, 528-535 (2000).
- [177] Dong, H., Tang, M. & Gong, Y. Noise properties of uniformly-rotating RRFP Stokes polarimeters. *Opt. Express* 21, 9674-9690 (2013).
- [178] Tyo, J. S. Design of optimal polarimeters: Maximization of signal-to-noise ratio and minimization of systematic error. *Appl. Opt.* 41, 619-630 (2002).
- [179] O'Leary, B. Weak field precession model. Tech. Rep., ACME Collaboration (2012).
- [180] Bevington, P. R. & Robinson, D. K. *Data reduction and error analysis for the physical sciences* (McGraw-Hill, Boston, 2003), 3rd edn.
- [181] Taylor, J. R. *An Introduction to Error Analysis* (University Science Books, 1996), 2nd edn.